UNIVERSITA' DEGLI STUDI DI MESSINA
DIPARTIMENTO DI SCIENZE MATEMATICHE E
INFORMATICHE, SCIENZE FISICHE E DELLA TERRA

DOCTORAL PROGRAMME IN PHYSICS (CYCLE XXXIII)

New frontiers in cultural heritage for polychrome wooden diagnostics: CT, MRI and micro-Raman imaging investigations.

Doctoral Dissertation
of:
Sveva Longo
S.S.D FIS/01-FIS/07

SUPERVISOR:
Prof. Enza Fazio

CO-SUPERVISOR:
Dr. Silvia Capuani

COORDINATOR:
Prof. Vincenza Crupi

Academic Year 2019/2020

Contents

Introduction 1

1. Cultural Heritage wooden objects investigations: state of the art 3
1.1 Wood structure..... 5
1.2 Softwood and Hardwood..... 8
1.3 Wood identification..... 9
1.4 Water and wood..... 15
1.5 Analytical methods for assessing archeological wood..... 18

2. X-ray Computed Tomography 26
2.1 Production of X-rays..... 27
2.2 Interaction of X-rays with matter..... 30
2.3 Principles of Computed Tomography..... 33
2.4 CT instruments..... 34
2.5 Multislice Compute Tomography (MSCT)..... 37
2.6 CT image processing and Hounsfield Units..... 39
2.7 X-ray Computed Tomography applied to Cultural Heritage..... 41

3. Nuclear Magnetic Resonance 44
3.1 NMR principles..... 46
3.2 Magnetization and its relaxation..... 53
3.2.1 Magnetization..... 53
3.2.2 Longitudinal relaxation time T_1..... 57
3.2.3 Transverse relaxation time T_2..... 59
3.2.4 Inversion Recovery and Spin-Echo pulse sequences..... 60
3.3 Magnetic Resonance Imaging (MRI)..... 63
3.4 Chemical shift..... 67
3.5 MRI scanners..... 68
3.6 MRI applied to Cultural Heritage..... 69

4. Raman Spectroscopy and Surface Enhanced Raman Scattering (SERS) 73
4.1 Raman Spectroscopy..... 75
4.1.2 Surface Enhanced Raman Scattering (SERS)..... 76
4.2 Surface plasmons in metallic nanoparticles..... 81
4.3 Raman imaging: principle and statistical data analysis..... 94
4.4 Raman imaging and SERS applications..... 100

5. Novel diagnostic approaches for wood characterization 104
5.1 Multislice Computed Tomography (MSCT) results on contemporary samples and wooden painted tablets..... 105
5.2 Nuclear Magnetic Resonance (MRI and μMRI)..... 124
5.2.1 MRI clinical scanner results on contemporary samples.....124
5.2.2 MRI clinical scanner results on archaeological waterlogged samples..... 142
5.2.3 μMRI results on contemporary samples.....145

5.2.4 μMRI results on archaeological waterlogged samples..... 151
5.3 FTIR, Raman/SERS and SEM-EDX..... 155
5.3.1 FTIR and Raman/SERS results on contemporary samples.. 155
5.3.2 SEM-EDX, FTIR and Raman results on archaeological waterlogged samples.....163
5.4 UV-vis optical absorption, FTIR and Raman/SERS results on painted wooden tablets.....168

6. MSCT characterization of an Egyptian Coffin 175
6.1 Egyptian coffin..... 175
6.2 MSCT and post-processing techniques..... 176
6.3 MPR and VRT results..... 179
6.3.1 Multi-planar Reconstruction (MPR)..... 179
6.3.2 Volume Rendering Technique (VRT)..... 185
6.4 Discussion and conclusions..... 192

7. MSCT characterization of a seventeen-century Dutch wooden painting 196
7.1 Dutch wooden painting..... 196
7.2 MSCT results and discussion..... 198

Conclusions 208

References 210

Appendix 228

Acknowledgments 233

Introduction

To understand what has happened to a historic object, it is important to know the structure of the original wood. All this must be done through non-destructive techniques without compromising the integrity of the observed object.

In recent years, it emerged the importance of defining the relationship between the morphological characteristics and the micro- and ultrastructure of wood tissues, as expressed by the thickness of tracheid walls, lignin content and crystallinity of cellulose as well as by its hydrophobic capacity. On the overall, it is essential a profound knowledge of the compositional-structural and morphological properties of wood and, particularly, a knowledge of their interdependencies. With this information, it will be possible to understand the degradation that has occurred over time and, in turn, to define a potential method of conservation and preservation of the artworks.

Technological progress has allowed the development of many non-destructive diagnostic methods, such as X-rays Computed Tomography (CT), ultrasounds (Zisi 2017), Nuclear Magnetic Resonance (NMR) (Proietti 2014) technique together new working configurations of the conventional FTIR and Raman spectroscopies (Macchioni 2012, Gierlinger 2007). CT and NMR techniques are very widespread in the field of medicine, allowing to observe internal parts of the human body without any harm to the patient. Although they are non-destructive diagnostic tool traditionally applied in clinical medicine, its application to materials science is a field in continuous evolution.

The research activities carried out during the PhD course in Physics whose results are reported in this thesis regard the development of a protocol suitable for the study of ancient wood by

clinical CT and NMR. First, contemporary wood samples were analysed to define and optimize CT and NMR procedures. Then, the same techniques were used to characterize archaeological waterlogged wood samples and ancient wooden objects. Then, CT and NMR results were combined to those obtained by micro-imaging NMR, micro-Raman and FTIR spectroscopies. The synergic use of these techniques, probing the system energies on different scales, is proposed as an innovative approach, which have allowed to carry out wood and wooden works analyses in a systematic and complete manner. Furthermore, for the first time, the interesting potentiality of the comparative analysis of all the collected data have allowed to characterize materials on an Egyptian Coffin and its implementation methods, making possible to recognize reuse wood planks. On waterlogged wood samples coming from Naples and Denmark information about water imbibition were collected. Identification of the species were performed for the first time with NMR-microimaging analysis.

CT analyses were carried out at Neuroradiology Unit-Department of Policlinico University Hospital of Messina, Italy.

NMR measurements were carried out in the NMR Laboratory of Institute of Complex System of the National Italian Council of Research (CNR-ISC) at Sapienza University of Rome and at IRCCS Santa Lucia of Rome, Italy.

Ultimately, FTIR and Raman analyses were carried out in MNS laboratories in the MIFT Department of the University of Messina.

Chapter 1

Cultural Heritage wooden objects investigations: state of the art

The evaluation of the conservation state of archaeological wood and, more generally, of degraded historical and architectural wood, is a very important question, because since ancient times wood has been widespread used for many purposes. The conservation of wooden artifacts is again today an actual challenge: big archaeological finds, such as ships, require not only to determine their chemical composition but also their structural-morphological properties in view to define their degradation state to choose a conscious and durable consolidation method.

Wood undergoes several degradation processes depending mainly on the conservation environment. Recently, waterlogged wood is the most studied.

A lot of conservative treatments have been tested mainly with a chemical approach using alum, colophony, poly (ethylene glycol) (PEG), and in situ polymerization. The aim to replace water in the cavities with a penetrating material having a rather low vapor pressure. However, during ageing, most of the methods show problems such as change of pH, lack of penetration, presence of metal ions and so on.

Thus, it is necessary to found more appropriate methods for the removal of old applied products, also investigating the effect of the application of new materials.

Nowadays, the instrumental techniques used for these purposes are:

• transmission and scanning electron microscopy (TEM and SEM-EDX) for a characterization of wood at microscopic level to obtain information on morphology, wood species, degradation state and effects of consolidation treatments.

•analytical pyrolysis coupled with gas chromatography/mass spectrometry (Py-GC/MS), which has the advantages to require minimal sample pre-treatment and very low amount of sample, to distinguish different kinds of wood, analyse separately wooden components (lignin and cellulose), evaluate the degradation state at semi-quantitative level.

• infrared spectroscopy (FT-IR) to investigate the changes in the linkages between wood polymers and nuclear magnetic resonance (NMR) to obtain information on the degradation state and the differences between wood species.

• X-ray diffraction (XRD) to understand the structure of wood at cellular level. Recently, X-ray microtomography (μ-CT) was proposed to highlight the presence of heteroatoms and map wood sections with a micrometric resolution.

However, todays, a well-organized protocol is not disponible since an optimization of CT parameters must be made and not all its potential has been exploited (see the possibility of obtaining information on the density of wood and the additional materials it contains). Therefore, the research on archaeological wood involves several aspects: optimization of analytical methods, study of reference (i. e. modern wood) and archaeological woods, investigation of new materials for conservation and consolidation, representing an interesting challenge.

These topics are presented and discussed in this thesis, in order to answer some still debated questions on archaeological wood and especially on wet wood, proposing the combination of results from recently used diagnostic techniques such as CT and NMR with those obtained with conventional techniques such as FTIR and Raman, whose setups have been upgraded to create compositional-structural maps and statistical analysis on a large portion of the same sample. Finally, since the analytical techniques employed for the research activities discussed in this thesis allow to collect large data set relating to a high number of samples and analytes, multivariate statistical techniques will be applied to interpret the results (i. e. principal component analysis). This will allow to compare samples in a quantitative way, to integrate the information from the same sample studied by more than one analytical technique.

1.1 Wood structure

In cultural heritage, the keen interest in determining the woody species of an artefact also implies a more in-depth knowledge of all those cultural aspects. By wood identification, it is possible to obtain information about raw materials offered by territory or about peculiar processing techniques and possible exchanges involving different communities.

To better understand the study of wood-based materials, some general information on wood and its properties is provided below.

Wood is an anisotropic material. As it is well known, wood material comes from Gymnosperm, most commonly call coniferous, or from Angiosperm plant also known as deciduous. Conifer wood has a homogeneous structure, and, for these reasons, it is also called softwood wood, while Deciduous wood presents inhomogeneous anatomy and it is called hardwood wood (Fig. 1).

Moreover, from the macroscopic anatomical details (within a growth ring or annual ring), it is possible to distinguish between springwood (early) and latewood. In Conifers, springwood is made up of cells with a large lumen and a thin wall, while latewood has cells with a much smaller lumen and

thicker wall. This difference in the thickness of the cell wall leads to the difference in colour and hardness. In Conifers, wood spring is lighter and more tender, latewood darker and more compact. In the Deciduous trees, moreover, it is possible to distinguish three main groups: porous-zoned wood species, semi-porous-zoned wood, and porous-diffused wood.

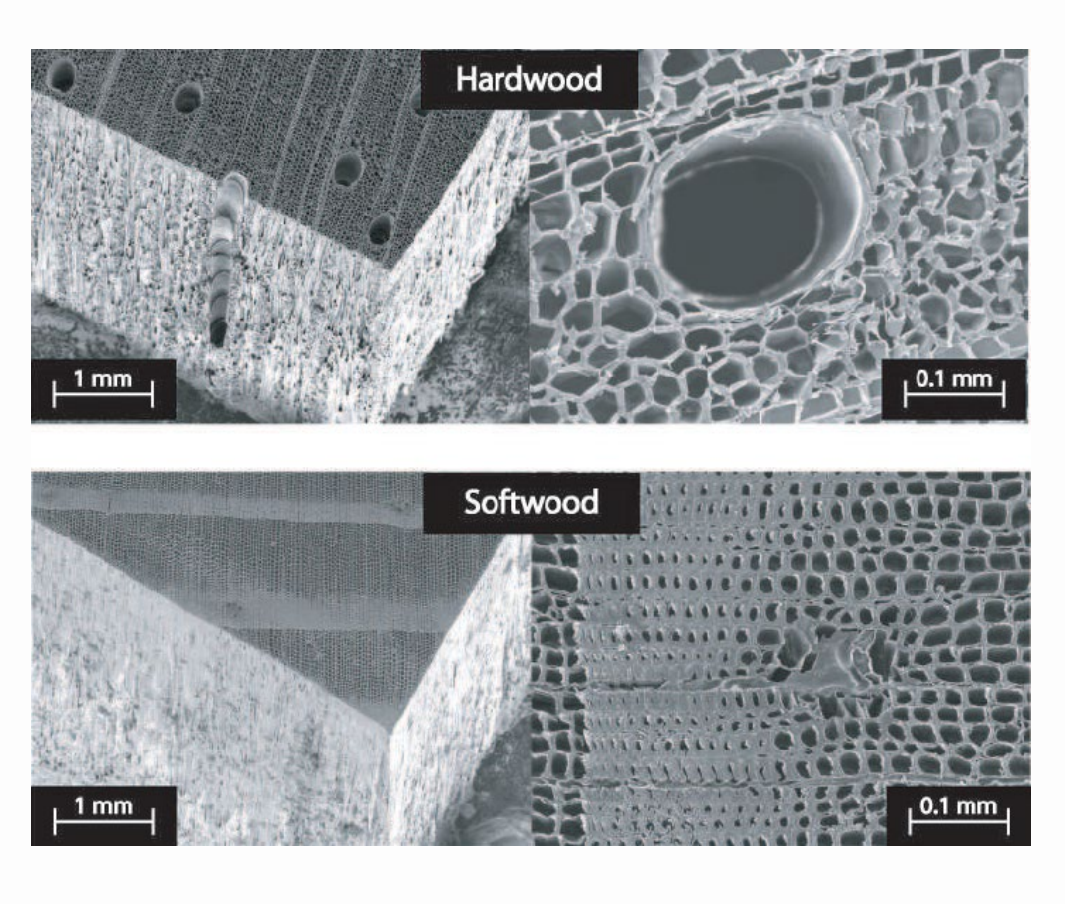

Figure 1 - Morphological details of different structures between hardwood and softwood. (Andersson et al. 2006, Optic Express Open Access).

Wood is a well-known structure. Starting from the bottom, a tree consists of 1) roots that have the function of both anchoring the tree on the ground, and the physiological function of absorption of water and substances in the soil; 2) stem covered with a protective layer called bark; 3) hair which includes the end of the stem, the branches, and the leaves.
The stem is the part that is most used and is divided into several zones. Starting from the end inwards we meet: 1) bark is formed by a more outer part, consisting of dead cells, called rhytidome with a function of protecting the stem from the attack of insects and by drying, and by a more internal

layer called phloem which is meant to transport to all parts of the trunk the sap processed by the leaves during the process of photosynthesis; 2) cambium is a very thin state of cells that varies during the vegetative season of the tree, ; 3) wood or xylem outs-of-body, the sapwood, which in addition to playing a supporting role in the plant, carries the raw sap from the roots to the leaves, while the innermost part is made up of heartwood, with the only function of supporting the plant; 4) Pith, made up of parenchymatic fabric, represents the primary nucleus around which are later developed the growth of the plant.

The tree consists mostly of lignified cells, rigid cell wall quarries (Brunetti 2009), the latter determines the characteristics and behaviour of the wood. Constituents cell walls are similar for all species: cellulose from 40% to 50%, lignin 18-25% in hardwoods, 25-30% for conifers, and hemicellulose from 13% to 27%. More details are reported in the Appendix.

Particularly, the cell wall (Fig. 2) is distinguished in several layers:

1. Primary wall, it is the first to form immediately after the birth of the cell.
2. Secondary wall, the thickest, formed once the cell lengthening is finished.

In addition to the cell walls, which make up the natural woody material, other substances such as water, extractives, and some cellular species are included. Extractives are the product of plant metabolism and can be contained within or deposited on or inside the cell wall, affecting some of the wood characteristics (colour, durability, and impregnability, etc.). The compounds that most found in extractives are terpenes, phenols, tannins, and nitrogen compounds. The cellular species included are usually granules of silica, oxalate or phosphate minerals mainly found in tropical timbers.

We now provide further details on softwood and hardwood structure, being two major classifications of primary importance in the study of archaeological woods

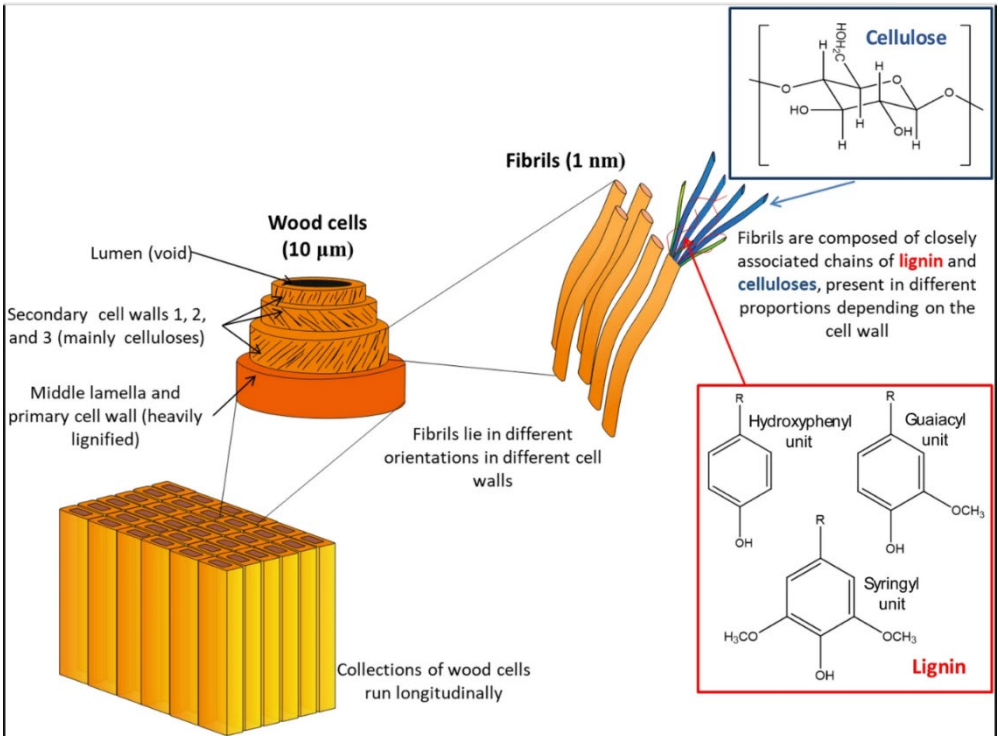

Figure 2 - Wood cell structure (High et al. 2020, Heritage Science Open Access)

1.2 Softwood and Hardwood

Coniferous wood is called *softwood* because it is made up of homogeneous elements, such as tracheid. These are long spindle-shaped cells which perform the function of lymph conduction and support. Some species, such as Douglas, have characteristic helical thickenings within the walls of tracheid. Parenchymatic cells are arranged in radial section and form uniseriate rays, that is formed by a single row of cells.

The main feature of coniferous wood is the presence of resin channels except for silver fir, cypress, yew, and cedars. In these species, however, resin channels are not excluded as consequences of injuries or trauma.

Softwood has well-marked growth rings due to the thicker walls of the tracheid's formed at the end of the vegetal period (late-wood) compared to those that have formed previously (early-wood). The accretion rings are

also called annual rings. This term, however, can be misled, as it may be suitable for plants that grow in temperate climates where climatic conditions are conducive to the development of the plant. Sometimes, however, due to accidental causes such as a mainly dry vegetative month or an insect attack, there may be an interruption in the development of the plant. Generally, it involves the formation of two rings in the same year; the innermost is called a false ring. The false ring stands out because it has the most faded exterior (Jacquiot 1955, Giordano 1981).

The wood of the angiosperms is much more complicated than that of conifers. There is a greater variety of cells due to the increased specialisation of them. There are cells for the conduction of liquids (vessels), cells that have mechanical resistance functions (fibers) and parenchymatic and secretric cells like softwoods.
The vessels are of different sizes and can be distributed in various ways within each accretion ring. In some species, if the vessels formed at the beginning or end of vegetative recovery, dimensional differences are visible. These differences give rise to porous circles visible to the naked eye. Fibres, on the other hand, are the main protagonists that determine the physical and mechanical characteristics of wood. Parenchymatic cells are more numerous in hardwoods than conifers and are arranged both radially and axially. They can form both uniseriate and multi-striates rays (formed by one or many cell rows) (Jacquiot 1973, Giordano 1981).

1.3 Wood identification

The identification of woody species in the field of cultural heritage and beyond, is a subject not of simple interpretation. Some timbers have macroscopic characteristics so obvious that recognition is certain even with the naked eye. Instead, others need microscopic observation that does not always lead to safe identification of the species.
This difficulty is further exacerbated by the fact that, even within the same species, wood can have different characteristics. There are variations in

the structure of wood due to external and internal factors such as the climate, the soil, and the age of the tree. For example, tree-ring analysis and the relationship between early-wood and late-wood can only be indicative features because they depend on the place where the plant grew more than the intrinsic characteristics of the woody species.

Besides, over time, we witness the phenomenon of the hardening of the innermost part of the trunk. The vessels vary in size, and this also applies to the length of tracheid and fibers as well as the length of the rays can also vary. Therefore, to facilitate the identification of the woody species, samples from the stem of adult plants, taken not near the center of the trunk, nor close to the insertion of branches, should be analyses. Healing fabrics, rubber or resin pockets should also be considered. In short, it should have a sample of wood that is structurally normal.

These conditions are sporadic in the field of cultural heritage, as often the samples to be analyses cannot be chosen with such accuracy. Only rarely is a given character so typical that it can immediately identify the species. Therefore, very often, it is possible to identify only the genus. Hence, to recognize some wood, the various characteristics are analyzed and proceed by exclusion.

First, wood elements are variously oriented and present different properties; as a result, it is essential to define reference direction concerning its anatomical structure. Ideally, assimilating the stem of the tree to a cylinder whose axis coincides with the pith and the accretion constitutes a succession of coaxial cylinders, three different anatomical sections can be defined (Fig. 3) (Nardi Berti 2006):

1) the transverse section or cross-section, perpendicular to the axis of the stem where the rings of accretion are visible.

2) the radial section, parallel to the medullary axis and passing by the center of the stem, where rings will appear as parallel lines.

3) the tangential section obtained from planes parallel to the medullary axis but not passing by the center of the stem.

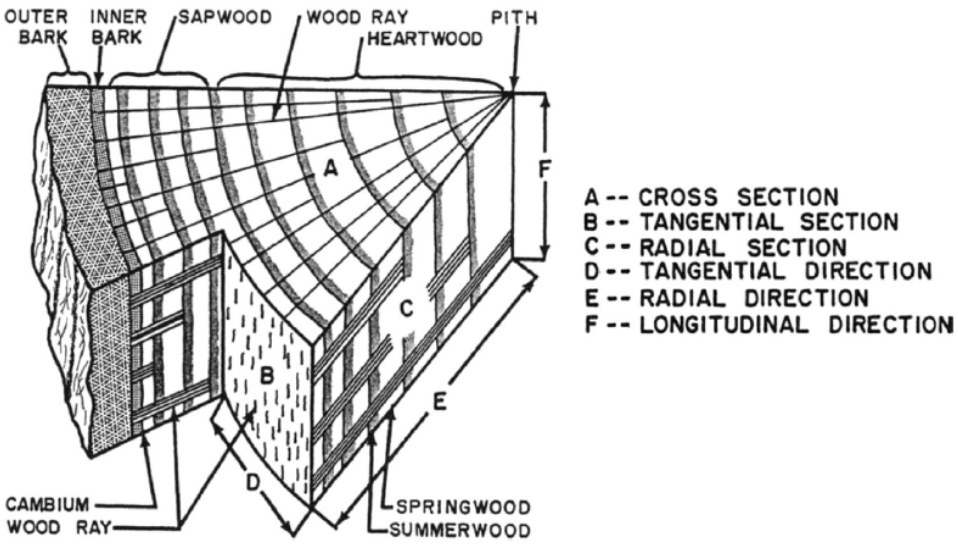

Figure 3 - Anatomical section of wood (Bajpai 2018, Elsevier with permissions).

Regarding the identification of softwood and hardwoods, the main characteristics that need to be observed are shown below.

For softwood identification, it is necessary to remember that everyone has a very similar structure with few differences, so microscope observation is preferable to macroscopic one (Giordano 1981).

For the macroscopic observation, initially, if the sample consists of a stem wheel, it should be observed whether the heartwood differs from the sapwood or not. The amplitude of the accretion rings and the width of the late-wood compared to the early-wood are then analysed, paying attention to whether the transition between the two is abrupt or gradual.

Finally, the presence or not of resin channels should be evaluated.

For the microscopic identification, the anisotropy of the material must be considered and then the information should be obtained following the anatomical section according to which the sample has been cut (Phillips 1941). For example, if a cross-section is observed, tracheid appear as sub polygonal cells with thicker or less thick cell walls and lumen. Further, resin channels appear as large circular holes and parenchymatic cells as cell cords. Conversely, if you look at a radial section, the tracheid will appear as rectangular tubes with large areolate punctuations inside them.

It is possible to find very large punctuations occupying a crossroads alone (rectangles formed by the walls of a radial parenchymatic cell and an axial tracheid), or other tiny ones located in various ways in the crossing fields (see Fig. 4). Therefore, the punctuations can be: 1) cupressoid; 2) piceid; 3) pinakoid; 4) fenes striform; 5) toxoided (Messeri 1967). Finally, another essential diagnostic character is the presence or not of helical thickenings within the walls of the tracheid.

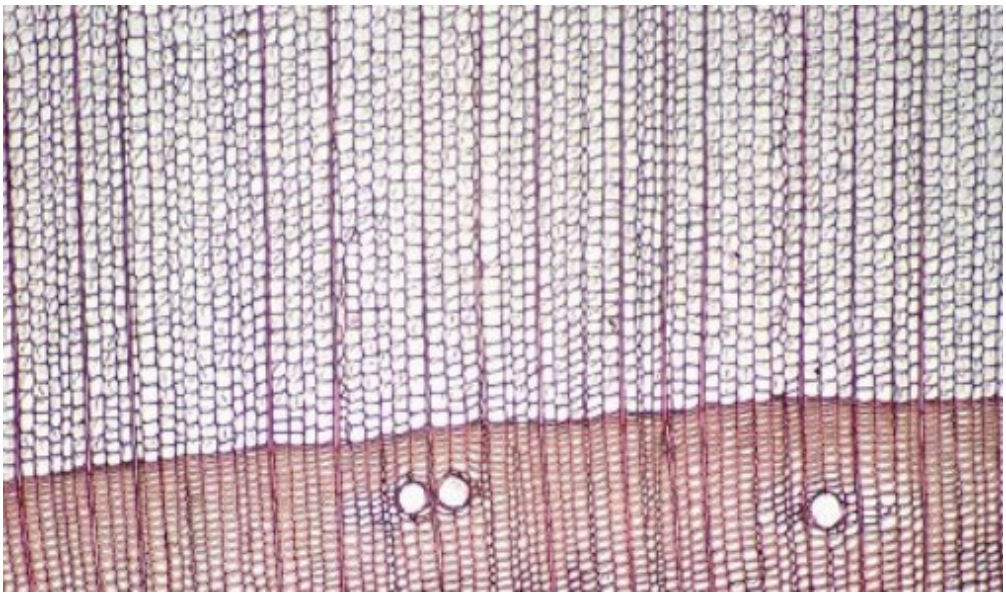

Figure 4 – Radial section of softwood Picea abies (InsideWood 2004, Open Access database, http://insidewood.lib.ncsu.edu/search)

In the tangential section, however, it is possible to observe the height of the rays and the number of rows of cells that compose them. Then it is possible to infer whether they are striates or biseriates, whether their shape is exhausted and the presence or not of horizontal resin channels (see Fig. 5). Finally, it is essential to check the thickness of the walls of the epithelial cells and their number. Also, in this section, you can observe the presence of helical thickenings.

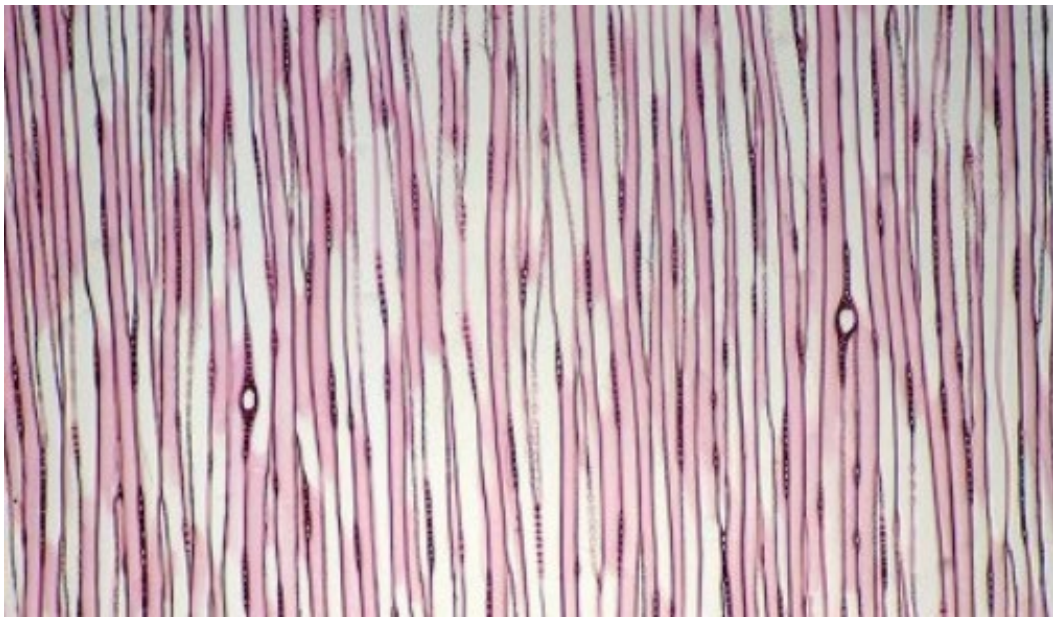

Figure 5 - *Tangential section of softwood Picea abies (InsideWood 2004, Open Access database, http://insidewood.lib.ncsu.edu/search)*

In the case of hardwoods, the macroscopic examination is fundamental (Hart 1971, Giordano 1981). In this case, the first step is to observe the presence or not of the porous ring. First, it is observed if the rays are visible to the naked eye and if the heartwood and the sapwood are differentiated. The changes in colour and in weaving are other essential features to classify the wood.

Furthermore, looking at the sample under a microscope, the shape and size of the vessels can be observed in cross-section. It is crucial to observe if there is a big difference between spring and autumn pots, their number, and their distribution within the accretion rings. By looking at the rays, it is possible to define whether they are striated, multi-striates or aggregated. Finally, it is essential to detect the presence of axial parenchyma for diagnostic purpose.

The analysis in the radial section, it is possible to observe the type of vassal perforation of the vessels and the type and distribution of the intervascular and radius-vase punctuations as well as helical thickenings. Some of these evidences could be confirmed by the analysis in the tangential section (i.e. the type of rays, vassal drilling and helical thickening).

All these features are difficult to remember; so, experts use dichotomic keys of identification to help identify woody species (Wheeler and Baas 1998). IAWA keys are the most used by experts (IAWA 1989). A scheme of softwood identification using dichotomic keys is reported in fig. 6. There are dichotomic keys with indications for macroscopic and microscopic recognition. Generally, it is essential first to identify the type of wood. Once it is established that the wood is softwood or hardwood, the anatomical characteristics must be considered, to narrow the field until the identification of the species.

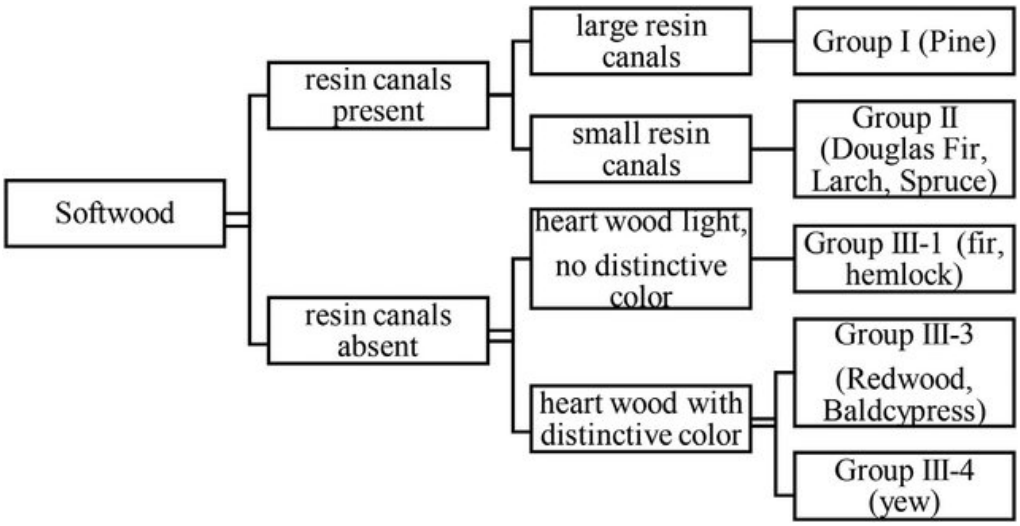

Figure 6 - Scheme of wood identification key. (Tri Bahtiar et al. 2016, Elsevier Open Access)

1.4 Water and wood

One of the peculiarities that distinguish the wood from all other materials is its hygroscopicity. It is so strong its affinity with water that we can speak of a "wood-water system". In the trees, the woody fabric is very rich in water, in the form of saline solutions contained in the cell lumen. Once the wood is at room temperature, a progressive loss of water from cellular cavities occurs; replaced by air at ambient pressure. Subsequently, even if the cellular lights are entirely emptied, in the wood it will continue moisture is present which can only be eliminated by drying the wood in oven at 103° C until it reaches the anhydrous state (Bonamini 1996). Generally, researchers distinguish:

- Free or imbibition water is the liquid water that fills the cellular lumens and can flow freely from cell to cell in fresh wood conditions. This type of water it only marginally influences the characteristics of the wood.
- Water connected to cell walls, known as saturation water: is the one that by the formation of hydrogen bonds is combined with free oxydrilic radicals, available walls and mainly related to the molecular structure of microfibrils of cellulose; this is the type of water that greatly influences the properties of wood (Bonamini 1996).
- The water of the constitution (or chemistry): water molecules that have become part of the chemical composition of the main molecules that make up the wood, so its release would lead to the destruction of the wall itself (Nardi Berti 2006).
- Water vapor in the air partially fills the cellular cavities and is in balance with saturation water and imbibing water.

As humidity has a significant impact on the size and characteristics of mechanical and stickiness by insects and fungi, it is crucial to establish the water content inside the wood.

Some physical parameters were analyzed. Among them, the absolute and relative humidity of wood. The absolute humidity is the amount of water vapour that can be contained within a given volume of air. More precisely,

the absolute humidity is the ratio of the mass of water vapour to the mass of dry air:

$$H = \frac{M_{vap}}{V_{air}} \quad (1)$$

where M_{vap} is the mass of steam contained inside the wood vessel and V air is the volume of air.

Imagine having a cylindrical vessel sealed tightly by a piston and partially filled with distilled water and the rest with air (at least initially) dehydrated. At a certain temperature and pressure condition, some water molecules will leave the surface of the liquid turning into steam that will be mixed with the air. The steam addition in the container determines an increase in pressure inside the container. If you consider the pattern of evaporation as a function of time, you will be able to obtain the ratio of steam mass contained in the cylindrical vessel and the volume that occupies the air. This ratio is called absolute humidity of the air.

Really, the evaporation process continues until the maximum value of steam has been reached, within a given unit of volume, defined as humidity air saturation. If you enter additional water vapour into an already saturated mass of air, the excess amounts will tend to condense (visible in the form of droplets suspended in the air or directly on the walls of the container that contains them). This effect can also be achieved, decreasing the temperature of a saturated air mass (keeping the pressure constant). The point dew is the temperature at which condensation of the vapour contained in a certain mass begins. At the level of the hygroscopic properties of wood, it is essential to know the relative humidity percentage ratio of actual absolute humidity (H_{eff}) humidity of saturation (H_{sat}) reachable from the air, at constant temperature and pressure.

$$H_{rel} = \frac{H_{eff}}{H_{sat}} \quad (2)$$

National and international standards describe wood moisture as the ratio between the weight of the water contained in the wood ($p - p_0$) and one of the woods in the anhydrous state (p_0), expressed in percentage:

$$M = \frac{p - p_0}{p_o} \%100 \quad (3)$$

The range of possible humidity values that wood can assume is called the hygroscopic range. It is between 0%, which is obtained when the wood is kept in a long-time dry air, and about 30% reached by placing the wood in an environment saturated with vapor.

Outside the hygroscopic range, wood can still absorb water but only for imbibition, i.e. by direct contact with liquid water which fills the cellular cavities in the form of free water. The imbibition water does not cause significant variations in physical and mechanical characteristics, excluding an increase in density. Generally, wood with 12% of moisture content at 20° C and 65% of relative humidity, it is considered in hygrometric equilibrium.

The moisture value of the wood when free water has been eliminated, and bound water is still present, is called the saturation point. This variable is significant because it indicates when significant variations in physical-mechanical properties of wood (volumetric shrinkage, stiffness, etc.) are occurring. It depends on several factors such as the wood species, the presence of extractives, the volumetric mass, the percentage of earlywood and latewood, temperature, and presence of reaction wood. Conventionally, the wood humidity corresponding to the saturation point varies from 28 ÷ 40% dry weight. In the case of wood in hygroscopic equilibrium, with the moisture content of 12%, absence of free water and partial presence of bond water will occur.

The variation of the water content in the wood involves dimensional variations, which are expressed with swelling, in the case of moisture absorption and with shrinkage, caused by loss of moisture. This phenomenon occurs only in a well-determined range, which goes from anhydrous state to the point of total saturation of the cell walls. Only when the binding water is involved, physical modifications that lead to significant dimensional changes will happen. Particularly, the anisotropy of the withdrawals is a characteristic parameter. For example, going from fresh to dry wood, in the axial section a dimensional change of less than 1% will occur; in the radial direction changes from 3% to 7,5% will happen and from 5,5% to 15% in the tangential section. All these modifications are related to the "biological nature" of wood.

1.5 Analytical methods for assessing archeological wood

The non-destructive assessment of the physical properties of wood originates in the need to solve practical problems without destroying the integrity of the object under inspection. The first non-destructive assessment of wood was a visual inspection, primarily used for the selection of timber used as supporting members for specific applications. Even today, this method is widely used for the classification of wood products for timber, poles, plywood, etc. and to assess the state of conservation.

At the beginning of the 20th century, with the development of the theory of elasticity and instrumentation for measuring the properties of wood, new scientific methodologies of the non-destructive evaluation were developed.

Initially, the focus was on determining the elasticity modulus using static methods (Horig 1935; Kollmann 1951). Subsequently, acoustic vibrations were used to determine the elastic constants of wood (Barducci and Pasqualini 1948; Hearmon 1948; Kollmann and Krech 1960; Jayne 1955; James 1959).

In the 1960s, the development of X-ray techniques for the evaluation of the internal structure of wood led to the development of densitometry (Polge 1978), and X-ray dispersion also came to light. It was developed in Japan precisely for the study of crystalline wood cellulose (Fukada 1965 and 1956).

In the same years, dynamic tests with vibrational methods for structural timber assessment were also used by Hoyle (1961), Senft et al. (1962) and Pellerin (1965).

In the late 1970s, a congress organized in the United States at Washington State University by Pellerin and colleagues in collaboration with the Forest Products Laboratory encouraged and paved the way for the development of non-destructive methodologies for wood science.

From that moment on, scientific production on the subject grew considerably. (Jayne 1972, Bodig and Jayne 1982, Torgovnikov 1993, Bucur 1995).

Ten years later, the first encyclopedia of wood science was published (Schniewind 1990).

The last 20 years of the 20th century have been characterized by an extraordinary development of techniques for the non-destructive evaluation of wood products. Particular attention should be given to imaging, a methodology par excellence non-destructive.

To date, non-destructive techniques are widely used for measuring physical, mechanical, chemical, aesthetic, etc. properties. For example, wood defects, porosity or density variations can be detected by techniques such as microwaves, thermals, X-rays or classic static methods. These methods can help to understand the behavior of matters under different environmental conditions. Other approaches, involving the use of non-destructive survey methodologies, may be the industrial field for the assessment of the quality of materials and the market for wood-based composites that are now booming (Youngquist and Hamilton 1999). Therefore, the need to characterize wood-based composites has stimulated the development of many non-destructive methodologies. This field also requires the synergy of many scientific disciplines, making the matter multidisciplinary. In this regard, Sobue (1993) proposed the classification of non-destructive methods (Table. 1) for the assessment of the physical properties of wood such as moisture, density, stress assessment, node detection, etc. These same methodologies are largely used for studying ancient wood (Bucur 2003).

Among the wood-based objects, submerged archaeological wood can present difficult challenges due to its vulnerability. Quantifying the conservative state and understanding the mechanisms of degradation is therefore crucial. An appropriate analysis manages to establish a solid baseline against which any further deterioration can be traced. For example, when a site is monitored (Brunning 2000) or when experimental data on decay mechanisms is collected (Lucejko 2018).

Another aspect essential in artworks preservation is the monitoring of the state of conservation.

Table 1 – Classification of non-destructive physical methods for solid wood analysis (Bucur 2003, Springer with permissions).

Wood parameter	Properties measured	Techniques
Moisture content	Dielectric properties	Impedance DC and high frequency, microwave, infrared, NMR
	Thermal properties	Infrared
	Ionizing rays absorption	X-rays; gamma rays
	Elastic properties	Frequency resonance method, ultrasonic method
Density	Weight	Gravimetrie method
	Ionizing rays	X-ray microdensitometry; attenuation of X, beta and gamma rays
	Dielectric properties	Microwave technique
	Mechanical properties	Pilodyne
Fiber direction	Elastic properties	Ultrasonic velocity
	Dielectric properties	Microwaves
	Light scattering	Laser, visible light
	Thermal properties	Infrared
Knots detection	Optical properties	CCD camera, colorimetry,
	Elastic properties	Ultrasonic CT
	Ionizing radiation	X-ray CT, gamma ray CT
	Thermal properties	Infrared thermography, laser thermography
	Electrical properties	Microwave, NMR
Decay detection	Elastic properties	Vibration, ultrasonic
	Mechanical properties	Penetration of pilodyn
	Dielectric properties	Microwave
	Ionizing radiation	X-ray CT
Mechanical capacity	Static properties	Bending stress grading, proof-loader
	Dynamic properties	Vibration and ultrasonic methods
	Acoustic properties	Acoustic emission

In this way, it is possible to identify when conditions are not conducive to the continued survival of an object (Lucejko 2020, Braovac 2016).Besides, scientific investigations during or after conservation allow assessing whether a protective or consolidating treatment worked or not (Christensen 1970).

As has been widely explained in Appendix 1, fresh wood consists of three main biopolymers, lignin, cellulose and hemicellulose. Archaeological wood is subjected to such a variety of chemical and biological degradation processes that it results in chemical composition and a very different structure than fresh wood (Fengel 1991). In the anoxic conditions provided underwater, decay processes are significantly slowed down and mainly driven by anaerobic biological agents (Blanchette 2000).

These agents mainly attack the hemicellulose, which, due to enzyme degradation, becomes vulnerable (I 1990). The chemical deterioration of cellulose occurs under extreme conditions such as low pH (High 2016). Lignin, thanks to its highly stable structure, is much more resistant to degradation (see Aappendix 1 for more detail). This explains why submerged archaeological wood is characterized by high lignin content (Martinez 2005). Instead, the structure of the wood is maintained because the cell walls are filled by water, but this aligned skeleton is a very fragile material (Björdal 2003). The decay of lignin is mainly due to the attack anaerobic fungi that digest lignin through enzymatic oxidation (Pedersen 2013). This results in a higher concentration of guaiacyl-type than the syringil one (Hedges 1990).

Another important aspect is the exchange with the surrounding environment. The chemical composition of the submerged wood can change because of this. Also, the highly porous structure of wood can incorporate inorganic minerals, such as iron sulphites, phosphates and calcium, into cell walls (Panter 1997). Identification of these inorganic components can be predicting the success of conservation treatments and possible long-term effects. However, the submerged wood study is quite complicated because of its heterogeneity. Generally, the degradation expands first on the surface and then proceeds inwards. For this reason, the heartwood is always better preserved than the sapwood, which is more external (Christensen 1970).

The methods for analyzing these processes traditionally consist of easily accessible and inexpensive techniques (Blanchette 2000, Jagels 1981). However, in recent decades, thanks to the interdisciplinary nature of diagnostics for cultural heritage, more complex methods have been adopted. An example is advanced microscopic methods that reveal structural alterations or spectroscopic techniques that give information at the molecular level (Daniel 2016). The principal diagnostic methodologies used to study submerged woods will be discussed below (Tab. 2, Tab. 3 and Tab. 4).

One of the techniques widely used to acquire information about the loss of woody substance, a fundamental parameter for determining the structural integrity of an artefact, is the calculation of mass or volume. It

is a very accessible and cost-effective methodology (Jensen 2006). The density and maximum water content (MWC) are also the commonly applied parameters (Macchioni 2012). Another method to assess the loss of woody substance, is the calculation of porosity by filling pores with an inert gas (helium) (Babinski 2014, Donato 2012).

Unfortunately, however, the main problem with these measurements is the difficulty in developing a standard. Once the sample has been removed from the oven, the high porosity of the wood results in very rapid reabsorption of air moisture (Panter 1997), also, to obtain reliable information, it would be necessary to have samples with a minimum size of 2x2 cm. It is not possible to detect small variations in the composition of the wood in a short monitoring period. Hence, one downside of the analysis of wood substance loss is that the methods are often destructive as they require irreversible drying of the sample. Therefore, the use of non-invasive instrumental methods is preferable. One of the most used methods is the X-ray imaging. Thanks to this method, it is possible, for example, to locate limestone deposits caused by marine organisms (Knight 2019). You can also identify elements inside, such as iron nails or joints (Karsten 2010). One drawback of X-ray analysis is that the object is represented as a 2D object.

However, this drawback is outdated by computed micro-CT microtomography (micro-CT) which is a version that can produce 3D images, thus providing a better spatial assessment than normal X-ray (Sodini 2012). Micro-CT can examine objects ranging from millimeter size. The micro-CT can be significantly improved using synchrotron sources (Mizuno 2010). Synchrotron radiation provides better contrast and organic conservation agents (i.e. polyethene glycol (PEG) could be highlighted (Bugani 2009)).

Another widely used method is ultrasound tests and have the advantage that the effect of water can be quickly recorded. However, the interpretation of the data can be complicated as the reflected signal is influenced not only by water content but also by factors such as the orientation of timber and natural variables within wood (Arnott 2005). Another experimental approach that involves the use of X-rays is the X-ray diffraction (XRD). It has been used to examine cellulose loss in

archaeological wood (Giachi 2003, Li 2014), but the exact location of the deterioration cannot be determined.

Concerning the study of the presence of inorganic salts or structural collapse of cell walls, microscopic methods (optical, SEM, UV, TEM) are the most suitable (Blanchette 2000). Unfortunately, however, the region of the sample analyzed under the microscope may not be representative of the entire object. Besides, preparing samples on degraded samples for a less experienced analyst can be difficult. A more established method for determining chemical composition is to determine the "insoluble lignin" or "Klason lignin" (Babinski 2014). However, the method requires chemical extraction of wood extractants, a high content of sample (> 1 g (Nilson 2012), long analysis times (several days) and the need to manage potentially harmful chemicals. Further, the certainty of the results may depend on the degree of decay that exists in the sample (Pizzo 2010).

Moreover, the potentiality of the thermogravimetric (TG) technique applied to the submerged wood has been demonstrated by Romagnoli (2018). However, despite its advantages, TG analysis tends to be applied to more for the evaluation of conservation methods linked to wood (Donate 2010).

Other methods widely used to establish relative amounts of cellulose and lignin are the spectroscopic techniques (FTIR and Raman), gas chromatography and nuclear magnetic resonance imaging (NMR) (see Tab. 3 and Tab. 4).

Concerning FTIR analysis, although it is a simple method in a practical sense, the complexity of the material leads to considerable difficulty in interpreting the data, as the water signal often tends to obscure signals from polymeric materials. In addition, only a small part of the sample is measured, as the penetration radius of an FTIR spectrometer is about 0.5-3 μm. The sample is usually analyzed dry, and for submerged wood, FTIR analysis is not suitable.

For this reason, recently Raman analysis in addition to the fact that no sample preparation is required, can be used in a non-destructive way. This method has been less widely applied to archaeological wood analysis than the FTIR since the Raman peaks on dry wood samples are often weak and difficult to compare.

Pyrolysis, on the other hand, is paired with gas chromatography (py-GC) and is a technique in which a sample is exposed to high temperature (> 500 degrees centigrade) in the absence of oxygen. The py-GC provides a more sensitive analysis than FTIR and subtler changes to their poly mechanical structure can be detected. The main factors that limit the routine use of this technique lie in the limited availability of the required instrumentation and the increased expenditure. Also, the analysis times are longer (between 40 mins and 2 h per sample) (Lucejko 2015).

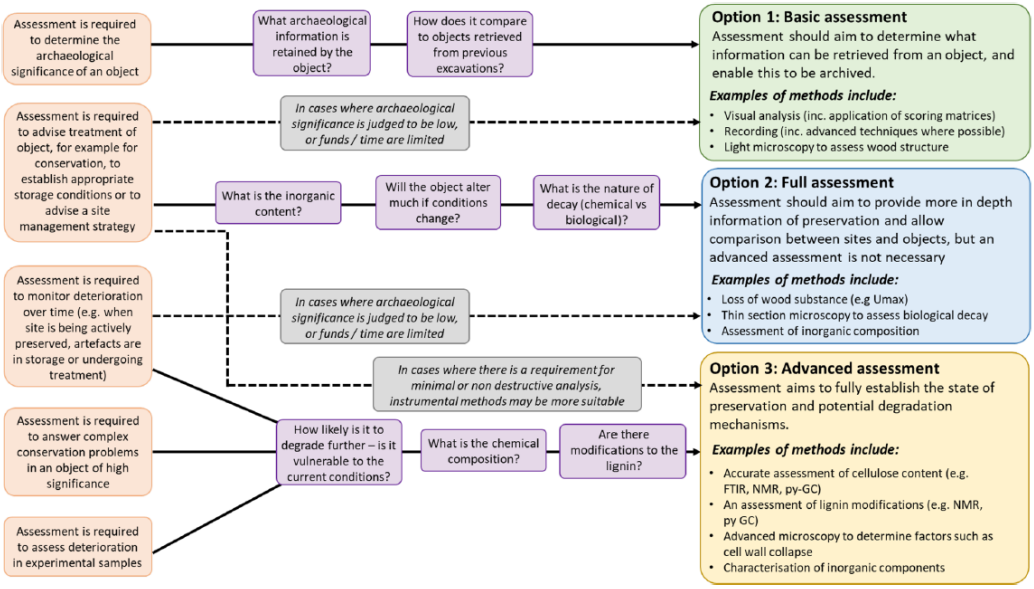

Figure 7 - Schematic summarising some of the key factors that may need to be considered in determining the level of preservation assessment that is necessary (High et al. 2020, Heritage Science Open Access)

Finally, the NMR spectroscopy (1H, 13C, 31P) provides information on the structural and spatial arrangement of organic molecules. This makes it ideal for the analysis of complex polymers such as those found in wood (Bardet 2009). In literature, it has been shown how 13C NMR proved to be a valuable technique for examining cellulose and lignin in solid-state archaeological samples (Zoia 2017, Bardet 2002). The limitations of NMR techniques mainly relate to the lack of availability of appropriate tools, their expense both initially and in terms of maintenance, and the high level of expertise required to perform them.

In conclusion, no single technique can be considered the best option, so it is preferable to take a multi-analytical approach (Fig. 7). In addition, emerging technologies and techniques are continually evolving, always enabling new challenges. It is precisely a multi-analytical approach that has been adopted for the study of the materials covered by this thesis. The correlation of CT, NMR, FTIR and Raman data made it possible to study the chemical-physical characteristics of archaeological woods representative of significant historical periods and coming from different geographic regions (Italy and Denmark). Furthermore, the crossing of these data gave the possibility to validate the multi-analytical approach adopted also on submerged woods. The protocols developed could be adopted to extend the study to other historical finds than those analyzed during the PhD course.

Chapter 2

X-ray Computed Tomography

Today, the use of X-rays in the arts sector is quite widespread. The ability to see through the paint film of canvases and panels, revealing the underlying paint, the author repentance, restoration work and hidden signatures, structural abnormalities, deficiencies etc…, justify the great fortune of radiographic techniques in the investigation on ancient and artistic objects.

Conventional radiographic image, even in its completeness, presents difficulties of reading: the refund on a two dimensional surface of the painting complex stratigraphy does not make more accessible the spatial localisation of the individual elements, sometimes making the decryption of the data rather complicated. Thus, the conventional radiographic technique is not considered the best type of cognitive scientific act to investigate the structural situation and a work of art material. On the contrary, X-ray Computed Tomography (CT) is a more valuable methodology for cultural heritage investigations. In this thesis, conventional clinical CT scanners were applied to wooden artefacts investigations. The choice was based on the principle that wood material has similar attenuation to human tissue. The reasons will be explained in detail below, together with a presentation of its operating principle

2.1 Production of X-rays

The equipment for the production of X-rays, the so-called X-ray tube, is shown in Fig.1. An X-ray tube consists of a glass ampoule containing two electrodes acting as an anode and cathode, respectively.

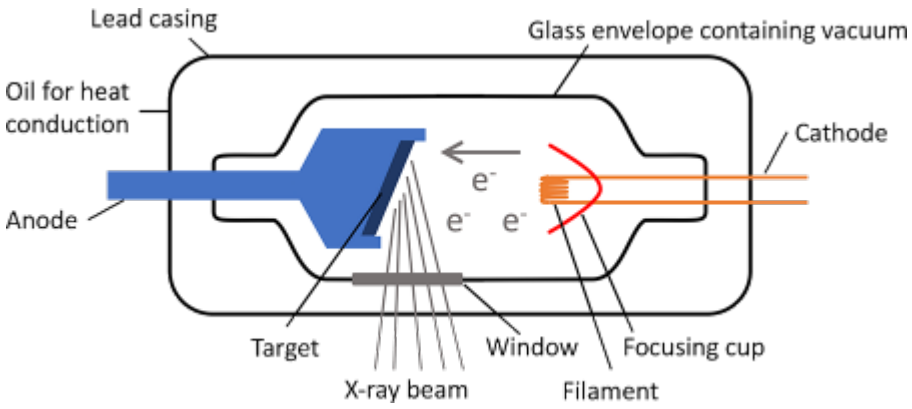

Figure 1 - X-ray tube schema (Courtesy of Prof. Francesca Granata).

The bulb, where the vacuum is created, is surrounded by a metal casing lined with lead. The emission of X-rays takes place through a small not-shielded area, known as 'window'. A current is passed through the tungsten filament and heats it. As it is heated up, the increased energy enables electrons to be released from the filament, usually tungsten, through thermionic emission. The electrons are attracted towards the positively charged anode and hit the tungsten target with maximum energy determined by the tube potential (voltage) (Erriu 2005).

As I will describe better soon when the electrons bombard the target they interact via Bremsstrahlung and characteristic interactions which result in the conversion of energy into heat (99%) and x-ray photons (1%). The x-ray photons are released in a beam with a range of energies (x-ray spectrum) out of the window of the tube and form the basis for x-ray image formation.

The loss of energy is proportional to Z; this is the reason why heavy materials are used for the anode so that higher production of X rays can be obtained. The radiation emitted in this process is known as "continuous Bremsstrahlung radiation" or "radiation of Bremsstrahlung", characterised by a continuous spectrum (energy distribution of the X photons).

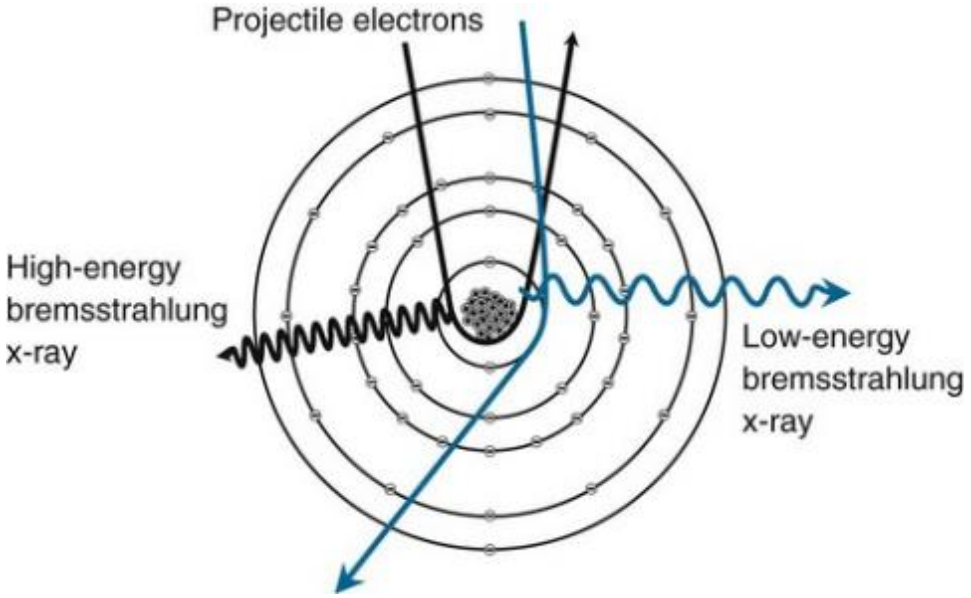

Figure 2 - Bremsstrahlung radiation (Courtesy of Prof. Francesca Granata).

A second X-ray production process takes place when the electron projectile has energy sufficient to cause the ejection of an electron belonging to an internal orbital of the atom. The gap which is thus created will tend to be occupied by an electron from an outer orbital. This process determines the emission of a photon of energy equal to the difference between the binding energies of the two levels. Since the binding energy for the electrons is different from element to element, the x-ray spectrum shows a distribution of energy according to a line spectrum, which is characteristic of the material constituting the target (characteristic X-rays). Hence, the resulting spectrum (Fig. 3) is given by the superposition of a continuous component (bremsstrahlung radiation) and a discrete component (characteristic radiation).

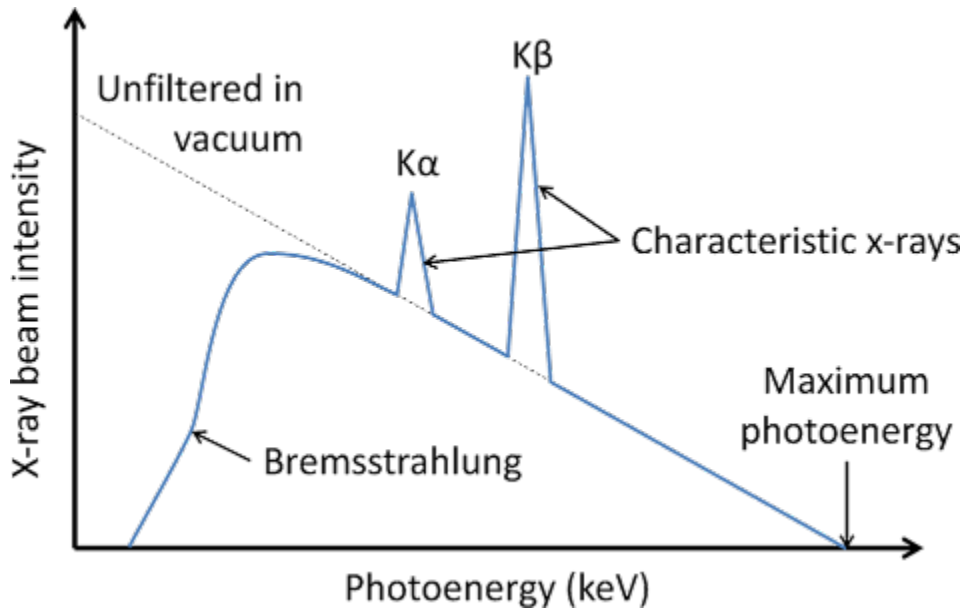

Figure 3 - Typical spectrum of x-ray photon energies released (Courtesy of Prof. Francesca Granata).

As already said, the anode must be comprised of a high atomic number material and a high melting point. In fact, in the process above described, only 1% of the kinetic energy of the electron's "bullet" gives rise to the production of X-rays; the remainder is converted into heat. For these reasons, the tungsten (with Z = 74 and T (melting) = 3370 °C) is the materials mainly used as the anode.

Further, "projectile" electrons often fail to transfer sufficient energy to extract electrons from the target atom, so they switch to a higher energy level; when they return to the initial state, the electrons emit infrared radiation which causes the continuous heating of the anode, resulting in its deterioration and possible merger. To obviate, rotating anodes are today used since, in such way, the electron beam is incident in different points of the anode itself, favouring the dissipation of the thermal energy. Finally, the target plate is inclined at an angle of about 20°, so the electrons act within the focal area, of rectangular shape, while the photons are emitted

from an area approximately square, much smaller, called the "focal spot" or "actual focal spot" (see Fig. 4).

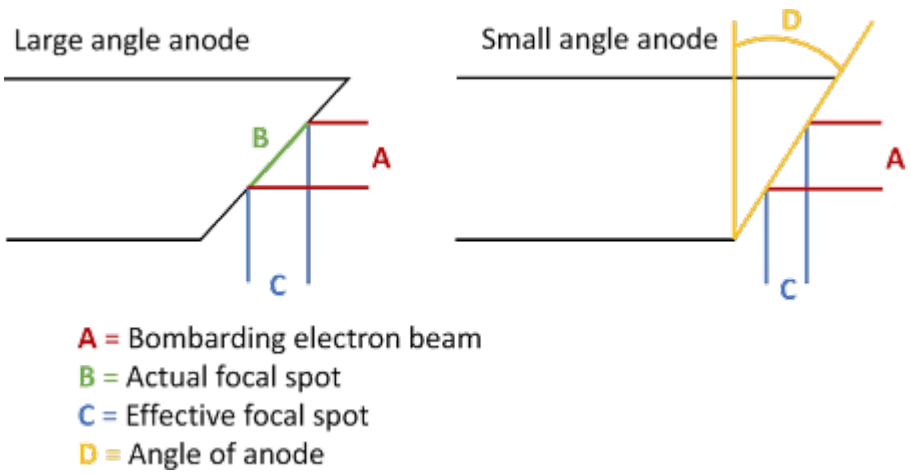

Figure 4 – Schematic representation of actual focal spot and effective focal spot (Courtesy of Prof. Francesca Granata).

2.2 Interaction of X-rays with matter

The radiographic techniques, as well as to all imaging systems that rely on the use of X-rays, exploit the fact that the constituents of the X-ray photons have a certain probability of interacting with atoms constituting the material that passes through, resulting in loss of energy and possible release of secondary charged particles.

The so-called cross-section is a measure of the probability that photons interact with matter by a particular process. There are several modes of interaction which depends on the atomic number Z of the target atoms and the energy of the photons. The higher the atomic number, the higher is the interaction probability with an electron in the atom of this element.

The amount of energy absorbed by a body and then the consequent attenuation of the beam changes as a function of the materials linear

absorption coefficient μ, and it is proportional to the thickness x of the material crossed, according to the following law:

$$I(x) = I_0 e^{x \times \mu} \qquad (1)$$

Where I (x) is the intensity of the beam collected after the interaction, *x* the thickness of the crossed materials and I_0 the intensity of the source.

Principally, three kinds of interaction with matter occurs:

a) Transmission: the radiation passes the material without altering energy or direction.

b) Absorption: the radiation is absorbed transferring its energy to the absorbing material.

c) Scattering: the direction of the radiation changes; the energy can also be diminished.

The primary process involved in the interaction of x-rays with matter is the so-called "photoelectric effect", which is one of the principal forms of interaction of x-ray with matter (Fig. 5).

A low energy photon interacts with an electron in the atom and removes it from its shell. The electron that is removed is then called a photoelectron, and the incident photon is wholly absorbed in the process. Hence, the photoelectric effect contributes to the attenuation of the x-ray beam as it passes through matter.

Briefly, a low energy photon interacts with an electron in the atom and removes it from its shell (e.g. K-or L-shell), which is subsequently ejected as a photoelectron, and the atom is ionised (Martin 2006). The vacancy in the shell is filled up with an electron from an outer shell—displacement to the less energetic shell results in the emission of element-characteristic X-ray radiation with lower energy.

On the other hand, the scattering phenomenon of X-ray photons is known as Compton scattering (Compton 1923). The X-ray photon hits an electron in the shell of an atom and is deviated by this collision. It loses energy to the electron, which is ejected from the shell causing ionisation of the atom.

Ultimately, the pair production occurred for X-ray photons with energies higher than 1.02 MeV: the photon collides with the nucleus producing an

electron and a positron, respectively. Pair production is not generally used by medical imaging.

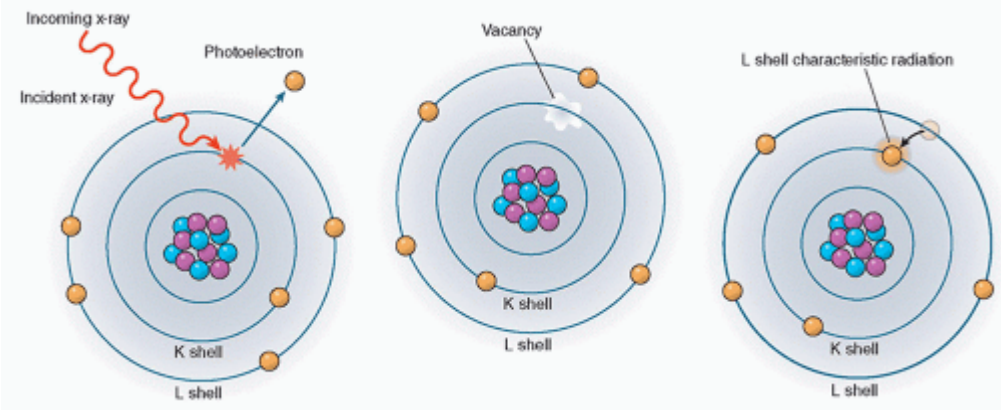

Figure 5 - Illustration of the photoelectric effect. For a photoelectric effect to occur, the incident photon energy must be equal to or greater than the binding energy of the ejected electron. For example, photons whose energies exceed the K-shell binding energies will most likely result in photoelectric interactions with the K-shell electrons. As a result of a photoelectric interaction, atoms are ionised with a vacancy of an inner shell electron. An electron from a more outer shell, with lower binding energy, will fill this vacancy. It will, in turn, create another vacancy, which is filled from an even lower binding energy shell, creating an electron cascade from outer to inner shells. The difference in binding energy is released as either characteristic X-rays or Auger electrons. As the atomic number of the absorber decreases, the probability of characteristic X-ray emission decreases. See Ref. (Fassbinder 2012, Wolters Kluwer with permissions).

All these are the basis of the functioning of the tomography instrumentation. Generated photons irradiate an object. Then, they traverse the material of the object, and it depends on their intensity and the nature of the material. In the end, some of the energy is lost (or attenuated), and less energy emerges from the other side. Traditionally, this energy was used to ionise a photographic plate for the creation of an image. Today, specific software is used to digitally encode density and spatial information about portions of the object, as will be described in the following paragraphs.

2.3 Principles of Computed Tomography

X-ray imaging was the first diagnostic imaging technology, invented immediately after the discovery of x-rays by Roentgen in 1895. As described in the previous paragraph, X-rays are a form of electromagnetic energy that propagates through space and are absorbed or scattered by interactions with atoms. The attenuation of beam energy on passage through physical objects provides a non-invasive means to gather information about the amount and type of material present inside the object.

By acquiring multiple x-ray views of an object and performing mathematical operations on digital data, a full 2D section of the object can be reconstructed. It is the mechanism of the Computed Tomography (CT), based on the theoretical work of Radon (Radon 1917; Brooks and Di Chiro 1975). The practical implementation of the principle is based on the work of Cormack (1963) and Hounsfield (1973; 1980) who designed the first functioning X-ray CT scanner.

Transmission images represent shadow images of the examined object. These projections thus contain information on the object's inner structure. This information consists of the integrated attenuation that the beam experiences on its way through the object, yielding information for every point in a two-dimensional plane. A projection of the object made from a right angle from the first viewing angle yields again two-dimensional information. With just these two projections, it is possible to make a rough estimate of the position of an object's structural features in three dimensions. It is nevertheless still scarcely possible to make assumptions about the actual three-dimensional shape of these features. Using projections from different angles can, therefore, help to ascertain the exact form. To reconstruct the actual shape of an object, a computational step called "computed tomography" is required.

Thus, computed tomography is a method using projections from different viewing angles to gather three-dimensional information on an object's inner constitution by reconstructing a three-dimensional virtual model of the object. So, the projections are transformed to tomography slices,

images, which are perpendicular to the projection-plane as well as to the rotation axis of the object (or of the source and detector, as is the case in most medical scanners). These tomography slices represent two-dimensional matrices of the attenuation coefficient values within the reconstructed plane. For every line within the detector, a tomogram is reconstructed. The stack of tomograms represents a three-dimensional array of the attenuation coefficient μ (*x, y, z*) within the reconstructed volume. By stacking the tomograms, a three-dimensional manipulation, visualisation, and evaluation are possible.

2.4 CT instruments

CT is widely used in clinical diagnostics since it allows to discriminate tissue density and to display specific organs body images (Dal Pozzo 2016). Correctly, industrial computed tomography, portable computed tomography, and micro-CT (μCT) are currently used obtaining detailed images with a resolution down to 1 micron (Kaick and Delorme 2005). These types of instruments consist of a fixed X-ray tube and a rotating platform of 360°, where the object or the sample is placed. However, industrial CT and micro-CT are not suitable for objects with large dimensions (30-40 cm) while portable devices regulations, especially in Italy, are quite restrictive due to the ionisation radiation. Furthermore, scanning times are quite long. Then, high-resolution 3D images reconstructions are possible only with micro-CT, giving only information on small samples (75.8 x 140 mm max.).

A good compromise between detailed images, short scanning time and high-resolution 3D reconstruction is given by the Multi-slice Computed Tomography (MSCT). It is nowadays the most used X-ray CT in medical images analysis. Over time, there have been some generations of CT scanners capable of better performances in terms of scanning speed (gradually reduced from several minutes to seconds to fractions of a second) and resolving power of the image.

The first-generation tomography was based on the emission of a linear beam of X-rays, emitted from an X-ray tube in translational and rotational

movement, and detected by a detector (Xenon or solid-state) entirely in movement. The running acquisition time was of few minutes (Fig. 6) (Kalender 2000).

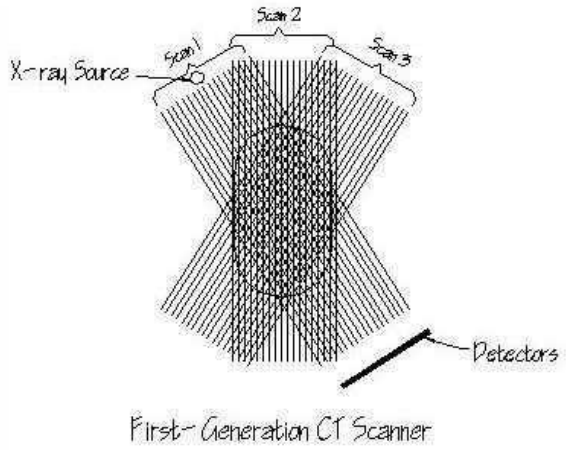

Figure 6 - Schematic representation of a first-generation CT scanner (Courtesy of Prof. Francesca Granata).

Technological improvements were designed to reduce data collection time drastically. In fact, in the second-generation tomography, the X-ray beam has a fan geometry of 20-30° connected with a group of 20-30 detectors: so, the execution time was reduced to tens of seconds (Fig. 7).

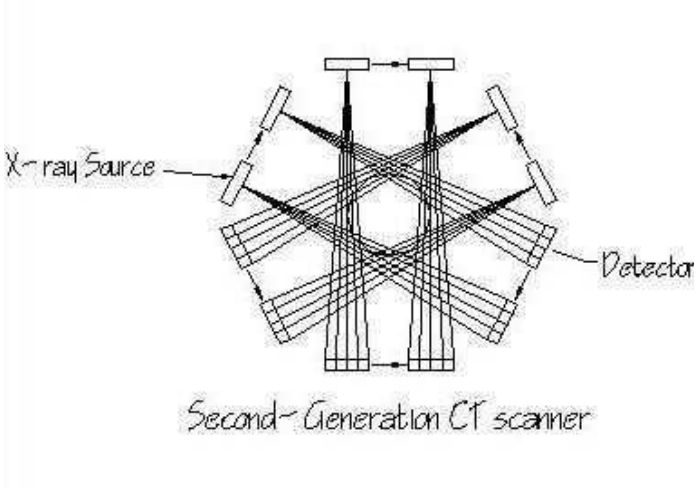

Figure 7 - Schematic representation of a CT scanner of the second generation (Courtesy of Prof. Francesca Granata).

In the third generation, the number of generators was increased, and the range of X-ray embraces the whole object to be examined. In this way, it is no longer necessary to provide translation for each direction.
The source-detector system rotates, continuously, on a 360 ° arc. Consequently, the time for an examination decreased up to 5-10 seconds, allowing the examination of bodies in motion (Fig. 8).

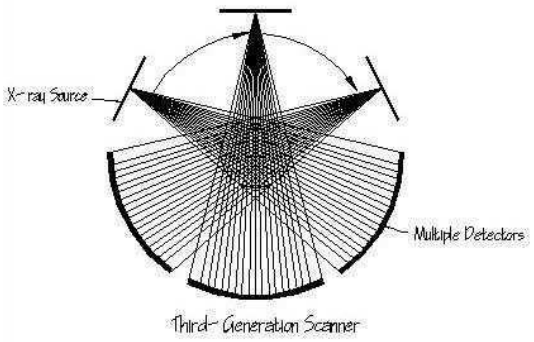

Figure 8 - Schematic representation of a CT scanner of the third generation (Courtesy of Prof. Francesca Granata).

The fourth-generation scanners showed fixed sensors, and soon it has been abandoned. Modern scanners derived from the third-generation scanner have a fundamental characteristic: a spiral configuration for the images acquisition. In a unidirectional continuous rotation tomography, the X-ray tube and detectors are mounted on a rotating ring that is fed to "wiping contacts", with no longer the problem of cables twisting themselves (Technology Slip Ring 6- 1987). This method allows the acquisition of images in a continuous way: while the table which leads the patient to moves on a sliding surface, the scanning planes describe a helix around the patient, obtaining a "spiral" scan.
The problem with this technology, working with oil, was the cooling of the X-ray tube, whose temperature reached 900 degrees during scans. The materials with which the tubes were initially constructed had a minimal heat capacity that did not allow to perform very high duration of scans due to significant overheating effects.
The devices of the spiral CT have evolved, from 1998 until today, characterised by the addition of multiple files (banks) of detectors, hence

the name of multilayer spiral CT: to each rotation, instead of a single layer, multiple numbers were acquired. At the beginning there were 4 layers, then 8, 16, 32, 64, 128, 256 etc. Other significant developments have occurred in the calculation systems and software for image reconstruction, in the sliding contacts and, finally, the X-ray tubes have been constructed to dissipate heat and therefore to allow continuous scans.

2.5 Multislice Computed Tomography (MSCT)

Multislice Computed Tomography (MSCT) is the instrumentation that allows performing scans in a short time. For example, it can acquire information about human organs in 1 second, about the heart in 5 seconds and the whole body in less than 10 seconds (Goldman 2008).

The units composing a tomograph are mostly three:

1. Scanning unit (gantry): high voltage generator, X-ray tube, collimation system, detectors, and the data acquisition system.
2. Software: handles the scanning and reconstruction of the data.
3. Control console: Display systems, storage, and playback of images (see scheme in Fig. 9).

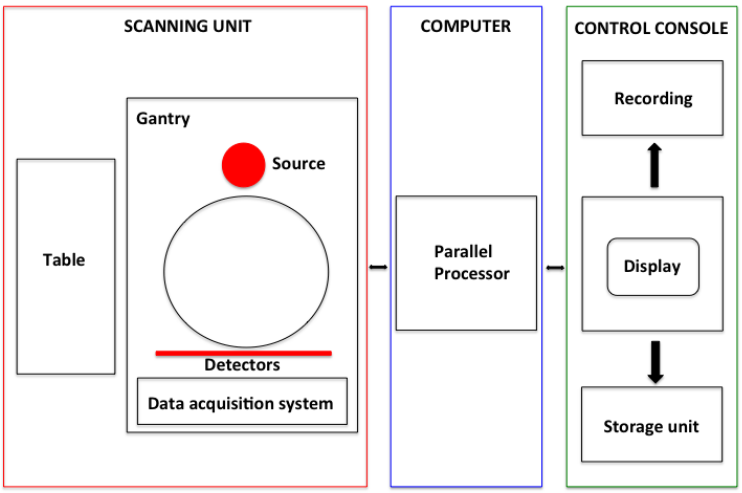

Figure 9 - Mulsitslice Computed Tomography system (Longo et al. 2018, PhD Report, University of Messina)

The working geometry has been optimised to obtain a correct reconstruction when the plane under examination is irradiated. The most simple tools reconstruct the planes of the cross-sections of the patient's body by directing on them collimated beams of X-rays while an X-ray detector is situated on the opposite side of the patient, relative to the source and the collimator. The source, collimators and the detector rotate by scanning along different directions of a specific plane of the patient's body said tomographic plane. The analysis of the collected data allows reconstructing the changes in the current material density to the plan.

Further evolution of MSCT technology consists of the Dual-Energy (DE). By using different hardware and software devices, this method can represent CT scans of data obtained from two different energy spectra, usually 80 and 140 kVp, to differentiate the composition of the fabrics or materials.

During a single spiral scan, data acquisition in DE can be obtained using two radiating sources operating simultaneously in a different energy range, as in CT Dual -Source, or using a single radiating element. In the latter case, the different energy spectra are obtained with systems capable of alternating hundreds of times per second, the voltage values of the tube during the rotation of the gantry, namely a single tube with rapid "switching" of the kVp.

Today, however, CT Dual - Energy is one of the most exciting technological innovations in computed tomography (CT), as evidenced by the growing number of jobs in the literature in various fields of clinical application (Primak 2009)

Hence, CT Dual - Source, thanks to the combined and simultaneous two-pipe systems - detector mounted orthogonally within the gantry- offers the possibility to take advantage of low energy without any loss of image quality. Finally, the combination of two different weighing data set is the goal of image fusion. Furthermore, CT Dual - Source technique offers two options for scanning approach. It is possible to separately assess the contribution of the two pipes, in order to take advantage from the increased conspicuity of the contrast medium (ICM)38 at low energy, or it is possible to melt together the two information to obtain images with quality

characteristics and noise fully superimposable to those of standard images to single energy with tube 120 kVp.
The fusion of the images, as well as with linear technique, is obtained applying a sigmoid technique. The latter allows reconstructing the voxels with high attenuation, such as those of iodine, mainly by the low-energy tube in order to exploit the increased conspicuity, and allows to reconstruct, in contrast, the low voxel attenuation (fat, tissues soft), mainly by the high energy tube, in order to reduce noise. So, it is possible to have a high-quality image comparable to those of the tube to 120 kVp; instead, the perception of enhancement is like that one obtainable at low kVp. Finally, thanks to the vast difference in the attenuation of iodine at different scans voltage, some specific software, based on decomposition systems at three materials (fat, iodine and soft tissue), allows to remove the iodine or superimpose it as a colour map on images in grayscale.

2.6 CT image processing and Hounsfield units

As already mentioned, the image of the object is created by measuring the attenuation of an X-rays beam. It varies depending on the electron density of the tissues crossed the spatial distribution of the electrons in the layer under examination. Since the resulting images are in a digital format, the object examined is divided into a discrete set of volume elements called voxels, which corresponds to pixel (area) for height (slice thickness) and follow the grayscale.
The voxel is three-dimensional while the pixel is two-dimensional. Size of the voxels depends on the type of collimation and the number and size of the detectors (Kalender 2000).
The smaller area is represented by a single pixel, more significant of the spatial resolution. The attenuation is directly proportional to the electron density of the tissues present in the voxel: its value is called "densitometry". A gradation of lighter grey represents a voxel with high density. The measurement of the electron density is made by using the HU

(Hounsfield units), which includes 2001 different shades of grey, from black to white.

The HU scale is a linear transformation of the original linear attenuation coefficient measurement into one in which the radio-density of distilled water, at standard pressure and temperature, is defined as zero Hounsfield units (HU). In contrast, the radiodensity of air at STP (Standard temperature and pression) is defined as -1000 HU. For any material with linear attenuation coefficient μ_x, the corresponding HU value is therefore given by:

$$HU = 1000 \bullet \mu - \mu^{water} / \mu^{water} - \mu^{air} \quad (2)$$

The Hounsfield units is a relative parameter, where water is taken as a reference substance (Fig. 10).

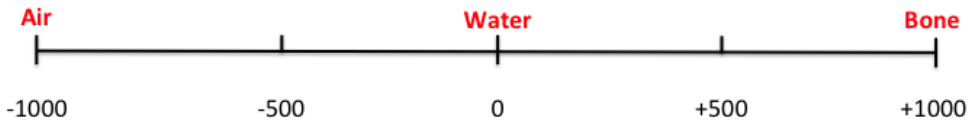

Bone	+400 → +1000
Soft Tissue	+40 → +80
Water	0
Fat	-60 → -100
Lung	-400 → -600
Air	-1000

Figure 10 - Attenuation values in HU of specific organs and tissues. The water-mail is 0, the expression of its measurement system. At the two extremes, the bone, +1000HU, and the air, -1000HU (Longo et al. 2018, PhD Report, University of Messina).

The Hounsfield numbers, assigned to each voxel, are subsequently attributed to an image matrix which usually has a size of 512x512x512 pixels. Finally, thanks to mathematical algorithms, powerful software can reconstruct the image. After the acquisition of the data, many post-processing operations are possible (e.g., the planar and 3D reconstructions). Moreover, there are several modes of visualisation of CT images that can be changed to enhance the information of particular interest or suppress others, if considered irrelevant, by changing the range of greys said Window Width. Changing these values, above and below the considered window, they will have respectively the colours black and white.

2.7 X-ray Computed Tomography applied to Cultural Heritage

In scientific literature, there are many studies which focus on structural investigations by X-ray CT. This technique has proved to be an excellent aid for materials research. Correctly, industrial and medical CT scanners are used in the timber industry to investigate the internal structure and integrity of wood (Lindgren 1991; Voichita 2003; Steppe 2004) and in archaeology and anthropology to study mummies (Hardwood- Nash 1979; Taconis 2005; Piombino-Mascali 2014) and dental, skeletal remains using microCT and synchrotron radiation (Zanolli 2014). X-ray CT technologies have been widely used for investigations of works of art (Rossi 1999; Sirr and Waddle 1999; Seracini 2005; Morigi 2007 and 2010; Casali 2008; Stoel and Borman 2008; Brancaccio 2011; Re 2012; Tuniz 2012; Parisi 2016). Other fields of X-ray CT application are in geology (Pralle, Bahner, and Benkler 2001) and airport safety (Kaufman 2003; Kaick and Delorme 2005). However, the great variety of size and composition that characterises archaeological findings and art objects requires the development of tomographic systems designed explicitly for Cultural Heritage analysis.

Furthermore, in the last few years, micro-CT is widely used for research on archaeological materials, obtaining pictures of the internal structure of materials (Haneka 2012). On the other hand, portable CT is used to characterise large objects (Brancaccio 2011). The most popular in Italy is the one developed by the University of Bologna, inside the neu_ART project (Re 2012). The instrument consists of a fixed X-ray tube and a rotating platform where the object is placed. This configuration makes it much easier to investigate the inner structure of large objects (as the Kongo Rikishi, a Japanese wooden statue of the thirteenth century. 2,2 m high) (Casali 2008). However, it does not allow to have three-dimensional images in high resolution or to perform densitometric measurements. Software processing is significantly lower than those of a standard medical CT. Indeed, a portable CT has not the limitation of the maximum diameter of the gantry, but it loses in terms of images definition.
In the last years, MSCT technique has been successfully adapted to carry out polychrome wooden cultural heritage analysis (Seracini 2005, Parkers and Watkinsons 2007). A multi-planar reconstruction (MPR) processing with very satisfactory results is always performed but, unfortunately, there is no available a volume rendering technique (VRT) processing approach to display a 2D projection of a 3D discretely sampled data set, typically a 3D scalar field.

As will be shown in this thesis, MSCT is not only useful to characterise materials. However, it can successfully be used to investigate artistic techniques: for example, to evaluate building techniques without damage the object, both using MPR reconstruction or make a 3D image with VRT elaboration. When the VRT approach is used, VRT images are rated on medical filters, in turn, calibrated on "human materials". This latter generally has an attenuation coefficient like that of Cultural Heritage Materials. (example: bones are made of calcium like plaster). More details will be reported in the following chapters.

A further exciting application of CT technique shown in this thesis will regard the estimation of the state of conservation. Thanks to the possibility to perform linear coefficient attenuation μ measurements on materials which are strictly correlated to the density expressed in Kg/m^3

or g/cm^3, volume variations and degradation process of a material can be detected.

Ultimately, the main goal of the work carried out during the PhD period has been to define, for the first time to our knowledge, an MSCT protocol method (by clinical scanners) suitable for wood and wooden works analyses.

Chapter 3

Nuclear Magnetic Resonance

In the last decade, there is an always growing understanding that the characterization of the state of conservation, the knowledge of the causes of degradation of materials, the development of new methods and materials aimed at lengthening the lifetime of the artifacts are mandatory for the correct safeguard of Cultural Heritage.

Although for 50 years Nuclear Magnetic Resonance (NMR) has been a very powerful tool in many fields, its application to Cultural Heritage is rather recent. One of the reasons is that, during its initial decades of existence, NMR was mainly a tool for the analysis of samples in the liquid phase, whereas materials of interest for Cultural Heritage, such as paper, wood, stones, textiles, resins, parchment, pottery, glass, leather cannot be solubilized without definitely changing or even fully destroying their molecular structure. Nevertheless, some NMR analyses in solution have been carried out to characterize soluble organic residues found in ancient artifacts (generally, liquid or gas chromatography followed by mass spectroscopy have been applied to separate molecular mixtures into their pure components). However recently complex mixtures of organic compounds may be successfully analysed by NMR taking advantage for example on the difference in the molecular self-diffusion coefficients. As will be better described in the following paragraphs, molecular self-

diffusion can be encoded into NMR datasets by means of pulsed gradients of magnetic field.

Many materials of interest for Cultural Heritage may be porous, such as porous stones, plaster, mortar, wall painting, fired clay, paper and wood. The most common NMR methods to probe the structures of porous media are based on the measurement of relaxation times and diffusion coefficients of water inside the porous system. In fact, relaxation times of fluids confined in porous media are strictly related to the geometry of the structure, as water in small pores relaxes rapidly, whereas water in large pores relaxes more slowly. The presence of relaxation sinks at the surface of pore grains and the inhomogeneity of pore dimensions, cause multi-exponential decay of the magnetization and a reduction of relaxation times. In many cases the properties of porous systems may be spatially resolved by means of Magnetic Resonance Imaging (MRI).

Today, three NMR large sub-areas of applications are broadly identified:

1. *Spectroscopy*: provides chemical information about the sample.
   After the finding of the chemical shift effect, this technique aroused a strong interest in the chemical community. However, the advent of other techniques like pulse NMR and spin echo, together with the implementation of pulse sequences, increased the number of possible applications, not only in chemistry.
2. *Imaging*: explores heterogeneity on a macroscopic scale. The most recent development has been that of magnetic resonance imaging (MRI), which uses frequency (and/or) phase encoding of the spins producing the NMR signal to record different kind of images on the micron scale of the samples under study.
3. *Relaxometry*: gives information about the physical properties of the sample at the molecular level. Since the early days of well-logging NMR, water-saturated natural rocks have been characterized by multi-exponential NMR relaxation behaviour which may be analysed in terms of distributions of relaxation times.

In this thesis, experimental results achieved by imaging and relaxometry applications, obtained respectively with a 3T clinical MRI scanner and a 9.4 T spectrometer equipped with a microimaging probe

(μMRI) on waterlogged contemporary and ancient wooden samples will be reported.

3.1 NMR principles

In the early stages, after the discovery of the Zeeman effect (the splitting of energy levels is proportional to an external magnetic field), the discovery of the spin nature of the proton and the interaction between the proton spin and a magnetic field, NMR was used just to do an accurate measurement of nuclear magnetic moment (Purcell 1946; Bloch 1946).
All microscopical particles like electrons, protons and neutrons possess an intrinsic magnetic moment called spin which assumes the value (+1/2) ħ and (-1/2) ħ, where ħ is the Planck's constant divided by 2π. In the absence of an external magnetic field, this property is not observable. Nuclei consist of protons and neutrons, so they possess an overall nuclear spin and angular momentum P.
Nuclei with non-zero spin could be classically described as an asymmetric positive charge distribution which causes a rotation around the spin axes. Anything that is charged and moves has a magnetic moment thus produces (and can interact with) a magnetic field.

Nuclear Magnetic Resonance (NMR) is based on these concepts and precisely:
the investigated sample is first subjected to a constant magnetic field which induces a separation of the energy levels of the nuclear spins and is then exposed to electromagnetic radio waves. When the frequency of the wave is such that its energy coincides with the difference in energy between the spin states (resonance condition), the system switches to a higher energy spin state. Studying the transition of the system to the equilibrium state provides information on how atomic and nuclear systems interact in the environment in which they are found (Serway 2015).
Here, more details are reported. The nuclei have an angular momentum $\vec{P}$ which, according to the rules of quantum mechanics, is quantized and its

module can be written as:

$$P = \sqrt{I(I+1)}\frac{h}{2\pi} \quad (1)$$

where I is the quantum spin number. The quantum number I can only take integer or half-integer values (I = 0, 1/2, 1, 3/2, etc.), which can be calculated according to the values of the number and atomic mass. To the angular momentum P corresponds a magnetic moment $\vec{\mu}$ with the same direction:

$$\vec{\mu} = \gamma \vec{P} \quad (2)$$

where γ is called nuclear gyromagnetic ratio and depends on the nucleus of the element. For the hydrogen atom nucleus (^{1}H), which is simply a proton, it is: γ = 2:675 x 10^8 rad/(s · T). Materials consisting of atoms, whose nuclei are characterized by a higher γ, are more sensitive to the NMR technique. So, the magnetic moment module is given by:

$$\mu = \gamma \sqrt{I(I+1)}\frac{h}{2\pi} \quad (3)$$

If an atom is placed in a static magnetic field, directed by convention along the z-axis, it turns out that the z component of the angular momentum P_z is quantized (Fig. 1):

$$P_z = m\frac{h}{2\pi} \quad (4)$$

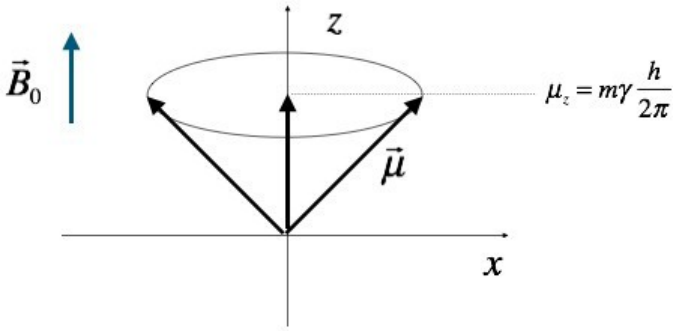

Figure 1 - The angular momentum component is quantized along the z-direction of application of the external magnetic field (Courtesy of Dr Silvia Capuani).

where *m* is called magnetic quantum number and can only assume (2 I + 1) values ranging from -I to + I units. So, the angular momentum has orientations that are quantized. The component along z of the magnetic moment $\vec{\mu}$ also has a similar directional quantization expressed by the relation:

$$\mu_z = \gamma m \frac{h}{2\pi} \quad (5)$$

The magnetic moment $\vec{\mu}$ can classically be a preceding vector around the direction of the static magnetic field $\vec{B}_0$.

This motion will occur with a frequency called "Larmor frequency" (Abragam 1961) proportional to the magnetic field (Fig. 2)

$$\nu = \frac{\gamma}{2\pi B_0} \text{ or } \omega = \gamma B_0 \, (\omega = 2\pi\nu) \quad (6)$$

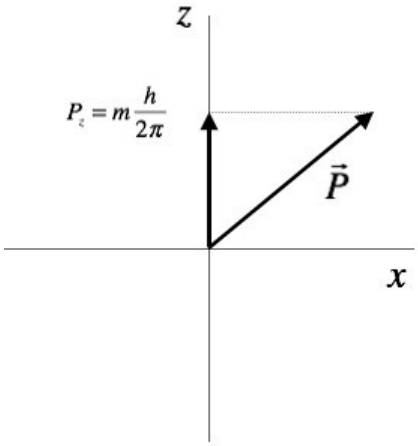

Figure 2 - Precession motion of the magnetic moment $\vec{\mu}$ around the direction of the magnetic field. Note that the projection values are quantized (Courtesy of Dr Silvia Capuani).

The magnetic dipole placed in the magnetic field takes on energy equal to:

$$E = \mu_z B_0 \qquad (7)$$

From this relationship, it emerges that a nucleus that has (2I + 1) possible orientations for the magnetic moment, also has (2I +1) energy states. Considering, for example, a proton, that is the nucleus of the hydrogen atom, of spin I = 1/2 we will have two possible values for *m*, *m* = + 1/2 and *m* = -1/2. Therefore, the z component of its angular momentum is:

$$P_z = \pm\frac{1}{2}\frac{h}{2\pi} \qquad (8)$$

Similarly, as regards the value of the magnetic moment in the z-direction, we have:

$$\mu_z = \pm\gamma \frac{1}{2} \frac{h}{2\pi} \quad (9)$$

The proton, therefore, has a magnetic moment whose component z can be parallel or antiparallel to the positive direction of the z-axis, i.e. to the direction of the applied magnetic field (Fig. 3).

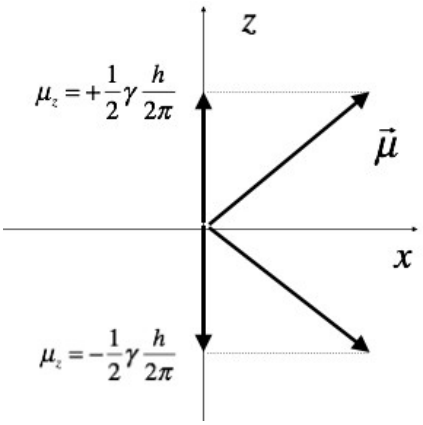

Figure 3 - A spin ½ core has only two possible orientations of the magnetic moment (Courtesy of Dr Silvia Capuani).

The energy associated with the two states is worth respectively:

$$E_\alpha = -\gamma \frac{1}{2} \frac{h}{2\pi} B_0 \qquad E_\beta = \gamma \frac{1}{2} \frac{h}{2\pi} B_0 \quad (10)$$

E_α represents the energy associated with parallel orientation (m = + ½) while E_β represents the energy associated with the antiparallel orientation (m = - ½) (Fig. 4).

Therefore, $E_\beta > E_\alpha$ and the difference between the two energy levels can be expressed as:

$$E_\beta - E_\alpha = \Delta E = \gamma \frac{h}{2\pi} B_0 = \frac{h}{2\pi} \omega \quad (11)$$

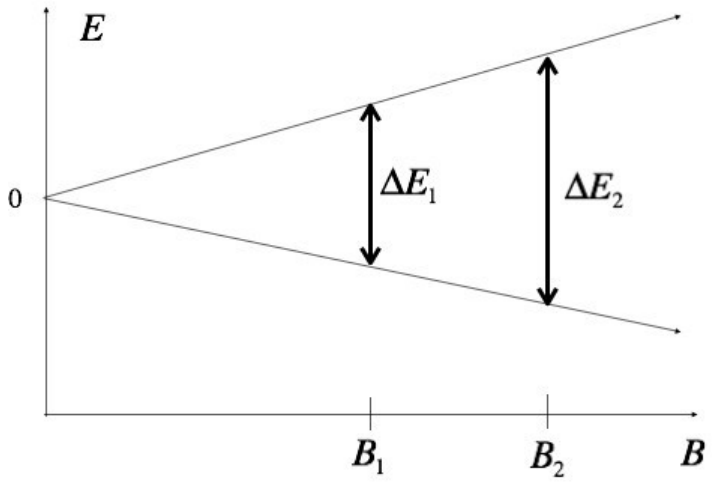

Figure 4 - shows the quantized energy levels of the magnetic moment-field system. The energetic separation is induced by the application of the magnetic field B_0 (Courtesy of Dr Silvia Capuani).

The separation between the energy levels is proportional to the intensity of the applied field B_0 (Fig. 5) and the gyromagnetic ratio factor.

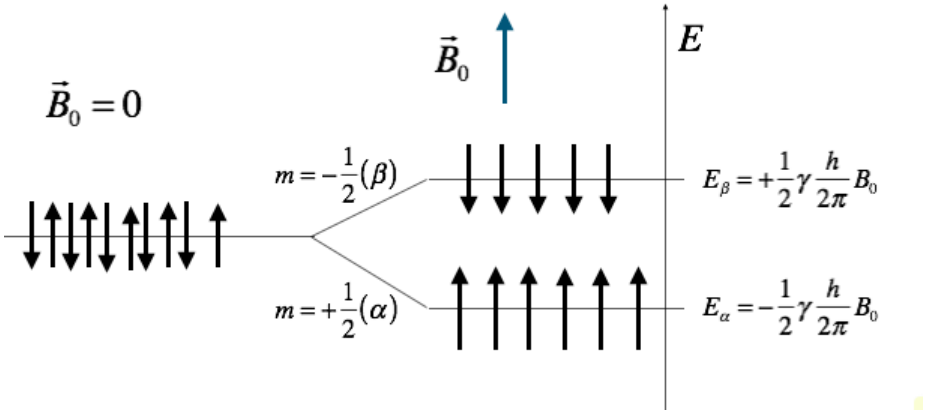

Figure 5 - The separation between the levels is directly proportional to the applied magnetic field (Courtesy of Dr Silvia Capuani).

Each energy level has a different population (N), and the population ratio is given by the Boltzmann statistics:

$$\frac{N_\beta}{N_a} = e^{-\frac{\Delta E}{k_B T}} \quad (12)$$

where ΔE is the energy difference between the two spin states characterized by a different population, k_B is the Boltzmann constant, and T is the sample temperature.
In a hydrogen nucleus, the energy difference is minimal compared to the energies related to the motions of thermal agitation, and it turns out that the difference between the two populations is minimal. Thus, applying a B_0 field of 1.41T using the relation (11), we found that:

$$\frac{N_\beta}{N_a} \approx 0{,}9999904 \quad (13)$$

It shows that the technique provides a weak signal in favor of the population with spin parallel to the field to which a lower energy corresponds. Therefore, if an appropriate radio frequency is sent, absorption can occur (resonance condition), which causes the spins to reverse their orientation (Günther 2013). Finally, when the radio frequency pulse ceases, the system tends to return to the original equilibrium condition and the overall signal is directly proportional to the population difference that in turn depends on the static magnetic field. The equilibrium recovery occurs through two characteristic relaxation phenomena that are fundamental in determine the NMR signal.

Summarizing, NMR spectroscopy is a spectroscopic technique to observe local magnetic fields around atomic nuclei. The sample is placed in a magnetic field and the NMR signal is produced by excitation of the nuclei sample with radio waves into nuclear magnetic resonance. The intramolecular magnetic field around an atom in a molecule changes the resonance frequency, thus giving access to details of the electronic structure of a molecule and its individual functional groups. As the fields are unique or highly characteristic to individual compounds, in modern organic chemistry practice, NMR spectroscopy is the definitive method to identify monomolecular organic compounds. Similarly, biochemists use NMR to identify proteins and other complex molecules. Besides

identification, NMR spectroscopy provides detailed information about the structure, dynamics, reaction state, and chemical environment of molecules.

3.2 Magnetization and its relaxation

3.2.1 Magnetization

The nucleus of a hydrogen atom (the proton) has a magnetic moment μ = 2.7927 in terms of nuclear magnetons, which are $5.05078 \cdot 10^{-27}$ JT^{-1} and has been studied more than any other nucleus. For example, the use of ^{1}H NMR for metabolic studies was described as early as 1977 when it was shown that ^{1}H signals could be observed from a range of compounds in a suspension of red blood cells, including lactate, pyruvate, alanine and creatine. A great deal of metabolic information can be derived from such metabolic studies and it was soon recognized that ^{1}H NMR of body fluids has a considerable role to play in areas of pharmacology and toxicology.

Water is the primary source of the signals used in NMR. The signal strength of water protons varies greatly depending on their physical relationships with other molecules and other magnetically active materials. Under normal conditions, the hydrogen nuclei in water are in a complete electromagnetic disorder or are randomly oriented in space. To align them, it is necessary to place it in a high intensity static magnetic field, produced by the coils of the magnetic resonance instrument. The preferred state of alignment of the protons is the one with the lowest energy level, so many of them will be on the lowest energy level and parallel to the external magnetic field. Furthermore, the protons are not fixed but turn on themselves (spin) with a movement, like a gyroscope, which is called "precession".

During the precession movement, the axis rotates describing a cone. The movement speed is not constant and depends on the strength of the magnetic field in which the protons are inserted: more intense the magnetic field is, higher is the speed and the frequency of precession.

The calculated frequency precession from the Larmor equation is:

$$\omega_0 = 2\pi\nu_0 = \gamma B_0 \qquad (14)$$

where the gyromagnetic ratio γ is a constant characteristic of the specific atomic nucleus, and $\nu_0 = (E_{\square} - E_{\square})/h$, where h is the Planck's constant. The system absorbs energy (resonance condition), and the magnetization vector rotates from the z-axis to the *xy* plane. Just the components of the vector M_0 along the *xy* plane lead to the detection of the NMR signal (Fig. 6).

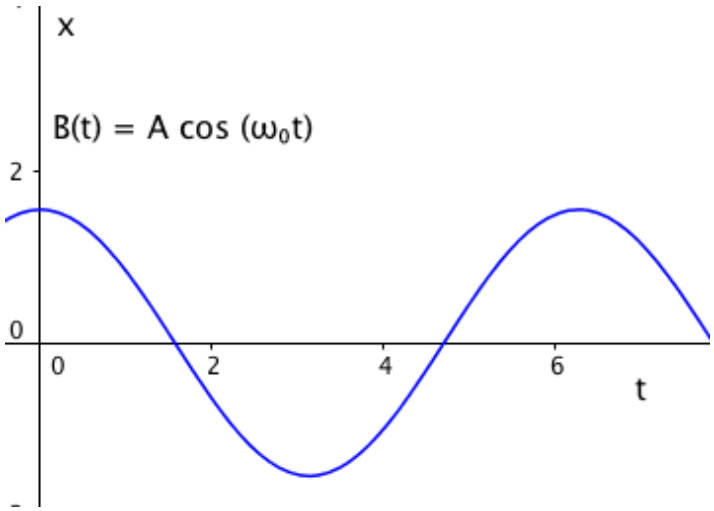

Figure 6 -Sinusoidal trend of the magnetic field $\vec{B}_1(t)$ at radiofrequency $\square_0$ (Courtesy of Dr Silvia Capuani).

The field $\vec{B}_1$ is an electromagnetic field of radiofrequency directed along the x-axis and orthogonal to the z-axis. A field with these characteristics can be broken down into two components rotating in the opposite direction (Fig. 7).

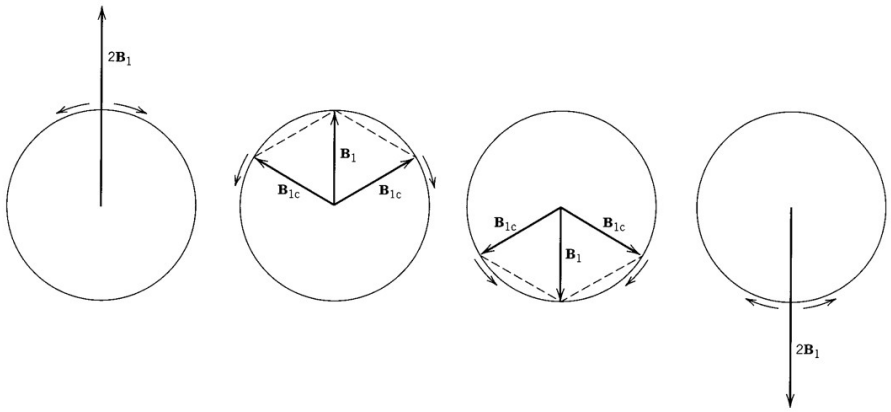

Figure 7 - Decomposition of the magnetic field variable in two components rotating in opposite directions (Courtesy of Dr Silvia Capuani).

One of the rotating vectors will have the same direction of rotation as the magnetic moments, while the other will have the opposite direction. Resonance occurs when the vector, rotating in the same direction, has the frequency ν_0 equal to that of Larmor. In this case, the absorption of energy by the nuclei takes place and therefore the magnetization vector rotates towards the *xy* plane. A suitable receiver can detect the component of the magnetization on the *xy* plane, and the signal will be maximum when the magnetization vector lies entirely on this plane. When the energy is stopped, the external field is lost, and the magnetization vector will tend to return towards the *z*-axis through a complex precession motion, restoring the distribution of the original spin populations (Fig. 8).

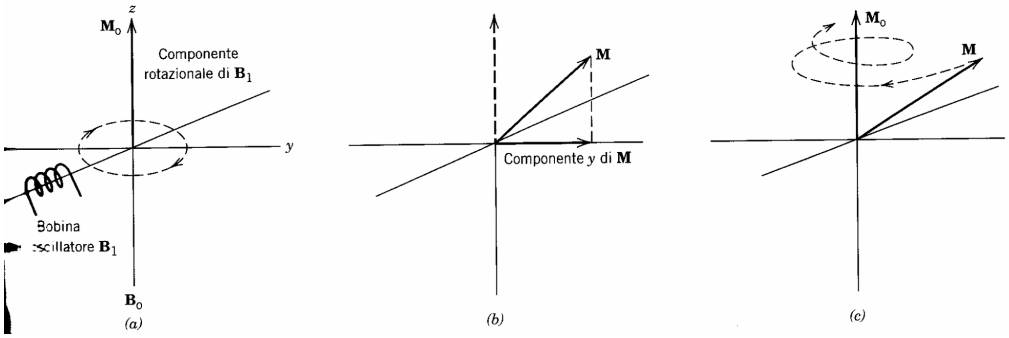

Figure 8 - The application of a magnetic field B_1 of suitable frequency can induce the rotation of the magnetization vector on the xy plane. When the impulse ceases, the magnetization returns to its original position through a precession motion (Courtesy of Dr Silvia Capuani).

The variation in time of M_{xy} generates a variable magnetic field whose flux, linked to the radiofrequency coil, induces a current in the coil, in agreement with Faraday's law. For example, the frequency ν_0 for protons ^1H is 21.29 MHz in a magnetic field with B_0 = 0.5 T, which is a typical value for compact permanent magnets of mobile NMR instruments.

Furthermore, after a radiofrequency (RF) pulse, the protons precede in synchrony with the same 'phase'. They now point in the same direction with the same precession frequency, and the magnetic vectors placed in this direction are added. The result is a single magnetic vector oriented in the direction of all the protons in the transverse direction (transverse magnetization). I outline that RF pulses could be applied for changing both longitudinal and transverse magnetizations.

When RF stops, the pre-existing situation is restored through relaxation processes. In other words, there is a transfer of energy also in the form of an RF signal with the appearance of damped oscillations called FID (free induction decay) (Fig. 9). On the contrary, the longitudinal magnetization increases again being characterized by the longitudinal relaxation time T_1.

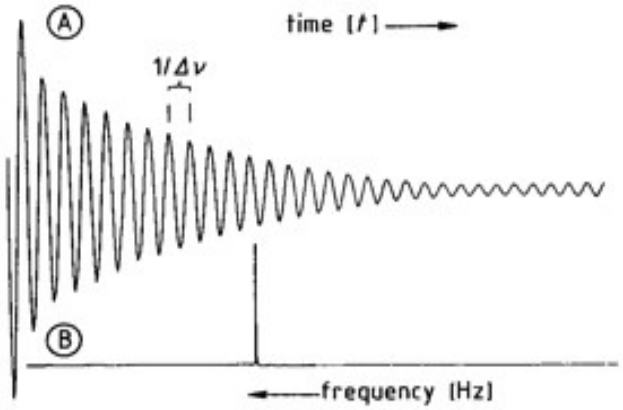

Figure 9 - Trend of an ideal NMR signal as a function of time (Courtesy of Dr Silvia Capuani).

Felix Bloch studied the motion of magnetization $\vec{M}_0$, both during the application of radiofrequency and relaxation (Bloch 1946). Based on the experimental observations, the magnetization returned to equilibrium through an exponential trend. The equations describing this process are:

$$\frac{d\,Mz}{dt} = \frac{-Mz-M0}{T_1} \; ; \frac{d\;Mx\,\prime}{dt} = \frac{-\,Mx\,\prime}{T_2} \; ; \frac{d\;My\,\prime}{dt} = \frac{-My\,\prime}{T_2} \qquad (15)$$

The deterioration of an NMR signal is analyzed in terms of two separate processes, each with their own time constants. One process, associated with T_1, is responsible for the loss of signal intensity. The other process, associated with the transverse relaxation or T_2, is responsible for the broadening of the signal. Stated more formally, T_1 is the time constant for the physical processes responsible for the relaxation of the components of the nuclear spin magnetization vector M parallel to the external magnetic field, B_0 (which is conventionally oriented along the z axis). T_2 relaxation affects the components of M perpendicular to B_0. In conventional NMR spectroscopy, T_1 determines the recycle time, the rate at which an NMR spectrum can be acquired. Values of T_1 range from milliseconds to several seconds. More details about relaxation times are reported in the next paragraphs.

3.2.2 Longitudinal relaxation time T_1

The equilibrium is disturbed when a radio pulse moves the net magnetization from the initial longitudinal plane. This disturbance of balance during which transverse magnetization is generated is called "excitation". The longitudinal magnetization is eliminated or saturated. The saturation of the longitudinal magnetization is complete in the presence of a 90° pulse. The equation describing the recovery of the longitudinal magnetization as a function of time (namely the temporal trend of the magnetization) can be represented by an exponential function (Fig. 10):

$$M_z = M_0\,(1-e^{-t/T_1}) \qquad (16)$$

Mathematically T_1 represents the time constant after which the magnetization returns to about 67% of the initial value.

If a 180° pulse is provided, the magnetizations will return to the equilibrium position according to the following relation:

$$M_z = M_0 (1 - 2\, e^{-t/T_1}) \qquad (17)$$

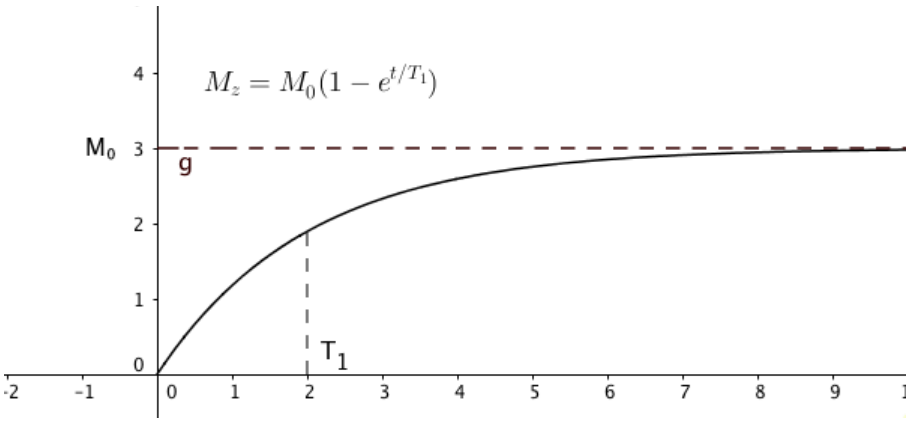

Figure 10 - Trend of magnetization M_z as a function of time (Courtesy of Dr Silvia Capuani).

After exposure to an RF pulse, the net magnetization returns to equilibrium. This recovery which requires no additional radio pulse is called relaxation. In general, relaxation processes are slower (326.95± 29.58 ms) in free water than in bound water (186.01±48.19 ms) (Abbasi-Rad 2017). As mentioned, the process by which longitudinal magnetization recreates is called longitudinal relaxation or T_1 relaxation. The time it takes for the protons to return to the longitudinal equilibrium orientation is expressed through a constant called relaxation time which at, a given magnetic field intensity, depends on the efficiency with which it can transfer energy to the surrounding nuclear structures. The transfer of the energy involved in T_1 relaxation is called spin-lattice interaction.

In particular, the value of T_1 is one of the most important variables to consider when applying a pulse sequence for imaging to emphasize the differences (contrast) between the T_1 relaxation times of different

structures within the studied sample. The two most important parameters that can be modified to control the weighing in T_1 of an image are the repetition time (TR) and the flip angle, that we will discuss in the next.

3.2.3 Transverse relaxation time T_2

The transverse magnetization, created by the rotation of the longitudinal magnetization on the transverse plane, decays at speed equal to or greater than the speed of recovery T_1. The decay of the transverse magnetization is defined as T_2 relaxation. The speed of this decay is defined by the T_2 relaxation time of the material. Transverse relaxation occurs because of the exchange of energy between protons of the same species and is called spin-spin interaction.
This type of decay follows an exponential law (Fig. 11) and it is described by the equation:

$$M_{xy} = M_{xy0}\, e^{-t/T_2} \qquad (18)$$

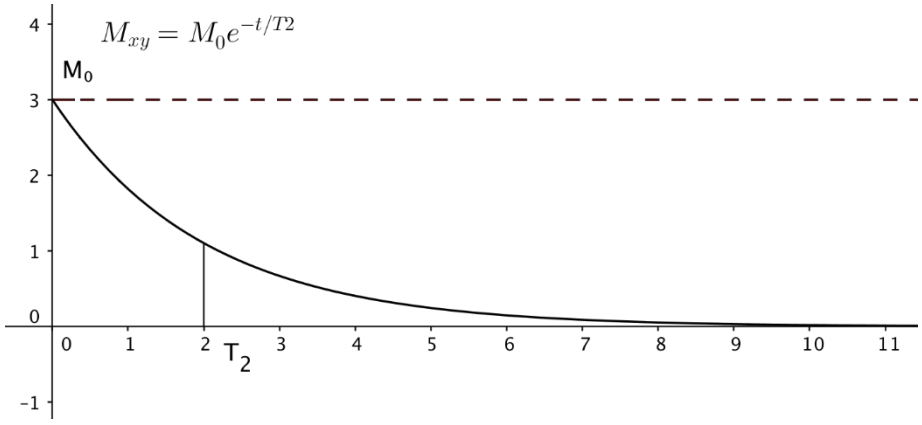

Figure 11 - Trend of magnetization M_{xy} as a function of time (Courtesy of Dr Silvia Capuani).

The random and rapid movement of the free water molecules makes the exchange of energy between protons inefficient and slow. Therefore, in free water, the magnetization decays slowly, and T_2 is long. On the contrary,

the T_2 relaxation of bound water, which has a more organized structure and is in tight contact with other molecules, is shorter.
Relaxation times T_2 is less affected by the intensity of the magnetic field than T_1. The additional decay of the transverse magnetization resulting from local magnetic effects, however, depends a lot on the intensity of the magnetic field. The decay of transverse relaxation resulting from the combination of T_2 relaxation and the inhomogeneities of the magnetic field is called apparent spin-spin relaxation time or T_2*.
Generally, T_2*<T_2 and therefore the decay is faster than that caused only from T_2 relaxation. The law that outlines the temporal evolution of magnetization is always an exponential function:

$$M_{xy} = M_{xy0}\, e^{-t/T_2^*} \qquad (19)$$

In the case in which the studied material is porous, there are further field inhomogeneities, caused by the different magnetic susceptibility between the water and the surface of the pores in which it is contained. In presence of smaller pores, characterized by a higher surface/ volume ratio, an increase in susceptibility occurs, leading to a decrease in relaxation times T_2 and especially T_2*.

3.2.4 Inversion Recovery and Spin-Echo pulse sequences

The relaxation times T_2 and T_1 are different depending on the material, and in general, their measurement allows us to know the physical and chemical characteristics of the investigated system.
They are measured by applying proper sequences of pulses: the most common are inversion recovery for the measurement of T_1 and the Spin-Echo sequence for the determination of T_2.

The inversion recovery method consists in the application of two radiofrequency pulses, one at 180° and the other at 90° separated by a specific time interval. The first pulse carries the magnetization along the negative direction of the z-axis and does not produce any signal. As previously mentioned, the magnetization vector will tend to regain the original direction following the exponential law (eq. 17). At a chosen time τ_1, the second pulse is applied, and the magnetization is rotated in the *xy* plane, in order to collect the signal by the instrumentation (Fig. 12).

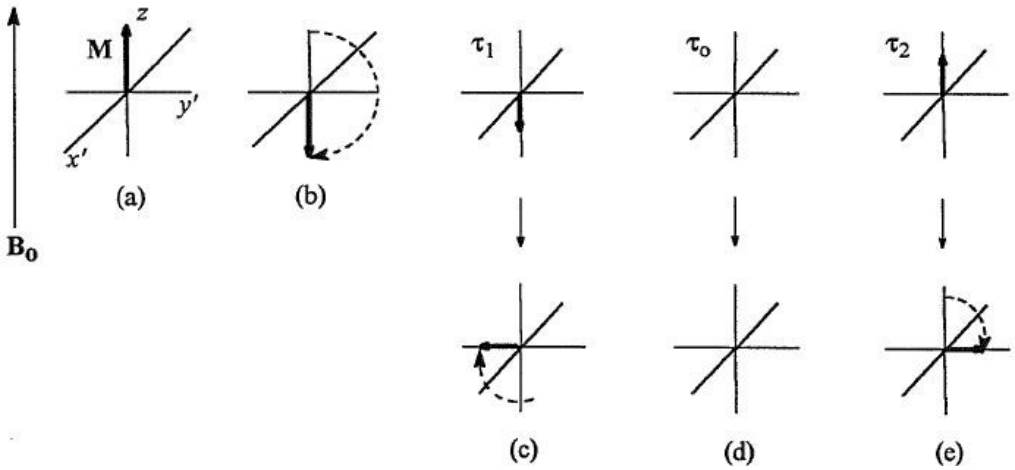

Figure 12 - Inversion Recovery scheme. The magnetization (a), rotated by 180° (b), tends to return to the original position with an exponential trend (eq. 17). The application of a further 90 ° pulse, at a chosen time (c, d and e), rotates this quantity on the xy plane, allowing its instrumental detection (Courtesy of Dr Silvia Capuani).

The inversion recovery pulse sequence considers the application of the 90° pulse after a chosen number of time delays in order to sample the equilibrium recovery of the longitudinal magnetization and measure T_1.
As mentioned, the free induction (FID) or phase coherence of the spin decays with the apparent transversal relaxation time T_2*, which depends on the strength of the intermolecular interactions inside the sample and on the static field inhomogeneities. In order to neglect the field inhomogeneities, so to measure the real T_2 we use the so-called Spin-Echo pulse sequence. It consists of two pulses one at 90° and the second,

applied after a delay time τ, at 180°. This approach, in fact, allows for refocusing the phase shift of the spin caused by the inhomogeneities of the applied external field, in order to be able to evaluate only the transversal relaxation of the magnetization, caused by the spin-spin interactions (Fig. 13). The application of the first 90° pulse projects the magnetization along the y'-axis. Moreover, by applying a 180° pulse after a time $\tau < T_2$, directed along the y'-axis, the spins undergo a reversal along planes parallel to x'z. In this way, after a further time τ, there is a refocusing of the spins, which translates into a signal of maximum intensity (echo).

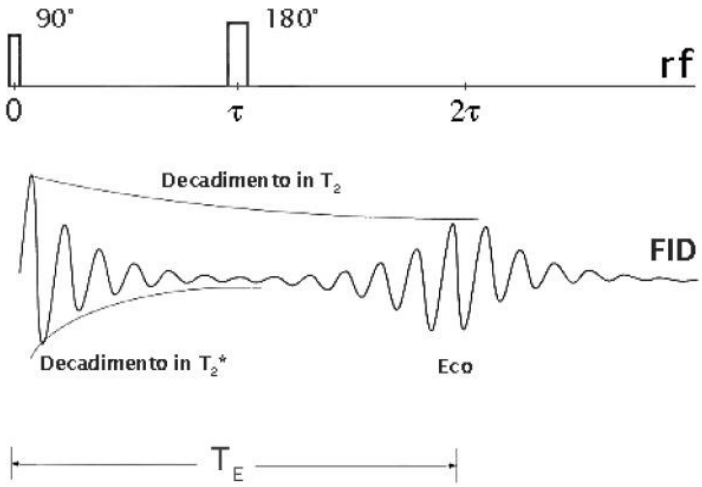

Figure 13 - Schematic representation of the effects produced by the spin-echo pulse sequence. Below the corresponding FID shows two decays with different time constants T_2 and T_2 (Courtesy of Dr Silvia Capuani).*

However, this amplitude will be less than that generated after the 90° pulse, as spin-spin relaxation is always present. From the analysis of the FID (Free Induction Decay) signals, collected at different acquisition times it is possible to determine the value of T_2 by using eq. 18. Note that the approach used to evaluate the relaxation time can vary among the different NMR sub-areas listed at the beginning (spectroscopy, imaging and relaxometry) due to the different characteristics of the acquired signals. Within high-resolution spectroscopy one usually deals with high-resolved spectra allowing the discrimination of the contribution of the individual molecular species. Within Imaging, as shown in the next, one deals with

images with sub-millimeters resolution weighed by different tunable parameters. Finally, relaxometry involves portable instrument with low magnetic field and so low resolution able to measure the relaxation times distribution of a macroscopic sample portion.

3.3 Magnetic Resonance Imaging (MRI)

Nuclear magnetic resonance imaging (MRI) is a non-destructive and non-invasive technique, widely used in clinical diagnostic field, which allows to visualize details on the internal structure of the studied tissue. Thus, MRI is a noninvasive modality, which produces multiplanar and true 3D datasets of subjects in vivo. It achieves high spatial resolution, typically of the order of millimeters in the clinical setting. Crucially, it differs from other techniques such as computed tomography (CT) by producing excellent soft tissue contrast without harmful ionizing radiation. MRI has transformed the role of radiology in medicine since its initial applications in structural imaging in the early 1980s and now encompasses wider areas of functional and molecular imaging. The ability of MRI to obtain non-destructive images from waterlogged wood samples, both prior to conservation and during consolidation, has been recently assessed (Capuani 2020).

Here, some specific aspects of MRI analysis compared to conventional NMR one is simply reported. First, I remark that the main difference between NMR spectroscopy and MRI imaging is that NMR generates information (spectral bands corresponding to the different chemical structures) based on the frequency of emitted radiation (which is related to the speed of the jiggling protons). MRI instead generates information (images) using the intensity of radiation (the quantity of re-emitted photons) arriving from various parts of body/material.

In NMR spectroscopy, the obtained FID signal provides information on a spin system. This signal is the superposition of many elementary signals

coming from the internal volume of the coil and therefore cannot be used for the tomographic reconstruction of the images. To spatially distinguish the origin of the signals, emitted by the nuclei returned to the initial conditions, it becomes fundamental to introduce a magnetic field gradient G which is added to the static magnetic field B_0. In this way, the resulting magnetic field is different in the various areas of the sample, and this affects the local resonance frequency of the spins being proportional to the intensity of the magnetic field (see eq. 14).
In this case, the Larmor frequency becomes a function of the spatial coordinates, and the distribution of the frequencies will become the distribution of the position of the spins in the space. This procedure allows to reconstruct the desired images.

In details, in order to discriminate these contributions in space, a magnetic field gradient G must be superimposed on the static field B_0. This gradient introduces a spatial dependence in the total magnetic field, which affects the resonant frequency of the spins:

$$\omega(\vec{r}) = \gamma B(z) = \gamma(B_0 + \vec{G}\cdot\vec{r}) \qquad (20)$$

The precession frequency thus becomes a function of the spatial coordinates and it can provide information on the distribution of spins in space.
The overall magnetic field experienced by a spin becomes:

$$B(z) = (B_0 + G_z \cdot z) \qquad (21)$$

If the gradient is linear, all the spins that are on a plane orthogonal to the axis will precede with the same angular velocity:

$$\omega(z) = \gamma B(z) = \gamma(B_0 + G_z \cdot z) \qquad (22)$$

By applying an appropriate radio frequency pulse, it is possible to selectively excite only the spins of a certain layer (slice) of the sample to be analyzed. This operation can be repeated for all the "slices" of the sample.

It allows processing the images of the various cross-sections. The thickness of the layer depends on parameters that can be modified by the operator, such as the intensity of the selection gradient and the bandwidth of the radiofrequency pulse. For example, to decrease the thickness of the slice, it is necessary to increase the intensity of the gradient and act on the radiofrequency pulse by increasing its duration and decreasing its intensity. However, this method provides the projection of the proton density along the z-axis only. It does not allow for processing each point of the analyzed slice. To solve this problem, it is appropriate to insert two other gradients, perpendicular to the first one, respectively:

1) the G_y phase coding gradient and

2) the G_x frequency coding gradient.

The G_y gradient is activated for a short time so that the spin phases become different along the y-direction. This gradient determines a coding according to the phase. The gradient G_x, applied during the reading of signal, permits distribution of precession frequencies along the x-direction. To obtains good images, this sequence is repeated several times, each time varying the amplitude of the phase gradient (Fig. 14). Generally, proceed with 128 or 256 acquisitions and then make a double Fourier transform (see Appendix) to obtain a two-dimensional image for each slice.

Therefore, there are applied three gradients (generated by the corresponding coils) oriented in the three directions x, y, z, which differentiate the total magnetic field from point to point, allowing to distinguish the origin of the signals in all directions.

In medical imaging, in order to make visible a pathology or any tissue of interest in an MRI image, there must be contrast. It is a difference in signal intensity between the structure of interest and the adjacent tissue (Fig. 16). There are many pulse sequences allowing a different contrast between the tissues structures and many other are being developed in order to improve the details achievable by the image acquisition. However, apart from the spin density images, the pulse sequences most employed in clinical MRI are just the inversion recovery and the spin-echo sequences discussed in the previous paragraph. By modifying the sequence parameters, such as repetition time (TR) and echo time (TE), different

contrasts can be achieved, as illustrated for example in Fig. 16, in the case of brain MRI images.

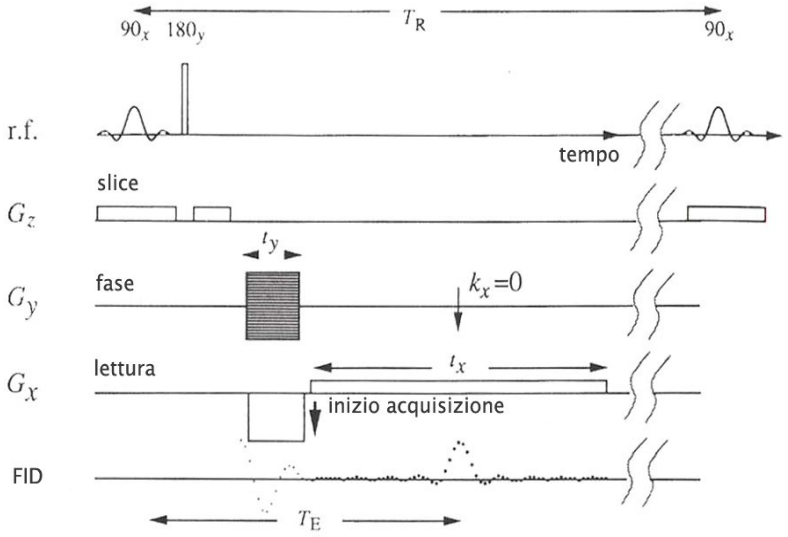

Figure 14 - The selection gradient along z can select only one "slice" of the sample. The application of the encoding gradient displaces the spins along the y-direction. The activation of the reading gradient creates a distribution of frequencies along the x-direction (Courtesy of Dr Silvia Capuani).

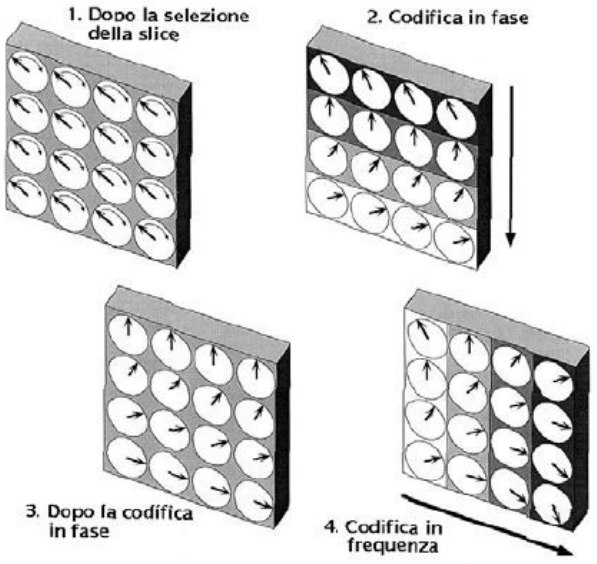

Figure 15 - Temporal diagram of a spin-echo sequence (TR = repetition time of the sequence; TE = echo time; tx = time interval in which the gradient Gx acts; ty = time interval in which the gradient Gy acts) (Courtesy of Dr Silvia Capuani).

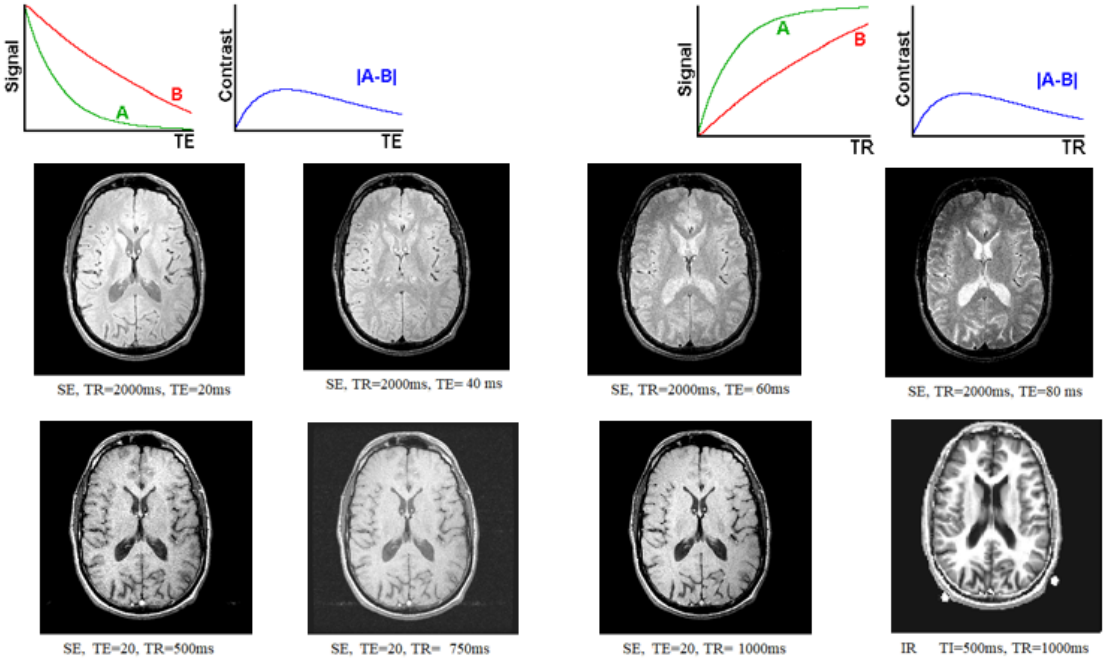

Figure 16 - Example of brain images weighed in a different way and with different contrast (Courtesy of Dr Silvia Capuani).

3.4 Chemical shift

Some atomic nuclei possess a magnetic moment, which gives rise to different energy levels and resonance frequencies in a magnetic field. The total magnetic field experienced by a nucleus includes local magnetic fields induced by currents of electrons in the molecular orbitals. The electron distribution of the same type of nucleus (e.g. ^{1}H, ^{13}C, ^{15}N) usually varies according to the local geometry and with it the local magnetic field at each nucleus. This is reflected in the spin energy levels and resonance frequencies. The variations of nuclear magnetic resonance frequencies of the same kind of nucleus, due to variations in the electron distribution, is called the chemical shift. Therefore, it provides information on the specific chemical environment around the considered nucleus. The size of the chemical shift is given with respect to a reference frequency or reference sample, usually a molecule with a barely distorted electron distribution.
It is expressed in parts per million (ppm) and could be calculated by:

$$\delta = \frac{\upsilon_{sample-}\upsilon_{ref}}{\upsilon_{res}} \quad (23)$$

where υ_{sample} is the absolute resonance frequency of the sample, υ_{res} is the spectrometer frequency and υ_{ref} is the absolute resonance frequency of a standard reference compound, measured in the same applied magnetic field B_0. Since the numerator is usually expressed in hertz, and the denominator in megahertz, δ is expressed in ppm and does not depend on the instrument being normalized for the working frequency. Factors influencing chemical shift are electron density, electronegativity of adjacent groups and anisotropic induced magnetic field effects. Electron density shields a nucleus from the external field; while a nucleus in the vicinity of an electronegative atom experiences reduced electron density and the nucleus is therefore deshielded. Anisotropic induced magnetic field effects are the result of a local induced magnetic field experienced by a nucleus resulting from circulating electrons that can either be paramagnetic when it is parallel to the applied field or diamagnetic when it is opposed to it.

3.5 MRI scanners

Magnetic Resonance Imaging equipment includes one or more computers, a radio frequency transmitter and receiver, one or more receiving and receiving transmitters, magnetic field gradient coils and the main magnet. In particular:

1. The magnet creates the magnetic field that directs the nuclei and places them in precession. The magnetic field is expressed in Tesla (T), and it could be from 0.2 to 7 T. The more the field intensity increases, the more the acquisition times are reduced, although the field inhomogeneities are enhanced.

   On the market, there are three types of instrument: 1. resistive, with low intensity and high energy cost; 2. superconductive, with high signal intensity and homogeneity but with very high maintenance and

management costs; 3. permanent, with low intensity and low running costs. The most used for clinical tomographs are superconductors.

2. The RF coils send the excitation pulses and receive the signal.
3. The gradient system modulates the static magnetic field and is fundamental for the reconstruction of the image. The field gradients introduce phase and frequency variation of the spin motion and allow the spatial coding of the signal. They can be oriented in space (x, y, z) but also obliquely according to the most appropriate direction, an essential characteristic of magnetic resonance imaging that allows you to perform direct multiplanar scans, oriented freely without having to move the patient.
4. The computer applies the phase control, the conversion, the reconstruction, and the archiving of the data.
   It samples and breaks down the analogic signal into its various frequency components with the analytical method of the Fourier transform. Then the computer presents the grayscale image on the display and stores the data in the central memory. Finally, it processes the data through post-processing (Neri 2008).

3.6 MRI applied to Cultural Heritage

The study of cultural heritage artefacts requires non-destructive tools of analysis fulfilling demands like those posed by medical diagnostics. Magnetic resonance imaging (MRI) and X-ray computer tomography (CT) are the most popular imaging methods in medicine. In art diagnostics X-ray analysis is well established but not MRI. In Cultural Heritage field, NMR-MOUSE or portable NMR is the most used technique (Blumich 2008, Capitani 2012).

The sensor of this kind of instrumentation is small and movable and permits to obtain information in situ.

It competes with other techniques like FTIR and Raman spectroscopy, UV imaging, X-ray-diffraction, X-ray fluorescence and

radiography analyses, multi-spectral imaging, optical coherence tomography, and terahertz spectroscopy. Each of these techniques uses electromagnetic waves at different frequencies and consequently with different absorption properties. NMR is the least sensitive one and it works well in presence of water and moisture and permits to obtain information about concentration, relaxation times and diffusion coefficients.

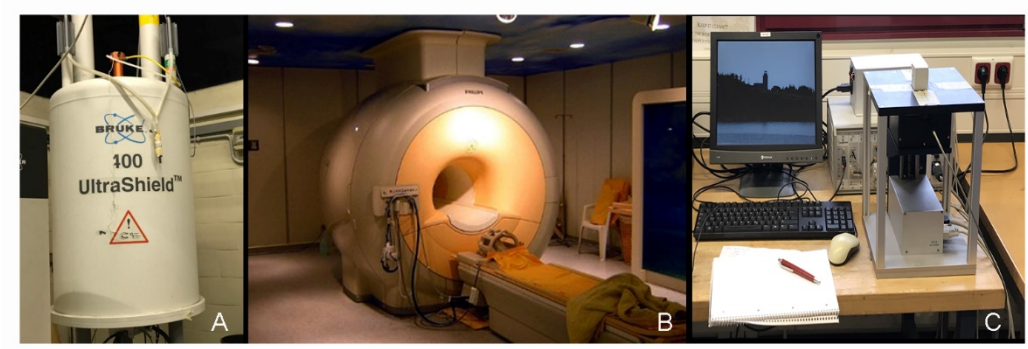

Figure 17 - The different instruments A) High-resolution NMR; B) clinical MRI scanner; C) NMR-Mouse device (Image provided by the author).

Single-sided NMR (the Profile NMR-MOUSE) has been employed for non-destructive testing of different types of objects of cultural heritage (Blümich 2010),including investigations of the structure of paintings (Proietti 2005, Proietti 2007), paper (Blümich 2003, Casieri 2004, Proietti 2004, Federico 2010), bones and mummies (Rühli 2007), porous materials (Proietti 2006, Sharma 2003, Blümich 2005 and 2008),and the moisture distributions of wood (Casieri 2004) and wall paintings (Proietti 2005 and 2007, Blümich 2010).

However, despite NMR is a very promising and attractive method for providing detailed, non-invasive, and quantitative information in living materials containing water, MRI in wood research is still far from being a routine tool (Dvinskikh 2011).

One of the first work that highlighted the potential of NMR technique for the study of wood was performed by Wang (1986) on a sample of cherry wood using a 0.15 T clinical scanner. Other authors, (Chang

1989), (Bucur 2003), obtained an image with an in-plane resolution of the order of 1x1 mm^2. Impressive results were obtained in the field of dendrochronology (Cole-Hamilton 1995), forest sciences (Homan 2007), (Muller 2001), (Florance 2005), materials sciences (Lindgren 2003) and on the archaeological woods (Cole-Hamilton 1990) (Kanazawa 2017).

In this regard, the archaeologically excavated wood generally has a very high moisture content (400%–800%), thus proving to be an ideal investigative subject for high-resolution NMR imaging.

One of the main aspects to investigate is the recognition of the wooden species. Currently it takes place through the destructive histological examination, which involves the cutting of thin slices of wood to be observed under an optical microscope.

The advantage of using this technique is that it can be used in vivo, without inducing any type of structural damage. Using NMR imaging, it is possible to observe structural inhomogeneities and the distribution of liquids present in the wood (water or solutions that can preserve the material) (Bucur 2003).

The contrast of the images is mainly influenced by the density of the protons and by the relaxation times T_1 and T_2 (Muller and Bammer 1998) and therefore by the presence of free water (Araujo 1993) (Hartley 1994) and bound water contained in the wood.

This allows us to obtain incredibly defined images, in which structural details are visible such as growth rings, the difference between sapwood and heartwood, parenchymal rays, veins, texture, porous ring, resin channels. All these characteristics make it possible to identify timbers. The obtained images are comparable to a macroscopic examination of the wood, which allows recognition of the group to which it belongs.

The purpose of this thesis was to investigate the possibility of obtaining sub millimetric information on wood with a clinical MRI scanner at 3 T. Furthermore, micro-imaging high-resolution NMR

images performed at 9.4 T were obtained in order to characterise the physical-chemical conditions of modern and ancient waterlogged wood, with particular emphasis on the water contribution that is the principal responsible for degradation effects.

As mentioned in the previous paragraphs, clinical MRI scanner are used for diagnostic purposes and are usually horizontal whereas high-resolution systems are mainly involved in research and are usually vertical. They are therefore characterized by different technical specifications suitable for the corresponding use. A picture with the two different instruments used for this thesis is reported in Fig. 17.

Chapter 4

Raman Spectroscopy and Surface Enhanced Raman Scattering (SERS)

Modern commercial inks are a complex mixture of several dyes and/or pigments constituting up to the 50% of the total ink formulation, carried either in a glycol-based solvent or benzyl alcohol. Analysis of commercial writing inks is usually carried out in the context of forensic examination in order to assess dating and originality of documents and to correctly assess cases of crimes like falsification, questioned signatures and threatening letters. Accordingly, a vast number of publications in the last 20 years have focused on characterization of writing pens (i.e., identification of dyes and pigment contents in ballpoint and gel pens) and on discrimination between inks. Therefore a number of techniques such as Thin Layer Chromatography (TLC) and mass spectrometry (MS) often coupled with optical analysis (ink absorption and luminescence) or image analysis have been routinely applied to the analysis, differentiation, and classification of writing inks.

Recently, Raman and infrared spectroscopies have also gained popularity as techniques for providing rapid information on the chemical

content of the ink mixtures or for the identification of colorants in artworks. Particularly, Raman and Surface Enhanced Raman Scattering (SERS) spectroscopies are increasingly pursued for their rapidity of analysis and non-destructive analysis, in order to assess dating, originality and to implement correct conservation procedures thus ensuring long-term preservation.

Another important consideration in the field of artwork preservation is the aging of the ink deposited on a substrate (usually, but not necessary, paper). As soon as an ink line is deposited on a substrate, compositional changes occur rapidly due to loss of volatile components, photodegradation of dyes or polymerization of resins. All these processes happen concomitantly, and they all contribute to significantly alter the aesthetic of paper works exposed to environmental conditions. Photofading of ballpoint pens has been traditionally performed by laser desorption/ionization (LDI) and matrix-assisted laser desorption/ionization (MALDI) mass spectrometry. However, considering the need to preserve the integrity of analyzed objects, non-destructive techniques are nowadays preferred for ink-based artworks. Accordingly, Raman/SERS spectroscopy has been successfully used for the investigation of dye aging dynamics in writing inks.

Specifically, in micro investigations, chemical imaging of fiber cell walls has become a reality and images of cellulose and lignin distributions in the plant cell wall have provided useful information on the compositional and organizational characteristics of woody tissues. Nevertheless, some information about wood characteristics are not well known mainly for soaked woods (such as those from ships found at the bottom of the seas). Then, the future of applying SERS spectroscopy to investigate cellulose and lignocellulosic materials is still bright.

In this chapter, an overview of the underlying principles of Raman and SERS spectroscopies, from the fundamental understanding of the effect to their potential applications are reported.

4.1 Raman Spectroscopy

When light is scattered from a molecule, most photons are elastically diffused. That is, most of the scattered photons have the same energy of the incident ones. However, a small fraction of light (approximately 1 in 10^7 photons) is scattered at energies different from, and usually lower than, the incident light energy. The process leading to this inelastic scattering is referred to as the linear Raman effect. If the incident light beam has frequency ω_L, and the scattered radiation has frequency ω_R the difference $\Delta\omega = \omega_L - \omega_R$ is called the *Raman shift*. The energy shift provides information on the vibrational properties of matter.

The classical treatment correctly predicts the appearance of emission at wavelengths different than the incident one of the scattered radiations, as well as some aspects of the selection rules. When a molecule interacts with an electromagnetic field E, an electric dipole moment P will be induced:

$$P = \alpha \cdot E + \frac{1}{2}\beta : EE + \frac{1}{6}\gamma \vdots EEE \qquad (1)$$

where α, β and γ are respectively the polarizabilities, the first, and the second hyperpolarizability tensors of the molecule. The first term, linear in E, is associated with Rayleigh and Raman scattering. The second-order term is associated with the hyper- Rayleigh and hyper-Raman scattering. The third-order, cubic in E, yields the second-hyper Rayleigh and second-hyper-Raman scattering, describing all the four-wave mixing processes, among which the coherent anti-Stokes Raman scattering is one of the most important. Limiting the description to the first term linear in E, the dependence of α on the nuclei positions can be accounted for, in case of small vibrations, by expanding each component of the polarizability tensor in Taylor series near the nuclei equilibrium positions as follows:

$$\alpha_{ij} = \alpha_{ij}^0 + \sum_k \left(\frac{\partial a_{ij}}{\partial q_k}\right)_0 q_k + \frac{1}{2}\sum_{k,l}\left(\frac{\partial^2 a_{ij}}{\partial q_k\, \partial q_l}\right)_0 q_k q_l + \cdots \qquad (2)$$

where α_{ij}^0 are the polarizability tensor elements at the equilibrium positions, and q_k the vibration coordinates. The polarizability tensor for the kth mode can be expressed as:

$$(\alpha_{ij})_k = (\alpha_{ij})_0 + \left(\frac{\partial a_{ij}}{\partial q_k}\right)_0 q_k \quad (3)$$

Or in tensorial form:

$$\alpha_k = \alpha_0 + q_k \alpha'_k \quad (4)$$

where α'_k is a tensor whose components are the derivatives of polarizability tensor concerning kth mode's coordinates.

Assuming anharmonic behaviour, the polarizability tensor related to the kth vibration mode turns out to be:

$$P = \alpha_0 E_0 \cos(\omega_L t) + \frac{1}{2}\alpha'_k E_0 q_{k0}[\cos(\omega_L + \omega_k)\, t + \cos(\omega_L - \omega_k)\, t] \quad (5)$$

The induced dipole has three components with different frequencies. The first one $P_1 = \alpha_0 E_0 \cos(\omega_L t)$ give rise to the Rayleigh scattering. The other terms refer to the anti-Stokes and Stokes Raman scattering. It can be envisaged that, for the Raman scattering to take place, some of the elements of α'_k must be different from zero. Therefore, the molecule must undergo a net change of its polarizability in order to change its vibrational state during the interaction with the external electric field.

4.1.2 Surface Enhanced Raman Spectroscopy (SERS)

Several variations of Raman spectroscopy have been developed. The general purpose is to enhance the sensitivity (e.g., Surface-Enhanced Raman), to improve the spatial resolution (Raman microscopy), or to acquire precise information (resonance Raman). The first case will be considered here.

Surface-Enhanced Raman Spectroscopy (SERS) is a more suitable technique comparing to Raman since the latter often has a microscopic cross-section and generally, the problem of fluorescence arises. SERS, as the name itself suggests, is a surface phenomenon where the intensity of

the signals are enhanced by a factor of $10^{12} – 10^{14}$ (Larmour 2010) respect to a conventional Raman spectrum.

Since Raman intensities scale as the product of the incident field intensity and polarizability derivative, it comes as no surprise that there are two commonly considered mechanisms for SERS, one of which involves enhancements in the field intensity as a result of plasmon resonance excitation, and the other the enhancement in polarizability due to chemical effects such as charge-transfer excited states.

The first is the well-known electromagnetic enhancement mechanism, and in this mechanism, the enhancement factor E at each molecule is (approximately) given by:

$$E = |E(\omega)|^2 |E(\omega')|^2 \quad (6)$$

where E(ω) is the local electric-field enhancement factor at the incident frequency ω and E(ω') is the corresponding factor at the Stokes-shifted frequency ω. In conventional SERS, E is averaged over the surface area of the particles where molecules can adsorb to generate the observed enhancement factor <E>, while in single-molecule SERS (SMSERS) it is the maximum enhancement E_{max} that is of interest. Note that E_{max} can be orders of magnitude larger than < E>, so the distinction between these two enhancement estimates is essential. Another point is that E is often approximated by assuming that E(ω) and E(ω') are the same, and hence $E = | E(\omega) |^4$. This approximation takes advantage of the fact that the plasmon width is often large compared to the Stokes shift. From this first concept, emerges that the simplest model that translates the excitation of surface plasmons into a SERS mechanism is the so-called electromagnetic model.

A preliminary analysis of the fields surrounding a small, isolated metal nanoparticle is useful in defining some of the essential criteria one needs to fulfill to see intense SERS. A small, isolated, illuminated metal sphere will sustain oscillating surface plasmon multipoles of various order induced by the time-varying electric-field vector of the light. As described above, the surface plasmons are collective oscillations of the conduction electrons against the background of ionic metal cores. Besides, light can induce a host of other excitations in the metal particle, including interband

transitions. For a particle much smaller than the wavelength of the exciting light, all the dipolar plasmon can be ignored. Systems with free or almost free electrons will sustain such excitations; and the freer the electrons the sharper and the more intense the dipolar plasmon resonance will be. When the new laser light is resonant with the dipolar plasmon, the metal particle will radiate light characteristic of dipolar radiation. This radiation is a coherent process with the exciting field, and it is characterised by a spatial distribution of field magnitudes (that reaches steady state a few femtoseconds after the light is turned on) in which the light intensity from certain portions of space surrounding the particle is depleted. In contrast, the intensity at certain portions near the metal particle is enhanced.

Let us call the field enhancement averaged over the surface of the particle *g*. The average magnitude of the field radiated by the metal particle E_s will be $E_s = gE_0$, where E_0 is the magnitude of the incident field. One should keep in mind that E_s is the average local near field at the particle surface. The average molecule adsorbed at the surface of the metal particle will, therefore, be excited by a field whose magnitude is E_s, and the Raman-scattered light produced by the molecule will have a field strength $E_R \propto \alpha R\ E_s \propto \alpha R\ gE_0$, where αR is the appropriate combination of components of the Raman tensor. The metal particle can further enhance the Raman-scattered fields in precisely the same manner as the incident field was. That is, the metal particle can scatter light at the Raman-shifted wavelength enhanced by a factor *g'*. (The prime is used to indicate the fact that the field enhancement at the Raman-shifted wavelength will, in general, differ from its value at the incident wavelength.) ESERS αRgg'E0 will, therefore, give the amplitude of the SERS-scattered field, and the average SERS intensity will be proportional to the square modulus of E_{SERS}. That is, $I_{SERS} \propto |\alpha_R|^2 |gg'|^2 I_0$, where I_{SERS} and I_0 are the "intensities" of the SERS-scattered and incident fields, respectively. For low-frequency bands when $g \sim g'$ the SERS intensity will be enhanced by a factor proportional to the fourth power of the enhancement of the local incident near field, i.e., $|E_L|^4 = |g|^4$. It is helpful to define the "SERS enhancement" G as the ratio of the Raman-scattered intensity in the presence of the metal particle to its value in the absence of the metal particle $G = |\alpha_R/\alpha_{Ro}|\ |gg'|^2$ where α_{Ro} is the Raman polarizability of the isolated molecule.

In this contest, SERS is one of the few phenomena that can truly be described as nanoscience. It usually means that the SERS-active systems must ideally possess structure in the 5 nm to 100 nm range (size smaller concerning the wavelength of the exciting light). Likewise, the dimensions of the active structure cannot be much smaller than some lower bound, which is usually more extensive than the average molecule. The upper dimensional bound of the SERS-active system is determined by wavelength. As features of the order of the wavelength or more astronomical are used, the optical fields no longer excite dipolar plasmons almost exclusively; instead, progressively higher-order multipoles are excited. Unlike the dipole, these modes are nonradiative. Hence, they are not efficient in exciting Raman (or other dipole-driven excitations). Accordingly, the SERS efficiency drops until, for large enough particles, so much of the exciting radiation is locked up in higher order plasmon multipoles that SERS is all but extinguished.

At the other end of the dimensional scale, as the nanostructure responsible for SERS becomes too small, the effective conductivity of the metal nanoparticles diminishes because of electronic scattering processes at the particle's surface. As a result, the quality factor of the dipolar plasmon resonance is vitiated, and the reradiated field strength reduced. When the metal particle becomes small enough, the pseudo bulk description implicit in the definition of the surface plasmon no longer applies. Instead, one needs to treat the metal particle as a fully quantum object whose electronic properties show so-called quantum-size effects. Reducing the size of the metal particle even further so that the particle is composed of only a few metal atoms, one passes into a regime in which a molecular description expresses the particles' properties best. Some of these points are illustrated using the following rudimentary model. The polarizability of a small metal sphere with dielectric function ε(λ) and radius R, surrounded by vacuum is given by:

$$\alpha = R^3 \frac{\varepsilon - 1}{\varepsilon + 2} \tag{7}$$

Combining this expression with the expression for the dielectric function of a Drude metal slightly modified for interband transitions we obtain:

$$\varepsilon = \varepsilon_b + 1 - \frac{\omega_p^2}{\omega^2 + i\omega\gamma} \quad (8)$$

in which ε_b is the contribution (generally wavelength-dependent) of interband transitions to the dielectric function.

ω_p is the metal's plasmon resonance whose square is proportional to the electron density in the metal and γ is the electronic-scattering rate that is inversely proportional to the electronic mean-free-path and therefore also inversely proportional to the metal's DC conductivity.

Thus, the polarizability expression is written as:

$$\alpha = \frac{R^3(\varepsilon_b \varepsilon^2 - \omega_p^2) + i\omega\gamma\varepsilon_b}{[(\varepsilon_b + 3)\omega^2 - \omega_p^2] + i\omega\gamma(\varepsilon_b + 3)} \quad (9)$$

The real and imaginary parts of the expression for α given in (4) have a pole when the frequency ω is equal to $\omega_R = \omega_p / (\sqrt{\varepsilon_b} + 3)$. The width of that resonance is given by $\gamma(\varepsilon_b + 3)$.

Hence, when γ is large either because of the inherent poor conductivity of the metal or because the metal nano features are so small that electronic scattering at the particle's surfaces become the dominant electron-scattering process, the quality of the resonance is reduced and with it the SERS enhancement.

Likewise, for metals whose dielectric properties are greatly modified by interband transitions in the wavelength range under consideration, i.e., for which the value of the function ε_b is significant, the width of the resonance is increased, and the SERS-enhancement decreases. This phenomenon explains why, all things being equal, the SERS enhancement of silver exceeds that of gold, which, in turn, exceeds that of copper. In that order, the participation of interband transitions in the dielectric function of those metals in the visible range of the spectrum increases. Most transition metals are poor SERS enhancing systems because, for them, the two effects combine to reduce their SERS enhancement ability, i.e., their conductivity is low (γ is large), and the interband contribution to the dielectric function is significant (ε_b is large). Finally, I show that light polarised with the E-vector along the interparticle axis can result in considerable enhancements in the gap between the two nanoparticles

while the orthogonal polarisation cannot (see Fig. 1). For light polarised along the interparticle axis, the proximity of the charges (induced by the optical fields) to the molecule can be made arbitrarily small and hence the field sensed by the molecule commensurately large as the nanoparticles are brought closer together. That capability is not available for light polarised orthogonally to the interparticle axis.

It is summarising, for a given metal system the SERS intensity will depend, to first order, on the size of the nanostructure responsible for its enhancement. It will be optimal when this size is small concerning the wavelength of the exciting light so long as that size is not much smaller than the electronic mean free path of the conduction electrons.

A second mechanism that could give rise to an increase in the Raman scattering is the "*chemical mechanism*". It provides for the generation of new electronic states due to the interaction between the metal surface and the adsorbed molecules. To better understand its physical basis, it is appropriate to refer to the energy levels diagram of a molecule adsorbed on a metal surface (see Fig. 2). The single molecule (not adsorbed), excited with visible radiation, does not spread for Raman effect since it has no absorption bands in this wavelengths range. When the molecule is adsorbed on the metal surface, the Fermi level of the metal moves toward the intermediate point of the HOMO-LUMO (*highest occupied molecular orbital- lowest occupied molecular orbital*) molecular gap. So, this shift allows the system the Raman excitations resonant with the visible light.

4.2 Surface plasmons in metallic nanoparticles

Surface plasmon (SP) resonance is the most outstanding optical property of metallic nanostructures. It consists of a collective oscillation of conduction electrons excited by the electromagnetic field of light. SP resonance is in the origin of optical properties hardly achievable with other physical processes. In the case of metallic nanoparticles (NPS), where the electrons are confined in the three dimensions, the electron oscillations

induce an electric field around the NP that can be much larger than the incident light one. SPs are one of the best examples that things are different at the nanoscale. When the size of a metallic particle is reduced to a few nanometers, the optical properties are dramatically modified by the appearance of SPs and its resulting behaviour is entirely different from the bulk metal one. SPs open the possibility to amplify, concentrate and manipulate light at the nanoscale, to overcome the diffraction limit of traditional optics and increasing resolution and sensitivity of optical probes. As indicated above, SPs corresponds to an interaction between matter and the electromagnetic field of the light. Thus, the accurate analysis of SPs implies solving the Maxwell equations with the appropriate boundary conditions. However, a simplified classical picture can be more useful to understand the physical meaning of SPs. A metallic NP can be described as a lattice of ionic cores with conduction electron moving almost freely inside the NP, as shown in Fig.1. When the particle is illuminated, the electromagnetic field of the light exerts a force on these conduction electrons moving them towards the NP surface. As these electrons are confined inside the NP, negative charge will be accumulated on one side and positive charge in the opposite one, creating an electric dipole.

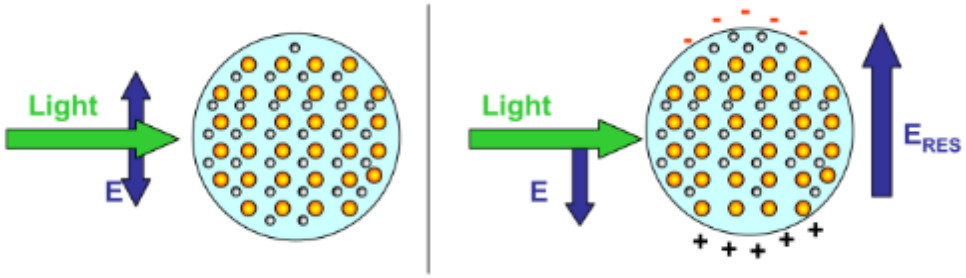

Figure 1 - Scheme of light interaction with a metallic NP. The electric field of the light induces the movement of conduction electrons which accumulate at the NP surface, creating an electric dipole. This charge accumulation creates an electric field opposite to that of the light (Garcia 2011, J. Phys. D: Appl. Phys with permissions).

This dipole generates an electric field inside the NP opposite to the light one. This process will force the electrons to return to the equilibrium

position (Fig. 1). The larger the electron displacement, the larger the electric dipole and consequently the restoring force.

The situation is similar to a linear oscillator with a restoring force proportional to the displacement from the equilibrium position. If the electrons are displaced from the equilibrium position, and the field is removed later, they will oscillate with a specific frequency that is called the resonant frequency; in the case of SPs, it is named the plasmonic frequency. The electron movement inside the NP exhibits some degree of damping. The ionic cores and the NP surface partially damp the electron oscillations. Thus, the system is similar to a linear oscillator with some damping. When an alternating force is applied to a linear oscillator, the system oscillates with the same frequency as the external force. However, the amplitude and phase will depend on both the force and the intrinsic parameters of the oscillator. In particular, the oscillating amplitude will be maxima for the resonant frequency (Fig. 2(a)). It is quite straightforward to understand that, if the frequency of the external force is the same as the plasmonic frequency of the NP, it will be easy to make the electrons oscillate, but as we move far away from this frequency the movement of electrons will be more difficult, i.e. with reduced amplitude.

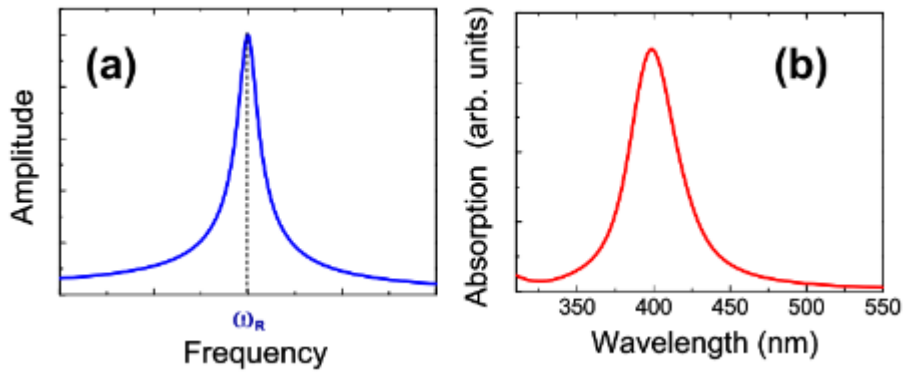

Figure 2 - (a) Oscillation amplitude for a linear oscillator as a function of the external force frequency. (b) Optical absorption spectrum corresponding to 10 nm silver NPs embedded in silica glass (Garcia 2011, J. Phys. D: Appl. Phys with permissions).

We cannot directly observe the movement of electrons to determine their oscillating amplitude. However, we can determine this amplitude indirectly.

The electronic oscillation implies an increase in kinetic and electrostatic energies associated with the electric fields of the dipole. As energy must be conserved, this increase in energy must be provided by the illuminating light. Therefore, the light extinguishes partially when exciting SPs inside the NP. The larger the electron oscillations, the larger the light extinction, so the optical absorption spectrum allows one to detect the excitation of SPs. The resonant frequency for these oscillations in metallic NPs corresponds typically to UV–Vis light and consequently, the SPs arise absorption bands in this region of the spectrum as Fig. 2(b) illustrates. At this stage, SPs can be considered as another electronic process in which light is absorbed to promote electrons from the ground level to an excited one. What makes the SPs unique are the numbers of these processes. Its absorption cross-section gives the absorbing efficiency of a particle. Classically it corresponds to the geometrical section of an ideal opaque particle absorbing the same number of photons as the studied particle. As Fig. 3 illustrates, the absorbing NP can be replaced by a perfect opaque one (absorbing any photon reaching its surface) that will absorb the same number of photons as a real particle. The section of this ideal particle represents the absorption cross-section of the NP. For instance, if we have an NP absorbing half of the photons reaching its surface, the absorption cross-section will be half of its geometrical section. In addition to absorption, light interacting with matter can be scattered, changing the propagation direction and eventually also energy and moment. For this process, also the scattering cross-section can be considered and defined as the geometrical section of an ideal scattering particle (that scatters any photon reaching its surface) with the same scattering efficiency as the real particle. The sum of absorption and scattering cross-section is defined as the extinction cross-section that represents the efficiency of the particle to remove photons from an incident beam (by both absorption or scattering processes). The maximum possible value of the extinction cross-section for perfect opaque particles is the particle section ($\pi \cdot R^2$). However, for a few nm NPs, extinction cross-sections more significant than 10% of the geometrical section are scarcely found for other processes different from SP excitation.

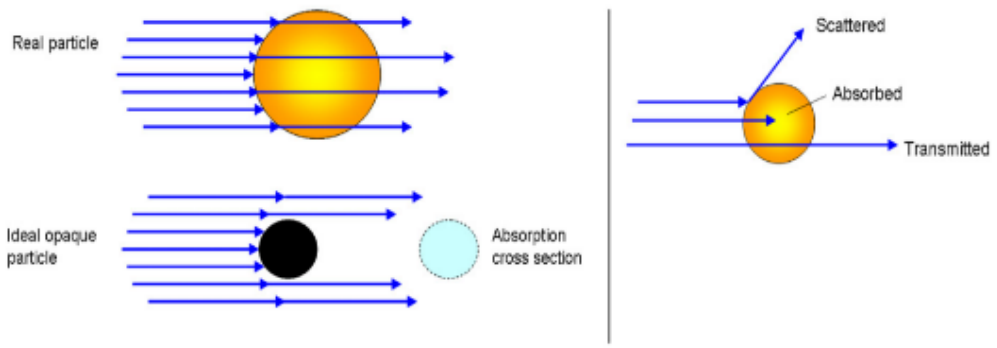

Figure 3 Left: illustration of absorption cross-section concept. Right: picture describing transmission, absorption, and scattering processes (Garcia 2011, J. Phys. D: Appl. Phys with permissions).

Fig. 4 shows the resonant wavelength and the extinction cross-section for 10 nm size metallic NPs. It is found that for noble metal NPs the extinction cross-section can be up to 10 times their geometrical section; that is, the NP is capable of absorbing and scattering photons even away from its natural position. Somehow, the excitation of the SP is equivalent to concentrate the light passing by the NP to induce a considerable extinction. It is worth noting that light absorption has an exponential dependence on the absorption cross-section. A light beam propagating across a medium with metallic NPs decay in intensity as:

$$I(x) = I_0 \cdot e^{-C\sigma x} \quad (10)$$

I_0 is the initial intensity, C the concentration of NPs per unit volume, σ their extinction cross-section and x the travelled distance. Therefore, a moderate increase in the extinction cross-section can lead to a considerable enhancement of light absorption. As an example, if we have a dielectric matrix containing 10^{20} NPs cm^{-3} with 10 nm size (1% in volume) and their extinction cross-section is equal to the geometrical section ($\pi \cdot R^2$), the light

transmitted across 1 μm of the material will be 45%; if the extinction cross-section of the NPs is increased to a factor of 10, the transmitted light is reduced to 0.04% (i.e. three orders of magnitude). These numbers make SPs unique since the cross-section values found here are more significant than other optical processes such as electronic transitions in semiconductors (band to band transitions), rare earth atoms, defect-related absorption processes in solids, and electronic excitations in molecules. The comparison provides a more direct example of the huge extinction in metallic NPs due to SP excitation with interband transitions.

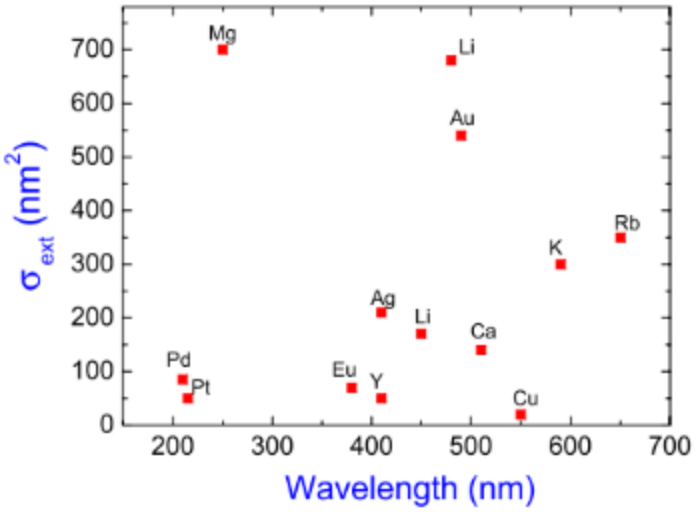

Figure 4 - The resonant frequency and extinction cross-section for metallic NPs with 10 nm size in air (Garcia 2011, J. Phys. D: Appl. Phys with permissions).

In addition to SPs, there are other possible electronic excitations in metallic NPs. In a metallic material, valence and conduction bands overlap, forming a continuous spectrum of free states. However, some inner levels do not split enough to overlap these bands so the system may exhibit interband transitions similar to those in semiconductors. Transitions between these inner levels and the conduction band induce an absorption edge like the case of semiconductors. Some metals present a weak luminescence emission due to electron decay between these bands. For bulk materials, these transitions are very unlikely, and optical absorption and emission associated with these transitions are very weak. For instance,

weak photoluminescence associated with interband transitions has been measured for bulk gold corresponding to transitions between the 3d level and the conduction band. However, for NPs with a reduced number of atoms, energy bands are not so well-formed because of the limited number of atoms, while interband transitions become more prominent. Fig. 5 shows the optical absorption spectrum of Ag and Au NPs. In the case of Ag, both SP band and interband transition absorption edges are well resolved. For Au NPs, both absorptions overlap. This overlapping is essential when analysing the shape of the SP. In particular, the width of the SP band (related to the NP size) must be determined, separating the contribution of the interband transitions.

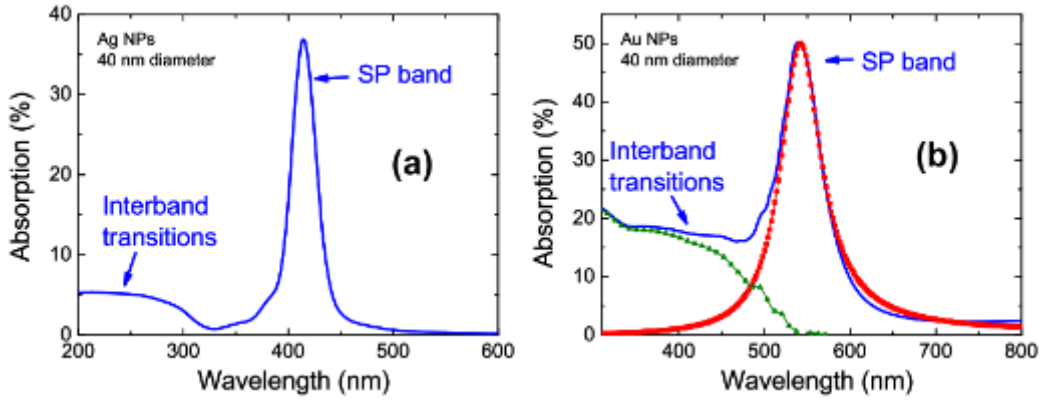

Figure 5 - Optical absorption spectra for (a) Ag and (b) Au NPs with 40 nm size (embedded in a silica matrix with ε = 2.25). For Au NPs, the contributions to the optical absorption of interband transitions and SPs are resolved (Garcia 2011, J. Phys. D: Appl. Phys with permissions).

We may observe how the SP absorption is more significant than that of the interband transitions, although the absorbing centre is the same for both processes. The reason for this surprising behaviour can be qualitatively explained with the same classical picture of SPs. When the incident light reaches the NP, the conduction electrons move to result in a charge accumulation at the NP surface. This charge creates a field inside the NP

(the restoring field) but also out of the NP. The large electron density and mobility in the metallic NP produces a considerable charge accumulation at the NP surface and consequently intense fields in a region more significant than the NP size as it is shown in Fig. 6a, there are vast regions where the electric field created by the particle is opposite to that of the light, so the interference is destructive, leading to light extinction beyond the NP volume. For other regions, the result of the interference between both electric fields is a net field with other propagating direction, hence inducing light scattering. This mechanism explains the huge extinction cross section of metallic NPs qualitatively when SPs are excited. The excitation of SPs with laser sources can even yield a modification of the NP shape by a local increase in the temperature associated with the considerable absorption.

The Mie theory provides an exact solution for spherical NPs assuming that they are non-interacting (i.e. the distance between the NPs is large enough so we may assume that the electric field created by an NP does not affect the rest of them.

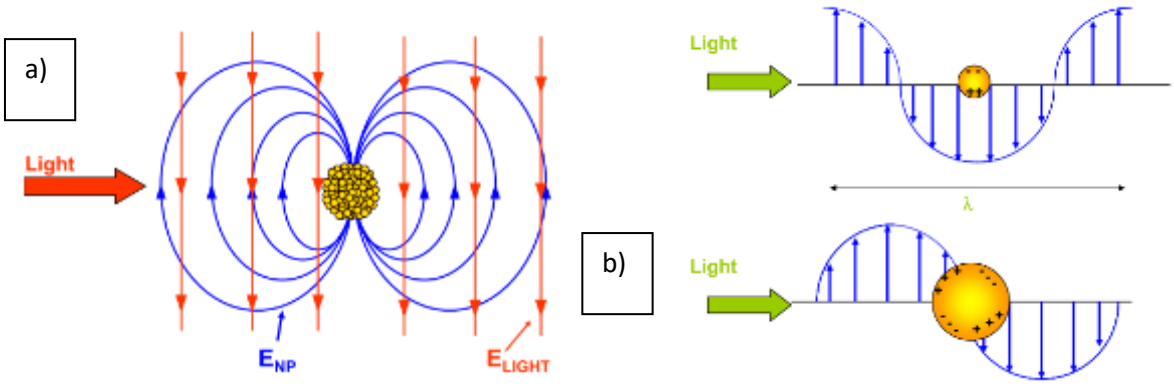

Figure 6 - (a) Illustration of electric fields of incident light and that created by the electron oscillations near the NP; (b) Electric field and charge distribution at the surface of NPs for size (top) much smaller and (bottom) comparable to the light wavelength (Garcia 2011, J. Phys. D: Appl. Phys with permissions).

In this case, Maxwell equations can be solved analytically, and the extinction cross-section is given by:

$$\sigma_{ex} = \frac{2\pi}{|k^2|}\sum_{L=1}^{\infty}(2L+1)\cdot Re[a_L + b_L] \quad (11)$$

where:

$$a_L = \frac{m\psi_L(mx)\cdot\psi'_L(x) - \psi'_L(mx)\cdot\psi_L(x)}{m\psi_L(mx)\cdot\eta'_L(x) - \psi'_L(mx)\cdot\eta_L(x)} \quad (11a)$$

$$b_L = \frac{\psi_L(mx)\cdot\psi'_L(x) - m\psi'_L(mx)\cdot\psi_L(x)}{\psi_L(mx)\cdot\eta'_L(x) - m\psi'_L(mx)\cdot\eta_L(x)} \quad (11b)$$

Are the refraction index of the metal (complex) and that of the surrounding dielectric medium, respectively, and ψ_L and η_L are the cylindrical Bessel–Riccati functions. These equations are not easy to handle, although there are codes available to carry on calculations. There is an extensive list of theories that allow calculating the light absorption associated with SPs for specific size ranges or when NPs are not spherical, or they are interacting.

The *dipolar approximation* offers simple equations to calculate light absorption of metallic NPs provided that the NP size is smaller than the light wavelength (in addition to the hypothesis of the Mie theory). As the SP resonance band falls at the visible part of the spectrum (~ 360–720 nm), the condition of small NPs is usually achieved for NP diameter below ~ 50 nm. In this case, the electric field inside the NP can be considered as uniform (see Fig. 6b), and an electric dipole can describe the particle. Mathematically, this approximation is achieved assuming that x is small enough, hence, in equation (2) we can just consider the first term L = 1. (Note that the term L = 0 corresponding to the total electric charge of the NPs is zero). Within this approximation, the absorption cross-section is given by:

$$\sigma_{ext} = \frac{24\pi^2 R^3 \varepsilon_m^{3/2}}{\lambda}\frac{\varepsilon_2}{(\varepsilon_1+2\varepsilon_m)^2+\varepsilon_2^2} \quad (12)$$

λ being the light wavelength, ε_m the real dielectric function of the medium and $\varepsilon_1 + i\varepsilon_2$ the complex dielectric function of the metal. As the size of NPs increases, the approximation is not valid anymore, since the electric field inside the NP cannot be considered uniform. In that case, more multipolar terms (i.e. more terms in equation 2) must be considered.

The *effective dielectric function theory* is another approach in calculating the optical properties of metallic NPs. This method consists of replacing the heterogeneous system formed by the NPs and the surrounding media by a homogeneous medium with a useful dielectric function ($\varepsilon_{eff1} + i\varepsilon\varepsilon_{ff2}$). Many these theories depending on the exact conditions that are imposed on the homogeneous medium. The best approach within the framework of effective medium theories was developed by Maxwell-Garnett (*Maxwell-Garnett 1906)* proposing to replace the NPs' dielectric medium system by a homogeneous material exhibiting the same dielectric polarisation upon light illumination. With this condition, the complex effective dielectric function is given by:

$$\frac{\varepsilon_{eff}-\varepsilon_m}{\varepsilon_{eff}+2\varepsilon_m} = f\frac{\varepsilon-\varepsilon_m}{\varepsilon+2\varepsilon_m} \quad (13)$$

Moreover, the extinction cross-section of the material is then given by:

$$\alpha(cm^{-1}) = \frac{8.88\times10^7}{\lambda(nm)}\sqrt{-\varepsilon_{1eff} + \sqrt{\varepsilon_{1eff}^2 + \varepsilon_{2eff}^2}} \quad (14)$$

For the case of spherical, small and isolated NPs, this model leads to the same result as the dipolar approximation. Furthermore, I outline that the size of NPs has a dramatic effect on the SP resonance processes and consequently on the optical properties of the NPs. As a general approach, we may distinguish two regimes corresponding to small NPs (smaller than the light wavelength) and large ones with a size comparable to the wavelength. For small NPs (radius up to ~ 50 nm), we may assume that a dielectric dipole correctly describes the NP. The size dependence of the SP

affects mainly the width and the intensity of the resonance band, while the effect on the resonance wavelength is entirely reduced. Dealing with side effects in this range, we can distinguish between intrinsic and extrinsic size effects. The intrinsic effects are related to the damping of the electron oscillations. When SPs are excited, the electrons are damped in their movement by the scattering with the ionic cores and with the surface. The damping constant for the electron oscillations is given by

$$\gamma = \gamma_0 + A\frac{v_F}{R} \tag{15}$$

The first term (γ_0) describes the damping due to the scattering of the oscillating electrons with the ionic cores. It is size-independent, and its value is given by $\gamma_0 = v_F/l_\infty$, v_F being the velocity of the conduction electrons (Fermi velocity) and l_∞ the electron means free path in the metal. This term depends just on the nature of the metal and the crystal structure. For Au at 300 K we have $v_F = 1.4 \times 10^6$ ms^{-1} and $l_\infty = 30$ nm leading to $\gamma_0 = 4.6 \times 10^{13}$ s^{-1} and for Ag we have $v_F = 1.39 \times 10\ 6$ ms^{-1} and $l_\infty = 52$ nm leading to $\gamma_0 = 2.6 \times 10^{13}$ s^{-1}. The second term corresponds to the scattering of oscillating electrons with the particle surface. The term *A* is a material-dependent constant that considers the features of the surface scattering. The electrons in a certain shell close to the NP surface will scatter this surface when they oscillate. The larger the velocity of the oscillating electrons (which is about the Fermi velocity), the larger the number of electrons scattering the surface during their movement (i.e. the thickness of the shell of electrons scattering the surface during oscillations). As the particle size increases, the fraction of electrons in the shell close to the surface decreases and therefore the total damping is reduced. Therefore, the surface damping is proportional to the Fermi velocity in the metal and inversely proportional to the particle radius. In addition to this intrinsic effect of the size of NPs on the SP, it has been reported that the dielectric function of small NPs is also size-dependent. At this scale, the energy bands are not so well defined as in a bulk solid, and consequently, the contribution of the interband transitions to the dielectric function becomes

size dependent. Accordingly, there is an additional dependence of the SP on the size of NPs through the dependence of its dielectric function. This effect is also appreciable for NPs below 5 nm size, and the value of the dielectric function can be calculated from the bulk one.

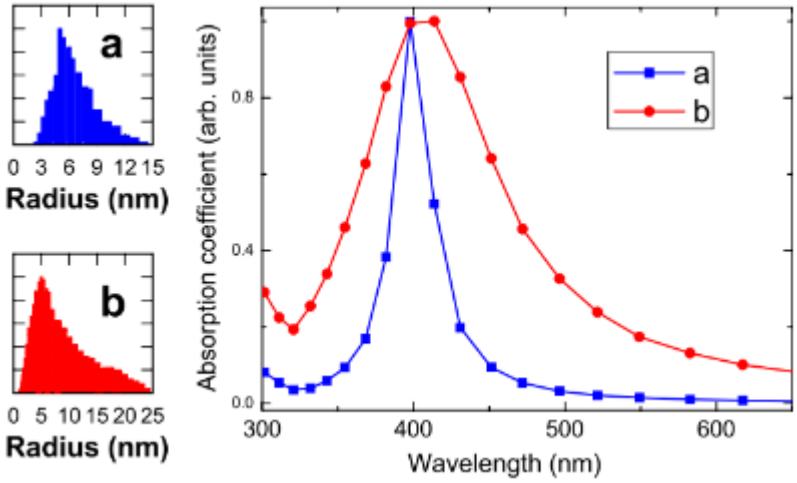

Figure 7 - (Left) size distributions and (right) optical absorption spectra for Ag NPs both with 10 nm average size but different size dispersions calculated according to the Mie theory and using n_m = 1.5 (Garcia 2011, J. Phys. D: Appl. Phys with permissions).

For large NPs (radius larger than ~ 50 nm), NPs cannot be considered much smaller than the light wavelength. Thus, the particle is no more described by a dipole (Fig. 6b), and further multipolar terms are required. SPs become propagating waves with well-defined modes or dispersion relations. The size dispersion induces a broadening of the absorption band. As shown in Fig. 7, the larger the size dispersion, the fuller the absorption band. For example, for a set of Ag NPs with an average size of 10 nm and dispersion of ± 4.2 nm, the FWHM of the SP absorption band is three times smaller than that for 10 nm Ag NPs with a size dispersion ± 8.5 nm. Thus, it is not possible to determine the size of the NPs just from the FWHM of the absorption band, as it depends on two parameters: average size and size distribution width. Furthermore, the resonance of SPs is strongly affected

by the particle shape and by the surrounding medium. It has two apparent effects on the SP excitation process. On the one hand, the dielectric function of the surrounding medium determines the light wavelength at the vicinity of the NP hence altering the geometry of the electric field at the surface of NPs. However, the most significant effect is related to the polarisation of the medium. During SP excitation, the charge accumulation creates an electric field in the vicinity of the NPs (in addition to that of the incident light). This field induces the polarisation of the dielectric medium, resulting in a charge accumulation at the edges of the medium (i.e. at the interface between the dielectric and the metallic NPs) that will partially compensate the charge accumulation due to the movement of conduction electrons in the NP. This reduction of charge will depend on the dielectric function of the media; the larger ε_m, the larger the polarisation charge, and hence, the more significant the effect on the SP. Reducing the net charge at the NP surface implies a reduction in the restoring force. For an oscillator, it is well known that reducing the restoring force leads to a smaller resonant frequency. Thus, increasing the dielectric constant of the surrounding media will shift the SP resonant band towards larger wavelengths (i.e. smaller frequencies).

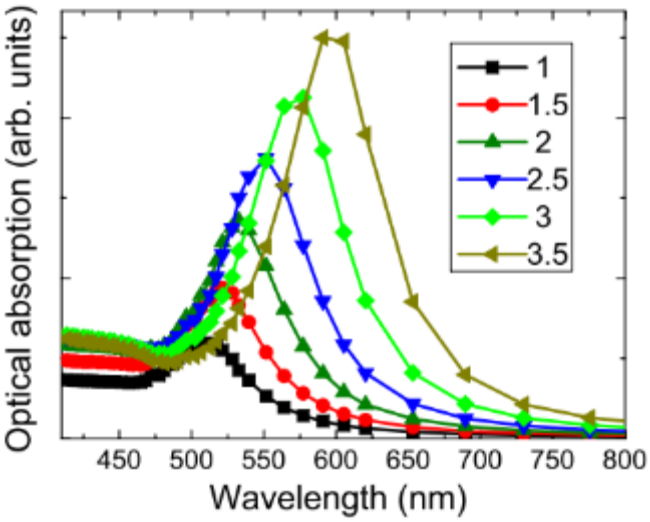

Figure 8 - Optical absorption spectra for Au NPs with 10 nm size in a dielectric medium with different dielectric functions calculated according to the Mie theory (Garcia 2011, J. Phys. D: Appl. Phys with permissions).

Fig. 8 shows the absorption spectra for 10 nm size Au NPs embedded in media with different dielectric functions. The surrounding medium has a limited effect on the bandwidth (measured in eV), that is mainly related to the particle size. The resonance intensity also increases with the dielectric function of the medium. It is the expected behaviour for a forced oscillator: when the resonance frequency decreases, the amplitude at resonance increases. It is mathematically reflected in equation (3), where the absorption cross-section is proportional to $\varepsilon_m^{3/2}$.

4.3 Raman imaging: principle and statistical data analysis

Raman imaging spectroscopy is a relatively new technique that has raised interest in several areas of knowledge due to the possibility of evaluating the spatial distribution of compounds based on their spectra. A complete spectrum is acquired at each pixel of the image, and then interrogated to generate false colour images based on material composition, phase, crystallinity, and strain. In standard operation, conventional confocal Raman microscopes are diffraction limited, with achievable spatial in the order of 250-300nm (depending on laser wavelength and objective) – features smaller than this can still be detected but without true spatial information.

Standard point-by-point mapping affords the ultimate sensitivity for materials with extremely low Raman scattering properties, and additionally allows high resolution, large spectral range capability. Typical acquisition times for such maps can be in the order of 1s-10s per point (or longer), and thus total measurement times can be significant. In Fig. 9 is shown a Raman mapping example *of poly-Silicon, characterized by crystalline, poly-crystalline and nano-crystalline phases.*

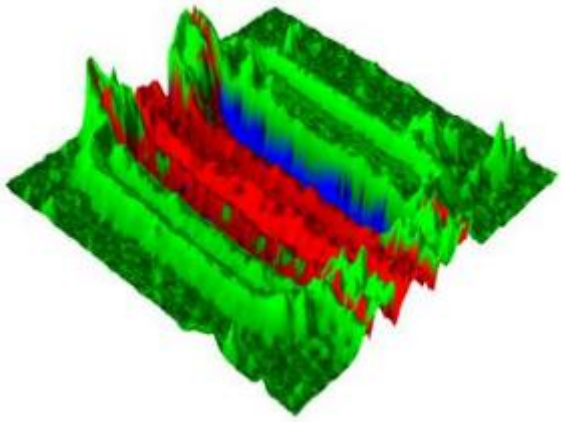

Figure 9 - Raman image of poly-Silicon showing crystalline, poly-crystalline and nano-crystalline forms (Horiba website, https://www.horiba.com)

Recently, 3D volume scans and depth profiles are valuable tools in providing information about the dimensions of objects or the distribution of a certain compound throughout the sample. In details, since Raman confocal microscope systems provide depth resolution and a strongly reduced background signal, depth profiles and 3D images with exceptional spectral and spatial resolution can be collected. Images are recorded point by point and line by line, while scanning the sample through the excitation focus. With this technique, the specimen can be analyzed in segments along the optical axis and depth profiles or 3D images can be generated. In Fig. 10 is reported an application to a polymer system: both Raman depth-profiling (x-z direction) and the corresponding Raman spectra are shown.

However, the main disadvantages of Raman imaging are spatial resolution, sample components with intrinsically low Raman signals, fluorescence, subsampling, spherical aberration/refraction and problems in signal focus or force. Spatial resolution is limited by diffraction, which depends on spot size, usually in the micrometer range. The lack of Raman signal or fluorescence depends on the type of sample, where the former is a consequence of polarizability of the molecule while the latter occurs when

the laser has enough energy to promote an electron to an excited electronic orbital.

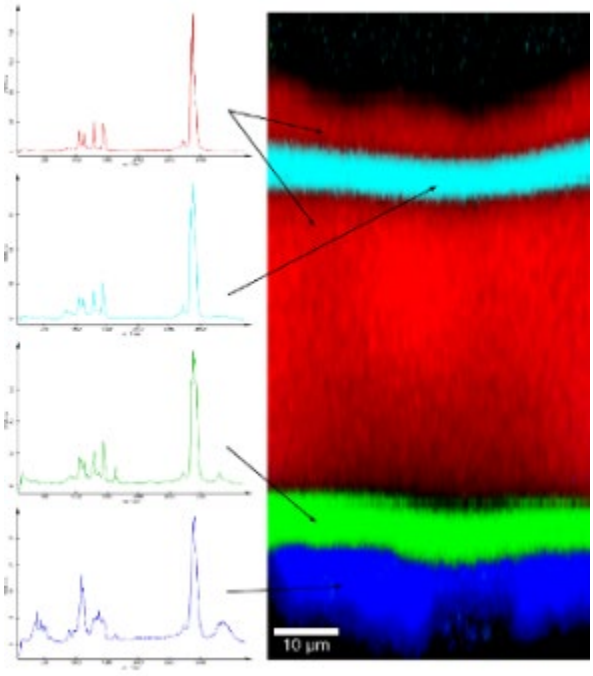

Figure 10 - Raman depth-profiling (x-z direction) of a multilayered polymer coating with corresponding spectra. 50 µm x 100 µm scan range, 120 x 200 pixels, 24 000 spectra, acquisition time per spectrum: 50 ms (WITec GmbH 2020, AZoM Open Access).

Here, we report some details about the different forms of Data Acquisition:1) Point Mapping, 2) Line Mapping and 3) Imaging. Mapping consists in obtaining the spectra from the movement of the sample in relation to the laser, while in the imaging technique, the spectra are obtained without this movement. Fig. 11 shows the different modes of data acquisition, where in red the number of pixels/wavelengths that can be obtained at each reading is highlighted.

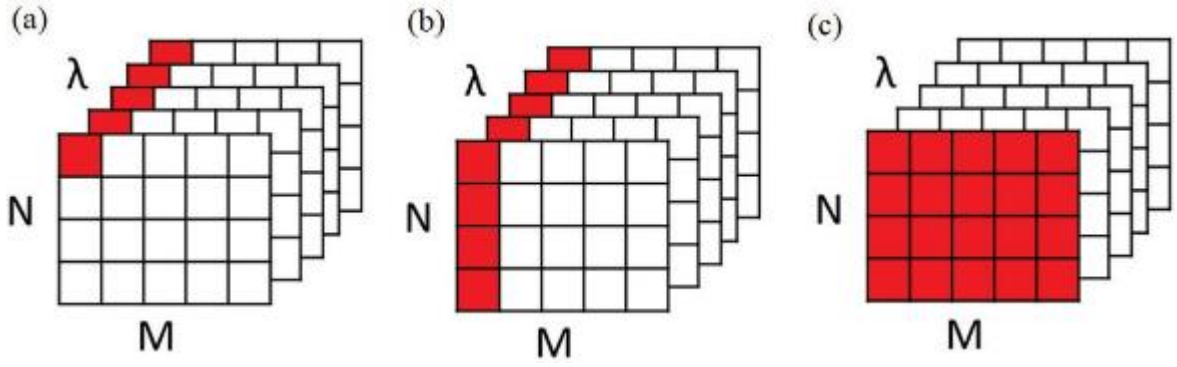

Figure 11 - (a) Point mapping, (b) line-scanning mapping and (c) imaging (Mitsutake et al. 2019, J. Braz. Chem. Soc. Open Access).

Within the mapping technique, there is point-to-point mapping or linear scan mapping. The first is also called point mapping, point-by-point mapping or raster mapping, while the latter is called line-scanning mapping. In point-to-point mapping (Figure 11a), the laser is focused on a point in the sample and a spectrum is acquired at this point/pixel, then the sample is moved and a new spectrum is acquired in the same region, and so on. In this case, the cube presents high spectral resolution, but low definition images. This is the most widely used method for obtaining the data and it provides more detailed images, although it is the most time-consuming. Linear scan mapping (Figure 11b) acquires the spectra of a line of pixels: the laser is defocused to cover all pixels in one direction, so that the data acquisition is faster than in the point-by-point method. However, since laser illumination is uneven, the spatial resolution of the image is not as good as in the first method.

Imaging techniques are also called global imaging or wide-field Raman imaging. In this case, the laser, as in linear scanning, is also defocused, but now it illuminates the entire sample, allowing the acquisition of spectra of the entire region simultaneously (Figure 11c). Most imaging techniques acquire the spectra in slices of the cube, i.e., one wavelength of the spectrum at a time. This makes it a faster method when the spectral range to be analysed is less than the number of points in point-by-point mapping or than the square root of the number of points in linear mapping. The

development of a method using a fiber-optic arrangement, called Fiber Array Spectral Translation (FAST), allows all spatial and spectral information to be obtained simultaneously, making data acquisition much faster. One of the problems encountered in linear mapping and imaging methods is that the laser is defocused. Since the Raman signal is low, this can significantly increase the possibility of fluorescence interference (Stewart, S. 2012, Opilik 2013).

Before using the Raman spectra for qualitative/quantitative purposes either by univariate or multivariate methods, a very important step is data pre-processing. The aim of this step is to eliminate disturbances that occur during the analysis or to limit the effect of undesired phenomena associated with the sampling arrangement and/or sample emission. In Raman spectra there are five main spectral artifacts to be corrected: baseline, noise, differences in scale, spikes, and dead pixels.

Then, the analysis of the real data can be performed. The main multivariate methods used for the treatment of Raman imaging data are principal component analysis (PCA), vertex component analysis (VCA), band-target entropy minimization (BTEM), classical least squares (CLS), multivariate curve resolution (MCR), partial least squares (PLS) and partial least squares- discriminant analysis (PLS-DA).

All the different methods begin with the process of unfolding the cube. In the unfolding, the pixels are placed one below the other (that is, in the rows), while the columns represent the variables (Figure 12a). After the unfolding, a chemometric method is applied, generating values that represent each pixel (for example, the PCA scores). These values are refolded, thus obtaining the concentration maps. The exceptions are the methods that require calibration (PLS and PLS-DA, for example). In these cases, the mean spectrum of each data cube is calculated (Figure 14b), a calibration model is constructed using these mean spectra and the values of the property of interest (or class in the case of PLS-DA). This model is applied to the unfolded matrices, and the concentration vectors obtained are refolded for the construction of the chemical maps.

One of the main disadvantages of calibration methods in relation to other methods is the number of samples required, usually a much larger number than for the curve resolution methods.

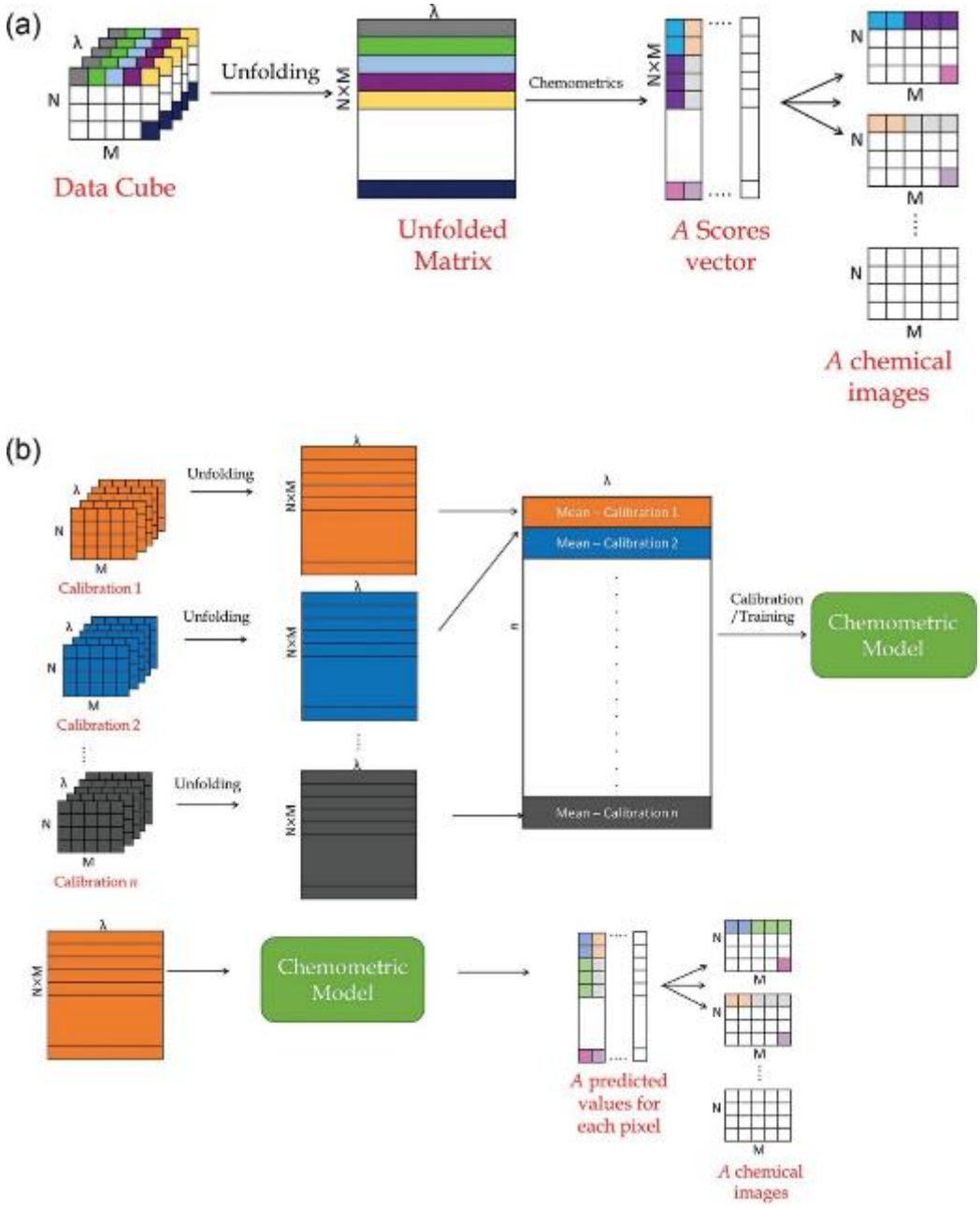

Figure 12 - Generation of chemical images (a) without and (b) with calibration methods (Mitsutake et al. 2019, J. Braz. Chem. Soc. Open Access).

PCA is one of the most important methods in chemometrics and widely used in spectral imaging treatments. It is an exploratory method used to reduce the amount of data based on the correlation between variables. Using PCA, hundreds or thousands of variables are reduced to a few, called principal components (PC). The PCA analysis transforms a large original set of data having a large number of variables into a new one described in terms of principal components (PC) with a lower dimensionality, while retaining as much of the original data information as possible. Principal components are individuated after a procedure successive axis rotation. The first PC is the one with the largest possible variance with respect to the original data. Usually most of the variance is contained in the very first PCs, so that a plot of the first two PC allows for the identification of groups with similar characteristic.

4.4 Raman imaging and SERS applications

Raman imaging spectroscopy has seen increasing interest in several areas. A bibliographic search was carried out on Raman mapping/imaging spectroscopy publications from the last 12 years (2006 to January 2019). A total of 1785 published articles were found, with the number increasing over time (see Figure 13). Regarding arts, archeology and paleontology, it emerges that usually Raman image spectroscopy is not the focus of these field. Instead, Raman spectroscopy is used in conjunction with other imaging techniques (such as SEM/EDS). These studies with Raman are still in the early stages, and in many cases the data analysis is performed by the equipment's own software. An example of this can be found in the work of García-Florentino et al. in the Punta Begoña gallery built in 1918 (García-Florentino 2016).

They analysed part of the wall mortars to find the effect of time on the different types of materials. It was also shown that dolomite was found in

the mapping, but not in the point Raman analysis. Furthermore, internal information can be obtained.

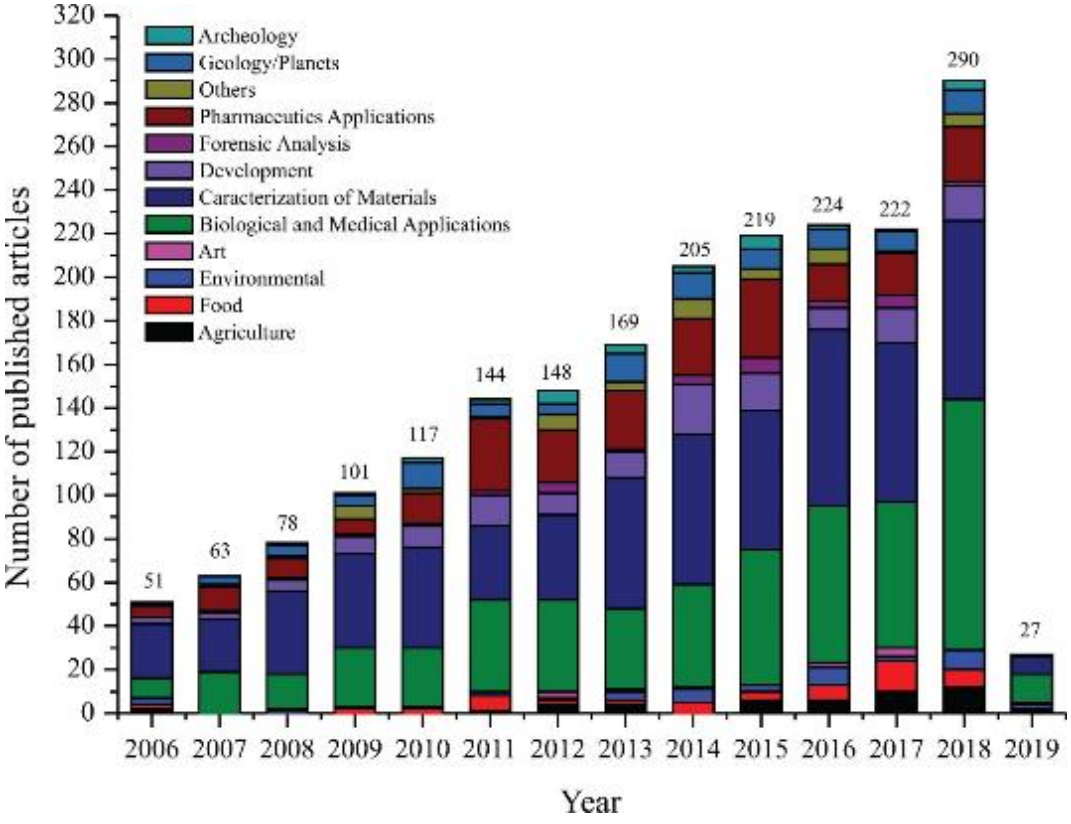

Figure 13 - Number of published articles using Raman imaging from 2006 to January 2019 (Mitsutake et al. 2019, J. Braz. Chem. Soc. Open Access).

An example of this use in cultural heritage can be seen in the work of Botteon et al. (Botteon 2017) in which they identified and created maps of layers of various pigments and raw materials hidden in the paintings. Recently, Aramendia (Aramendia 2019) carried out Raman imaging and Laser Induce Breakdown Spectroscopy (LIBS) analysis on dolomitic marble samples. Samples covered or not by a calcium oxalate (whewellite, $CaC_2O_4 \cdot H_2O$) layer have allowed to determine the concentration of hydrated mineral phases by LIBS and non-hydrated compounds by Raman spectroscopies, respectively.

Gierlinger et al. (Gierlinger 2007) used Raman imaging approach to study a 40x40 µm poplar cells. This research illustrates the great potential of

Raman imaging to monitor the intensity distribution of the observed various functional groups attributed to the cell wall polymers.

Recently, a review is published in literature regarding the analysis of cellulose and lignocellulose materials by Raman spectroscopy (Umesh 2019) while FT-Raman spectroscopy was applied to Eucalyptus wood meal samples, not only to determine cell types, cell morphology, and wood constituents (α-cellulose, hemicellulose and hemicellulose sugar composition, lignin and lignin syringyl-to-guaiacyl ratio, extractives, etc.) but also to develop a rapid quantitative method for accessing wood properties for kraft pulp production. Multivariate data analysis, including cross validation, produced highly significant correlations between conventionally measured and Raman-predicted values for several traits (Ona 2003). Non-destructive monitoring of wood decay and evaluation of acid–base properties of wood (Wariishi 2009, Kami 2002, Shen 1998) are two other areas of research that have taken advantage of the capabilities of FT-Raman spectroscopy. In the former case, both the C==O and the glycosidic-bond bands were used to monitor wood decay by *Coriolus versicolor, Dichomitus squalens,* and *Ceriporiopsis subvermispora*. Further, FT-Raman spectroscopy was used to investigate the acid–base properties of bulk pine wood and it was concluded that the pine was largely acidic. In the investigation, various solvents were used as probe liquids, and spectral changes at ~2936 and ~1657 cm^{-1} were used as measures of acid–base properties.

Studying wood, it is relevant to consider that water plays a central role since it affects all material properties relevant to the performance of wood materials. Therefore, experimental techniques for characterising water within wood are an essential part of nearly all scientific investigations of wood materials. However, while the gravimetric and fibre saturation techniques are useful for determining total amount of water in wood or amount of cell wall water in the over-hygroscopic range, they are not able to provide a deeper insight into wood–water interactions or the distribution of water within the wood structure. For this purpose, spectroscopic techniques are needed allowing to distinguish water in

different environments or provide more detail about molecular interactions and chemistry within cell walls.

The experimental data obtained from the various techniques show the many different aspects of wood–water interactions which can be probed. However, many aspects on soaked wood have not yet been understood. Thus, the combination of results obtained from different spectroscopic techniques (such as NMR, SERS, Raman imaging) will provide new insights into water interacting with wood materials for the conservation of work of art found in the sea.

In this thesis, we will provide preliminary data obtained combining MRI, CT, SERS and Raman imaging results on contemporary wood samples and archaeological waterlogged samples of wooden barrels found in Køge (Denmark) in 2018.

Chapter 5

Novel diagnostic approaches for wood characterization

As described in previous chapters, the identification and characterization of wood of different species used in ancient times represent still today an interesting task in order to discriminate a production of a precise geographic area or to trace out the ancient commercial networks. The research on archaeological wood still today involves several aspects, such as optimization of analytical methods, study of reference (i. e. modern wood), investigation of new materials for conservation and consolidation, to know the structure of the original wood and mainly the relationship between the morphological characteristics and the micro- and ultrastructure of wood tissues, lignin content and crystallinity of cellulose as well as by its hydrophobic capacity.

In this chapter, the combined results of a multi-analytical approach for characterizing contemporary woods are presented and discussed. Principally, the goal of this doctoral thesis was to define, for the first time to our knowledge, a Multislice Computed Tomography (MSCT) and Nuclear Magnetic Resonance imaging (MRI) protocol, performed by clinical

scanners, suitable for wood, to be considered as a useful guide for this kind of investigation. These techniques were applied in combination with the Conventional Fourier transform infrared spectroscopy (FTIR) and micro-Raman (MRS) spectroscopies, first for a full discrimination of the contemporary wood belonging to different species, and then have been extended to impregnated and waterlogged wood of historical findings.

5.1 Multislice Computed Tomography (MSCT) results on contemporary samples and wooden painted tablets

Samples preparation

Simple pieces of untreated modern wood and painted wooden tablets were taken as reference to optimize the diagnostic CT and MRI methodologies to be later used for cultural heritage characterization. Seventeen pieces of contemporary wood, commonly used for the construction of furniture, were provided by a carpenter who works in the province of Messina (Tab. 1). For this reason, the shape of the various woods is different: a round stick, a tablet and finally an axis. Before the characterizations, the woods have not been subjected to any treatment and were always stored at room temperature in a domestic environment.

Then, to simulate a polychrome artwork, three of these tablets were painted with different techniques and then characterized to understand the morphological variations of modern woods, once impregnated with dyes generally found in historical finds, looking for similarities with the historic wet woods.

In detail, the following woods have been analyzed:

- *Two chestnut oak (Quercus prinus) wooden tablets*, measuring 33x14 cm^2 and painted with inorganic and organic pigments from Zecchi Florence (www.zecchi.it). Among the pigments, we used red ochre, natural ultramarine, white lead, cinnabar, madder lake, malachite, red lead, and azurite pigments. Rabbit skin glue tempera was chosen as a binder, and two types of wooden support were used: one with Bologna plaster

preparing and the second with 'incamottatura', both widely used on wooden paintings from XI to XVI century, which consists of a layer of linen canvas applied on the wooden support to simplify the colour expanse.

- *A wooden tablet of acacia wood (Robinia pseudoacacia),* 40x15x1,5 cm in size and painted with the same technique of an Egyptian coffin (Amenta 2014): first ground layer of clay mixed with plant gum; second layer of yellow colour made with orpiment; third layer with pigment palette such as Egyptian blue, orpiment, black charcoal, calcite, malachite and animal glue as a binder.

Tab. 1 – Species of wood analyzed: on the left sample P1; on the right sample P2. Here, a selection between modern Conifer and Deciduous wood (Longo et al. 2020, submitted to Studies in Conservation).

SPECIMEN 1 (P1)			**SPECIMEN 2 (P2)**		
N°	**RIF.**	**Wood sample**	**N°**	**RIF.**	**Wood sample**
1	A	English Walnut – Common Walnut (*Juglans regia*)	1	A	White Poplar (*Populus alba*)
2	B	African Walnut (*Lovoa Trichilioides*)	2	B	European Silver Fir (*Abies alba*)
3	C	Red Spruce (*Picea rubens*)	3	C	Red Spruce (*Picea rubens*)
4	D	Holm Oak (*Quercus ilex*)	4	D	Anigre (*Aningeria altissima*)
5	E	Maritime Pine (*Pinus pinaster*)	5	E	Australian Red Cedar - Toona (*Toona ciliata*)
6	F	Limba (*Terminalia superba*)	6	F	Russian Silver Fir (*Abies alba*)
7	G	Anigre (*Aningeria altissima*)	7	G	Abura – Bahia (*Mitragyna ciliata*)
8	H	Maritime Pine (*Pinus pinaster*)	8	H	European Silver Fir (*Abies alba*)
9	I	Sapele (*Entandrophragma cylindricum*)			

MSCT experimental parameters and results

A Somatom Sensation 16 MSCT (Siemens Healthcare) with a gantry

opening of 70 cm was used for both spiral and sequential acquisition of the wood samples (see Tab. 1 pag. 2), chestnut painted, and acacia painted tablets.

The spiral acquisition was performed setting the following parameters: 330 mAs, 120 kV, slice thickness of 0.75 mm, B60s smooth and B20s smooth Kernels, respectively. The sequential acquisitions were obtained applying 320 mAs, 120 kV, at the slice thickness of 4.5 mm and 0.75 mm, respectively. The reconstruction process is performed with soft tissue or bone kernels. This choice is justified since the bones and soft tissues are characteristic like wood. Kernel number indicates the sharpness of edges and the smoothness of images. Soft tissue algorithms are performed with a kernel setting of 20-40 and bone algorithms with 60 or 70 kernel setting. These acquisition parameters are chosen after an optimization procedure, so obtaining the highest spatial and contrast resolution in wood. Specifically, low kernel setting (smoother image) improves better contrast resolution, low noise level and edge definition poorer. Moreover, the higher number of the kernel (sharper image) provides a better spatial resolution, a higher noise level and a better edge definition reference (Longo 2020).

Images reconstruction was made applying Multi Planar Reconstruction (MPR) and Volume Rendering Technique (VRT) techniques, by the SYNGO software by Siemens Leonardo Workstation. VRT images were obtained by using standard filters calibrated to specific HU of the human body. As described in Chapter 2, these filters allow to virtually dissect an object, and to distinguish region of the sample made of materials characterized by different density. In this case, the SYNGO and OsiriX software were used to acquire HU measurements. In detail, measurements were performed on the sequential scan data with a slice thickness of 4.5 mm. On wooden samples, two types of density measurements were carried out selecting specific Region of Interest (ROI). The first type has involved the area measurement in the visible image of each component of the wood specimens (circular symbols in Fig. 1a); while the second type of measures takes into account of the different radiopacity of tree-rings and wood grain, observed in the MPR images (for example see Fig. 1b). Finally, on pigments, ROIs measurements were done on every single pigment on the coronal view (see Fig. 2).

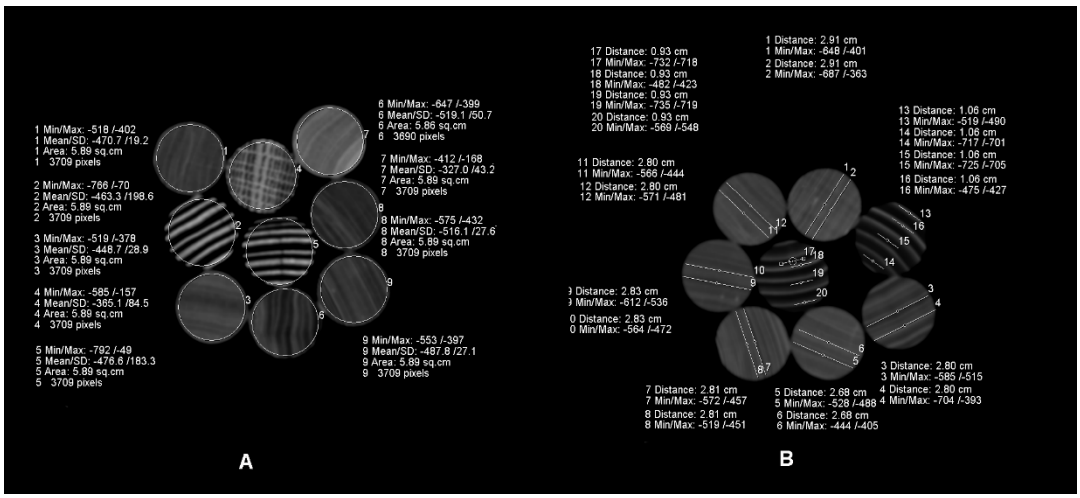

Figure 1a – Area linear CT coefficient measurements (Circular measurements); 1b - Tree-rings and wood grain linear CT coefficient measurements. Different species have a different radiopacity which means different linear coefficient attenuation. Min (HU) corresponds to minor HU values in that measurement area; Max (HU) to major HU values; distance expressed in cm to the length of the measure. Equal species have equal radiopacity and similar value in linear coefficient attenuation (Longo et al. 2020, submitted to Studies in Conservation).

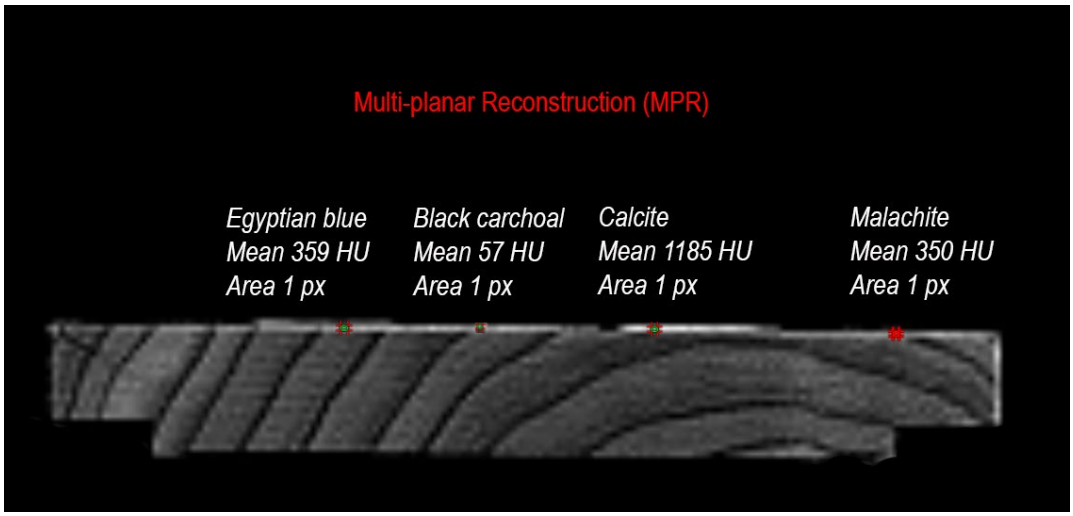

Figure 2 - MSCT MPR reconstruction: HU values measurements of the different pigments on the wooden support (Longo et. al. 2020, Science ABC Poster Presentation).

At this point, wood species densities (d=M/V) and average dried weight values were obtained by the conventional gravimetric method (Bonamini et al. 1996) for each wood specimens. Masses (M) of each wood sample were measured with an analytical balance BP211D Sartorius and the volume (V) were so indirectly estimated. Subsequently, the same samples were dried inside the Universal Memmert Oven stove, at the temperature of T = (103,5 ± 0,5) °C for 24 hours. After the treatment, the woods masses have been re-measured. This procedure has been repeated for a second time to achieve 48 hours of drying time. In this case, the As density values, we considered those reported in literature for ancient pigments (http://webmineral.com/) while a Pearson correlation analysis was performed to compare CT radio-opacity, quantified using the Hounsfield Scale and having measured the dried weight density d of each wood species and of each pigment.

In Fig. 3 are shown MSCT images of all the investigated wood samples. Each wood has its radiopacity translated into shades of grey.

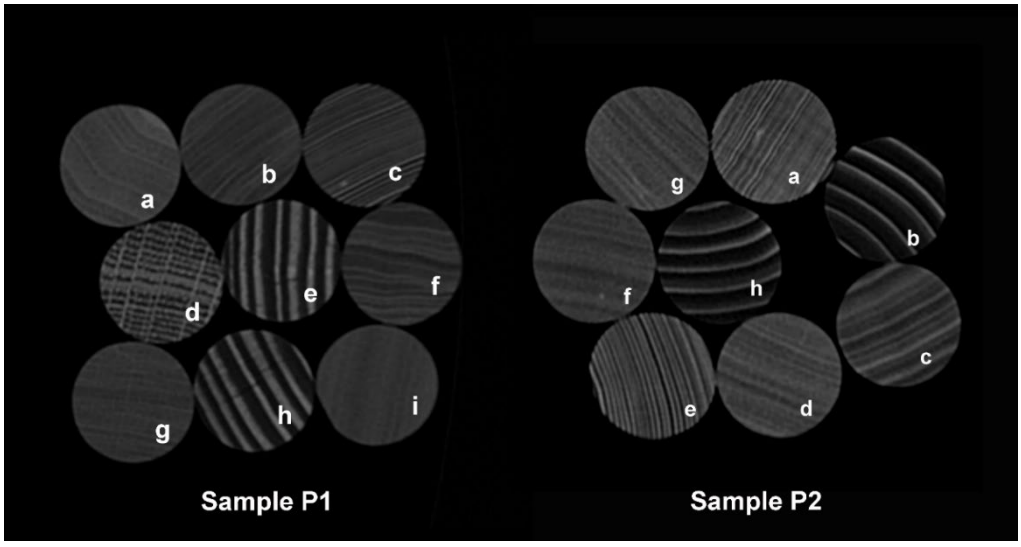

Figure 3 – Multi-planar images reconstruction: on the left sample P1; on the right sample P2. Each wood has its radiopacity translated into shades of grey. In P1, oak (D) and pine (H and E) and in P2, silver fir (B and H), differ considerably. Macroscopic characteristic like parenchymal rays and growth rings are visible (Longo et al. 2020, submitted to Studies in Conservation).

From Fig. 3 it is evident that oak (*Quercus ilex* – D) and pine (*Pinus pinaster* – H and E) differ considerably in radiopacity and grain compared to other species. The same is for the silver fir (*Abies alba* – B and H).

The black and white images obtained by MPR reconstruction have allowed to identify the wood species by comparing the macro-anatomical features with dichotomous keys commonly used by wood anatomists (Wheeler and Baas 1998).

Oak (*Quercus ilex* – D) parenchymal rays are visible (Fig. 4a). Moreover, by MPR reconstruction it is possible to distinguish pine (*Pinus pinaster* – H and E), and silver fir (*Abies alba* – B and H) growth rings: lighter areas represent earlywood, darker areas show latewood (Fig. 4b) It is important to outline that B and H have the same type of radiopacity and annual rings, while it not evident in Abies alba F sample. This effect could be traceable and index of a different growth environments: B and H comes from Europe; F comes from Russia.

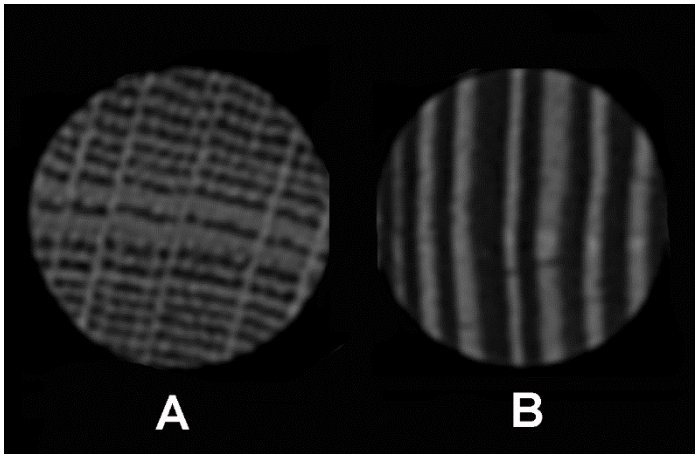

Figure 4a – Deciduous parenchymal rays (Quercus ilex); 4b Conifer earlywood and latewood (Pinus pinaster). By MPR reconstruction is possible to distinguish determinate macroscopic characteristic. Parenchymal rays in oak and pine transition from early to latewood in growth rings are perfectly visible (Longo et al. 2020, submitted to Studies in Conservation).

As reported in Chapter 2, for any material with linear attenuation coefficient μ, the corresponding HU value is given by the relation:

$HU=1000x\ (\mu-\mu_w)\ /\ (\mu_w-\mu_{air})$ where μ_w and μ_{air} are the linear attenuation coefficients of water and air, respectively. In our case, the estimated HU values range between -327 HU (*Juglans regia*) and -646.5 HU (*Abies alba*) (Table. 2).

A distinction between latewood and early-wood samples has been made by MSCT analyses. In fact, Latewood region (light voxels) has higher values than early-wood ones (dark voxels) (Longo 2019) Latewood has a range value between -307.5 HU to -558.5 HU, while earlywood between -363.5 HU to -727 HU, respectively (Tab. 3). Full HU range values of each investigated wood species are reported in Tab. 3, which collect all the HU measurements taken on early and latewood inside tree-rings.

The estimated values from MSCT agree with the typically known characteristic of wood. In fact, compared to springwood, latewood has more mass volume and strength as well as higher values of the parameters related to shrinkage and swelling (Berti et al. 2007). Indeed, earlywood ensures the rapid transport of the sap at the beginning of the vegetative season, while latewood formed in the summer is mainly due to support task.

Finally, a significant linear correlation between HU values and the density (in Kg/m^3) of each wood was found (see the data shown in Fig. 5). This linearity indicates that higher HU values (positive range) correspond to higher densities. Analogously, lower HU values (negative range) to lower densities.

Moreover, wood with lower HU values (in our study, Abies alba), means that have a more significant quantity of air in the inner structure or higher volume occupied by tracheid and vessels compared to volume of wood parenchyma (Capuani et al. 2020). Conversely, wood species with lower volume occupied by vessels are characterized by higher HU values (Fig. 5).

It agrees with the typically known characteristic of wood. In fact, compared to springwood, latewood has more mass volume and strength as well as higher values of the parameters related to shrinkage and swelling (Giordano 1982). Indeed, earlywood ensures the rapid transport of the sap at the beginning of the vegetative season, while latewood formed in the summer is mainly due to support task.

Table 2 – P1 and P2 HU values: values are always negative. This is correlated to -1000 HU, which is the air density because wood is a porous material "full" of air, expecially inside tracheids and vessels (Longo et al. 2020, submitted to Studies in Conservation).

Specimen P1					**Specimen P2**				
Wood	**Image Ref.**	**Mean (HU)**	**Min (HU)**	**Max (HU)**	**Wood**	**Image Ref.**	**Mean (HU)**	**Min (HU)**	**Max (HU)**
Junglans regia	A	-329	-426	235	*Populus alba*	A	-512	-624	-357
Lovoa Trichilioides	B	-482	-593	-303	*Abies alba*	B	-620	-899	96
Picea rubens	C	-475	-565	-235	*Picea rubens*	C	-469	-571	-107
Quercus ilex	D	-355	-589	-88	*Aningeria altissima*	D	-443	-576	-195
Pinus pinaster	E	-453	-892	123	*Toona ciliata*	E	-497	-626	-276
Terminalia superba	F	-509	-672	-70	*Abies alba*	F	-477	-566	-306
Aningeria altissima	G	-453	-611	-285	*Mitragyna ciliata*	G	-462	-568	-306
Pinus pinaster	H	-480	-891	47	*Abies alba*	H	-600	-897	169
Entandrophragma cylindricum	I	-445	-608	-262					

Table 3 – Annual rings HU values: late-wood values and early-wood values. Min (HU) corresponds to minor HU values in that measurement area; Max (HU) to major HU values; distance expressed in cm to the length of the measure. Late-wood values are higher than early-wood values. While the early wood ensures the rapid transport of the sap at the beginning of the vegetative season, the late wood formed in the summer is mainly due support task. Compared to spring wood, late wood has more mass volume and strength as well as higher values of the parameters related to shrinkage and swelling (Longo et al. 2020, submitted to Studies in Conservation).

LATE WOOD (Light)

P1	Mean (HU)	Min (HU)	Max (HU)	Distance (cm)	P2	Mean (HU)	Min (HU)	Max (HU)	Distance (cm)
E	-359	-630	-88	2.85	C	-524,5	-648	-401	2.91
H	-307,5	-496	-119	2.84	A	-548,5	-704	-393	2.80
D	-363	-588	-138	3.00	G	-424,5	-444	-405	2.68
D	-408	-619	-197	3.00	F	-485	-519	-451	2.81
C	-467	-495	-439	2.65	E	-518	-564	-472	2.83
I	-521	-647	-395	2.80	D	-505	-566	-444	2.80
F	-465	-496	-434	1.63	B	-504,5	-519	-490	1.06
F	-456	-507	-405	0.70	B	-451	-475	-427	1.06
B	-450,5	-470	-431	2.54	H	-452,5	-482	-423	0.93
G	-506	-596	-416	2.89	H	-558,5	-569	-548	0.93

EARLY WOOD (Dark)

P1	Mean (HU)	Min (HU)	Max (HU)	Distance (cm)	P2	Mean (HU)	Min (HU)	Max (HU)	Distance (cm)
E	-651	-714	-588	2.85	C	-525	-687	-363	2.91
E	-726,5	-766	-687	2.85	A	-550	-585	-515	2.80
H	-724,5	-778	-671	2.84	G	-508	-528	-488	2.68
H	-692,5	-755	-630	2.84	F	-514,5	-572	-457	2.81
D	-488,5	-792	-185	3.00	E	-574	-612	-536	2.83
D	-554,5	-871	-238	3.00	D	-526	-571	-481	2.80
C	-590	-685	-495	2.65	B	-709	-717	-701	1.06
C	-501	-536	-466	2.65	B	-715	-725	-705	1.06
I	-519	-552	-486	2.80	H	-725	-732	-718	0.93
F	-512,5	-541	-484	1.63	H	-727	-735	-719	0.93
F	-597,5	-606	-589	0.70					
B	-512,5	-544	-481	2.54					
G	-523,5	-587	-460	2.89					
A	-363,5	-398	-329	2.79					
A	-365,5	-396	-335	2.79					

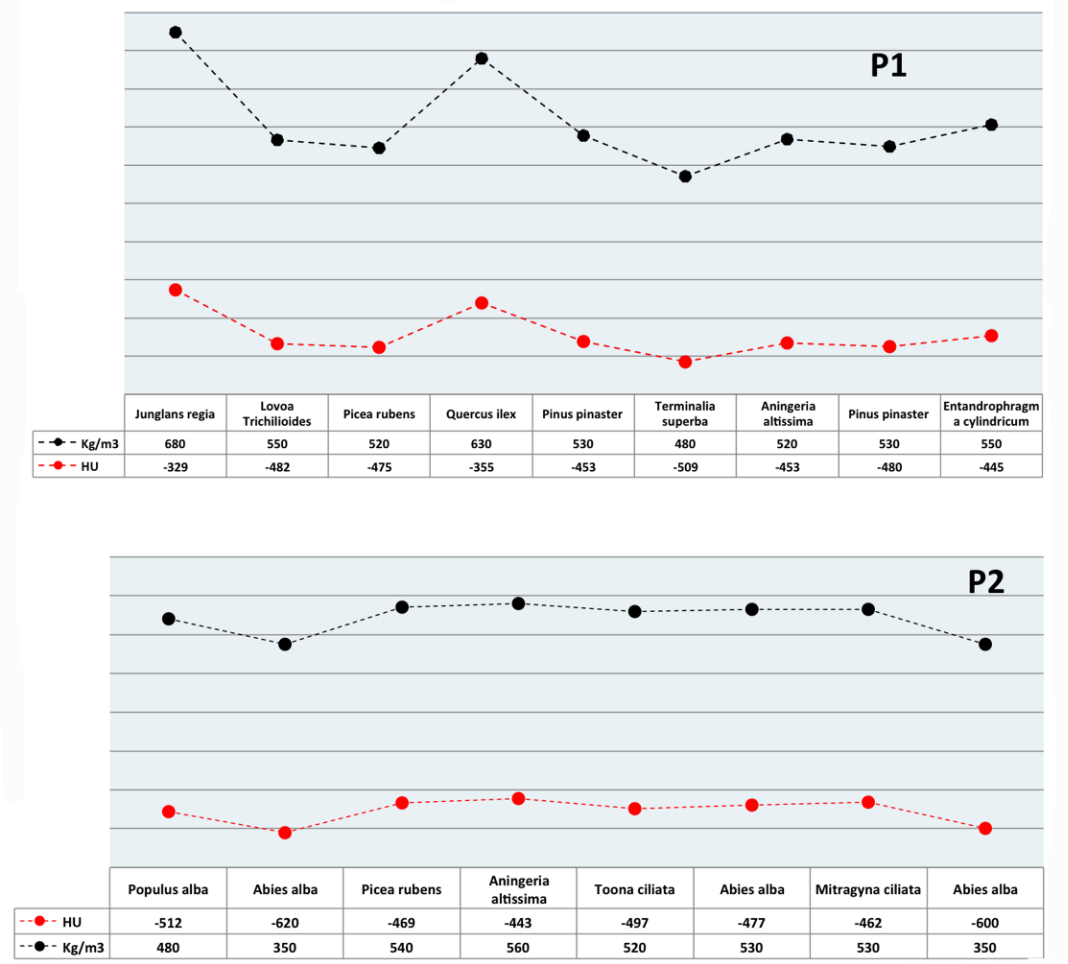

Figure 5 – Pearson correlation between HU and wood density in Kg/m³. HU values in positive ranges correspond to higher densities. Lower HU values in negative ranges to lower densities. Wood with lower HU values means that have a higher quantity of air in the inner structure, while wood with higher HU values has a less porous structure (Longo et al. 2020, submitted to Studies in Conservation).

At this point, HU values of different pigments on the wooden support have been estimated too, looking for an analogous correlation of the HU values with the well-known density values of the various dyes. Table 4 shows the density in g/cm³, obtained by literature data (http://webmineral.com/) and the corresponding HU value for each pigment, estimated by us.

Table 4 – Density in g/cm³ (http://webmineral.com/) and the corresponding HU value for pigments painted on chestnut tablet. As aspected, higher densities values correspond to higher HU values (Longo et al. 2020, submitted to Studies in Conservation).

Pigment	Chemical	Average weight (g/cm3)	Hounsfield Units (HU)
Madder lake	C14H8O4, C14H8O5	1.5	218
Malachite	$CuCO_3 \cdot Cu(OH)_2$	3.8	674
Red Lead	$2PbO{\cdot}PbO_2$	8.2	1456
Azurite	$2\ CuCO_3{\cdot}Cu(OH)_2$.	3.8	356
Red Ochre	$\propto$-Fe_2O_3	5.3	775
Ultramarine	$Na_7Al_6Si_6O_{24}S_3$.	2.4	297
White Lead	$2\ PbCO_3{\cdot}Pb(OH)_2$	11.37	2852
Cinnabar	HgS	8.1	1534

Also, in this case, pigments with higher density values show higher HU values. In details, we found that:

On chestnut painted tablet, HU values for each pigment are:

white lead: 2852 HU;

Red lead: 1456 HU;

Cinnabar: 1534 HU;

red ochre: 775 HU;

malachite: 674 HU;

azurite: 356 HU;

natural ultramarine: 297 HU and

madder lake: 218 HU.

On acacia painted tablet, HU values are:

Egyptian blue: 359 HU;

black charcoal: 57 HU;

calcite: 1185 HU and

malachite 350 HU.

It has not been possible to estimate orpiment HU values since the layer was too thin (a limit of MSCT technique).

On the overall, we have found that all these values are strictly related to the concentration and the density of the materials (wood or pigment), expressed in g/cm^3. Significant linear correlation between HU values and density (g/cm^3) of each pigment was found. This correlation trend is more clearly evidenced by the trend shown in Fig. 6.

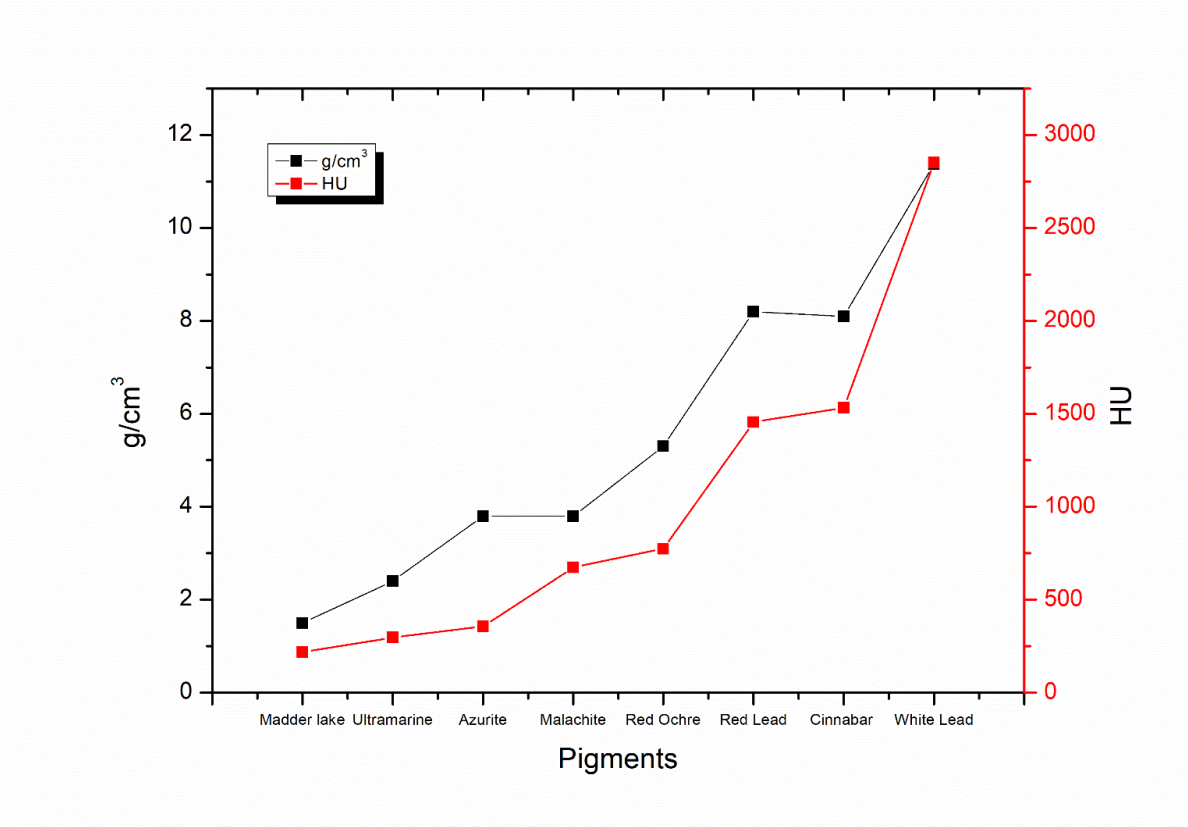

Figure 6 - HU and density values for each pigment (Longo et al. 2020, submitted to Studies in Conservation).

The potential of the MSCT technique in indirectly assessing the density of materials (such as pigments on wooden supports) is given by the fact that it is able to distinguish, in some cases, samples that have comparable density values.

For example, cinnabar and red lead have both density but HU values of 8.2 HU and about 1500 HU, respectively. Similarly, azurite and malachite have density values of 3.8 g/cm3, but different HU values (356 HU vs 674 HU). In this case, however, the observed differences are probably due to the inhomogeneities of the pigment layer, which measure less than 0.6 mm

(CT slice thickness). Azurite is less opaque than malachite and probably an area with less concentration of azurite was measured.

Finally, an MSCT drawback must be outlined. The estimated HU madder lake values are not realistic, and this can be explained considering the mechanisms underlying the functioning of MSCT technique. Attenuation coefficients values are affected by the weight of absorption and scattering processes of the incident radiation. At the X-ray energy used in our CT investigation, equal to 120 keV, a competition between Compton scattering (incoherent scattering, for Z less than 20) and photoelectric absorption, (that increases for Z>20), occurs. Thus, the influence of these mechanisms seems relevant when considering organic pigments such as madder lake. We also evidence that the madder lake value is invalidated by the presence of calcium sulphate hydrate (Bologna plaster) used during the sample preparation, which has a density value of around 2.9 g/cm3.

Ultimately, HU ROIs measurements were performed on wooden support. For Chestnut oak wood, the estimated HU value is around -300 HU, while those of acacia wood is around -331 HU.

For the VRT images processing, we have chosen medical VRT filters calibrated on the human body and characterised by density values such as those of the materials specimens investigated. It is expected (as already proved with preliminary tests) that conventional densiometric similarities between wood and tissues correspond to an analogous behaviour, in terms of attenuation of the X-ray beam, during CT characterisations. No VRT image of the wood samples was obtained using the filters optimised for positive ranges. On the contrary filters, calibrated on negative ranges, showed VRT images of woods.

Then, an optimization of the VRT reconstruction filters procedure has been performed. The systematic analysis has allowed to produce a database (see Tab. 5) where all VRT reconstruction filters are reported together the relative HU ranges. Some of them have different HU ranges because more types of windows adjustment are possible. Further, each filter is calibrated over a range in HU, which corresponds to radio-density of different tissues, and organs that constitute the human body. The values change between -1000 (air attenuation), 0 (water attenuation) and +1000 (bone attenuation). On the overall, as in medicine procedure, filters are calibrated on positive

HU ranges and others on negative. In our case, wood is collocated in the negative range (from 0 to -1000), because it is a very porous material and it is "full" of air.

Table 5 – Volume Rendering Technique SYNGO software Siemens filters: each filter is calibrated on human tissues densities. Filters suitable for wood analysis are highlighted in grey and are located in the negatives HU ranges (Longo et al. 2020, submitted to Studies in Conservation).

	VRT Filters	**HU Ranges**
1	Abd_Shaded_A	162 < HU < 1699 72 < HU < 184
2	Abd_Shaded_B	60 < HU < 2533
3	Abd_Shaded_C	127 < HU < 3071
4	AngioRunOff_ 1.0_ B30f	157 < HU < 3071
5	Carotid_Sha_A	-981 < HU < -229 249 < HU < 710 157 < HU < 273
6	Carotid_Sha_B	-1005 < HU < -253 -42 < HU < 2470 -1024 < HU < 3071
7	Carotid_Thin	92 < HU < 176 -587 < HU < 44
8	Colon	189 < HU < 390 230 < HU < 600 1097 < HU < 3071
9	CT_Colon	-749 < HU < -512 -603 < HU < -101 -143 < HU < 77
10	CT_Colon_Unshaded	-485 < HU < 82 -969 < HU < -110 -695 < HU < -183
11	CT_Extremities_Shade	200 < HU < 500 261 < HU < 1875

12	CT_Extremities_Shade2	382 < HU < 3071
13	CT_Greyscale_Heart	100 < HU < 400 200 < HU < 500 300 < HU < 600
14	CT_RunOff	-28 < HU < 1832 72 < HU < 360 72 < HU < 159 183 < HU < 346 267 < HU < 3071
15	CT_Scapula	58 < HU < 273 200 < HU < 500 162 < HU < 390 229 < HU < 1843
16	CT_Thin_Lung	-7 < HU < 167 -1024 < HU < -624 -831 < HU < -212
17	CT_Thin_Slice_Heart	100 < HU < 400 200 < HU < 500 300 < HU < 600
18	CT_Thin_ Slice_ VRT	34 < HU < 1960 -96 < HU < 1843 100 < HU < 400 200 < HU < 500 300 < HU < 600
19	CT_Thin_Slice_ VRT_abd	-13 < HU < 1846 100 < HU < 400 200 < HU < 500 300 < HU < 600
20	CT_UHR_Spi	200 < HU < 500 181 < HU < 409 58 < HU < 1843
21	CTA_Head	124 < HU < 2547 128 < HU < 243 -988 < HU < -709 -1024 < HU < 3071

22	Extremities	35 < HU < 3070
23	Heart_Colored	-100 < HU < 3071 -1024 < HU < 3071
24	Heart_Soft_Plaque	-304 < HU < 11 -97 < HU < 14 163 < HU < 458 94 < HU < 2788
25	Knee	42 < HU < 2451 230 < HU < 600 175 < HU < 470
26	Lung	-905 < HU < -440 -646 < HU < -502 -1024 < HU < -22
27	Spine	189 < HU < 390 200 < HU < 500 230 < HU < 600 284 < HU < 3071
28	Spine_Shaded	-1024 < HU < 3071
29	Transparent_Bone	66 < HU < 3071
30	Vessels_Coils	904 < HU < 4095 521 < HU < 720

Based on the collected data, we concluded that filters with values from -700 HU to -300 HU are the most suitable for wood VRT reconstruction. In Figure 7 is shown the results applying the lung VRT filter. Its range goes from -905 HU to -440 HU, from -646 HU to -502HU and from -1024 HU to -22 HU, because more types of windows adjustment are possible. More morphological details of the investigated woods are evident. In the image shown In Fig. 7, purple shades correspond to lower HU values densities and white shades to higher HU values.

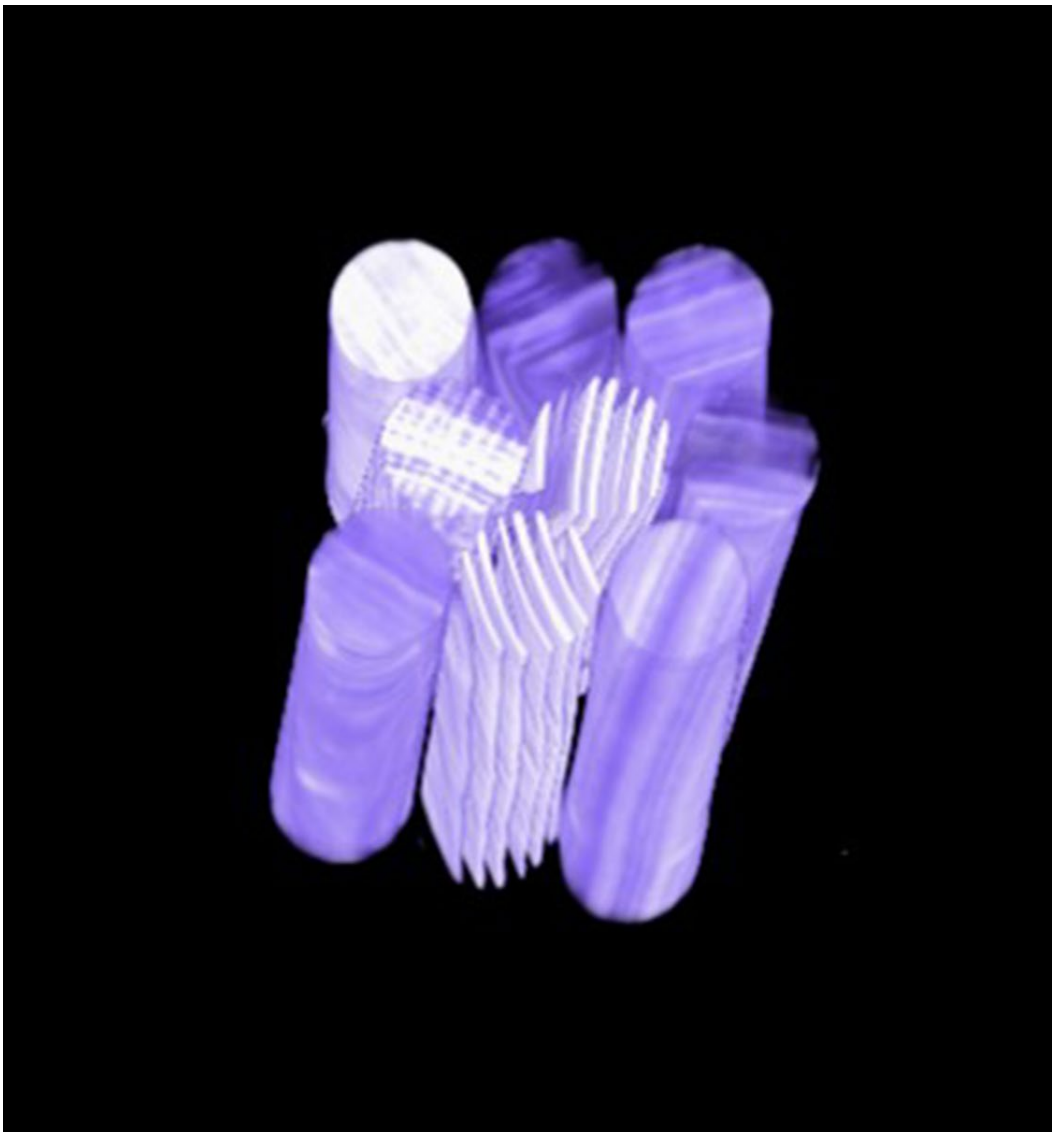

Figure 7 – Lung VRT filter on sample P1 (see table 1 at pag. 2). Its range run from -905 HU to -440 HU, from -646 HU to -502HU and from -1024 HU to -22 HU. Purple shades correspond to lower HU values densities and white shades to higher HU values (Longo et al. 2020, submitted to Studies in Conservation).

As made for MSCT analysis on wood, also in this case, VRT reconstruction approach was applied to investigate the painted wooden sample. In this

way, it has been possible to divide the sample into white areas (pigments based on lead and mercury) and blue colour zones (wood) (see Fig. 8).

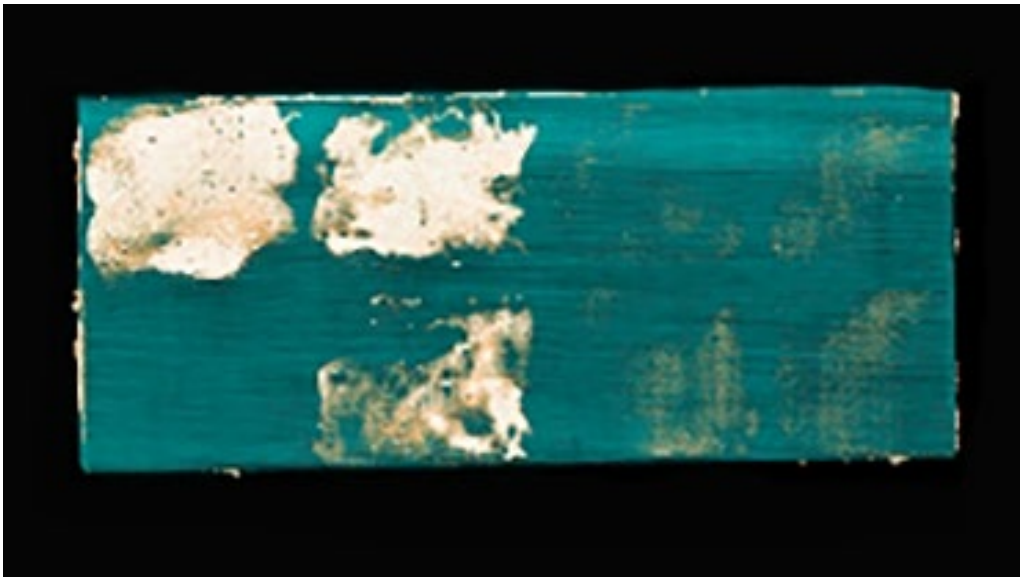

Figure 8 – Bones and skin VRT filter applied on the wooden painted sample. White areas correspond to pigments based on lead and mercury and blue colour zones to wood (Longo et al. 2020, submitted to Studies in Conservation).

In conclusion, in this first part of this chapter, the results of a MSCT analysis on different species of contemporary wood and wooden tablets painted with the most used ancient pigments are presented and discussed. For the first time MSCT (using a clinical scanner) approach are adopted to characterize the morphology and the physical properties of the investigated wood and the pigments on the wood tablets. Images were reconstructed by Multi-planar (MPR) and Volume Rendering Technique (VRT) post-processing analyses. The black and white images obtained by MPR reconstruction have allowed to identify the wood species by comparing the macro-anatomical features with dichotomous keys commonly used by wood anatomists (Wheeler and Baas 1998). We have distinguished latewood and earlywood in Conifers by the wide rings. This type of information can be efficiently obtained by MPR images and it is essential

for dendrochronological and provenance analysis which uses, as a first reference, the difference between latewood and earlywood (Bill et al. 2012, Stelzner 2015).
It is a significant preliminary result but, optimizing the approach and the further development of the technique to ensure an increase of the spatial resolution, could
in perspective be a useful tool to obtain dendrochronological information also on Deciduous or Conifers through the analysis of thinner grain. As shown in this thesis, MSCT approach is particularly useful to characterize a painted wooden object in which it is generally hard to identify the type of wood without peel off a piece of the sample. Otherwise, MSCT analysis allow to collect information on wood-based materials (and not only) in a non-destructive way. Moreover, in future, MSCT images recognition will be made automated thanks to machine learning as it was recently done on industrial CT images for wood identification (Kobayashi 2019).
Another interesting aspect offered by MSCT images analysis is the possibility to estimate HU values, which are directly correlated with densitometry features of each wood and pigments. As shown previously, VRT reconstruction is useful for artistic techniques studies. This type of three-dimensional reconstruction, based on calibrated filters on human body materials, let made possible to select one density and, virtually, erase the others, like restoration support, restoration integrations without doing any damage (Longo 2018, Montaina 2020). It allows to virtually "dissecting" an object and studying it more in-depth. We looked for human body HU calibrated filters, with a range as close as possible to those of lung attenuation, because it is very close to wood attenuation since they are both full of air.

Ultimately, combining the two types of images, VRT and MPR, information about materials, conservation state and artistic techniques can be obtained carrying out only one analysis. Of course, there are some limitations, primarily related to the minimum slice thickness that could be set (0. 6 mm in our case). Nevertheless, this problem is now partially overcome since new Siemens scanners have been constructed with a spatial resolution of 0.2 mm. Another actual limitation is the gantry opening because the maximum available on the market is 78 cm in

diameter. In this case, this method can be applied only to small and medium-size objects, which is a considerable part of artefacts. Finally, MSCT scanners are the most common instrumentation of a hospital radiological department and permits to obtain complete information in only 12s scan time. During the weekend and closing, time scanners could be used for diagnosis in cultural heritage instead of leaving them inactive.

5.2 Nuclear Magnetic Resonance (MRI and μMRI)

5.2.1 MRI clinical scanner results on contemporary samples

Samples preparation

Some of the samples characterized by MSCT were also characterized by NMR, using a clinical scanner Philips Achieva 3.0 T X-series, equipped with a 3T static magnetic field, high-performing imaging gradients with an 80 mT/m maximum intensity with 200mT/m sloping ramp, and a FreeWave 32 SENSE-HEAD canals coil was used.

In particular, sixteen cylinders of wood (Tab. 6) with diameter d = (2.95 ± 0.05) cm and height h = (20.0 ± 0.1) cm were assembled together in order to obtain a phantom with dimensions of about 15 cm x 12 cm x 20 cm.

To carry out NMR characterization, the woods were soaked. To obtain a full water imbibed sample, each wood specimens was properly and completely immersed in 5 l of distilled water. The container was covered with plastic wrap so that water could not evaporate, and dust particles could not contaminate the solution. Four days later, the woods were boiled, in order to let water penetrate the log more easily, in distilled water for 30 minutes each (Bonanimi 1996).

This procedure was repeated four times for sinking most of the samples in water. After the first boiling procedure A, I, M, N, O sank; H sank after two days from the first boiling procedure; F, L and P after the fourth. Nonetheless, B, C, D, E, G and Q never sank.

Table 6 - Denomination species for this work (right column) with the associated letter on the left (Longo et al. 2020, in preparation for Wood Science and Technology).

	Sample
A	Abura – Bahia (*Mitragyna ciliata*)
B	White Poplar (*Populus alba*)
C	Limba (*Terminilia superba*)
D	Red Spruce (*Picea abies*)
E	Silver Fir (*Abies alba*)
F	Anigrè (*Aningeria altissima*)
G	Silver Fir (*Abies alba*);
H	Sessile Oak (*Quercus petraea*)
I	English Walnut – Common Walnut (*Juglans nigra*)
L	Anigrè (*Aningeria altissima*)
M	Sapele (*Entandrophragma cylindricum*)
N	Australian Red Cedar - Toona (*Toona ciliata*)
O	Virginia Pine – Scrub Pine american (*Pinus ponderosa*)
P	African Walnut - Dibetou (*Lovoa trichilioides*)
Q	Red Spruce (*Picea abies*)
R	Virginia Pine – Scrub Pine american (*Pinus ponderosa*)

Pieces of dried wood cylinders, 2.5 cm in height, were cut to obtain little samples for mass and density measurement.
The wood density was obtained from the relation:

$$d = \frac{M}{V} \quad (3)$$

where d is the density, M is the mass and V is the volume.

The following procedure was used to obtain the masses and volumes of the woods. Initially, the mass of empty weighing bottles was measured with an analytical balance BP211D Sartorius. Subsequently, the masses of the samples inserted in the weights were measured. The samples, in the appropriate open containers, were positioned inside the Universal Memmert Oven stove at the temperature of T = (103,5 ± 0,5) °C for 24 hours. The container was then closed before extraction from the stove, as the wood instantly began to absorb the humidity present in the laboratory. Once the masses have been measured, this procedure has been repeated for a second time, to achieve 48 hours of drying time. Using this technique, it is believed that the samples were released from most of the moisture present (Bonamini 1996).

The obtained data have been processed to know the mean mass value and the SD, before and after the cooking of 24 and 48 hours. A T-test was then carried out to assess whether the differences in the masses before and after the drying cycles were significant and not the result of statistical fluctuations. In all cases, the test ensures that the mass decrease is due to an observed physical phenomenon and not to a statistical fluctuation of the measurement process. Once all the values of the masses were collected, the density of each species of the samples was calculated. The M net mass of the samples was calculated by subtracting:

$$M = M_{cp} - M_{ps}$$

where M_{cp} is the mass of the weighing bottles with the inserted samples, measured after the drying procedure, and M_{ps} is the mass only of the weighing bottles. The error on the mass was obtained by summing the absolute errors of the two subtracted quantities. Then, the volume of samples was evaluated according to the relation:

$$V = A_{base} \cdot h$$

where V is the volume, A_{base} is the area and h is the height. The mean volume of all the samples was equal to: V = (17,1±1,3) cm^3 Pearson's correlation was used to study correlations between variables. A p value

less than 0,05 was considered for statistical significatively.

Totally, 16 species of soaked wood were analyzed, cut and grouped to form two samples (see Tab. 6). In this way, it was possible to carry out an NMR survey with images and measurement of the relaxation times of 16 different wood species characterized by different microstructures.

The timber used belong mainly to two categories: those of the Gymnosperms (known as softwoods) and that of the Angiosperms (known as hardwoods). These two groups present important structural differences. The softwoods for the presence of the same elements that perform more functions (tracheids) are called “homoxils”. Instead, the hardwoods are called "eteroxils": they consist mainly of two different types of cells, one with mechanical function (fibres), the others with conduction function (vessels). The species chosen are commonly used in the field of cultural heritage (Signorini et al. 2014).

MRI experimental parameters and results

At this point, MRI characterization were performed, and the following acquision sequences were used for the soaked contemporary woods:

T_2 –weighted (T2-w) images were performed with a 0,3x0,3 mm^2 plane resolution and 5 mm slice thickness (STK), number of averages, NS= 1, matrix size, MTX =880x880 mm^2 and Field Of View (FOV) =260x260 mm^2, using a Multi echo sequence with Echo Time (TE) = 16 ms, Ripetition Time (TR) =1500 ms. T_2*-weighted (T2*-w) images were performed with a 0,25x0,25 mm^2 plane resolution, STK= 5 mm, NS= 2, MTX =1024x1024 mm^2 and FOV = 260x260 mm^2, an Multi echo sequence with TE = 4 ms, TR = 1000 ms.

In order to obtain T_1-weighted (T_1-w) images, an Inversion Recovery Turbo Spin Echo sequence was used with a 0,25x0,25 mm^2 plane resolution, a STK= 3 mm, NS=1, MTX =1024x1024 mm^2 and FOV= 260 x 260 mm^2, TE = 30 ms, Inversion recovery (IR) = 1800 ms, TR = 2000 ms.

For T_2* measurement an axial view Multi-echo sequence was used, with 0,90 x 0,90 mm^2 plane resolution, a STK=5 mm, NS=4, MTX =288x288 mm^2 and FOV =260x260 mm^2. TE = 3,0 ms (10 echos at 3, 9, 15, 21, 27, 33, 39, 45, 51, 57 ms), TR = 2000 ms, the numer of slices is twenty.

For T_2 measurement, an axial view Multi-echo sequence was used, with

0,40x0,40 mm^2 plane resolution, a STK=5 mm, NS=1, MTX =640x640 mm^2 and FOV=260 x 260 mm^2 was used. TE = 10 ms (10 echos at 10, 21, 32, 42, 52, 63, 74, 84, 94, 105) ms e TR = 1500 ms, the numer of slices is twenty.

In order to measure T_1, an axial view Inversion Recovery Turbo Spin Echo sequence was used, with 0,39x0,39 mm^2 plane resolution, STK=5 mm thickness, NS=1, MTX =672x672 mm^2 and FOV= 260 x 230 mm^2, IR = (100, 200, 400, 800, 1200, 1600, 1800) ms, TR = 2000 ms, TE = 20 ms, the numer of slices is twenty.

Dicom Viewer 3.0 software was used to analyze DICOM (Digital Imaging and Communications in Medicine) images, and to obtain regions of interest (ROI) in each wood cylinder of soaked and the dry samples.

For each one of the sixteen-soaked cylinder, some slices with homogeneous areas in signal intensity have been chosen. For each slice, a ROI has been selected manually to obtain the signal intensity, taking care that, within that slice, each sample maintained a region of interest of similar extension. Then, the relaxation constants T_2, T_2* and T_1 related to the sample's microstructure were extracted through the appropriate fit of the theoretical functions to experimental data. To measure the relaxation time T_2 e T_2* of the wood species, the signal intensities have been fitted with the following functions: (Farrar, Becker 1971)

$$\boldsymbol{S(TE) = c + S_0 e^{-\frac{TE}{T_2}}}$$

(1)

where S(TE) is the signal intensity in the function of the Echo Time (TE), c is a constant, S_0 is the value of S at equilibrium and T_2 is transverse or spin-spin relaxation time; and the function:

$$\boldsymbol{S(TI) = S_0(1 - 2e^{-\frac{TI}{T_1}})}$$

(2)

where S(TI) is the signal intensity in the function of the Inversion Time (TI), S_0 is the value of S at equilibrium and T_1 is longitudinal or spin-lattice relaxation time.

The average values of the T_1, T_2, T_2* parameters extracted from each slice were obtained with their standard deviation (SD).

Now, known the treatment of the samples and the main elements to analyse NMR data, MRI evidences are reported and discussed.
First, it was analyzing the cross-section because there are distinguishable growth rings, knots, regions of deterioration and other structural characteristics of the wood (Hoadley 1990). Wood MRI macroscopic characteristics were then compared with macroscopic wood identification key (Nardi Berti 2006 and insidewood.lib.ncsu.edu/) usually utilized by wood experts. In Fig. 9a, Fig. 9b and Fig. 9c are shown axial T_2, T_2* and T_1 weighted images of the imbibed wood samples.

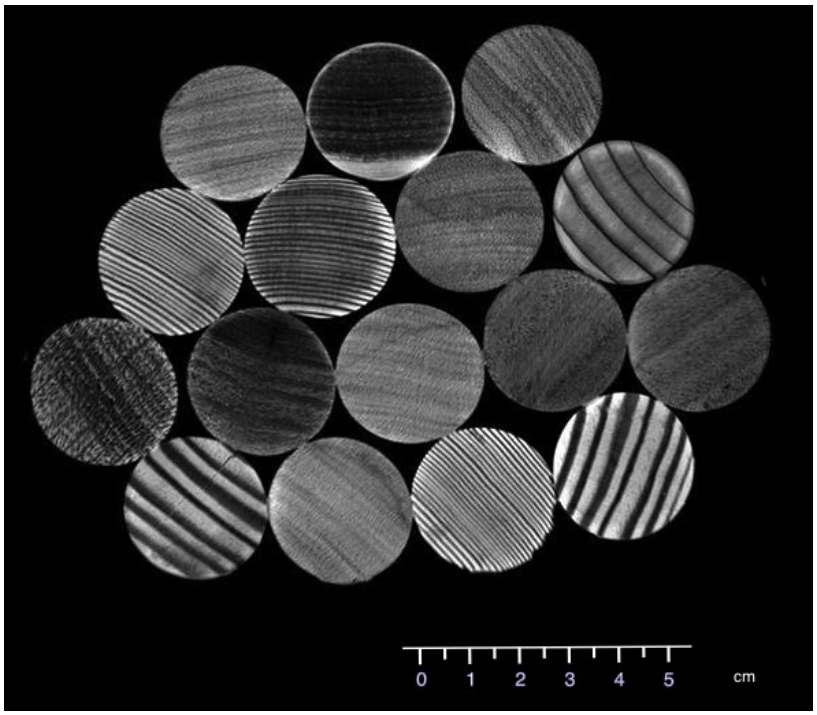

Figure 9a - High-resolution T2-weighted image of the imbibed contemporary wood samples. The in-plane resolution was 0,3x0,3 mm² with a thickness of 5 mm. A Spin Echo acquisition sequence was used with TE = 16 ms, TR = 1500 ms, NS=1 (Longo et al. 2020, in preparation for Wood Science and Technology).

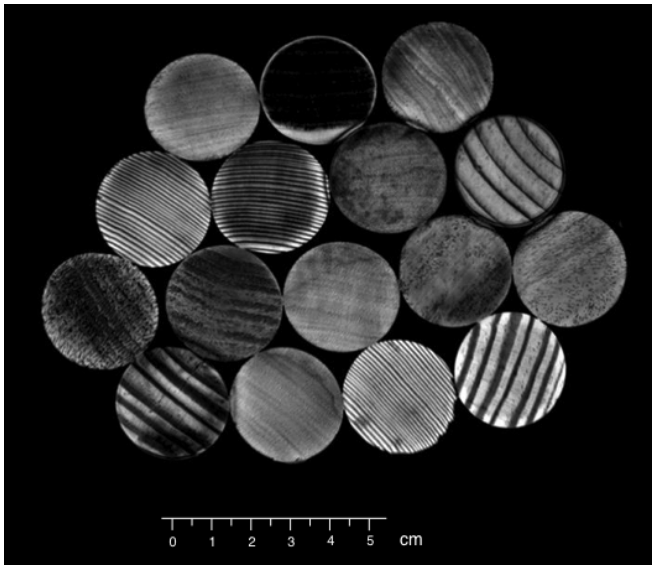

Figure 9b - Contemporary wood samples high-resolution T2-weighted image of the imbibed contemporary wood samples. The in plane resolution was 0.25x0.25 mm2 with a slice thickness of 5 mm. A Gradient Echo acquisition sequence was used with TE = 4 ms, TR = 1000 ms, NS=1 (Longo et al. 2020, in preparation for Wood Science and Technology).

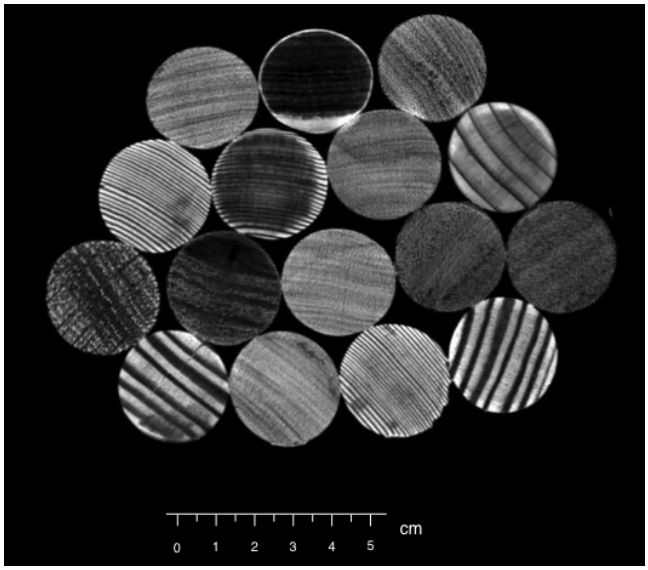

Figure 9c - High-resolution T1-weighted image of the imbibed contemporary wood samples. The in-plane resolution was 0.25x0.25 mm^2 with a slice thickness of 5 mm. An Inversion Recovery acquisition sequence was used with TE=20 ms, IR = 1800 ms and TR = 2000 ms (Longo et al. 2020, in preparation for Wood Science and Technology).

To our knowledge, images in Fig. 10b is the first images of wood samples acquired with an in-plane resolution of 250x250 μm^2, using an NMR clinical scanner. Images definition is high, due to the high signal intensity. To obtain such high-quality images, the bulk water in vessels and tracheid was exploited due to its longer T_2 relaxation (see Table 7) compared to those of bound water in wood parenchyma which is about 1ms or less. This allowed evaluating all the high-definition images of the internal sections of the material without taking or cutting out samples. This characteristic of non-invasively is fundamental for cultural heritage investigations.

Therefore, thanks to the inhomogeneous distribution of water (Hall et Rajanayag 1986), for each species of wood it is easy to distinguish macroscopic identifying aspects such as growth rings, veins, parenchymatic rays, texture, the difference between sapwood and heartwood, possible knots and plant defects, without having to dissect samples.

In the images obtained by this methodology (Fig. 9a, Fig. 9b and Fig. 9c), the annual rings are well marked in Softwood (D, E, G, O, Q, R). In the growth rings the light tones are ascribed to the beginning of the vegetative growth (earlywood), characterized by cellular elements with a broad lumen and thin cell walls to allow better management of nutrients from the roots to the foliage (Giordano 1988). From the scan, it appears that these areas have been filled with free water. A very strong signal, recognizable in NMR images with whiter tones, identifies porous areas in which there is a greater penetration of free water. Instead the dark areas, represent the latewood, characterized by cells with small diameters and thick cell walls, which therefore have a lower water content, which is more closely bound to cell walls.

In the Pines (*Pinus ponderosa)*, samples O and R (in tab.1) are characterized by well distinguishable annual rings, there is a quite abrupt transition between earlywood and latewood. It can be noted that latewood occupies from one-third to one-half of the annual ring. In this species, the resin canals are visible in the latewood portions or around them. From the high-resolution images, it is evident a medium texture typical of all the species of pines, found especially in the image weighed in T_2*.

Figure 10a - Photograph image of the soaked contemporary wood samples before scanning NMR. 10b Image position of the samples within the clinical scanner with corresponding letter in the table of right (Longo et al. 2020, in preparation for Wood Science and Technology).

In the Spruces (*Picea abies*), samples D and Q, we observe that the accretion rings are well evident even if thinner than those of the pines. Furthermore, there is a gradual passage between the early and late zone. By enlarging the image, the rings in some parts are slightly wavy. All these features are perfectly following what is expected for spruce.

In the Silver firs (*Abies alba*), samples E and G, the annual rings are distinct, and the two samples have a variable amplitude, probably due to different growth conditions. This causes a different absorption of water, observable by a darker tone of F. Typical of silver firs is the absence of resin canals and texture that goes from medium to fine.

Furthermore, one of the main characteristics to distinguish hardwood is the arrangement of the pores. There are three main groups based on the size and arrangement of the vases in the annual ring. Ring-porous wood, semi-ring porous wood and diffuse-porous wood (Hoadley 2000). The first one present vessels in earlywood, cells with conduction function, larger than those in latewood. This consist of a well-defined zone in which there is an abrupt transition between earlywood and latewood which is visible. Semi-ring porous wood could present vessels in earlywood larger than the one in latewood or it could not. It presents a gradual transition between earlywood and latewood. The last type, present vessels with the same diameter. This characteristic is typical of tropical and temperate species (Ruffinatto 2015).

In the Sessile Oak (*Quercus petraea*), the sample H, the presence of multiseriate parenchymal rays and the ring-porous, typical of deciduous oaks, could be distinguished. The texture is coarse with the diameter of the vessels in the earlywood of about 300 μm.

In the English Walnut (*Juglans nigra)*, which correspond to sample I, on the other hand, it is possible to recognize a semi-ring porous, with identifiable growth rings in the image weighed in T_2*. This species presents a medium texture.

Some samples such as Sapele (*Entandrophragma cylindricum*) and Australian Red Cedar (*Toona ciliata*), respectively M and N, observed with a greater magnification present, especially in the weighted T_2 * images, a diffuse-porous ring and an indistinct growth ring boundaries. There is a

medium texture, with vessels visible to the naked eye, with a diameter of about 200-300 μm.
In White Poplar (*Populus alba*), sample B, as it happens for the silver fir, the different water absorption in the wood structure causes the darker and the lighter areas. There are annual rings that can be clearly identified in the weighed T_2 images or T_1, their trend is quite regular, and the amplitude is about 2 mm.

On the market, there are species of different origins which, although are not part of the Juglandaceae family, they are usually improperly referred to the common language as "Walnut" (Urso 2014). Examples are the Abura (*Mitragyna ciliata,* A), the Aniegrè (*Aningeria altissima*, F-L), the Limba (*Terminilia superba*, C) and the Dibetou (*Lovoa trichilioides*, P). The texture of these species, belonging to different families, ranges from coarse (C) to medium (F-L and P) or fine (A). The border of the growth rings can be distinct from the images. This type of Harwood could be referred to as diffuse-porous wood species.

Finally, by comparing the different T_2 and T_2* images contrast, it is possible to highlight different details. For example, in the T_2* weighted image, some darker areas and black dots appear in some species (*Mitragyna ciliata, Aningeria altissima, Entandrophragma cylindricum, Toona ciliata, Pinus ponderosa)* (Fig. 9a – 9b). This is due to magnetic field inhomogeneities generated by air pockets confined in the pores, or by paramagnetic substances present in the wood.
T_2 and T_2* maps of relaxation parameters values (Fig. 11) of waterlogged woods were provided. The alteration of the colour on the maps, each with its characteristic tonal scale on the right, allows identifying the alterations of the parameters T_2 and T_2*. Areas with warmer colours include species with longer T_2 and T_2*. On the other hand, samples with colder colours have lower relaxation time values. Interestingly, the water has been differently absorbed within the samples due to the different structures present in the wood. For example, it can be noted that growth rings are distinguishable in the T_2 map.

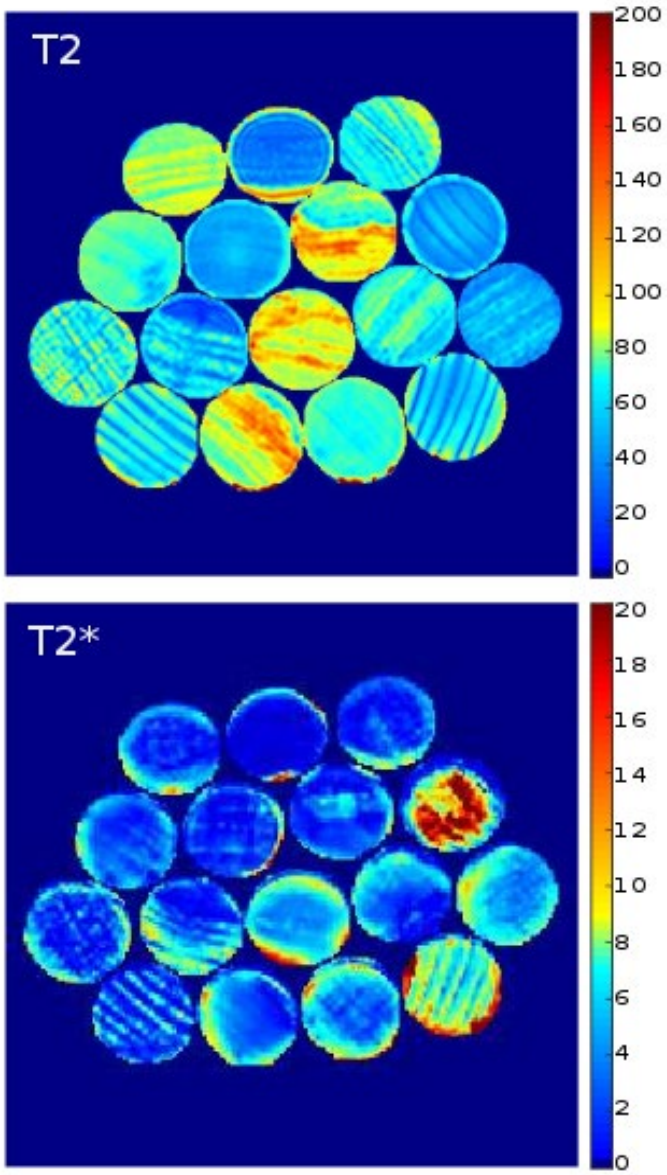

Figure 11 - Contemporary wood samples T_2 and T_2 maps are displayed. Colours of the right bars are proportional to T2 and T2* respectively (Longo et al. 2020, in preparation for Wood Science and Technology).*

In softwood, where the early and latewood areas are distinguished, it is possible to see a difference in relaxation times. In the latewood areas, the T_2 values are lower, and this indicates the presence of smaller vessel diameters (Javed 2014) compared to those of earlywood. Furthermore, from the figure of the proton density, it is possible to notice that in the larger vessels (earlywood) there is a greater concentration of free water. It is reflected in a more intense signal.

At this point, by making a comparison with the values in the relaxation timetable obtained with the ROI (tab 7, 8), it can be noted that the values are slightly different. This discrepancy is because the data in the tables refer to averages over several slices. In the lower part of the figure, the proton density is shown, where the signal is more intense in the zones with a higher concentration of protons or hydrogen atoms. That indicates the presence of water.

The values reported in tables (Tab n. 7,8,9) are obtained by averaging the relaxation values in different slices taken into consideration. Table n. 7 shows the average T_2 values of completely and partially soaked woods. Table n. 8 reports the values of the T_2 * of the dry and imbibed samples. For the imbibed samples, a further subdivision between fully and partially soaked was carried out. Table 4 shows the relaxation values T_1 obtained for the imbibed woods.

We conclude that under the same conditions of imbibition, the lowest values were found for T_2*. These values are included in a range from a minimum of about 2 ms for wood B up to a maximum of about 25 ms for wood S. Larger values were recorded for T_2 times, ranging from a minimum of 10,7 ms for wood B to a maximum of 51,5 ms for sample D. According to Araujo et al. (1993) these values are compatible with T_2 signals arising from lumen water. Finally, the highest values were obtained for the relaxation time T_1. The last parameter varies from a minimum of 81.6 ms for the sample G up to about 577 ms for the sample M. Concerning the dry samples, the values of T_2* are about one order of magnitude smaller than the corresponding ones wet and range from a minimum of 0,307 ms (wood R) to a maximum of 0,741 ms (wood M). Probably these values are due to the cell-wall water signal.

Table 7 - Contemporary wood samples average values of T_2 in ms with respective errors. The values with the star refer to samples that are partly soaked. The order of magnitude of the obtained values is some tens of milliseconds and vary from species to species (Longo et al. 2020, in preparation for Wood Science and Technology).

	T_2 (ms)	
Wood specimen		
	Mean	**SD**
A	37,33▪	± 0,18
B	10,70 *	± 0,14
C	32,8*	± 1,1
D	51,5*	± 1,9
E	36,82*	± 0,98
F	47,51▪	± 0,32
G	37,96*	± 0,64
H	35,9 ▪	± 1,3
I	35,608▪	± 0,066
L	45,62▪	± 0,23
M	34,84▪	± 0,17
N	34,39▪	± 0,22
O	46,0▪	± 1,2
P	47,77▪	± 0,59
Q	49,4*	± 2,7
R	43,04▪	± 0,94

▪ 100% soaked.
* partly soaked specimens.

*Table 8 - Contemporary wood samples average values of T_2 * in ms with respective errors. A distinction has been made between the wet woods and the dry woods. The wet ones are further subdivided into wholly imbibed samples and samples that have not homogeneously absorbed the water. The latter is distinguished by a star. The values obtained for dry woods are always lower than a millisecond, while for wet woods they range from a few ms to a maximum of 25 ms. On average, the values for partially soaked wet samples are lower than those completely soaked (Longo et al. 2020, in preparation for Wood Science and Technology).*

	T_2* (ms)			
Wood specimen	**Waterlogged**		**Environmental humidity**	
	Value	**SD**	**Value**	**SD**
A	11,87▪	± 0,30		
B	2,085*	± 0,046		
C	5,47*	± 0,21	0,337	±0,063
D	10,3*	± 1,0	0,422	±0,069
E	4,90*	± 0,11		
F	6,49▪	± 0,11		
G	5,831*	± 0,054	0,402	±0,022
H	5,957▪	± 0,040	0,580	±0,012
I	9,01▪	± 0,13		
L	10,78▪	± 0,26		
M	12,84▪	± 0,50	0,741	±0,004
N	11,38▪	± 0,43	0,474	±0,004
O	12,03▪	± 0,20		
P	8,47▪	± 0,20	0,553	±0,027
Q	5,80 *	± 0,28	0,716	±0,034
R	25,43▪	± 0,19	0,307	±0,054

▪ 100% soaked.

* partly soaked specimens.

Table 9 - Contemporary wood samples average values of T_1 in ms with respective errors. These values are of the order of hundreds of ms and vary from a minimum of 81 up to a maximum of about 580 ms. In one case it was not possible to get a fit (Longo et al. 2020, in preparation for Wood Science and Technology).

	T_1 (ms)	
Species		
	Value	**Error**
A	264,62	± 4,88
B	-	-
C	287,26	± 6,33
D	338,46	± 20,00
E	85,02	± 1,51
F	324,29	± 5,04
G	81,58	± 0,20
H	519,16	± 3,19
I	466,36	± 4,18
L	312,62	± 5,21
M	577,43	± 3,57
N	445,79	± 4,00
O	82,30	± 1,04
P	366,83	± 5,63
Q	319,97	± 9,59
R	82,95	± 0,75

Furthermore, in Table n. 10 are shown the density values calculated by gravimetric method for each species of wood. The density values agree with those present in the literature (Urso, Piva, Crivellaro 2014).

Table 10 - Contemporary wood samples density in Kg/m³ calculated for each species of wood (Longo et al. 2020, in preparation for Wood Science and Technology).

Sample	density
A	530 ± 40
B	480 ± 40
C	480 ± 40
D	540 ± 40
E	350 ± 40
F	560 ± 40
G	350 ± 30
H	630 ± 50
I	680 ± 50
L	520 ± 40
M	550 ± 40
N	520 ± 40
O	510 ± 40
P	550 ± 40
Q	520 ± 40
R	530 ± 40

In Fig. 12 is shown the correlation graph between the values of dry T_2 * and the density. A weak correlation seems to emerge (r = 0,38) from the analysis, but since the p value is greater than 5% (p = 0,39), it is assumed that the correlation is not statistically significant. Also, graphically the experimental points are on average too far from the theoretical value. The proton density depends on the water content in the wood and is not directly related to its density. However, density is influenced by the content of empty spaces in the wood and this may be related to its ability to absorb water.

For this reason, the correlation between the proton density and the density of the woods has been studied. No correlation was identified from the tests

performed. In figure n. 13, the correlation graph is shown between the values of wet T_1 and the density.

The correlation this time is higher as underlined by Pearson's coefficient (r = 0,60). Il *p* value is lower than the 5% threshold and therefore, it is concluded that there is a significant correlation. The correlation shown in Figure 6 is positive, i.e. with increasing density, the parameter T_1 also increases.

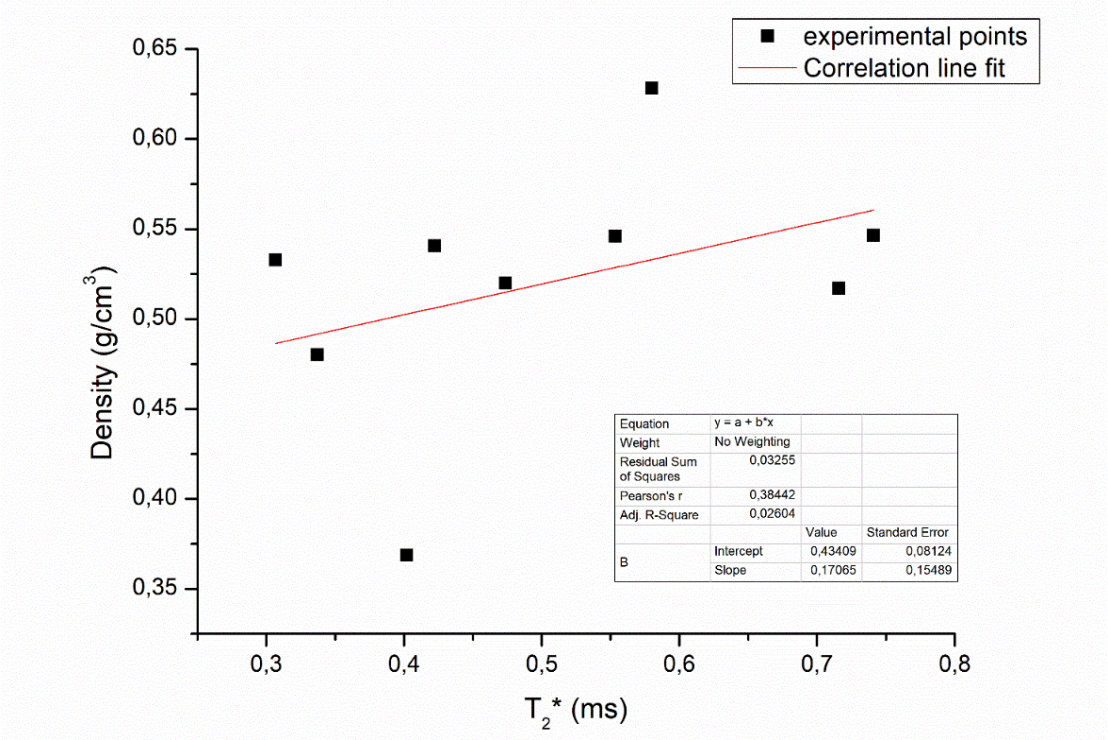

*Figure 12 - The figure shows the correlation between the contemporary wood samples density (on the y-axis) and the parameter T_2 * (on the x-axis) (Longo et al. 2020, in preparation for Wood Science and Technology).*

From the analysis of the images and of the parameters, it is possible to obtain information on the species, moisture content, on the porosity and the density of the material. Furthermore, in this work, a small database has been created with the values of the relaxation parameters for the analyzed species. It can be implemented and improved with future studies.

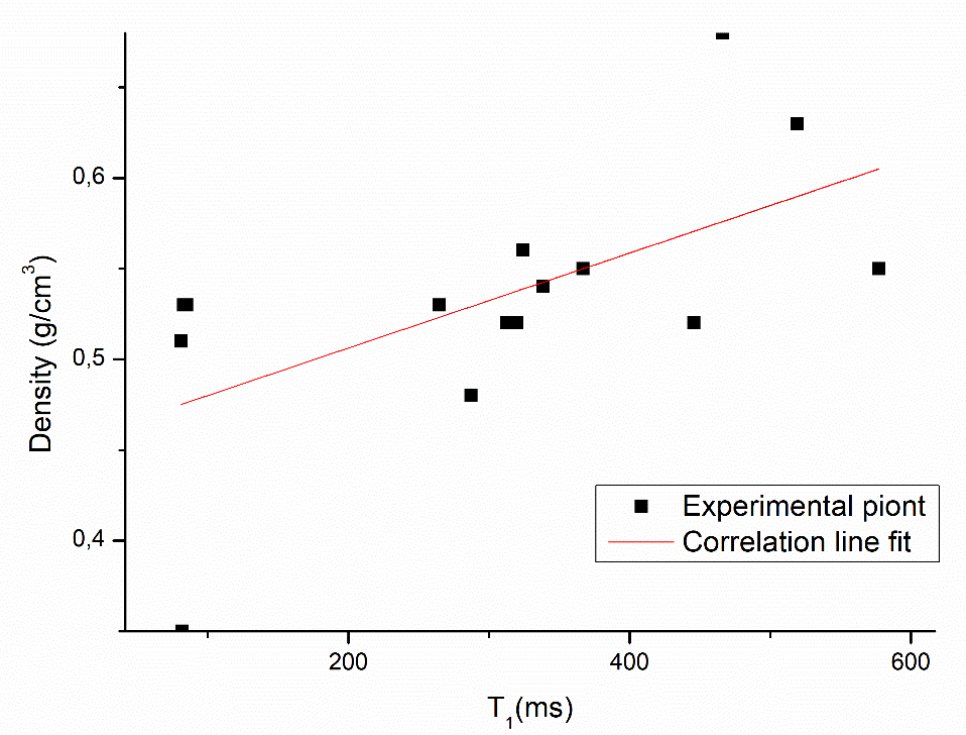

Figure 13 - The figure shows the correlation between the contemporary wood samples density (on the y-axis) and the parameter T_1 (on the x-axis) (Longo et al. 2020, in preparation for Wood Science and Technology).

5.2.2 MRI clinical scanner results on archaeological waterlogged samples

Samples

Waterlogged archaeological wood from the Roman port of fifth century AC, found in piazza Municipio Naples (Italy) was investigated. It has a diameter of 8.7 cm and it is Ash tree.

MRI experimental parameters and results

MRI protocol descripted in the above paragraph was applied to obtain an image from an archaeological wood sample (Fig. 14).

The following acquisition sequences were used for the archaeological waterlogged wood: T_1-weighted (T_1-w) images, an Inversion Recovery Turbo Spin Echo sequence was used with a 0,25x0,25 mm^2 plane resolution, a STK= 1,5 mm, MTX =1024x1024 mm^2 and FOV= 240 x 240 mm^2, TE = 5.5 ms, TR= 25 ms, Inversion recovery (IR) = 8 ms, TR = 112 ms.

Multi-echo sequence was used, with 0,90 x 0,90 mm^2 plane resolution, a STK=1 mm, MTX =320x320 mm^2 and FOV =230x230 mm^2. TE = 20 ms (20 echos at 3, 9, 15, 21, 27, 33, 39, 45, 51, 57 ms), TR = 500 ms, the numer of slices is 106.

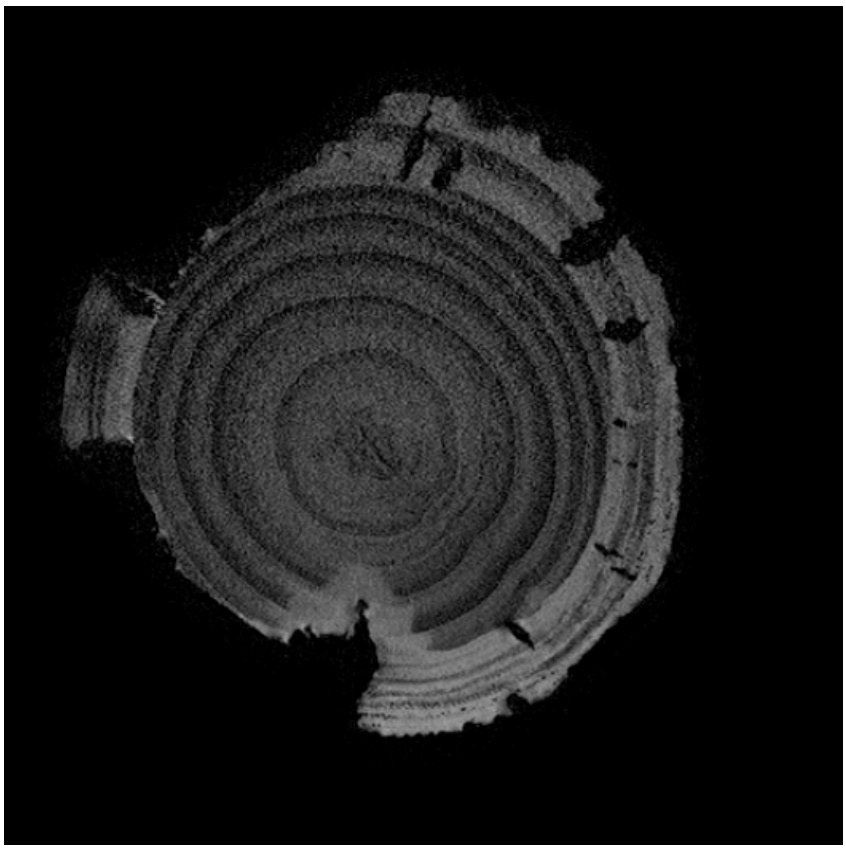

Figure 14 - T1-weighted images of archaeological waterlogged wood. Inversion Recovery Turbo Spin Echo sequence was used with a 0,25x0,25 mm^2 plane resolution with a slice thickness of 1,5 mm. TE = 5.5 ms, TR= 25 ms, Inversion recovery (IR) = 8 ms, TR = 112 ms (Longo et al. 2020, in preparation for Wood Science and Technology).

In fig. 14 it is possible to distinguish growth rings: lighter areas represent earlywood; darker areas show latewood. This agrees with the typically known characteristic of wood. Compared to springwood, latewood has more mass volume and strength as well as higher values of the parameters related to shrinkage and swelling (Berti 2003). Indeed, earlywood ensures the rapid transport of the sap at the beginning of the vegetative season, while latewood formed in the summer is mainly due to support task.

We are probably dealing with a diffuse-porous (or semi-ring-porous) broad-leaf wood. Rays are not visible, so the rays are probably uniseriate or 2-3 seriate (IAWA 1989), and there are probably no aggregate rays. The layout of the pores in the transversal section cannot be determined. These few observations are not enough to point us in the direction of identifying the genus. However, anatomically it is possible to see some macro-characteristics, such as the general shape of the pith (star form with five points) that could be useful to extract information from this archaeological wood. This might allow the list of possible genera to be reduced considerably.

If we should be able to narrow down the identification, a much higher resolution of the radial and tangential sections would be needed, examine perforation plates and ray thickness.

A color difference between the wood of the core of the object and the outer c. two rings might show us that the wood has sapwood, but this might also be an indication of differential preservation of the object. Wide rings can be distinguished.

On the overall, results reported in this section demonstrate that MRI method could be successfully suitable for ancient wood investigations. It could be the most important non-invasive analysis for waterlogged wood and not only. In fact, submarine archaeological wood is a difficult material to investigate and MRI analysis could help in this field. By this method, in fact, it is possible to characterize the species of wood by macroscopic details identification, understand construction methods and, at the same time, obtain information on moisture content, porosity and density, principal clue elements of conservation status. It could also be a valid alternative to X-Ray Computed Tomography investigations or a valid complementary analysis (Longo 2019). Furthermore, the possibility of

processing 3D images cannot be excluded. At the same time, it could be useful to dendrochronological analysis. Taking advice from DendroCT (Bill 2012, Daly 2017), it could be valid totally non-invasive analysis for dating waterlogged wood.

5.2.3 µNMR results on contemporary samples

Samples preparation

Magnetic resonance microimaging (µMRI) analyses on a sample of silver fir (*Abies alba*) of 2x0,5 cm was carried out.

µNMR experimental parameters and results

A 9.4T magnetic field Bruker Avance spectrometer with a microimaging probe was used. T2-weighted acquisition was performed with a 16x16 μm^2 in-plane resolution and 0.2 mm slice thickness (STK), number of averages (NS) =128, matrix size (MTX)=512x512 and Field Of View (FOV) =0.8x0.8 mm2, Repetition Time (TR) =1000 ms.

To evaluate T2, T2-weighted images, using the same parameters but choosing MTX=256X256, were obtained with echo times (TEs)= 6, 12, 18, 24 ,30 ms. For T1 evaluation, saturation recovery acquisitions at different TR: 300, 450, 700, 1000, 2000 ms were carried out (STK=0.2 mm, NS=64, MTX=256x256, FOV =0.8x0.8 mm2, in plane resolution 32x32 μm^2, TE=3ms).

To evaluate global water diffusion coefficient D, a Pulse gradient stimulated echo (PGSTE) was used with TR=3s, NS=64, 32 gradient strength values (g) from 2.5 to 121 Gauss/cm, gradient pulse duration δ=3ms, diffusion time Δ=80ms.

An inversion recovery with TR=6s and 30 inversion times from t=1ms to t=4000ms was used to obtain detailed T1 values, whereas a Carr Purcell Meiboom Gill (CPMG) with TEs=n*0.5ms (n=1 to 128) and TR=6s was used for extracting T2 values belongings to different water pools (Alesiani 2004, Pirazzoli 2005).

Three different regions of interest (ROIs) (see Fig. 15) were chosen in T_2 and T_1 weighted images being interested to investigate wood features related to a different amount of water. Specifically, T_1 and T_2 were evaluated in each

late-wood (dark pixels), early-wood (light pixels) ROI and in the whole sample.

From imaging data, the recovery of the equilibrium magnetization (M0) along the direction of the static field was fitted to a single exponential function of the form:

$$M(TR) = M0[1-\exp(-TR/T_1)] \quad (1)$$

so, obtaining the corresponding relaxation time T_1. To obtain T_2, the signal intensity versus TE was fitted using the function:

$$M(TE)=M0*\exp(-TE/T_2) +c \quad (2)$$

On the other hand, considering the global signal (no-imaging modality) T_1 and T_2 were obtained by using bi-exponential fitting functions (Alesiani 2005):

$$M(t) = M0_1[1-2*\exp(-t/T_{11})] + M0_2[1-2*\exp(-t/T_{12})] \quad (3)$$

and

$$M(TE)=M0_1*\exp(-TE/T_{21}) +M0_2*\exp(-TE/T_{22}) \quad (4)$$

respectively.

Finally, diffusion coefficients D_1, D_2 and D_3 characterizing the diffusion of bulk water, restricted water and cellulose hydration water, were obtained by fitting PGSTE data with the function:

$$S(g)= \Psi_1*[\exp(-(\gamma g\delta)^2(\Delta-\delta/3)D_1]+ \Psi_2*[\exp(-(\gamma g\delta)^2(\Delta-\delta/3)D_2]+ \Psi_3*[\exp(-(\gamma g\delta)^2(\Delta-\delta/3)D_3] \quad (5)$$

where Ψ_1, Ψ_2 and Ψ_3 are proportional to the water molecules content in each pool.

In Fig. 15 micro-MRI cross-section images of the sample, *Abies alba,* is shown. The homoxyle structure, typical of coniferous wood, is visible. Early and latewood are clearly distinguishable: latewood and earlywood correspond to dark and light pixels, respectively, while the transition between them is abrupt. Moreover, few resin canals with a diameter of about 0.25 mm are also visible. Generally, there is no presence of resin canals in silver fir; thus, we think that they refer to traumatic resin canals (Nardi berti 2006). All these observations agree with guidelines from dichotomous keys, commonly used by wood experts as reference for the microscopic identification of the wood species (www.woodanatomy.ch).

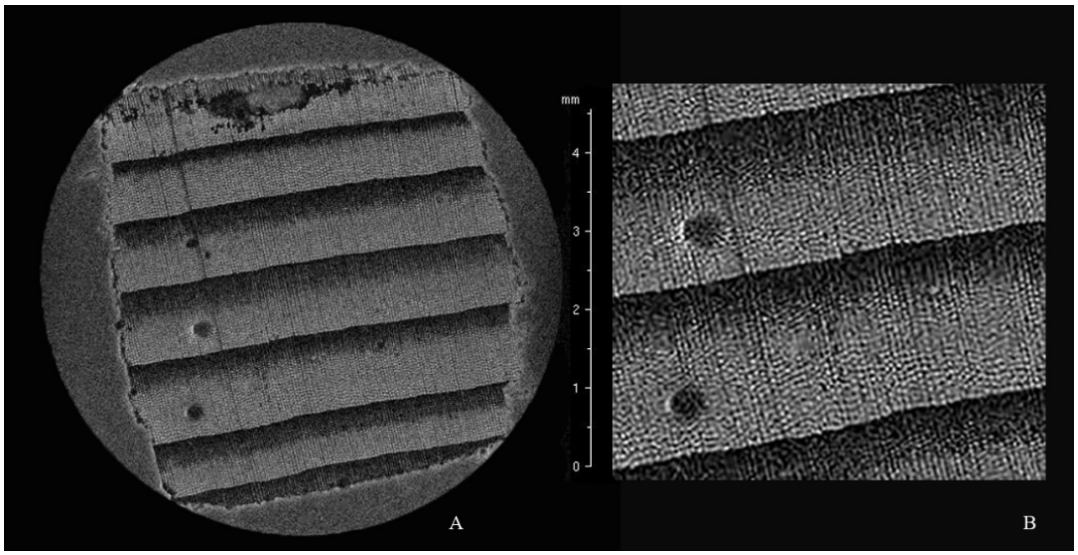

Figure 15 - Abies alba cross-section T_2-weighted micro-MRI obtained at 9.4T magnetic field. In plane resolution was 32x32 μm^2 (Longo et al. 2020, IOP Conference Series: Materials Science and Engineering, Open Access).

Fig. 16 (upper image) displays T_1-weighted image and the signal intensity as a function of the repetition time (TR), in the two different ROIs (dark and light pixels regions) corresponding to latewood and earlywood and in an extended ROI including a mean area of the sample. From T_1 imaging data, we find T_1=(476±42ms) and T_1=(261±57ms) for the light and dark region, respectively. The value in the extended ROI gives rise to the average T_1=(411±44ms).

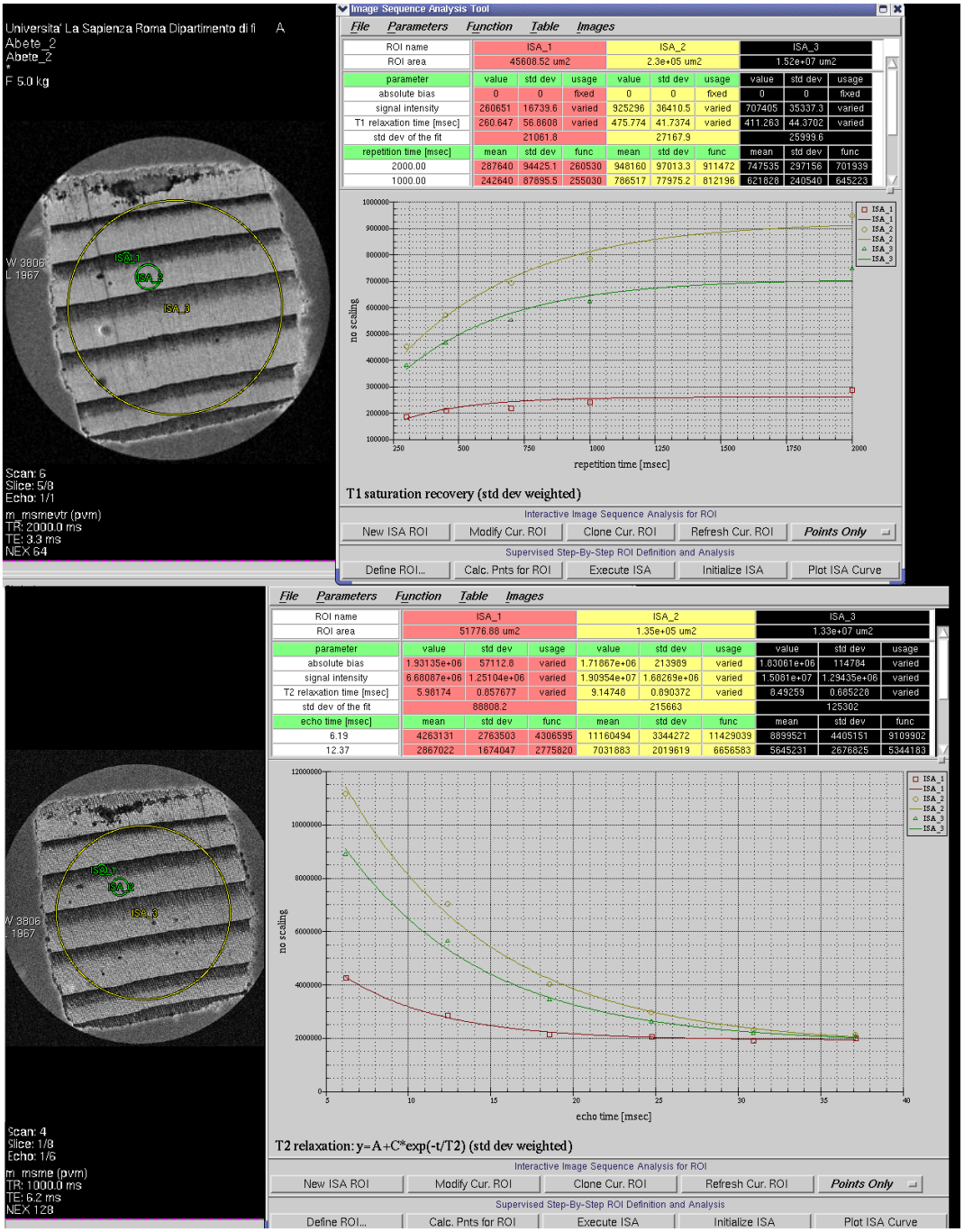

Figure 16 - Abies alba cross-section T_1-weighted (upper image) and T_2-weighted (lower image) together with T_1 data recovery and T_2 signal decay used to extract T_1 and T_2 values, respectively. Data analysis was performed in dark and lighter pixels regions using Eq. 1 and 2 (Longo et al. 2020, IOP Conference Series: Materials Science and Engineering, Open Access).

Fig. 16 - (lower image) displays T_2-weighted image and the signal intensity as a function of the echo time (TE), in the two different ROIs (dark and light pixels regions) corresponding to latewood and earlywood. Note that, from T_2 imaging data, we find T_2=(9.2±0.9ms) and T_2=(6.0±0.2ms) for the white and black region, respectively. Moreover, in the mean ROI, we obtain T_2=(8.5±0.7ms).

However, since the value of 6 ms coincides with the lowest TE, we have performed a more detailed investigation (see the details of CPMG pulse sequence reported in the Material and Method section) on the global sample and, using Eq. 4, we obtain T_{21}=(17.0±0.8ms) and T_{22}= (2.7±0.2ms) in agreement with the results reported in references (Gezici-Koc 2017). Conversely, the quantification of the longitudinal relaxation times, performed using Eq. 3, gives us a single value of T_1 equal to (440±54) ms.

All the obtained values reflect the state of water in the considered regions and, therefore, characterize the system under study in its specific conditions. Known the wood structure alterations induced by water, different actions could be taken to preserve it.

Figure 17 shows the signal decay, obtained using a PGSTE sequence, as a function of the gradient strength g and the best fitting function. Three different contributions, belonging to three different mobile water molecules, have been discriminated. In particular, the biggest value of the diffusion coefficient D_1 = (1.881+-0.013)*10^{-9} m^2/s belongs to bulk water (we remember that the sample is immersed in liquid water), that is the water inside vessels.

D_2 = (2.140+-0.120) *10^{-10} m^2/s belongs to water at the fibres interface of the wood sample and inside the cells. Finally, D_3 = (1.30+-0.10)*10^{-11} m^2/s belongs to tightly bound water molecules, strongly confined (pore on the order of nm) or bonded to hydroxyl groups of cellulose and lignin and that remain also on drying. The normalized water population Ψ associated with estimated diffusion coefficients are: 96.4%, 3.1% and 0.5% of the total magnetization. Therefore, the 96.4% of the total observable water protons in sample belongs to bulk water, i.e. water in vessels, the 3.1% belongs to intracellular water and the 0.5% to water inside Silver Fir, as hydration water of cellulose and lignin.

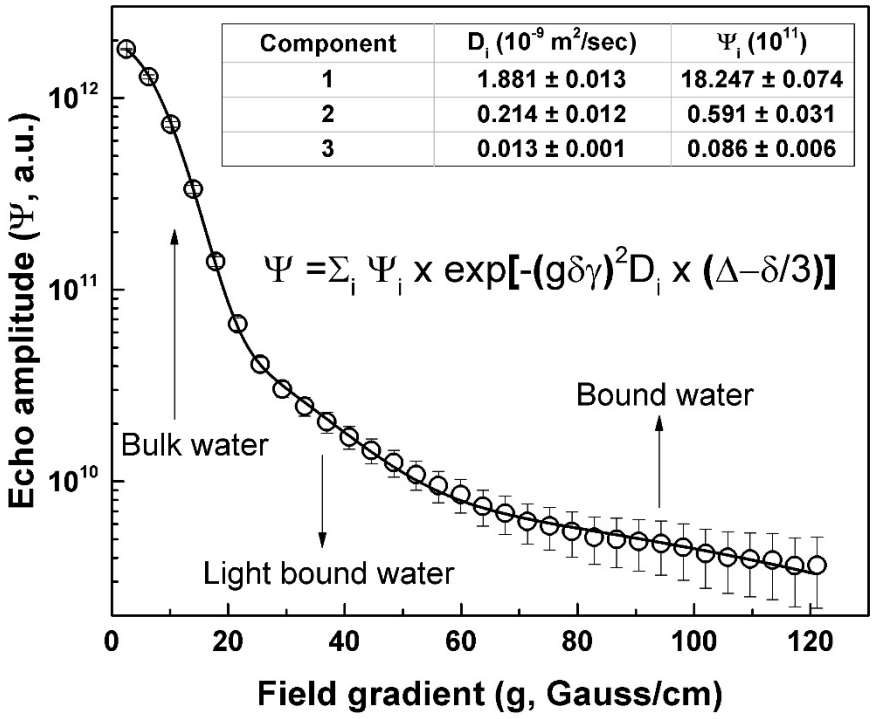

Figure 17 - The decay of the echo amplitude, evaluated by means of PGSTE pulse sequence, as a function of the gradient strength g (γ= 42.58 MHz/ T is the proton gyromagnetic ratio). Three exponential contributions have been identified and ascribed to bulk water, light bound water between fibres and bound water inside fibres (or cellulose hydration water) (Longo et al. 2020, IOP Conference Series: Materials Science and Engineering, Open Access).

In terms of degradation, wood pore size distribution is a key parameter in water accumulation. As shown above, diffusion NMR techniques may provide an indication on separate wood-bound water, restricted light bound water, and confined water in vessels (bulk water) fractions by measuring diffusion NMR parameters together with relaxation times T_1, T_2 estimation.

5.2.4 μNMR results on archaeological waterlogged samples

Samples

Archaeological wood extracted from a pole belonging to the old Roman port of Naples (5th century AD) that was found during the underground excavations at Piazza Municipio (Naples, Italy).

μNMR experimental parameters and results

Micro-magnetic resonance imaging investigations were performed using a Bruker Avance- 400 spectrometer operating at 9.4 T with a 10 mm micro-imaging probe equipped with high performance and high strength magnetic field gradient unit characterized by a maximum gradient strength of 1200 mT/m and a rise time of 100 μs. ParaVision® 3.2 software was employed for data acquisition and image processing.

A multi-slice multi-echo (MSME) sequence with minimum echo time (TE) of 2.1 ms, repetition times (TR) equal to 350 ms and 64 signal averages (NSA) was used to obtain T1- weighted images. Six slices of 400 μm in thickness (STK) were selected, field of view (FOV) was 0.70 cm, imaging matrix (MTX) equal to 256x256, or 512x512 voxels.

MSME with TR=1 s and different TE was used to obtain T2-weighted images at about 20x20 μm2 in plane resolution were acquired with acquisition parameters optimized for each wood species.

A gradient echo fast imaging (GEFI) sequence with TR=1 s, TE=4 ms, STK=300 □m, FOV=0.9 cm, matrix=512x512 voxels, NS=128 was adopted to achieve axial T2*-weighted images and with the same parameters but with TR=1.5 s and TE=5 ms to obtain radial and tangential view T2*-weighted images. Moreover, to improve image resolution, acquisition matrices of 1024x1024 voxels were also used by selecting TE=6 ms.

An imaging Pulse Gradient Stimulated Echo (PGSTE) sequence was used to investigate water diffusion in wood samples. The sequence parameters were TR=1.5 s, TE= 14.8 ms, matrix 256x256 voxels, FOV=0.8cm, diffusion gradient pulse duration δ=3 ms, diffusion time Δ=80 ms. The diffusion gradient was used both in z and x-direction, i.e. along and perpendicular

to the long axis of wooden vessels/tracheids, respectively. The effective b-values were approximately equal to: 260, 960, 1260, 2060 s/mm2.
By observing and comparing the two images in Fig. 18, it is possible to discriminate microstructures characterized by different T1 and T2 contrasts that provide valuable information about the dynamics and surroundings of the microstructures. Indeed, the different single parameter image gives a better insight into the morphology of wood anatomy. It is immediately possible to conclude that the unknown archaeological wood specimen is a softwood species. Indeed, according to Kekkonen et al. results (Kekkonen 2010) the softwood is characterized by higher and lower signal intensity zones in T1 and T2 –weighted images, representing earlywood and latewood areas, respectively. Image contrast is due to lower T2 values associated with smaller pores (cross-sectional areas of tracheids) in latewood and higher T2 values associated with larger pores in earlywood.

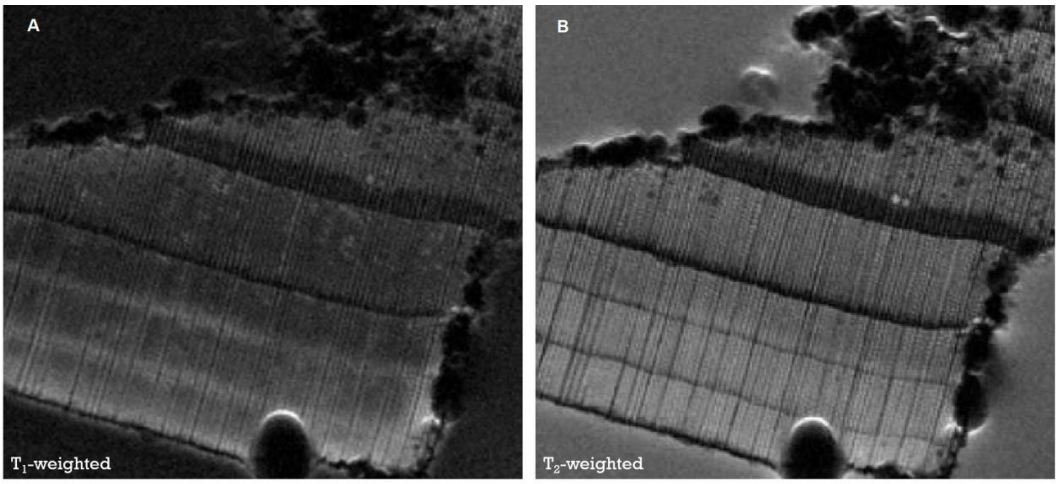

Figure 18 - Transversal-view MRI of an archaeological waterlogged wood specimen (from an ancient port in Naples of the 5th century AD): T1-weighted image with TE=2 ms and TR=350 ms (left) and T2-weighted image with TR=1000 ms and TE=6 ms (right). The images are characteristic of softwood species. Indeed, it is possible to detect the typical alternation of lighter and darker bands that corresponds to the alternation of earlywood and latewood (Capuani et al. 2020, Magnetic Resonance in Chemistry with permissions).

The images also show the presence of artifacts due to air bubbles and/or

the presence of paramagnetic agents. As expected, such artifacts are amplified in the T2*-weighted images of the same archaeological wood specimen shown in Fig. 19. Here, images with an in-plane resolution of 18x18 μm2 and 300 μm of slice thickness and obtained along the three principal anatomical planes of wood are displayed. Different kinds of microstructure are recognizable and highlighted with arrows of different colors in the images (see Fig. 19). The unknown archaeological wood has also resin channels (see the zoomed image in Fig. 19b) that appear as large (larger than the cross-section of tracheids) white circles surrounded by a thin darker ring due to parenchyma cells that delimit the resin canal (red arrows in Fig. 19a). In Fig. 19c) unicellular rays comprised of a few cells and with resin canal (red arrow) are also observable.

Not all the softwoods have large resin canals in the tangential section, therefore this observable microstructure is a potential identification key to identify the wood species of the archaeological wood sample. Even the identification of the number of cells in rays is a potential identification key to recognize a wood species. However, the impossibility to distinguish, by current MRI, the type of cells (another key anatomical feature) composing rays has to be pointed out. Parallel to the great potential of MRI for the non-invasive investigation of waterlogged wood, the limits of the technique are principally related to the insufficient MRI resolution compared to the optical one when the wood radial section is examined. In this work (Fig. 19c) the diagnostic features of wood, such as the walls and pits of cross-fields and the presence of radial tracheids, are not visible due to their small size (lower than 10 μm) and the specific image-contrast selected. However, the linear NMR image resolution below 10 μm is not a physics limit, but it is due to the specific hardware and software of the spectrometer. Since the resolution of an NMR image depends on the magnetic field gradients strength, in principle it is possible, using higher gradients strength than those used in this work, to obtain images with a resolution around the micrometre. However, a good signal to noise ratio (SNR) of the image must be ensured, which decreases with increasing resolution. To increase the SNR, it is possible to increase the number of signal averages, or to increase the static magnetic field strength.

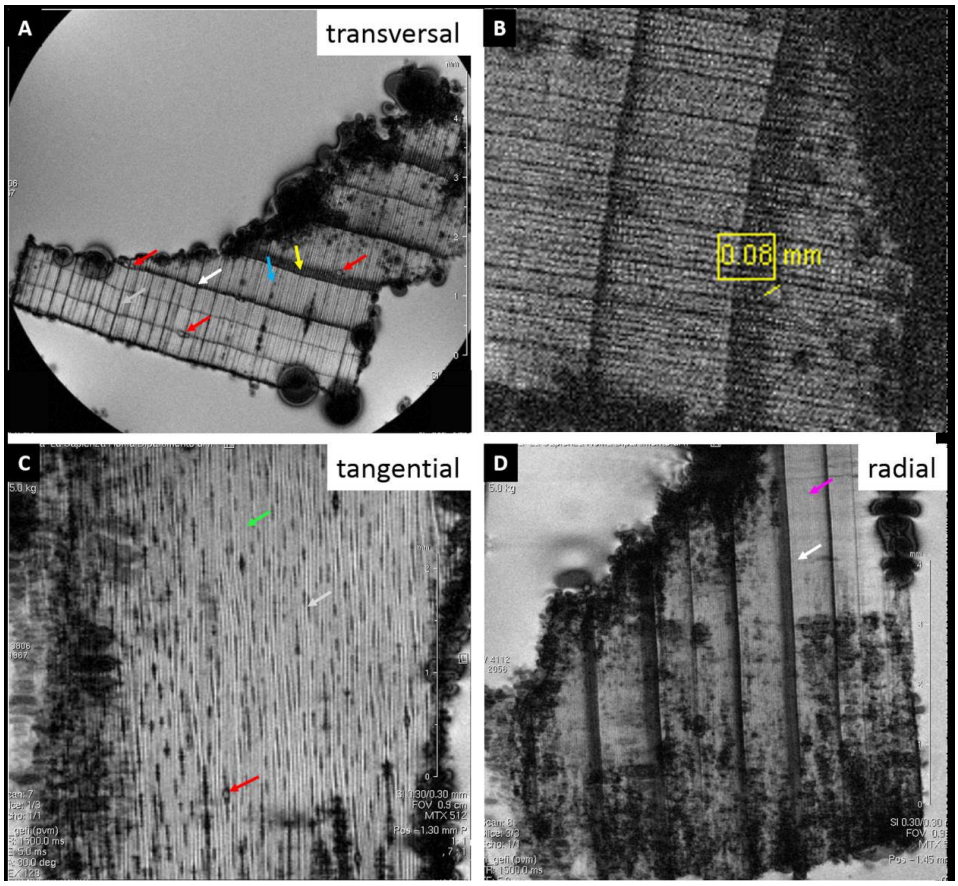

Figure 19 - Transversal a), tangential c), and radial d) –view T2-weighted images of an archaeological waterlogged wood specimen (from an ancient port in Naples of the 5th century AD). Different kinds of microstructures are recognizable. In Fig. 19a): earlywood (blue arrow), latewood (yellow arrow), resin canals (red arrows), annual ring limit (white arrow), and ray (grey arrow). In Fig. 19b) a zoomed portion of the image shown in Fig. 19a) is displayed with the measured diameter of the resin canal around 0.08 mm. In Fig. 19c): tangential resin canal (red arrow), the tangential section of tracheids, fibers and axial parenchyma of wood (green arrow), and the rays that seem unicellular i.e. composed by a single line of cells (grey arrow). Fig. 19d): annual ring limit (white arrow), the radial section of tracheids, fibers and parenchyma (pink arrow) (Capuani et al. 2020, Magnetic Resonance in Chemistry with permissions).*

In conclusion, this work suggests that high-resolution multiparametric MRI may be a useful tool to obtain physiological and microstructural information from both full waters imbibed wood samples and waterlogged archaeological wood remains in a completely non-invasive and non-destructive approach. This is particularly important especially when the mechanical sectioning necessary for the optical investigation is not easy to perform due to the fragility and decay of the wood remains. In this case, virtual histology can be a valid alternative to optical microscopy. The major limit to the development of dendrology performed using 3D virtual histology based on MRI concerns the size of the image voxel, still too large compared to fundamental microstructures for the discrimination of similar types of wood. However, this is a limit related to the instrument, it is not a physical limit. Therefore, it would be desirable to further develop the hardware and functional characteristics of MRI scanners to improve their potential application in the field of wooden cultural heritage.

5.3 FTIR, Raman/SERS and SEM-EDX

5.3.1 FTIR and Raman/SERS results on contemporary samples

Samples

Silver fir (*Abies alba*), acacia (*Robinia pseudoacacia*) and cedar (*Cedrus libani*) wood samples were analysed by FTIR and micro-Raman spectroscopies.

Experimental parameters and results

FTIR measures were carried out by a Perkin-Elmer apparatus (mod. Spectrum 100), working in ATR configuration. FTIR spectra were collected in a few minutes in the 800-4000 cm^{-1} spectral range, and the resulting

spectra are the average of ten acquisition. Moreover, micro-Raman measurements were carried out on wood samples using the Horiba XploRA micro-Raman apparatus with an exciting wavelength of 532 nm from a diode laser focused onto the sample surface through an Olympus BX40 microscope equipped with a 50X FL objective. The latter was also used to collect the backscattered radiation that was analyzed by a Jobin-Yvon monochromator and sent to a cooled charge-coupled (CCD) device detector. The same apparatus was used to perform Surface-Enhanced Raman scattering-(SERS) measurements.

Raman signal enhancements in the presence of metallic nanoparticles (namely Surface-Enhanced Raman scattering-(SERS) effect) are related to chemical and electromagnetic mechanisms. The electromagnetic mechanism, believed by most to be the dominant contribution, is related to the collective oscillation of the conduction electrons in noble metals that creates a localized surface plasmon resonance (LSPR) induced by the incident laser light. The Raman signal of Raman active molecules in the vicinity of such LSPR is greatly enhanced. All these phenomena endow SERS with extreme sensitivity. We adopt this approach to overcome Raman limitations. Colloidal solutions of gold (Au)- silver (Ag) were prepared by pulsed laser ablation of a (50/50) silver/gold target immersed in distilled water. The second harmonic (532 nm) of a neodymium-doped yttrium aluminium garnet (Nd: YAG) laser operating at 10 Hz repetition rate with a pulse width of 5 ns irradiated the target at the laser pulse energy of 50 mJ and for an ablation time of 20 min. The colloids were transferred on wood by a simple drop-casting method and then dried in air at room temperature before Raman measurements.

Micro-Raman maps were acquired to collect a sufficient number of spectra to perform a significative statistical analysis. So, Raman spectra were collected over a 20 µm × 30 µm area of each sample and the points were spaced at 4 µm along the x and y directions. After mapping a samples area of interest, Raman images were calculated by integration over bands assigned to, e.g. lignin or cellulose or on the entire spectral region (following fluorescence signal) to visualize the distribution of the wood cell wall.

To improve PCA analysis, all SERS spectra were previously subjected to some data treatment. First, Raman spectra showing some sharp spikes which are not related to the sample were excluded from the statistical analysis. For all other spectra, a continuous baseline correction was performed, then normalized to their area and slightly smoothed using the Savitzky–Golay smoothing-derivative procedure. The resulting spectra were loaded into rows of a matrix, which was used as input for principal component analysis (PCA) and hierarchical clusters analysis (HCA) procedures.

Fig. 20 shows the FTIR spectra in the three main spectral regions where the cellulose, lignin, and H-stretching contributions are located (Giordano 1981). The spectral transmission profiles of the three samples differ significantly in intensity, which indicated that the internal composition of these samples was almost identical, but there were differences in the specific content. From a simple inspection of the spectra, one can note that the spectral band in the cellulose region is more intense and structured for silver fir and cedar with respect to acacia. In particular, being the most intense band at about 1024 cm^{-1} assigned to the C-O stretching in primary alcohols in cellulose, the data reveal that the cellulose content is lower in the acacia sample. Instead, the acacia sample, having a most intense band at about 1735 cm^{-1} (middle part of Fig.20), assigned to the C=O stretching of carboxylic acid in hemicelluloses ester group, has a higher hemicellulose content (Jiangtao 2012). Concerning the right panel of Fig. 20, there are no marked differences in the OH stretching region, suggesting that the samples were exposed to, and indeed contain, the same level of humidity (Kubosky 2020). To perform a precise and quantitative spectral analysis, we executed a Gaussian deconvolution of the main bands that allows achieving the internal composition and other important information. According to literature data (Tamburini 2017, Gupta 2015) the band in the 3200 and 3650 cm^{-1} range is ascribed to the –OH-stretching vibrations, those centred in the 2500- 3200 cm^{-1} is mainly due to C-H stretching vibration while CO_2 features, not fully deducted from the background of the air, are located in the 2000– 2500 cm^{-1} range (Li 2018). The double peak at 3000–2800 cm^{-1} is generally assigned to C-H stretching vibrations from impregnated wood (Müller 2009).

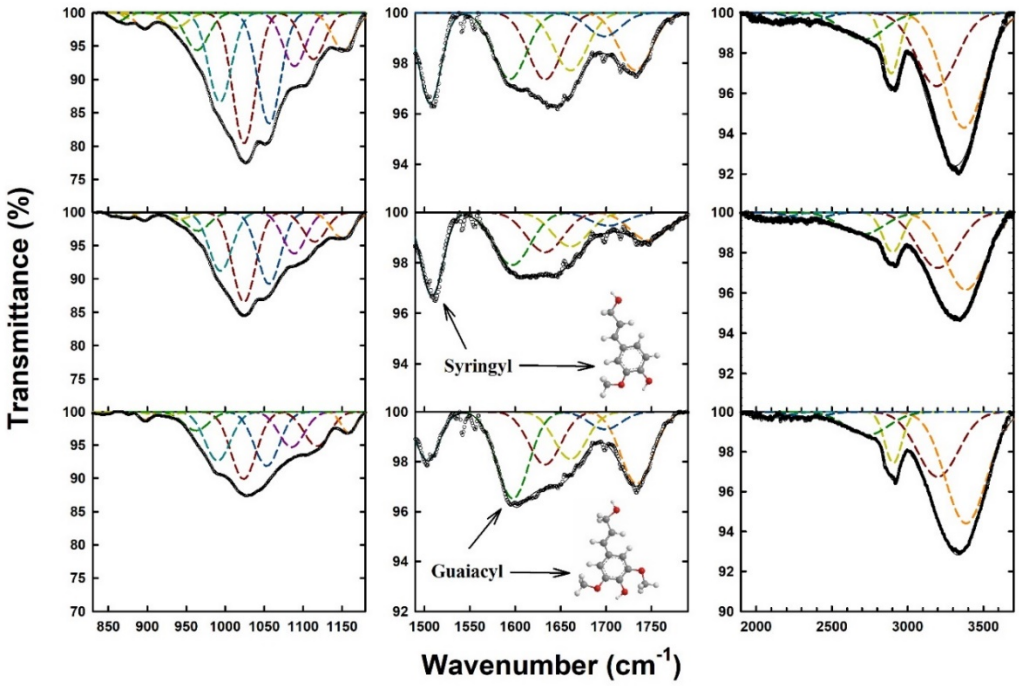

Figure 10 - FTIR spectral deconvolution of all the investigated samples (top: abete, center cedro and bottom acacia) in three different regions. Left Cellulose region, middle Lignin region and right H-stretching region (Longo et al. 2020, IOP Conference Series: Materials Science and Engineering, Open Access).

Regarding the 1500– 2000 cm^{-1} range, the main bands are attributed to the in-plane C=C aromatic vibration, O–H bending of absorbed water, and C=O stretching in ester groups, respectively while the C–H-bending vibrations are located in the 1300–1500 cm^{-1} range. Furthermore, all the single bond-stretching vibration frequencies and vibration frequencies of the molecular skeleton are in the 910–1300 cm^{-1} region. For simplicity, the main relevant FTIR bands and their assignments are summarised in Table 11.

By looking at intensity changes of specific bands, or better at changes of intensity ratio between selected bands, it is possible to perform quantitative analyses for different purposes. For example, the intensity (or area) of the band at about 1500 cm^{-1}, assigned to the C=C stretching of the aromatic ring of the guaiacyl unit, and normalized to the corresponding

value of the 1024 cm^{-1} band (assigned to the C-O stretching in primary alcohols in cellulose), can be used to estimate the lignin percentage (Popescu 2006).

Here, we have compared the area between specific bands to infer specific and unique properties for each wood. The lignin percentage obtained from the A_{1500}/A_{1024} area ratio furnishes an average value of 23% +/- 3% for all the three wood samples while the (syringyl/(syringyl+guaiacyl)) ratio, obtained estimating the $\log(A_{1600}/A_{1500})$ quantity, is of 0.04 and 0.02 respectively for silver fir and cedar. This behaviour indicates that both the woods are softwoods. On the contrary, the (syringyl/(syringyl+guaiacyl)) ratio equals 0.38 for acacia which is characteristic of hardwood (Faix 1988). Huang et al. showed that the area ratio (or its logarithmic) between the lignin bands at about 1600 and 1500 cm^{-1} well correlates with the syringyl ratios (syringyl/(syringyl+guaiacyl)) calculated from nitrobenzene oxidation products (Alves 2011; Huang 2012). Then, this parameter is significant for the lignin structural analysis, in turn, to determine wood characteristics, such as the hardness. According to Huang et al. conclusion, softwood mainly contains only guaiacyl units while hardwood contains both guaiacyl and syringyl units. So, analogous considerations could be extended to our samples.

Concerning the H-stretching region, our analysis shows that the area ratio corresponding to the bands centred at about 2900 and 3200 cm^{-1} is constant and equals to 0.34 for the three species, suggesting that the content of bound internal water of cellulose is the same. Instead, the area ratio corresponding to the bands at 3400 and 3200 cm^{-1} goes from 1.39 for cedar to 1.57 for silver fir up to 1.72 for acacia, indicating that this latter has a slightly higher amount of poorly bound water with respect to the other two woods.

In Fig. 21 are shown Raman spectra of silver fir (*Abies alba*), acacia (*Robinia pseudoacacia*) and cedar wood *(Cedrus libani)* samples. No clear features are visible in the Raman spectra collected on the wood samples. This is explained since Raman intensity is very low and its activity is affected by fluorescence signal, acting as background, that prevents wood identification. However, this limitation was overcome using SERS approach, as shown in Fig. 21a where a comparison between normal

Raman and SERS spectra on acacia wood is reported. An analogous behaviour (not shown) was observed for the other woods.

Table 11 - Main FTIR bands and their assignments (Longo et al. 2020, IOP Conference Series: Materials Science and Engineering).

Wavenumber (cm^{-1})	**Assignments**
3358-3372	Free OH in lignin; free water
3195	Free OH in cellulose; bound water
2935	CH stretching of cellulose and hemicelluloses
2901	Asymmetric CH_2 stretch
2862	CH_2 stretching of cellulose and hemicelluloses
2679	CH stretching of cellulose and hemicelluloses
2350	CO_2 asymmetrical stretching
2100	Scissoring and rocking vibrations of water
1770	C=O stretching in conjugated ketones
1735	C=O stretching of carboxylic acid in hemicelluloses ester group or in unconjugated ketones
1698	C=O vibration in the carboxylic group in resin acid
1660	C=O stretching in cellulose
1640	H-O-H angle vibration of adsorbed water (peak assigned to bound water)
1600	C=C stretching of the aromatic ring (Syringyl)
1500	C=C stretching of the aromatic ring (Guaiacyl)
1275	Characteristic peak of lignin (Stretching vibrations of C-O in guaiacyl)
1240	C-O of acetyl in pectin or hemicelluloses
1160	anti-symmetrical deformation of the C-O-C band
1150	Symmetric C-O-C and asymmetric stretch in cellulose in hemicellulose
1112	Aromatic C-H out-of-plane deformation C=O stretch
1087	C-O; C-C; -C-H stretching mode of alcohol in lignin
1056	C-O stretching of secondary alcohols
1024	C-O stretching in primary alcohols in cellulose
990	C-O stretching in cellulose
964	C-H out-of-plane deformation in lignin
939	Aromatic C-H out-of-plane deformations

895	C-H deformation of beta-glycosidic linkages in cellulose
871	C-H deformation of hemicellulose
860	C-H out of the plane in position 2, 5, and 6 of guaiacyl units

As shown by false colour imaging, obtained following the fluorescence signal in the 300 - 2500 cm^{-1} and the Raman spectra in a different point of the samples (see Fig.21b), the wood structure of silver fir and cedar woods is formed by several bundles of filaments whose surface is relatively smooth and flat. Otherwise, a more wrinkled and richly veined structure is visible for acacia.

The presence of noble metal nanoparticles induces a giant amplification of the Raman signal of the investigated wood, as already observed identifying organic pigments (Fazio 2013). The representative SERS spectra of the three species of wood are shown in Fig. 21c. The most significant Raman peaks, whose assignments are reported in Table 12, are located in the 900-1700 cm^{-1} range while weak broader features, arising from the guaiacyl (G) lignin contributions, were detected at about 360 cm^{-1}. It is evident that the intensity of some contributions, in the 1600-1556 cm^{-1} and in the 1275-1460 cm^{-1} regions, of acacia sample differs to the other woods.

To define the efficiency and sensitivity of Raman approach for wood classification, we combined SERS spectra analysis with a multivariate statistical method. The results of the PCA analysis and the subsequent HCA procedure are shown in Fig. 21d, where the PC1 vs PC2 values are reported. Three groups can be identified, although the silver fir and cedar groups have some overlap. In addition, the spreading of these clusters points out for the presence of subtle wood-to-wood variations within the same wood. In any case, the three clusters are reasonably separated from each other, pointing out for the presence of clear differences in the Raman spectra of the three woods. The most striking differences between the three wood seem to be due to the change of syringyl and guaiacyl lignin content, as evidenced by the PC loadings plot shown in Fig. 21e. This behaviour is in good agreement with the trend of FTIR data, confirming the possibility to discriminate between hardwood and softwood samples.

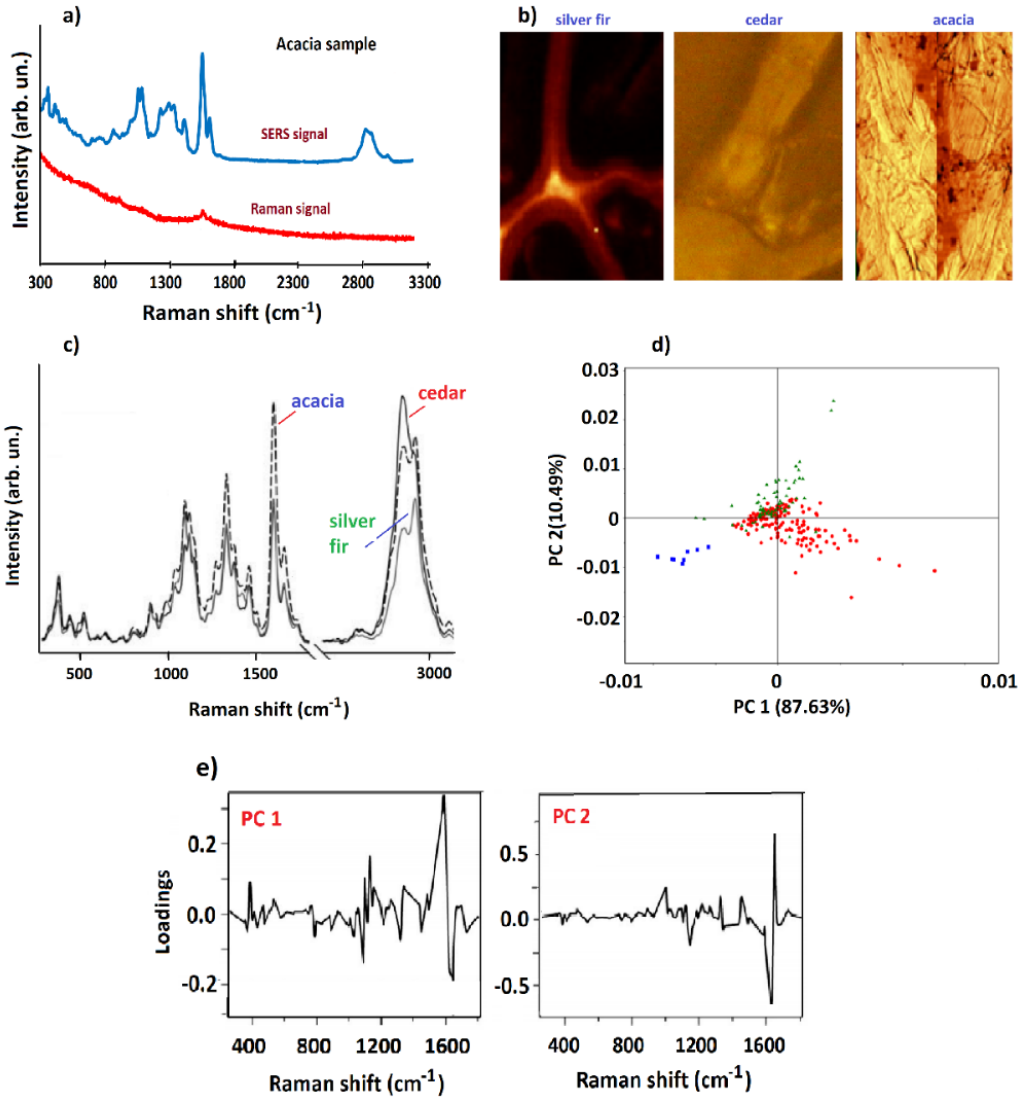

Figure 21a - Comparison between Raman and SERS spectra on acacia wood; 21b False colour imaging of the investigated woods, obtained following the fluorescence signal in the 300 - 2500 cm−1 and the Raman spectra in different point of the samples; 21c SERS spectra of the three woods and 21d PCA plot (PC2 vs PC1), obtained using SERS spectra, and showing the classification of samples by genus. The blue squares represent the acacia; the red and green circles depict silver fir and cedar, identified by HCA analysis procedure as reasonably belonging to three distinct groups; 21e PCA loadings corresponding to PC1 and PC2 (Longo et al. 2020, submitted to Microchemical Journal).

Table 12 - Raman peak position and assignments (Longo et al. 2020, submitted to Microchemical Journal).

Raman shift (cm^{-1})	**Assignments**	**Wood components**
1095	C-C and C-O stretching modes in aliphatic ethers (syringyl)	Cellulose, Hemicellulose
1123	C-C and C-O stretching modes	Cellulose, Hemicellulose
1163	C-C and C-O stretching modes plus H-C-C and H-C-O bending modes	Cellulose, Hemicellulose
1275	aryl-O of any OH and aryl O-CH_3; guaiacyl ring with C=O group	Lignin
1331	H-C-C and H-C-O bending modes	Lignin, Cellulose, Hemicellulose
1378	H-C-C and H-C-O and H-O-C bending modes (syringyl)	Cellulose, Hemicellulose
1460	H-C-H and H-O-C bending modes	Lignin, Cellulose, Hemicellulose
1603	Any ring stretching mode, symmetrical vibration	Lignin
1656	Ring conjugated C=C stretching modes of coniferyl alcohol; C=O stretching mode of coniferaldehyde (guaiacyl)	Lignin
2889	CH and CH_2 stretching modes	Cellulose, Hemicellulose
2940	CH stretching mode in OCH_3 asymmetric mode	Lignin, Cellulose, Hemicellulose

5.3.2 SEM-EDX, FTIR and Raman results on archaeological waterlogged samples

Samples

Four pieces of XVI century oak barrels from Køge shipwreck (Denmark) found in 2018 were analysed.

In tab. 13 denomination of each sample and provenience obtained by

conventional dendrochronological analysis, are reported.

Table 13 – Sample denomination and provenience obtained by dendrochronological analysis

Sample	**Provenience**
x88	Baltic area
x68	France
x73	France
x430	Netherlands

Experimental parameters and results

Scanning Electron Microscopy (SEM) technique equipped with the Energy-Dispersive X-Ray (EDX) probe have been successfully employed in analysis of waterlogged wood, not only to analyze the morphology of the wood under stress (being embedded of water) but also to obtain information about the elemental composition of the different layers of the wood, of pigments which have possibly used to decorate the woods and eventual contaminants.

SEM results revealed damage in pit membranes in the fenestriform crossfield pits connecting longitudinal tracheids with radial ray parenchyma cells (see Fig. 22 a-d). This damage could be due to the different degree of water absorption in the samples, going from different geographic area. The first sign of wood deterioration is the enlargement of apertures of bordered pits in radial walls of tracheids. SEM images show a structural breakdown and deterioration of the middle lamella, the separation of fibersand bundles of microfibrils fro the surface and the enlargement of bordered pits. These processes seem to be confined to the surface layer and that most cell walls on exposed transverse surfaces are separated at the middle lamella region, apparently because of the degradation of lignin (Sehlstedt-Persson 2006, Nilson 1990)

Further details about the microstructure of woods are shown by Atomic Force Microscope (AFM) images. AFM analyses (see Fig. 22 e-f) revealed a honeycomb-like structure where tracheids have an average size of about 40 μm in the tangential direction with respect to the annual rings, and an average size of about 30 μm in the radial direction. Finally, the mean

surface roughness is very different comparing the tested samples, a further index of wood morphology changes.

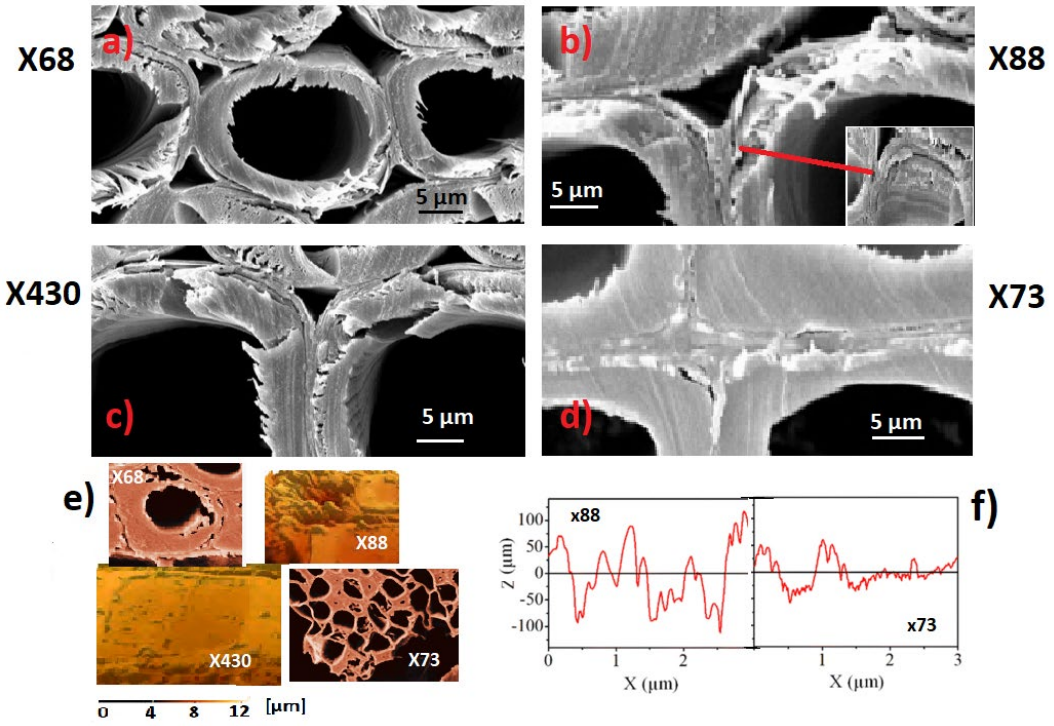

Figure 22 (a-d) SEM images of the koge shipwreck barrels and (e-f) AFM images and the estimated roughness.

Regarding EDX analysis (Table 14 and Fig. 23), the presence of C and O is mainly ascribed to fiber-heart wood while Na element is due to the permanence of woods in water. All other elements detected (i.e. Si, Al, F, Au, Ag, Ca) are considered contaminants in the water environments. However, to support this hyphotesis some other investigations correlating different experimental data are still necessary.

Raman spectra of the sample labelled x68 and x73 revealed well defined and narrow peaks: the phenolic contributions indicated by the high aromatic band (1600 cm^{-1}) and the shoulder at 1657 cm-1(assigned to the C=O group typical of conifer aldehyde/sinapyl aldehyde and the aromatic

ring conjugated C=C) from lignin. The presence of these Raman features indicates the presence of stilbenes besides lignin.

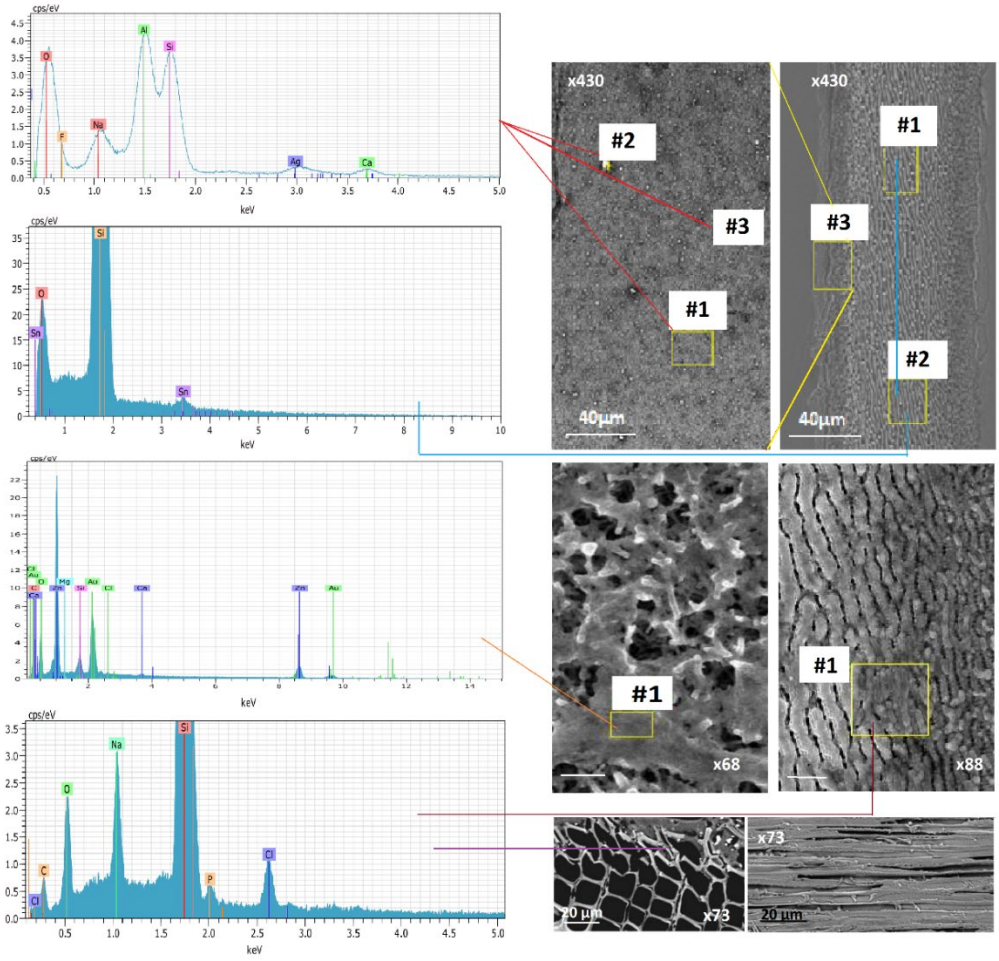

Figure 23 - SEM-EDX analysis.

Further, other lignin bands at 1334 (S-lignin), at 1274 (G-lignin) and at1138 cm^{-1} (coniferyl aldehyde/alcohol) are evident. In addition, the sample x68 is characterized by a broad band centred at about 2500 cm^{-1}, generally attributed to D_2O contribution. Then, Raman features around 3000 cm^{-1} could be due to lignin features but also to carbohydrates contributions as well as pectins and hemicellulose components (Agarwal 2014).

Similar Raman features are visible for the sample labelled X88 and X430, even if less pronounced. In fact, Raman spectra in Fig. 24b show a very high background with hidden peaks above 1500 cm^{-1}. This high

background could be due to heartwood extractives or to the elemental species detected by EDX probe.

SEM-EDX and Raman evidences are very interesting. However, these results should be considered preliminary and a more accurate investigations carrying out Raman mapping on specific regions will be useful to understand the real status of the waterlogged samples.

Table 14 - Percentage of the elemental species detected by EDX probe.

Sample	El AN	C norm. (at %)	Sample	El AN	C norm. (at %)
X430	O	31.79	X88	Si	82.33
	Si	25.46		C	6.26
	Al	19.03		O	5.46
	F	8.03		Na	2.46
	Na	6.67		Cl	2.93
	Ca	3.44		P	0.56
	Ag	5.58			
X430			X73	Si	72.76
	Si	81.02		C	17.34
	O	18.46		O	4.33
	Sn	0.52		Na	2.77
X68				Cl	2.80
	O	33.78			
	C	30.41			
	Zn	24.33			
	Au	5.53			
	Si	4.16			
	Ca	0.82			
	Mg	0.73			
	Cl	0.24			

In Fig. 24 are shown Raman spectra on the waterlogged woods.

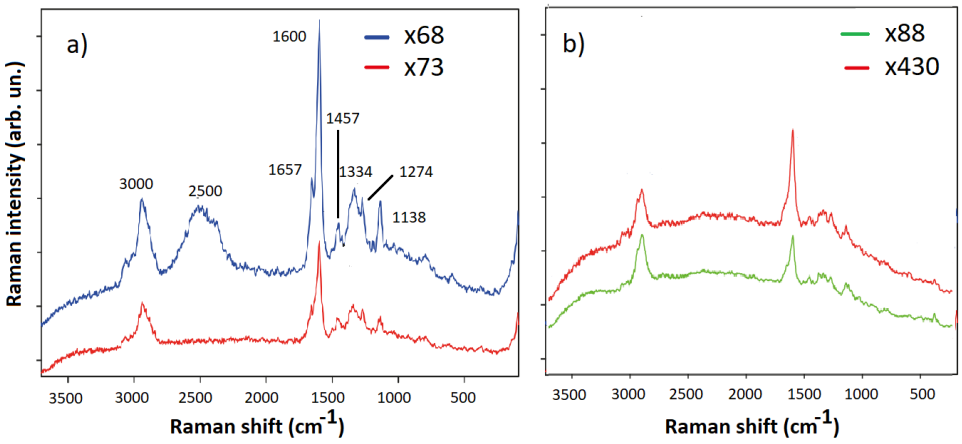

Figure 24 - Raman spectra of all the samples.

5.4 UV-vis optical absorption, FTIR and Raman/SERS results on painted wooden tablets

Once we have characterized the woods which are the base materials of the painted tablets, we carried out a complete chemical-structural characterization of pigments on the wooden tablets. To this purpose, we adopted the conventional FTIR and Raman techniques and the obtained results were useful in order to support the evidences emerged from MSCT and NMR analyses.

UV-vis optical absorption spectra of some powder samples are shown in Fig. 25a-d. The analysed samples show similar UV–visible absorption spectra characterised by a structured band, lying between 400 and 700 nm. The different chromophores cannot be discriminate and, thus, cannot be ascribed to a specific pigment. Only, carmine lake powder shows two defined absorption features at about 300 nm and 370 nm, together with a structured group in the 400-600 nm range. These bands are probably due to the different acid-base forms of carminic acid when it is dispersed in water (as in our case): CA, CA−, CA2−, CA3−and CA4−.

In Fig. 25e-g are shown FTIR spectra of dyes on the painted tablet. The prominent FTIR feature at about 1400 cm-1 and the two well-defined contributions around 1600 cm-1 (Fig. 25e) are similar to ones observed for lead white pure inorganic pigments, while FTIR bands in Fig. 25f-g are similar to ones already observed for azurite and malachite which are ascribed to copper carbonate minerals constituents. Finally, cinnabar FTIR spectrum (not shown) is analogous to ones reported in Ref. (see ATR-FTIR database). The infrared analysis detected complex fingerprints in all the samples. Some of FTIR contributions are due to wood features, such as lignin (around 1275 cm-1) and cellulose-hemicellulose (around 1650 cm-1). Hence, net discrimination cannot be made using only UV-vis optical absorption and FTIR spectra. Complementary information to the complex

FTIR evidence was obtained from micro-Raman. Raman spectroscopy has the advantage *over* FTIR for identifying pigments in painted wooden tablets.

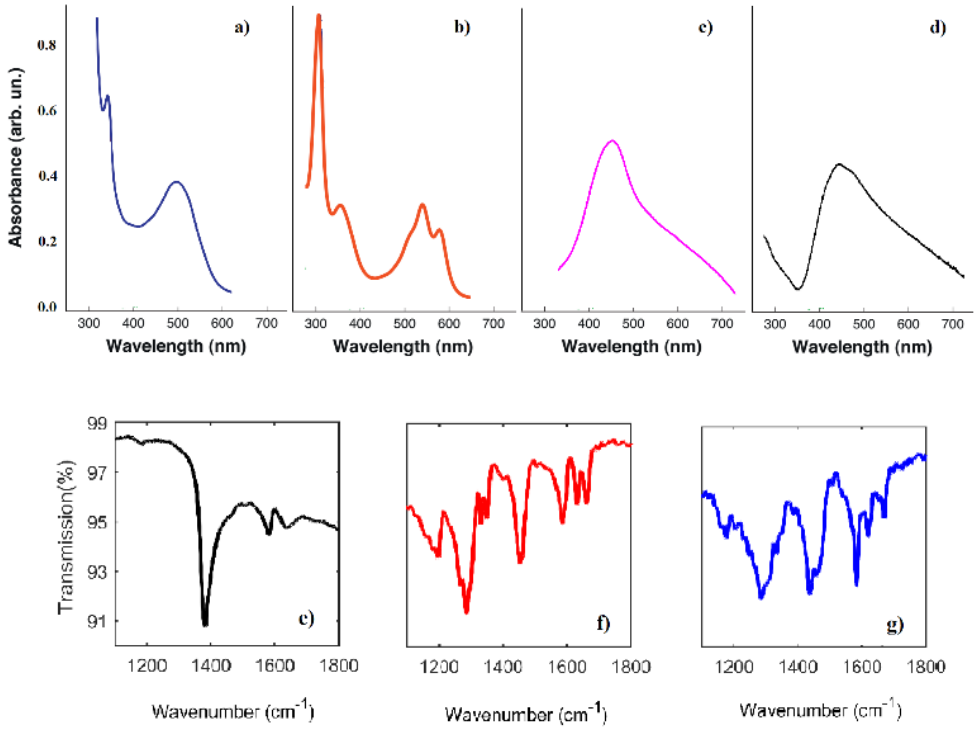

Figure 25 - UV-vis absorption spectra of nominal cinnabar, carmine lake, red lead and malachite powders (a-d) and FTIR spectra of (e-g) pigments on tablets. Some of FTIR contributions could also be ascribed to wood features, such as lignin (1275 cm-1) and cellulose-hemicellulose (1650 cm-1) (Longo et al. 2019, IMEKO TC4 MetroArchaeo 2019 Proceedings)

Both organic and inorganic paints can be infrared active, but their absorptions are so low that it is difficult to distinguish between two samples using only the IR spectra. Instead, pigments show a strong response in the Raman spectra, mainly below 600 cm-1 where the IR does not strongly absorb. The capability of Raman spectroscopy to detect these low-frequency vibrations makes Raman spectroscopy a useful tool for differentiating painted tablets by their pigments. Further, Raman spectroscopy has another advantage over the FTIR. Since the Raman peaks are sharp and do not overlap, it is much easier to resolve mixtures of pigments than it is using FTIR. Also, Raman is sensitive to even small differences in the intensities of various peaks. Since paints are a complex

mixture of many components, Raman can be used to distinguish between two similar paint samples that have slightly different amounts of each component.

In Fig. 26 are shown Raman spectra of nominal malachite, cinnabar and red lead powders, used as references for a subsequent comparison with Raman spectra collected on the painted tablets. The plotted red spectrum in Fig. 25a shows the characteristic bands of malachite (see ATR-FTIR database and see also Table 15) together with the typical features, centred at 1300 and 1600 cm^{-1}, identified as carbon black. In the 300-550 cm^{-1} range shown in Fig.26b, the Raman spectrum is characterised by the features typical of the red lead (mixed Pb (II) and Pb (IV) oxide with the general formula Pb_3O_4). Finally, the green plotted Raman spectrum in Fig. 26b displays prominent bands at about 278, 290, 353 cm^{-1}, assigned to HgS bending and stretching modes, and characteristic of cinnabar pigments.

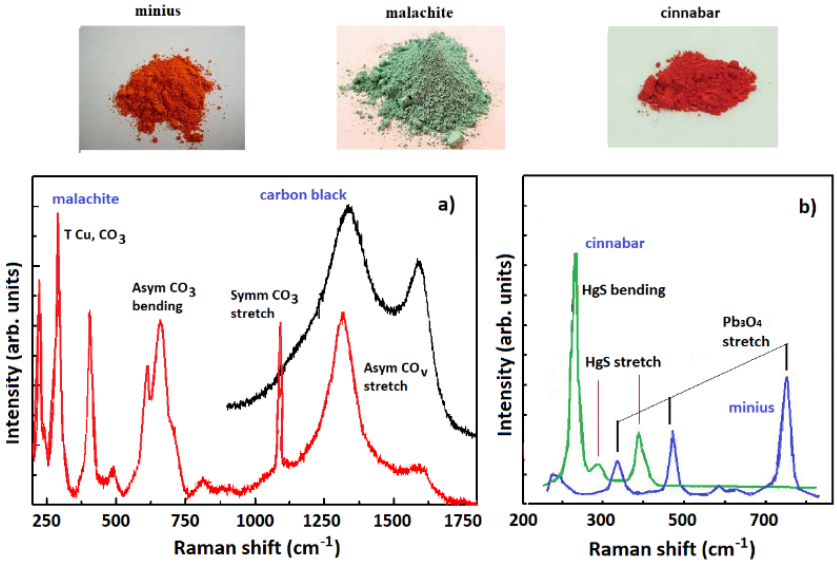

Figure 26 - Raman spectra of nominal malachite, cinnabar and red lead powders. The plotted red spectrum (panel a) shows the characteristic bands of malachite, whose assignments are reported in Table 2. In some point of the same powder, the typical Raman bands of a carbon black material have been collected. Raman spectra shown in panel b are characterised by a mixed Pb (II) and Pb (IV) oxide phase and by the typical HgS stretching modes, which are respectively constituents of red lead and cinnabar (Longo et al. 2020, submitted to Acta IMEKO Special Issue).

At this point, Raman measurements were also carried out on the pigments painted on tablets to identify their composition, also in terms of chemical configurations. For this case, no clear Raman signals were collected. It is in good agreement with already reported in the literature for natural and synthetic dyes found in textiles, inks and paints. The low Raman scattering cross-sections and the significant fluorescent background put severe limits to the quality of Raman spectra.

Table 15 - Raman bands position (cm^{-1}) and assignments typical of malachite (Longo et al. 2020, submitted to Acta IMEKO Special Issue).

	Malachite	
Frost et al. (2002)	**Mattei et al. (2008)**	**Assignments**
130, 142, 151, 166, 176, 205, 217, 249, 267, 294, 320, 389, 429, 514, 531, 563, 596	157, 171, 182, 204, 224, 272, 352, 435, 513, 537, 601	T Cu, CO_3
718	723	ν_4-Asymmetric CO_3 bending mode
750	753	
807		ν_2-Symmetric CO_3 bending mode
817		
1098	1058	ν_1-Symmetric CO_3 stretching mode
	1101	
1365	1370	
1423	1463	ν_3- Asymmetric CO_ν stretching mode
1493	1497	
1514		O-H bending mode
3349	3380	O-H stretching mode
3380		

Overcoming these drawbacks, we used surface-enhanced Raman scattering (SERS). It is well known that Raman cross-sections of molecules adsorbed on artificially roughened noble metal surfaces show dramatic enhancements thanks to the amplification of the incident field produced by the excitation of the localised plasmon resonance modes corresponding to the metallic nanostructure. Thus, we expected that this approach could be appropriate to characterise the pigments present on the tablets. In contrast, Raman spectra acquired on the commercial powder of the dyes are now used as a reference for SERS measurements made on the painted tablets.

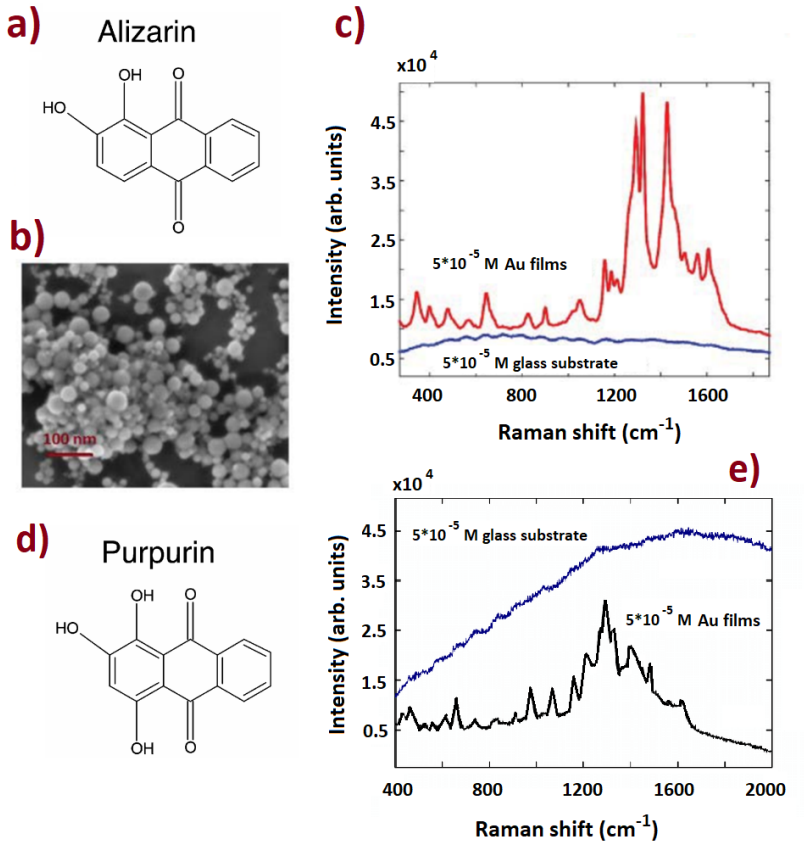

Figure 27 - a,d) Chemical structure of alizarin and purpurin; b) SEM images of the synthesised gold film; c,e) Raman spectra of alizarin and purpurin powders adsorbed on the surface of Au nanostructured substrate (Longo et al. 2020, submitted to Acta IMEKO Special Issue)

Here, SERS behaviour of two dyes of interest in the cultural heritage field: alizarin and purpurin adsorbed on gold nanostructured substrates are analysed. Their molecular structures differ by the presence of another hydroxy group in purpurin. In Fig. 27 are shown: a,d) the chemical structure of alizarin and purpurin; b) the surface morphology (studied by scanning electron microscopy (SEM) of the gold nanostructured film used for SERS, characterised by islands (agglomerates) with smooth edges; c,e) Raman spectra acquired on the surface of substrates soaked in the alizarin and purpurin aqueous solutions. The spectra acquired on the bare glass substrate show no evidence of Raman peaks related to the presence of the dye. On the contrary, SERS spectra obtained on the surface of the gold-covered substrates show clear Raman contributions typical of the investigated dyes. The precise SERS spectra acquired on the powders gave us hope for similar results on the tablets. Therefore, we proceeded collecting the Raman spectra directly on the wooden support (previously prepared using Firenze Zecchi pigments), covered with gold colloid and then air-dried before to carry out Raman analyses. SERS approach allowed the identification of different red pigments (alizarin, purpurin, madder lake, lac, and ochre) and white lead, whose Raman features are shown in Fig. 28, and Fig. 29, respectively.

Raman spectra in Fig. 28a is characterised both by the characteristic alizarin and purpurin vibrational bands, respectively. Alizarin peaks are located at about 580 (skeletal vibrations), 1015 (C-C stretching, C-C-C bending), 1185 (C-C stretching, C-H and C-C-C bending), 1285 (C-O and C-C stretching) and 1558 (C-C stretching) cm^{-1} while those centred at about 740, 980, 1027, 1218 and 1398 cm^{-1} nearly coincide with purpurin features. Thus, the madder lake dye was correctly identified by SERS as well as the mixing of red ochre and Lac dyes (see Fig. 28b) that had been brushed on the wooden tables. Finally, the SERS spectrum shown in Fig. 29 nearly coincide with those of gypsum (hydrated calcium sulphate), whose Raman bands are generally located at about 181, 415, 493, 617, 670, 1008, 1134 cm^{-1} and those of a carbonate material (i.e. 2PbCO3). Ultimately, all the pigments present on the wooden tables have been correctly identified, so confirming the reliability of MSCT data.

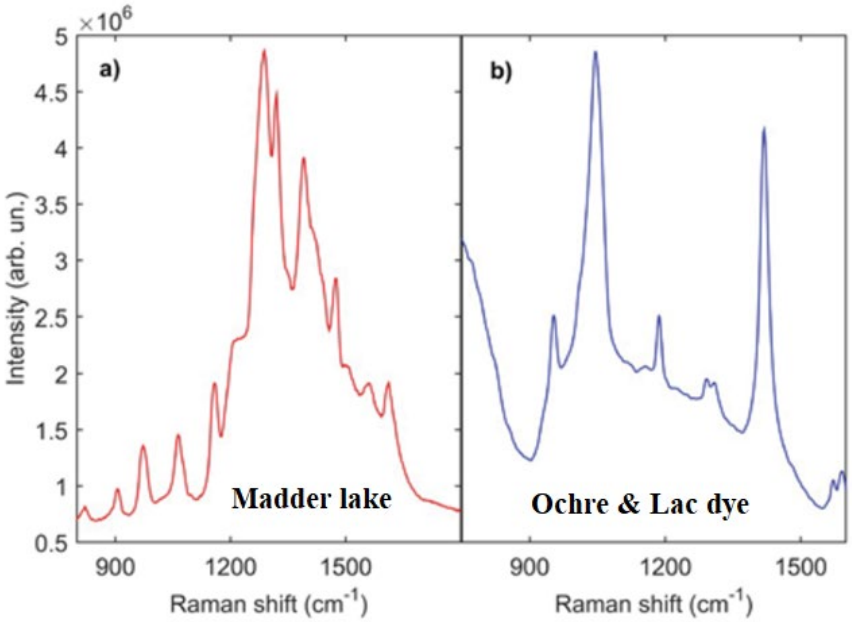

Figure 28 - Raman spectra of (a) madder lake (which contain both alizarin and purpurin) and ochre/Lac on painted tablets covered with gold nano colloids and then dried in air (Longo et al. 2019, IMEKO TC4 MetroArchaeo 2019 Proceedings).

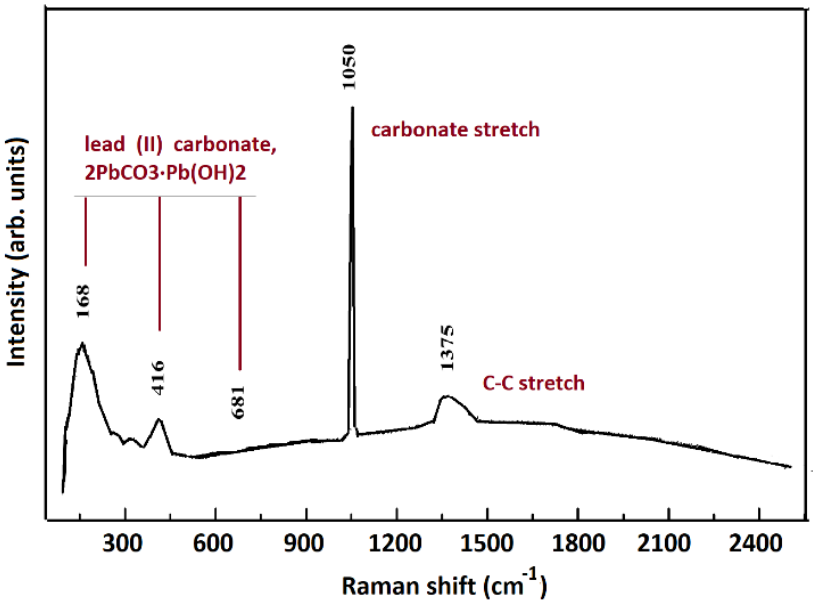

Figure 29 - Raman spectra of white lead pigment on the painted tablet, covered with gold nano colloids and then dried in air. Raman modes of hydrated calcium sulphate and carbonate modes, such as those of 2PbCO3, have been identified (Longo et al. 2020, submitted to Acta IMEKO Special Issue

Chapter 6

MSCT characterization of an Egyptian Coffin

As reported in previous chapters, imaging with computed tomography (CT) and nuclear magnetic resonance (NMR) are promising technologies for analysis of cultural heritage in a non-destructive manner. Industrial and medical CT scanners are recently used in the timber industry to investigate the internal structure and integrity of wood and, in archeology and anthropology, to study mummies.

In this chapter, experimental evidences obtained by a new generation of clinical CT (based on the Dual Energy and multi-slice acquisition principle) to investigate an Egyptian wooden mummy board (inv. 25022) belonging to a collection of the Vatican Museums (http://www.museivaticani.va/content/museivaticani/it/collezioni/musei/museo-gregoriano-egizio/progetti-scientifici/vatican-coffin-project.html) are reported.

6.1 Egyptian coffin

The anonymous sarcophagus cover (Fig. 1) used for this experimental study belongs to the Egyptian collection of the Vatican Museums and comes from the Necropolis of Luxor (800 B.C.) and measure 166x38x14

cm.
In 2008, several scientific routine surveys were performed to assess the state of its conservation, carried out by the Laboratory of Diagnostics for Conservation and Restoration of the Vatican Museums, under the direction of prof. Ulderico Santamaria. The find underwent a real complete "check-up" which involved the best-known diagnostic techniques for the study of Cultural Heritage.

Figure 1 - Coffin lid inv. 25022 (Courtesy of Dr. Alessia Amenta)

Here, it shows how the use of dual source MSCT has been fundamental for an internal inspection of the Egyptian coffin and in helping us to identify the mummy board artefact as an example of Egyptian era reuse.
Artefact induced by ultraviolet fluorescence shots were strictly evaluated in order to check conservation state and, afterwards, reflectographic locations were performed to assess the used techniques (Amenta 2014). Stratigraphic investigations of the same sample on film paint were made as well as a fluorescent X survey investigation of decorative surface paint pigments was performed. The final aims is an analysis by sampling and a woody essence microscopic observation. Avove all, an X-ray investigation was carried out in order to reproduce/simulate its construction technique, whose results are described and discussed in the following paragraphs.

6.2 MSCT and post-processing techniques

To perform CT examination, we used a Dual Source CT (Siemens Somaton

Definition, Siemens AG, Healthcare Sector, Forchheim, Germany), characterized by two X-ray sources to collect a maximum number of simultaneously acquired
data sets (number of slices) equal to 128,672 detectors per row, and 40 detector elements along the *z*-axis. The dual energy is based on the scanning of identical structures using different X-rays energies. Attenuation data received from dual energy beams are combined and compared to a known density (such as those of water and iodine) gaining more information on investigated tissue structure. The main feature of the dual source CT is the flexibility of modes of operation and the possibility to combine acquisition data in a multitude of ways with an improved temporal resolution. Another benefit is that a dual source CT system offers an unconventional image acquisition technique. In particular, it has been possible to scan large object (gantry diameter of 78 cm and maximum tube power of 160 kW) and use long scan ranges. Single energy CT imaging has limitations in the separation of smaller HU values. HU-based dual source CT imaging with the use of two different energies has the potential to differentiate sample zones characterized by smaller HU values. In particular, the main benefits of dual source CT in a conservation context include improved materials analysis and artefact reduction (for example, from metal parts).

Mummy-board was transported from Rome (Vatican Museums) to Messina (Department of Neuroradiology Messina Policlinic) with a dedicated transport in tailored cash by Montenovi srl. (Fig. 2; 3; 4; 5). Afteewards, the entire mummy board was scanned with the following acquisition parameters:
detector collimation 2x32x0.6 mm;
tube voltage, 140 - 80 kVp;
quality reference, 200 mAs;
pitch factor, 0.4;
slice thickness = 1.5 mm;
FOV = 40 cm;
matrix= 512 × 512.
Total acquisition time = 93.23 s.

2D images through Multi-planar reconstruction (MPR) and 3D

images with volume rendering technique (VRT) reconstruction. 2D images through MPR and 3D images with VRT were obtained by using a Siemens Fujitsu workstation with SYNGO software provided by Siemens. Specific filters calibrated on the human body were applied to MSCT images to increase their information content with densities similar to the materials from which coffins are made (example: plaster is constituted, as are bones, by calcium; wood is 'filled' by air, as with lungs). Because the CT densitometric characteristics of the heart, vessels, and lungs are similar to those of wooden artefacts, and plaster is characterized by higher CT density (it is constituted by calcium as with bones), cardiovascular and pulmonary filters were used during image post-processing. In particular, a cardiovascular filter provides a high contrast in the images between plaster and wood while a pulmonary filter improves the contrast of the wooden parts, as wood is a porous material very similar to pulmonary tissue (with a lot of air inside). Hence, with the cardiovascular filter, it has been possible to divide the artefact into white areas (plaster) and red colour zones (wood). Specifically, it was only highlighted the white colour density (original plaster), eliminating the red colour density (wood). Then, the reverse process was applied, and the red colour density (wood) was shown after deleting the white colour density (plaster).

Figure 2 and 3 - show transport of the cover to Neuroradiology Unit, University of Messina.

Figure 4 and 5 - show coffin lid during the CT-scanning at Neuroradiology Unit, University of Messina.

6.3 MPR and VRT results

6.3.1 Multi-planar reconstruction (MPR)

The images obtained by MPR are displayed in Figures 6. Since the images clearly show the arrangement and density of the wood growth rays in different views, these images allow a first general discrimination of the wood species. The images obtained by MPR technique revealed the presence of numerous circular holes on the whole manufactured object (Fig. 6) and two regular wigs (Fig. 7).

Most of them are filled with plaster, which is represented by hyperintense white pixels proportional to the high Hounsfield numbers (HU) of the plaster. Conversely, dark pixels represent voids, that is, lack of material.

Several cracks and cleavages caused by the machining are visible at feet level and between the two large central axes; (Fig. 8 and Fig. 9). Furthermore, at feet level, there is a gap covered with a remarkable layer of plaster, under which are still visible the original wooden nails embedded in the filling (Fig.10). Unfortunately, it is unclear if this intervention should be ascribed to the nineteenth-century restoration.

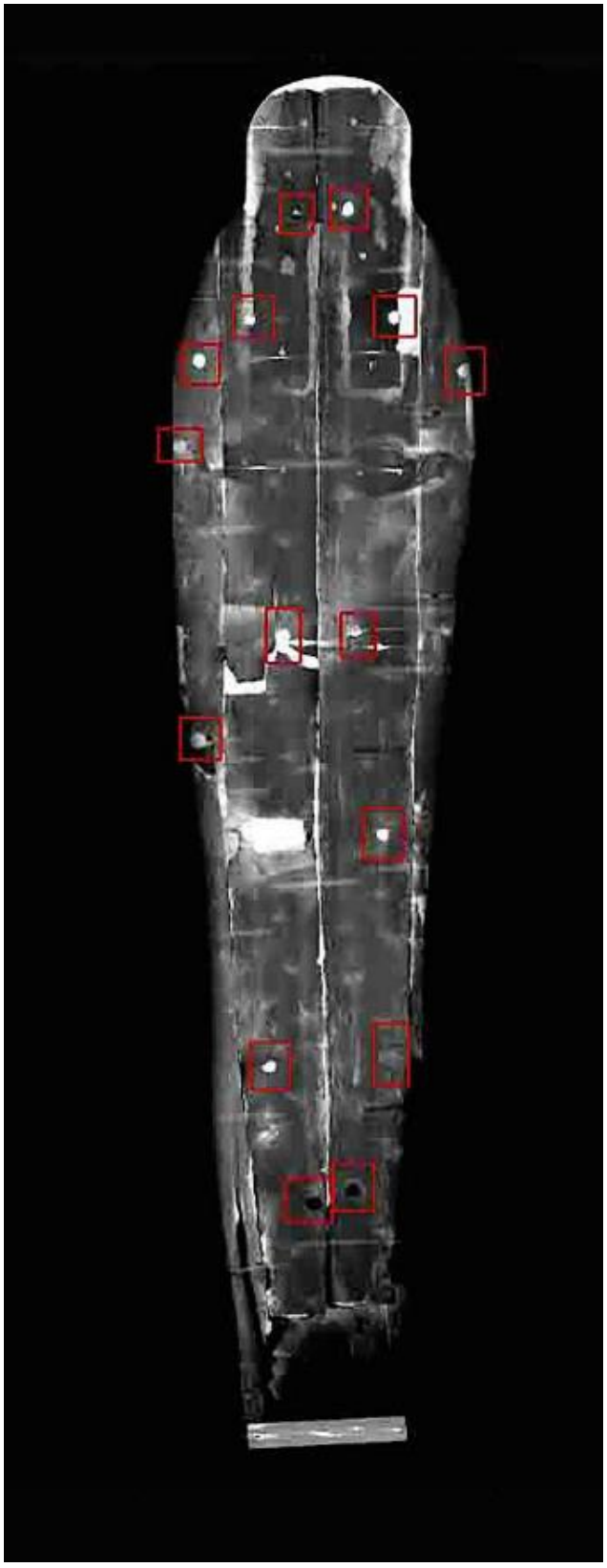

Figure 6 - Map of circular and regular holes (Longo et. al 2018, Studies in Conservation with permissions)

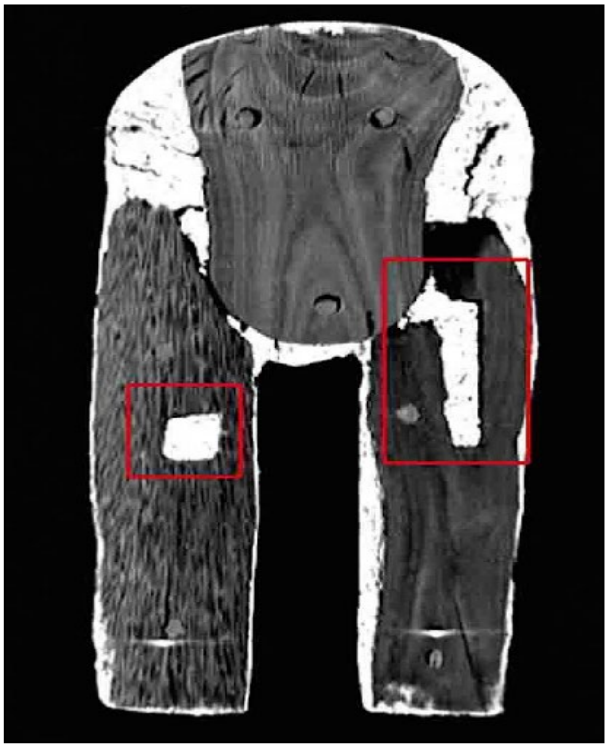

Figure 7 – Particular of regular Holes (Longo et. al 2018, Studies in Conservation with permissins).

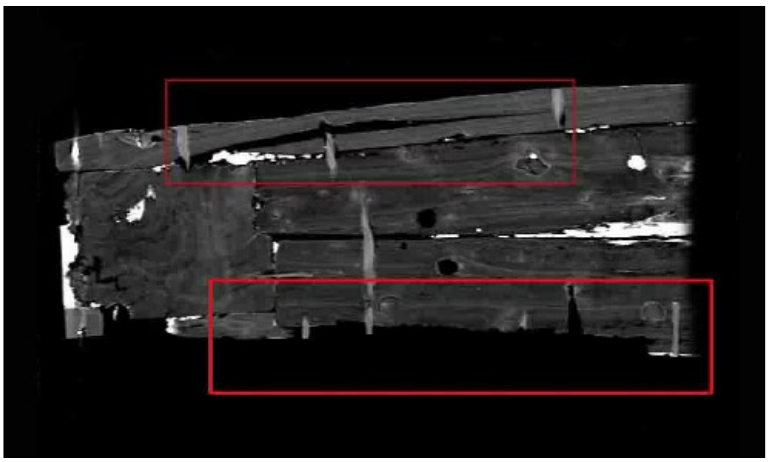

Figure 8 - Cracking due to processing step (Longo et. al 2018, Studies in Conservation with permissions)

Figure 9 – Split (Longo et. al 2018, Studies in Conservation with permissions)

The woody material appears to be similar for all axes and the left wig, while the part that constitutes the feet, the face, hands and the right wig seem to be made from a different type of wood (Fig. 11). As regards spatial orientation, all the boards have their cross-section visible in section, the radial section visible laterally and the bypass section visible from the front and the back. The only variable is the marrow orientation. Indeed, if we imagine looking at the front cover, the marrow results to face the front side in some boards and the rear side in other ones

Furthermore, comparing images with those reported in work of Parkers and Watkinsons (Parkers 2007, axes and left wig woody material reported similar macroscopic characteristics. Probably the coffin lid is made by Ficus sycomorus. This hypothesis is also confirmed by CT attenuation (Hounsfield numbers) measurements. CT values of the axes and left wig are in the same range (values included around -650 HU). The face and right wig have different CT attenuation values. The face had values included around -500 HU and the right wig had values included around -420HU. Wooden nails were measured, too, and they have CT attenuation values included around -250 HU.

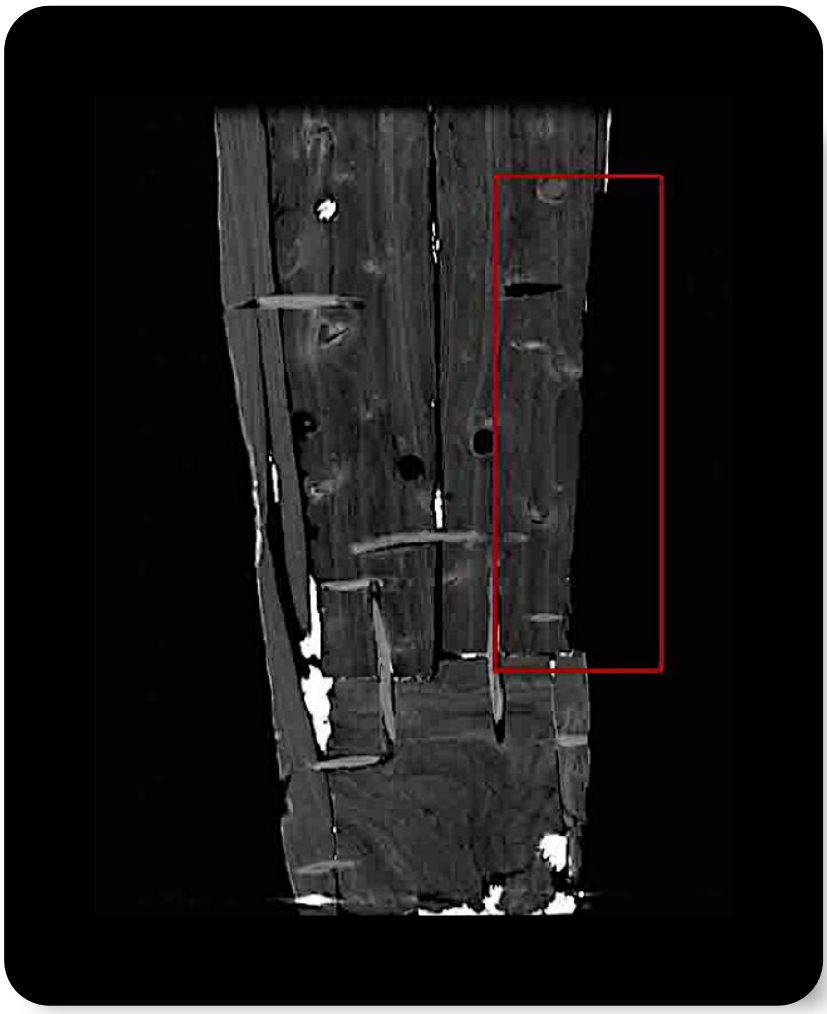

Figure 10 - Missing Piece (Longo et. al 2018, Studies in Conservation with permissions)

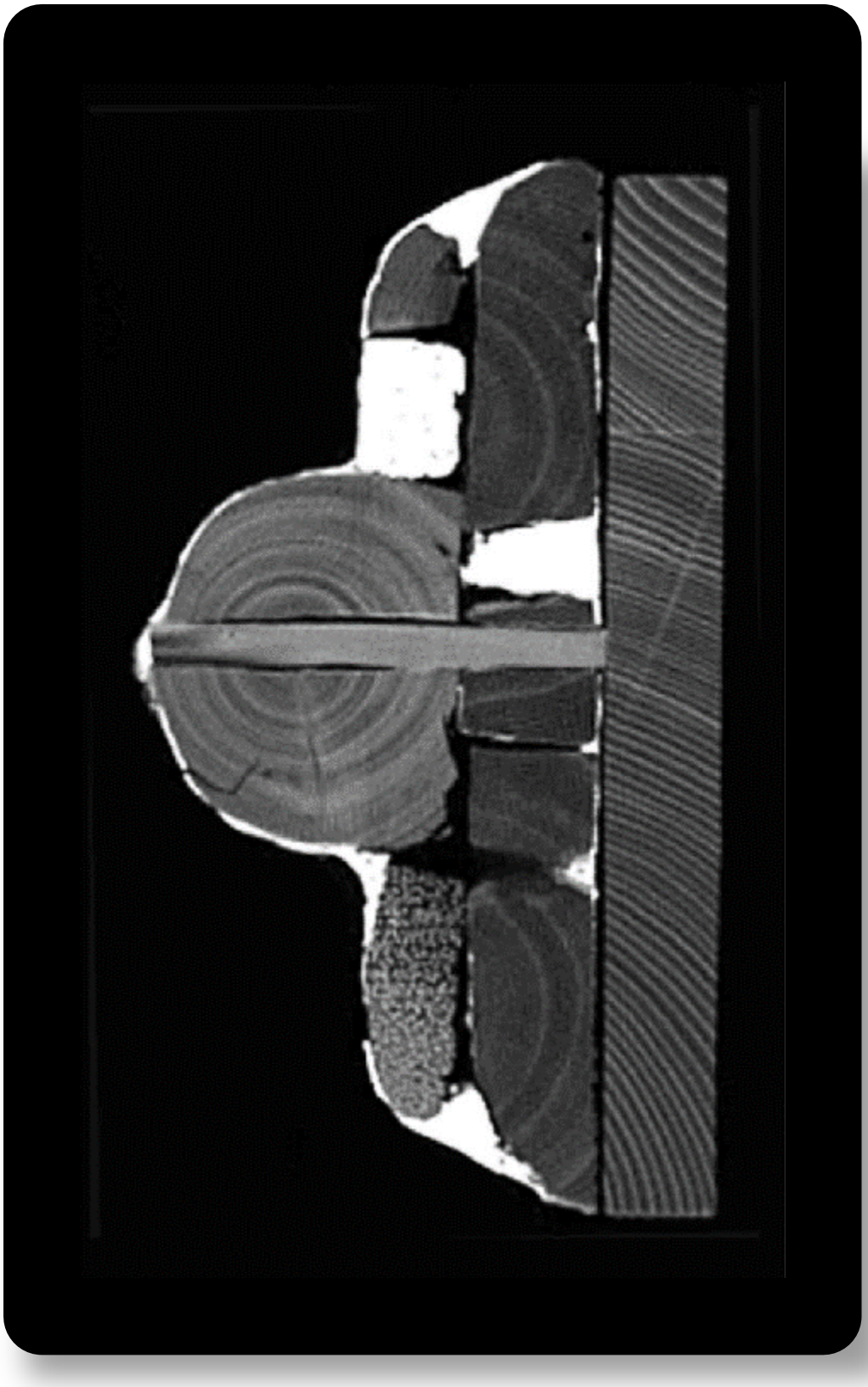

Figure 11 - Section of the head (Longo et. al 2018, Studies in Conservation with permissions)

6.3.2 VRT results

In Fig. 12 is shown the image processed by cardiovascular filter while original plaster density is shown in Fig. 13). The artefact was investigated by discriminating white areas (plaster) and colour zones (wood) (see Fig. 12).

Figure 12 – Particular differentiation of densitometry by cardiovascular filter:red/wood; white/plaster (Longo et. al 2018, Studies in Conservation with permissions)

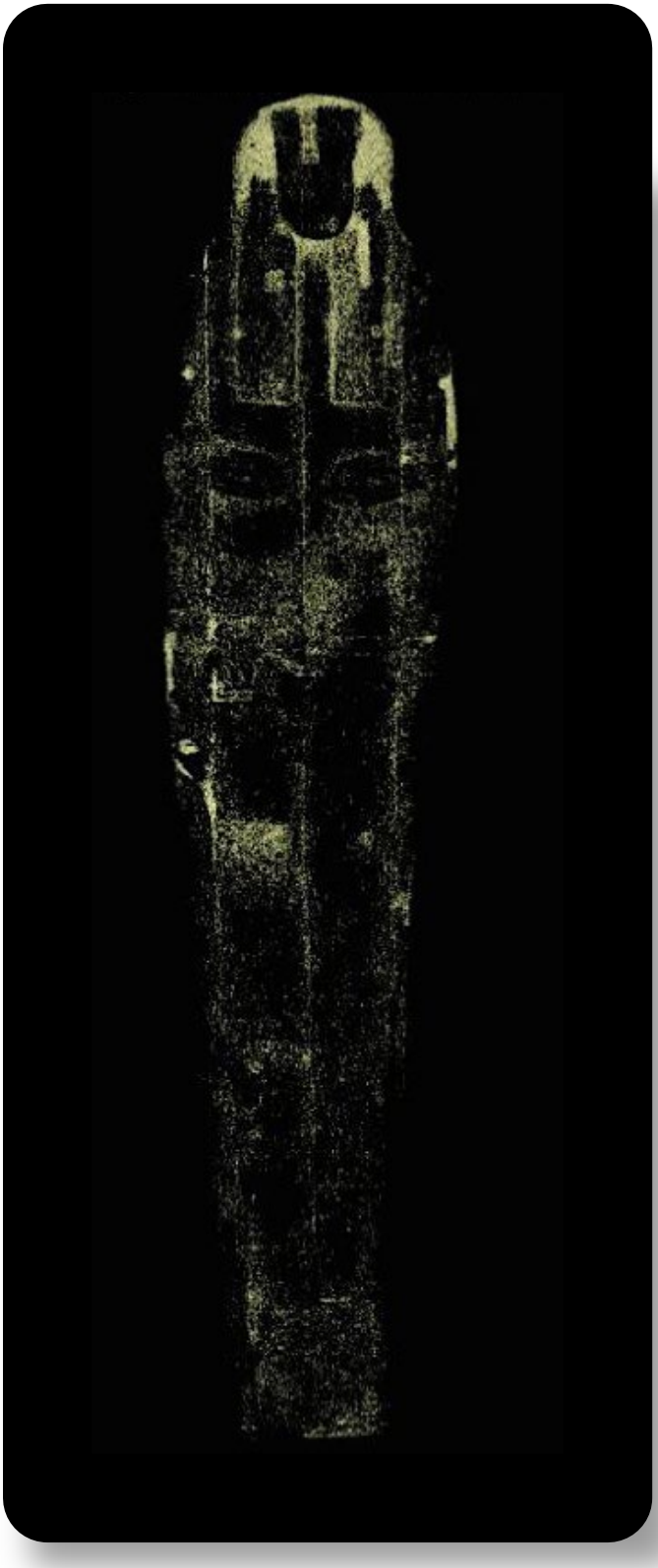

Figure 13 - Cardiovascular filter: plaster density (Longo et. al 2018, Studies in Conservation with permissions)

In details, VRT Reconstruction (panel a) is such that white pixels show the spatial distribution of plaster while coloured pixels show wood. VRT Reconstruction (panel b) allows the selection of one density and the virtual elimination of the other. In this image, the wood density is selected and the plaster density is erased. In panel c is shown the map with plaster density selection and erased wood density. On the overall, by the image highlighting wood density emerges that cover is composed of thirteen wooden parts (Fig. 14). Red falls in a negative range of HU scale (from 0 to −1000) and white zones have a density in a positive HU range (from 0 to +1000).

With the virtual elimination of the support, applied in the nineteenth-century restoration, it was possible to see the back of the object covered for over a century (Fig. 15 and Fig. 16). The image was obtained by VRT with a pulmonary filter, by virtually rotating the object. The pulmonary filter allows detecting that the wooden parts constituting the lid are joined together using tree-nails inserted horizontally; hands and parts forming the head, are superimposed and fixed, with other wooden nails, to the two big central axes.

Further, thanks to this filter, it was also possible to map the exact location of the numerous original nails (Fig. 17).

With the virtual elimination of the support, applied in the nineteenth-century restoration, it was possible to see the back of the object covered for over a century (Fig. 15 and Fig. 16). The image was obtained by VRT with a pulmonary filter, by virtually rotating the object. The pulmonary filter allows detecting that the wooden parts constituting the lid are joined together using tree-nails inserted horizontally; hands and parts forming the head, are superimposed and fixed, with other wooden nails, to the two big central axes.

Further, thanks to this filter, it was also possible to map the exact location of the numerous original nails (Fig. 17).

Figure 14 – Cardiovascular filter: wood density and mapping of axes (Longo et. al 2018, Studies in Conservation with permissions)

Figure 15 - Cardiovascular filter: back side of the sarcophagus (Longo et. al 2018, Studies in Conservation with permissions)

Figure 16 - Cardiovascular filter: particular virtual support elimination (Longo et. al 2018, Studies in Conservation with permissions)

Figure 17 - Pulmonary Filter: mapping of the original nails (Longo et. al 2018, Studies in Conservation with permissions

6.4 Discussion and conclusions

As evidenced by MSCT and VTR approaches, the cover is composed by a total of thirteen wooden parts (Fig. 14) joined together using horizontally-inserted tree-nails (Fig. 17): two large central axes (broken at the centre), five small lateral axes (initially six, one is missing), a part of square-shaped wood which constitutes the feet, two small portions that represent the hands and the head, which is composed in turn of three pieces, two for the wig and one for the face (Fig. 14). Moreover, images obtained through MPR reconstruction, suggest that the conspicuous presence of fractures and cracks, be due to a fast implementation (Fig. 8 and Fig. 9). Furthermore, by using the cardiovascular filter, it was possible to differentiate areas with thicker grout and then to understand what the height differences in wood were, differences that the craftsman was forced to tighten (Fig. 12). In this regard, the sarcophagus lid is low manufacturing and surface decorations have not great value. Besides, wooden materials are not of the same type and were probably deteriorated since implementation (Fig. 7 and Fig. 11). Finally, the presence of numerous grouted circular holes suggests that they were not used for construction purpose (Fig. 6 and Fig. 7). Data obtained by CT-scan allowed to confirm the thesis of wooden material reuse and to reconstruct the various stages of implementation:

1) Firstly, the craftsman has combined all the wooden parts with wooden nails.
2) Secondly, he filled with grouting the existing holes and the cracks caused by the insertion of nails during the crafting process, since the wood was probably very deteriorated from the beginning of its reuse.
3) Then, he levelled the surface by covering it with stucco, bridging the gap with thicker fillings.
4) Finally, he performed a decoration of the painted surface.

Considering this, we can say that the MSCT technique allows to:

- view the structures.
- figure out the number of wooden planks that make up the coffin.

- recognize any errors or repairs made during implementation.
- recognize subsequent restoration.
- study the conservation state of manufacture and materials (for example, tunnels caused by xylophagous insects are perfectly visible).

On the overall, MSCT analyses will allow to identify the type of wooden artefacts, or, as in the case of this thesis, the types of wood used (Fig. 6; Fig. 7; Fig. 8; Fig. 9 and Fig. 11). However, the most important innovation that follows from this method is the possibility to indirectly define the different densities of materials (Fig. 12; Fig. 13; Fig.14; Fig. 15; Fig. 16 and Fig. 17). Comparing densitometric measurements performed on the acacia wooden tablet (*Robinia pseudoacacia*) and on a sample of cedar wood (*Cedrus libani)* (see chapter 5), respectively acacia wood has HU values around -331 HU and cedar around -575 HU. These HU values were compared with those obtained on the coffin. The wood that constitute manufacts has HU values around -582 HU as cedar wood HU values (Fig. 18).

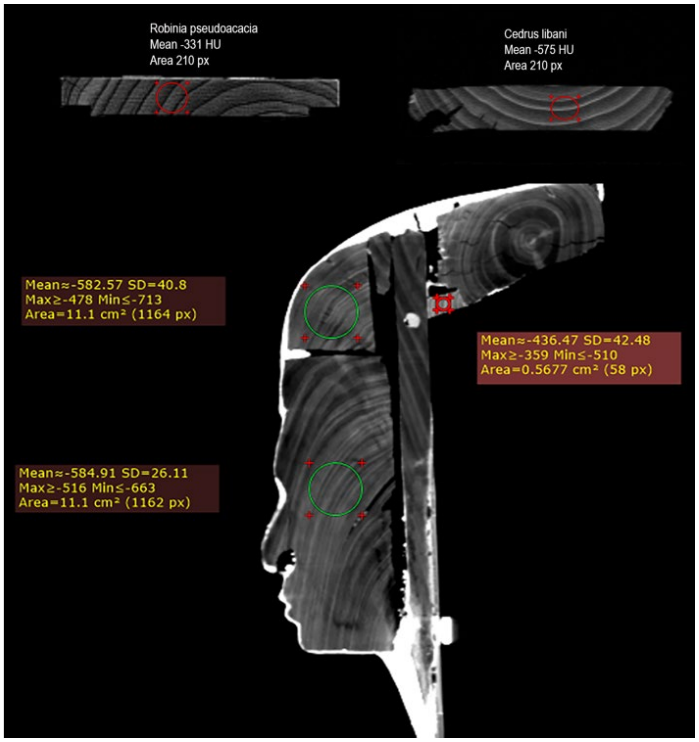

Figure 18 – (Upper) HU densitometric values of acacia and cedar wood

contemporary tablet; (Lower) HU densitometric values of the Egyptian coffin

Thanks to the use of three-dimensional reconstruction VRT (volume rendering technique), based on calibrated filters on human body materials (for. example, tissues, bones, lungs, cardiovascular system etc.), it is possible to select one density and virtually erase the others. Ultimately, it allows to virtually "dissect" an object, studying it from every angle. For this reason, the chemical composition of the materials studied is taken as a reference point.

In our approach, medical filters calibrated on the human body, have been chosen. Among them, filters with densities similar to the materials that coffins are made were chosen (for example, plaster is made by calcium as the bones; wood is "filled" by air, as lung etc).

In fact, lung filter was used on sarcophagus lid (Fig. 17), allowing to visualize and map all the original joints that connect the axles while, thanks to the different materials densities, to distinguish them from the restoration ones and to differentiate the types of wood that were used. Finally, other 3D filters used, namely the one for the cardiovascular system and the one for bones, have allowed to virtually "separate" the wooden surface by the decorative one.

In view of further cultural heritage studies, as shown in this chapter, MSCT and VTR image processing procedures successfully allow to virtually eliminate the sizeable wooden support which had been anchored to the artefact, as happened for our investigated coffin during a XIX century restoration (Fig. 17). MSCT-VTR approach avoid subjecting the object to a dangerous restoration surgery for the removal of modern support. In our case, it has allowed to study depth preservation state and, therefore, to see the back of the article which, for the past two centuries, had been unknown.

Although the advantages of MSCT are manifold (an extremely rapid acquisition time, in this work about 93 seconds for the entire coffin), the main drawbacks to the routine use of MSCT in cultural heritage are the limited accessibility of such systems. undoubtedly the variety of information obtained by this technique is very dependent on the object

examined and, above all, on its size. The main limitation of CT is precisely the diameter of the scanning tunnel (gantry), which is based on the size of the human body. However astonishing results, in a non-invasive way, can be obtained on artefacts of small or medium size.

Aside from the interesting results obtained, I can still say that “it was an enormous fortune to study such a rare and precious archaeological finding”, but undoubtedly the use of MSCT has been a fundamental help to consider this artefact as an example of the Egyptian era reuse.

Chapter 7

MSCT characterization of a seventeenth-century Dutch wooden painting

Clinical multislice X-Ray Computed Tomography investigation was performed on a 17th-century panel painting from the collection of the National Academy of San Luca Gallery in Rome. The use of MSCT allowed us to detect the numerous peculiarities related to the wood used, the execution technique and its conservation, leading to a complete preliminary interpretation of structural characteristics of wooden panel.

7.1 Dutch wooden painting

The artefact object of study is the Dutch wooden painting “Interior of a tavern” with dimensions of 46x42 cm^2, depicting the interior of an inn, and conserved by Galleria dell’Accademia Nazionale di San Luca in Rome (Fig.

1). It is part of a testamentary bequest commissioned by a French art collector naturalised in Italy, Maurice Dumarest, a close friend of Roberto Bompiani, president of the National Academy of San Luca in 1903. The painting appeared to be in a poor state of preservation, as it was characterised by fractures in the central area and in the left part. It had also been the subject of a previous and updated restoration project which involved the placing of a linen cloth strip to the central back area of the panel. At the same time, a rigid support structure consisting of 11 wooden slats glued using a protein adhesive, was applicated.

Figure 1 - Front and verso of the painting "Interior of a tavern" analysed (Montaina et. al 2020, Studies in Conservation with permissions).

The execution technique of the painting involved the creation of a support consisting of two planks of oak wood obtained by sub-radial longitudinal sawing and juxtaposing them in a parallel direction to the grain using a live joint, and gluing with a protein-based adhesive.

The two planks have dimensions of 200x420 mm^2 and 260x420 mm^2 respectively for the left and right ones, while the thickness of the boards gradually decreases proceeding from the center towards the edges: close to the central area, there is a thick peak corresponding to about 11,5 mm in the upper portion and 11 mm in the lower portion. The minimum value

recorded, equal to 5,5 mm, is found on the right side, while the specular value on the left side corresponds to 6,4 mm.

The painting characterised by a thin layer of light-colored preparation based on calcium carbonate which acts as a substrate for the pictorial film, which is composed of an oily binder mixed with mineral pigments.

During the early stages of the work, it was possible to observe how the peculiarity of the painting (characterised by an executive technique that involved the application of the pictorial film also on the edges of the boards) together with the high invasiveness of the previous restoration, and the presence of the frame, had made the structural features of the panel almost illegible, altering the perception of the real extent of the degradation phenomena involved.

7.2 MSCT results and discussions

MSCT characterization were carried out by a Somatom Definiton MSCT (Siemens Healthcare) with a gantry opening of 80 cm was used. Abdomen total body spiral acquisition was performed setting the following parameters: 120 kV energy tube voltage, 35 mAc of electricity, slice thickness of 0.6 mm, pitch factor of 1 mm, field of view (FOV) of 445 mm, matrix of 512x512, spatial resolution of 0,87 mm and scan time of 14.84s (Fig. 2).
Images reconstruction by a B60f Kernel for Multi-Planar (MPR) and 3D reconstruction by Volume Rendering Technique (VRT) were obtained. Post-processing images analysis were evaluated by SYNGO Siemens and Horos Project © software.

In Fig. 3 is shown a longitudinal CT section of the wooden panel from the 17th century. The MSCT investigation on the artefact under study showed that it is made up of two distinct planks, coming from a sub-radial section of the trunk and originally joined in correspondence with the current central crack.

Figure 2 - Example of a longitudinal CT section of the wooden panel from the 17th century. The black line about in the centre on panel shows that it is composed of two distinct parts (Montaina et. al 2020, Studies in Conservation with permissions).

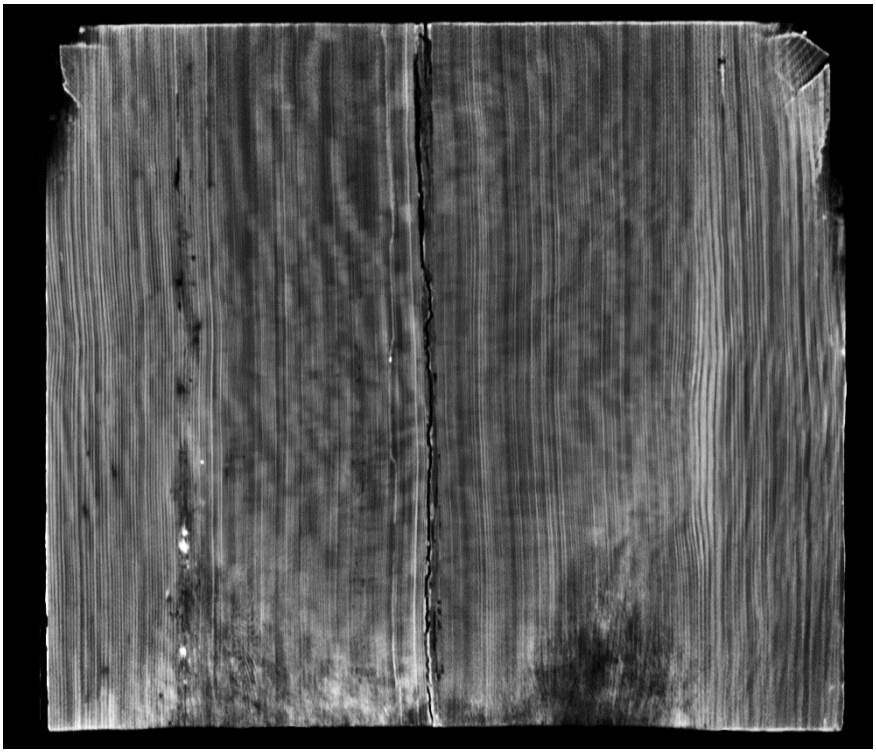

Figure 3 - Longitudinal CT section of the wooden panel from the 17th century (Montaina et. al 2020, Studies in Conservation with permissions).

Three-dimensional reconstruction by VRT allowed us to investigate the spatial geometry of the two planks: the examination of the sections identified near the upper and lower edges, as well as the central area of the artefact, made it possible to reconstruct the deformation pattern compared to an ideal horizontal plane. The boards are normally loaded in the opposite direction to the pith, and through this, it was possible to identify the profile of the deformation of the panel (Fig. 4).

Regarding the morphological characteristics of the wood structure, the growth rings are well distinguishable, with the alternation of the earlywood zones which are less dense and the latewood zones which are denser, visible as darker and lighter bands, respectively (Fig. 5).

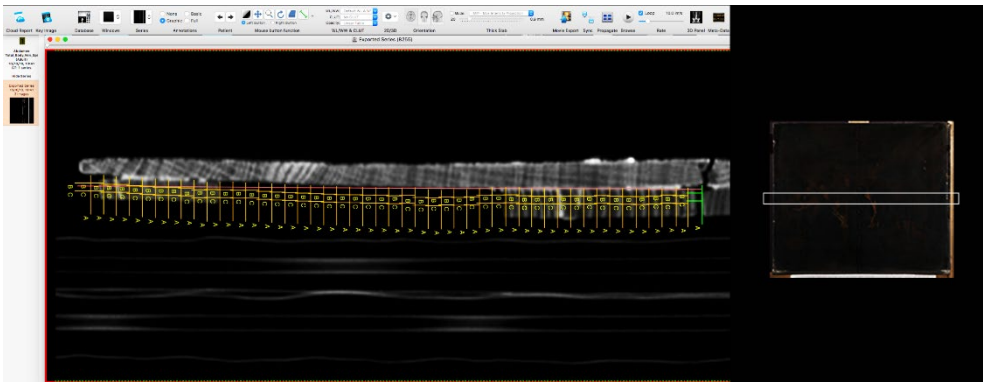

Figure 4 - General of the painting in the transverse tomographic section (high) to identify growth rings. The inserted image on the right shows where the slice was obtained. The slice is the number 236 of 512 and its thickness is equal to 0.6 mm (Montaina et. al 2020, Studies in Conservation with permissions).

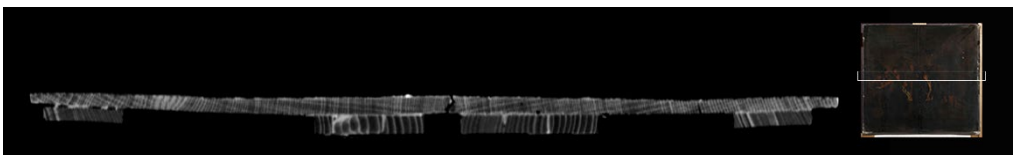

Figure 5 - Morphological characteristic of wood: earlywood zones which are less dense and the latewood zones which are denser are visible as darker and lighter bands, respectively. The inserted image on the right shows where the slice was obtained (Montaina et. al 2020, Studies in Conservation

with permissions).

Both on the cross-section of the head and in the longitudinal section, the traces of very wide parenchyma rays are clearly visible. They represent a peculiar anatomical feature referable to oak wood (Quercus sp.). Specifically, on the longitudinal vision, it is possible to identify the variation of the pattern of the rays, with a sub-radial cut towards the centre that gradually tends to the tangential towards the peripheral, both on the right and on the left side. It was also possible to measure the HU values for different woods. We obtained average values of -450 HU for the panel and –600 HU for the restoration support. These results are following our wood HU database which identifies panel as oak wood (Quercus) and restoration support as a softwood species with mean HU compatible with some species like Abies alba or Picea abies (Fig. 6). Traditional xylotomic investigations performed on wood specimens by observation of thin sections under an optical microscope assessed that the restoration support was Picea abies.

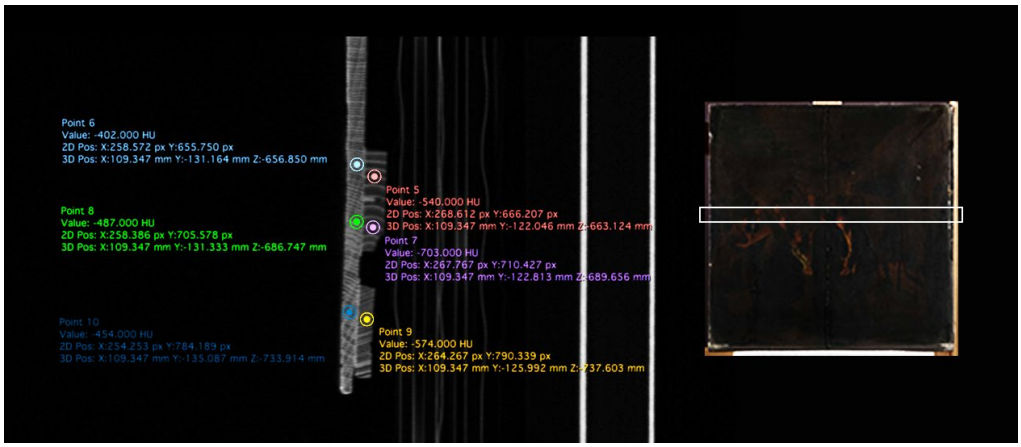

Figure 6 - Detail of HU measurements in specific selected rois. The inserted image on the right shows where the slice was obtained (Montaina et. al 2020, Studies in Conservation with permissions).

The two panels have a very different state of preservation. The left plank appears more decayed than the right one: two adjoining restored fractures were found, located respectively about 1 and 3 cm from the central one (Fig.7).

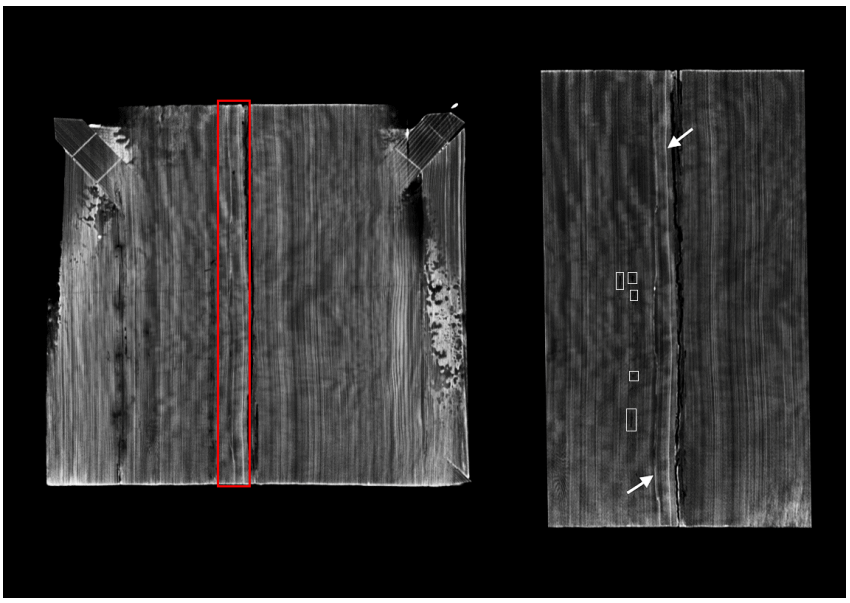

Figure 7 - General and detail of the tomographic recovery with highlights of the fractures in the support. A very different state of preservation characterises the two panels of oak. The left wood appears more deteriorated than the one on the right: two adjoining restored fractures were found, located respectively about 1 and 3 cm from the central one (indicated by arrows). Dark spots, marked by white squares, are compatible with the deterioration of the wood due to conductive to xylophagous insects' tunnels. They appear like rounded black pixels zones due to the presence of air density, with an irregular pattern (Montaina et. al 2020, Studies in Conservation with permissions).

The second fracture has instead arisen later, as it shows signs of rupture also in correspondence with the pictorial film. During a previous restoration, a canvas for reinforcement was affixed on the back of the panel, which was in turn damaged by the third and last fracture, which arose at the original junction between the boards and is now immediately visible in the centre of the painting. The panel also shows damage from wood-boring beetles at the crack located in the central area of the table, as shown in the image of figure 7.

The right panel has a better state of conservation than that on the left, since only a small discontinuity, invisible to the naked eye, can be found at the lower-left portion of the wood near the fracture and referable to a tunnel caused by xylophagous (marked by white squares in Fig. 7). They appear like rounded black pixels zones due to the presence of air density, with an irregular pattern.

The insect outcome, however, cannot be detected on the restoration canvas on which no exit holes were observed. The xylophagous attack exhausted before restoration with canvas, since no more insect holes are visible on it.

The study of the containment structure applied on the back of the panel confirmed that it is made up of 11 wooden slats. The incisions made on the strips are also easily identifiable to make them adhere better to the surface of the board. In the slats, several knots were identified (Fig. 8)

Through the three-dimensional reconstruction by VRT, it was finally possible to highlight the different densities of the materials making up the product. In the 3D rendering of the panel, the wooden elements with a mean density of -500 HU (brown) and metal-like elements with a mean density values equal to +2000 HU (red) are displayed.

This procedure made it possible to detect all the metallic or metal-like elements present in the panel (Fig. 9). Three nails were found: two in the upper left corner and one in the lower right corner. The measurements are respectively about 25,1 mm and 7,7 mm for the first two: about 13,8 mm for the third. In the same way, it was possible to observe the thickness of the preparation and the areas characterised by consistent use of white lead, a pigment-based on Lead Oxide that produces high x-ray attenuation due to its high atomic weight, and therefore white image pixels (Fig. 10).

On the basis of MSCT evidences, it was possible to carry out assessments regarding the fractures identified in the central area of the artefact (Fig. 7): the onset of these discontinuities could refer to temporally distinct moments, where the oldest fracture is the nearest the central junction, as it shows no sign of interaction with the pictorial film. It is therefore possible that it may have occurred in a phase before the implementation of the pictorial film, that is it dates to the time when the raw board was being worked. The nature of these discontinuities, mainly related to the presence of a slope of the grain in the lower central part of the left plank, represents

a point of fragility for the board which manifests three adjacent interruptions of continuity in that area.

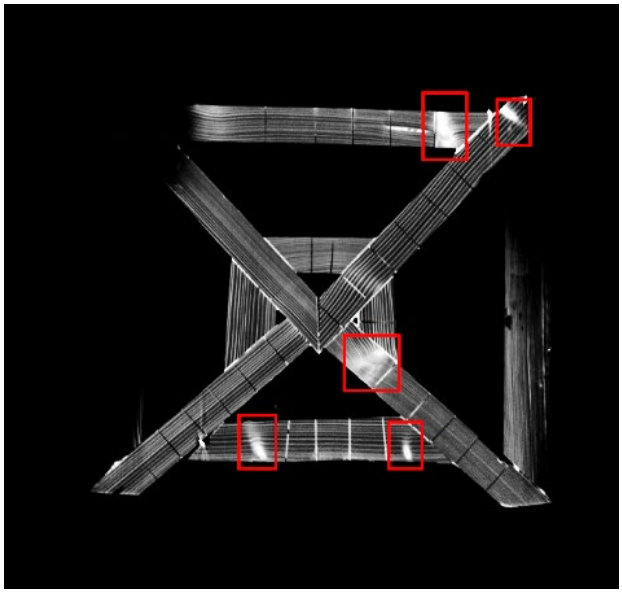

Figure 8 - General of the frame. The red squares show the presence of nodes in the wood, characterised by a higher density (Montaina et. al 2020, Studies in Conservation with permissions).

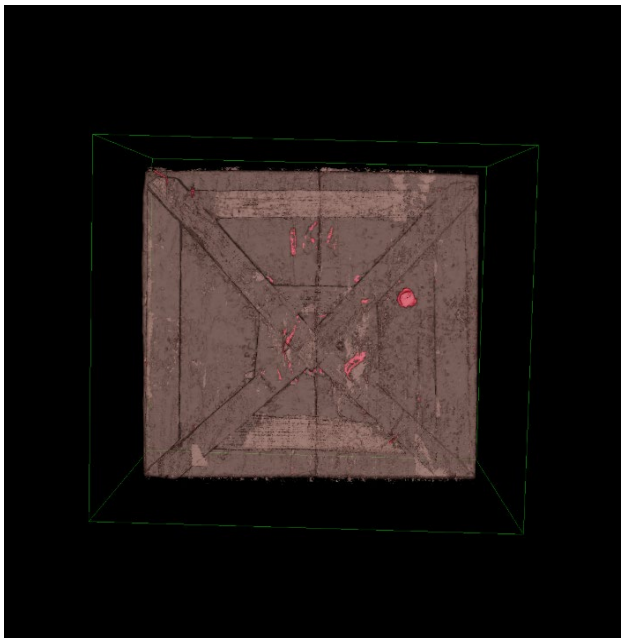

Figure 9 - 3D Render of the verse with the different material densities. Wooden elements with a density of -500 HU (brown) and metal-like elements with density values equal to +2000 HU (red) are displayed (Montaina et. al 2020, Studies in Conservation with permissions).

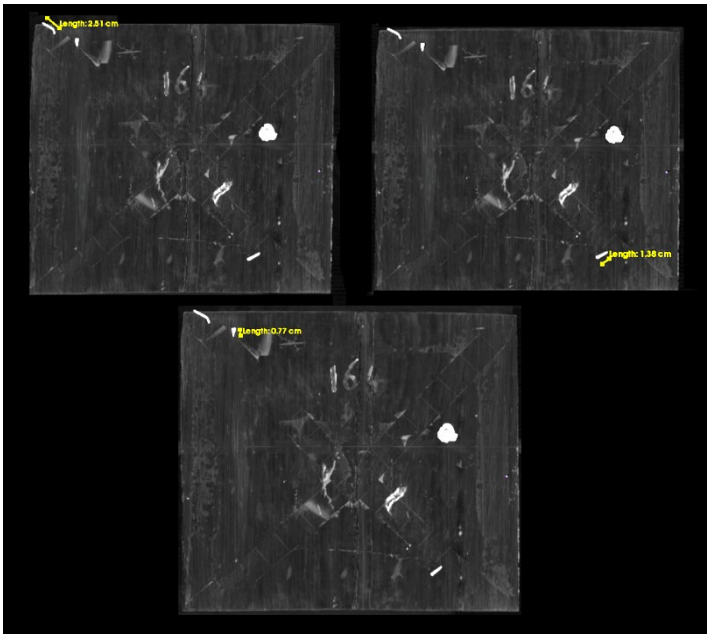

Figure 10 - Detail of the sealing wax, number 164 painted with a red varnish on the back of the panel, metallic nails and white lead, which are characterised by a high atomic number leading high x-ray attenuation (i.e. maximum absorption) and, as a consequence, white pixels in the image (Montaina et. al 2020, Studies in Conservation with permissions).

Regarding the study of the xylem structure by macroscopic characteristics observation on CT images and from linear coefficient attenuation (μ) measurements expressed in HU (Fig. 6) the growth rings of the wood species used are distinguishable, thus making it easy to distinguish between the hardwood table and the softwood used in the restoration strips. In general, latewood shows light voxels due to higher density whereas earlywood is characterized by dark voxels. Latewood is characterized by an HU values range between -300 HU and -560 HU, while earlywood between -360 HU and -800 HU.

Oak wood (Quercus) was identified for the panel with average value of around -450 HU and European spruce (Picea abies), with average value of -600 HU, for the restoration support. Density expressed in g/cm3 reported

in literature are respectively between 0,82 and 0,96 g/cm3 for oak wood and 0,42 g/cm3 for spruce (Nardi Berti 2006).

Moreover, due to the presence of very large wood rays, the panel wood could be identified as oak, as this is a typical anatomical character of this genus. However, low density wood of the restoration support, could belong to few different softwood species having about the same mean wood density, due to the absence of any anatomical character large enough to be observed with CT methodology. In fact, the resolution of the CT image and the study of the correlation between measured densities and groups of species with similar characteristics, allows us to easily make distinctions only between groups. In the case of softwoods, it is difficult to identify the individual species, considering that many have similar, if not the same, wood HU density as in the case of *Abies alba* and *Picea abies*. Therefore, sometimes is better to collaborate with other methods to obtain the exact identification of wood species. On the other hand, this method permits to choose the better place to take a sample for cross-section analysis, which permits to distinguish between the species. Combining, these two methods, there is the possibility to perform targeted micro-invasive investigations.

On the overall, the main advantages of using CT investigations consist in the possibility of analyzing parts of the object that are inaccessible to the view (for example due to the presence of surface finishes) and at different levels of depth. If the study is applied to the wooden supports, it can clearly show the progression of the growth rings (Cardinali 2013), as well as identify the discontinuities and defects present within the wood, such as galleries produced by xylophagous insects and knots.

In our study, it was possible to identify through MSCT scan all the xylophagous insects' galleries and calculate their extension. This application was useful for restorers to individuate the right place for consolidation treatments. At the same time identifying knots on the coniferous wood support was helpful to understand possibly critical areas in the manufacture.

Thanks to the opportunity of exploring the work in its entirety, it is possible to have many elements of evaluation. We were able to identify the kind of

wood, distinguishing between hardwoods and softwoods, directly from the observation on the CT images of the tree-ring and from HU measurements. In this way, a physical procedure was introduced in the inspection of the work. Moreover, depending on the resolution of the images, it will be possible to perform dendrochronological analysis (Bill et al. 2012, Krivankova 2018).

Another important element was the opportunity to distinguish the different material through VRT filters (Longo et al. 2019). This new application allows us to identify white colour as white lead pigment and, at the same time, it was possible to detect metallic nails that were not visible without a CT scan. They were found in the upper left corner and in the lower right corner and it was possible to measure their extension.

Ultimately, this ability of CT to make measurements of the structures was also useful to understand the thickness of the preparation and deformations of the panel.

Conclusions

In this thesis instructions on how to adapt the optimised acquisition and processing procedures for clinical diagnostics to wooden objects diagnostics are reported. Toward this goal, MSCT and MRI acquisition, CT attenuation measurement and relaxation times T_1, T_2 and T_2* were performed in different types of wood.

CT density values were compared to those determined in laboratory by gravimetric method (in Kg/m^3) for wood species. Besides, multi-planar (MPR) images and three-dimensional reconstruction filters (Volume Render Technique) most suitable for wood studies were analysed.

MRI images with an in-plane resolution of 250x250 μm^2 were obtained. The correlation of NMR parameters with the density of the wood was carried out considering both wood-imbibed and naturally hydrated samples.

Another methodology developed and optimized during this doctoral period, was NMR Microimaging (μMRI) investigations. Preliminary investigations were performed on a sample of Silver fir and then it was applied to archaeological waterlogged wood.

CT and MRI data were integrated by conventional methods such as Scanning Electron Microscopy (SEM), Fourier Infrared spectroscopy (FTIR) and micro-Raman (MRS). Besides, the more recent Surface-Enhanced Raman Scattering (SERS) and Raman imaging were adopted too. For the first time, to our knowledge, they were applied to archaeological waterlogged wood.

Concerning samples, seventeen samples of contemporary wood; two chestnut oak (*Quercus prinus*) wooden tablets, measuring 33x14 cm^2 painted with the same technique and pigments used on wooden paintings from XI to XVI century and a tablet of acacia wood (*Robinia pseudoacacia)*

measuring 40x15x1,5 cm painted with the same technique of an Egyptian coffin were analysed.

As archaeological samples, waterlogged archaeological wood from the Roman port of fifth century AC, found in piazza Municipio Naples (Italy) and waterlogged archaeological pieces of barrels found inside the Køge shipwreck in Køge (Denmark).

As polychrome wooden artefact, the Dutch wooden painting *Interior of a tavern* with dimensions of 46× 42 cm^2 and an Egyptian coffin from the collection of the Vatican Museums were evaluated.

In conclusion, in this thesis, it was shown through a multi-analytic approach that investigations in the field of Cultural Heritage using medical imaging equipment can be carried out. The use of these techniques generally adopted in biomedical field allows obtaining useful micro-structural information of the examined specimens, identifying false interpretations, even to the point of rewriting chapters of our history.

For this reason, substantial development of fossil and archaeological findings studies, based on technologies developed to investigate human tissues, is desirable. In many diagnostic centres, there are days every week (often Saturday afternoons and Sundays) when diagnostic tests are not carried out. This time could be efficiently used to increase the diagnostic research in the field of Cultural Heritage.

References

[Abagram 1961] Abragam A, (1961) The Principles of Nuclear Magnetism, Oxford press

[Alesiani et al, 2005] Alesiani M, Proietti F, Capuani S, Paci M, Fioravanti M, Maraviglia B. (2005) 13C CPMASNMR spectroscopic analysis applied to wood characterization. Appl Magn Reson. 29(2):177–84.

[Amenta 2014] Amenta A (2014) The Vatican Coffin Project, in Pischikova E., Budka J., Griffin K. (eds.), Thebes in the First Millennium BC, Cambridge, 483-499.

[Andersson et al, 2006] Andersson M, Persson L, Sjöholm M, and Svanberg S (2006) Spectroscopic studies of wood-drying processes, Opt. Express 14, 3641-3653 https://doi.org/10.1364/OE.14.003641

[Aramendia 2019] Aramendia, J, Gómez-Nubla, L, Fdez-Ortiz de Vallejuelo, S, Castro, K, Arana, G, Madariaga, JM (2019) The combination of Raman imaging and LIBS for quantification of original and degradation materials in Cultural Heritage. J Raman Spectrosc. 50: 193– 201. https://doi.org/10.1002/jrs.5546

[Araujo1993] Araujo CD, MacKay AL, Whittall KP, Hailey JRT (1993) A diffusion model for spin-spin relaxation of compartmentalized water in wood. J Magn Reson B 101(3): 248–261. Doi: https://doi.org/10.1006/jmrb.1993.1041

[Argawal 2014] Agarwal, U. P. (2014). 1064 nm ft-raman spectroscopy for investigations of plant cell walls and other biomass materials, Front Plant Science 5: 490

[Arnott et al, 2005] Arnott SHL, Dix JK, Best AI, Gregory DJ (2005) Imaging of buried archaeologi- cal materials: the reflection properties of archaeological wood. Mar Geophys Res. 26(2–4):135–44.

[Babiński et al, 2014] Babiński L, Izdebska-Mucha D, Waliszewska B. (2014) Evaluation of the state of preservation of waterlogged archaeological wood based on its physical properties: basic density vs. wood substance density. J Archaeol Sci. 46(1):372–83.

[Bajpai 2018] Bajpai P (2018) Biermann's Handbook of Pulp and Paper, Elsevier (Chapter 2)

[Bardet et al, 2009] Bardet M, Gerbaud G, Giffard M, Doan C, Hediger S, Le Pape L. (2009) 13C high- resolution solid-state NMR for structural elucidation of archaeological woods. Prog Nucl Magn Reson Spectrosc. 55(3):199–214 https:// doi.org/10.1016/j.pnmrs.2009.02.001.

[Bardet et al, 2002] Bardet M, Foray MF, Trân QK. (2002) High-resolution solid-state CPMAS NMR study of archaeological woods. Anal Chem. 74(17):4386–90.

[Barducci 1948] Barducci I, Pasqualini G (1948) Misura dell'attrito interno delle costanti elastiche del legno. (Measurement of the internal friction and of the elastic constants of wood). Nuovo Cimento 5: 416-502

[Berti et al, 2003] Berti S, Crivellaro A, Nocetti M, Rescic L, Sozzi L (2003), Conoscere il legno, CNR IVALSA, Italy, (Chapter 3).

[Bill et al, 2012] Bill J, Daly A, Johnsen T, Dalen KS (2012) DendroCT-Dendrochronology without damage. Dendrochronologia Vol 30(3): 223-230. Doi: 10.1016/j.dendro.2011.11.002

[Björdal 2012] Björdal CG. (2012) Microbial degradation of waterlogged archaeological wood. J Cult Herit.13(3 SUPPL.):S118–22. https://doi.org/10.1016/j.culhe r.2012.02.003.

[Blanchette 2000] Blanchette RA. (2000) A review of microbial deterioration found in archaeo- logical wood from different environments. Int Biodeterior Biodegrad. 2000;46(3):189–204.

[Bloch 1946] Bloch F, 1946 Phys. Rev. 70 460.

[Blümich 2003] Blümich B, S. Anferova, S. Sharma, A.L. Segre & C. Federici (2003) Degradation of historical paper: nondestructive analysis by the NMR-MOUSE. Journal of Magnetic Resonance, vol. 161, no. 2, pages 204 – 209

[Blümich 2008] B. Blümich, J. Perlo & F. Casanova. (2008) Mobile single-side NMR. Progress in Nuclear Magnetic Resonance Sprectroscopy vol. 52, no. 4, pages 197–269, 8

[Blümich 2010] B. Blümich, F. Casanova, J. Perlo, F. Presciutti, C. Anselmi & B. Doherty (2010) Noninvasive testing of art and cultural heritage by mobile NMR. Accounts of Chemical Research, vol. 43, no. 6, SI, pages 761–770

[Blümich 2010] B. Blümich, A. Haber, F. Casanova, E. Del Federico, V. Boardman, G. Wahl, A. Stilliano & L. Isolani (2010) Noninvasive depth profiling of walls by portable nuclear magnetic
resonance. Analytical and Bioanalytical Chemistry, vol. 397, pages 3117–3125

[Blümich 2003] Blümich B. (2003) NMR Imaging of Materials. Clarendon Press; Oxford, UK: 2003. (Monographs on the Physics and Chemistry of Materials 57).

[Bodig and Jayne 1982] Bodig J, Jayne BA (1982) Mechanics of wood and wood composites. Van Nostrand Reinhold,
New York, 712 pp

[Bonamini 1996] Bonamini G, Uzielli L, Zanuttini R (1996) Elements of wood technology and forest utilization. Printshop service University of Trento

[Botteon 2017] Botteon, A.; Conti, C.; Realini, M.; Colombo, C.; Matousek, P.; Anal. Chem.. 2017, 89, 792.

[Brancaccio 2011] Brancaccio R., Bettuzzi M., Casali F., Morigi M.P., Levi G., Gallo A., Marchetti G. and D. Schneberk. (2011) Real-Time Reconstruction for 3-D CT Applied to Large Objects of Cultural Heritage. IEEE Transactions on Nuclear Science 58:4 1864-1871. doi: 10.1109/TNS.2011.2158850

[Braovac et al, 2016] Braovac S, Tamburini D, Łucejko JJ, McQueen C, Kutzke H, Colombini MP. (2016) Chemical analyses of extremely degraded wood using analytical pyrolysis and inductively coupled plasma atomic emission spectros- copy. Microchem J.124:368–79.

[Brooka and Di Chiro 1975] Brooks, R.A., Di Chiro, G. (1975) Theory of image reconstruction in computed tomography.
Radiology 117:561-572

[Brunning et al, 2000] Brunning R, Hogan D, Jones J, Jones M, Maltby E, Robinson M, et al. (2000) Saving the sweet track: the in situ preservation of a neolithic wooden trackway, Somerset, UK. Conserv Manag Archaeol Sites.

4(1):3–20.
[Bucur 2003] Bucur V (2003) Nondestructive Characterization and Imaging of Wood. In: T.E. Timell (ed) Springer Series in Wood Science, Berlin, pp 215-279
[Bucur 1995] Bucur V (1995) Acoustics of wood. CRe Press, Boca Raton, 284 PP
[Bugani et al, 2009] Bugani S, Modugno F, Łucejko JJ, Giachi G, Cagno S, Cloetens P, et al. (2009) Study on the impregnation of archaeological waterlogged wood with consolidation treatments using synchrotron radiation microtomogra- phy. Anal Bioanal Chem. 395(7):1977–85.
[Capuani et al. 2020] Capuani S., Stagno V., Missori M., Sadori L., Longo S. (2020), High-resolution multiparametric MRI of contemporary and waterlogged archeological wood", Magnetic Resonance in Chemistry Special Issue dedicated to Donatella Capitani https://doi.org/10.1002/mrc.5034
[Casali 2008] Casali F., Morigi M.P., Bettuzzi M., Berdondini A., Brancaccio R., D'Errico V., Re A., Staiano A., Mello E. and M. Nervo (2008) Kongo Rikishi, la tomografia computerizzata [Kongo Rikishi. Computed tomography investigation] in Restaurare L'Oriente. Sculture lignee giapponesi per il MAO di Torino [Restoring the East. Wooden japanese scultures of MAO, Turin] edited by Pinin Brambilla Barcilon 38-43. Florence: Nardini Editore.
[Casieri 2004] C. Casieri, L. Senni, M. Romagnoli, U. Santamaria & F. De Luca (2004) Determination of moisture fraction in wood by mobile NMR device. Journal of Magnetic Resonance, vol. 171, no. 2, pages 364 – 372
[Cavallaro et al, 2011] Cavallaro G, Donato DI, Lazzara G, Milioto S. (2011) A comparative thermo- gravimetric study of waterlogged archaeological and sound woods. J Therm Anal Calorim. 2011;104(2):451–7.
[Christensen 1991] Christensen BB. (1991) The conservation of waterlogged wood in the National Museum of Denmark. Copenhagen: National Museum of Denmark; 1970.
[Cole-Hamilton 1990] Cole-Hamilton DJ, J. A. Chudek, G. Hunter, C. J. M. Martin (1990) "NMR imaging of water in wood, including waterlogged

archaeological artefacts". Journal of the Institute of Wood Science 12 111-113

[Cole-Hamilton 1995] Cole-Hamilton DJ, B. Kaye, J. A. Chudek, G. Hunter (1995) "Nuclear Magnetic Resonance Imaging of Waterlogged Wood" Studies in Conservation, Vol. 40, No. 1 pp. 41-50

[Compton 1923] Compton, A.H. (1923) A quantum theory of the scattering of X-ray by light elements. Phys. Rev. 21(5):20pp.

[Cormack 1963] Cormack, A.M. (1963) Representation of a function by its line integrals, with some

radiological applications. J. Appl. Phys. 34 (9):2722-2727

Fengel D. Aging and fossilization of wood and its components. Wood Sci Technol 25(3):153–77.

[Daly et al, 2017] Daly A, Streeton NLW (2017) Non-invasive dendrochronology of late-medieval objects in Oslo: refinement of a technique and discoveries. Appl. Phys. A 124, 246. Doi: https://doi.org/10.1007/s00339-018-1658-6

[Dal Pozzo 2016] Dal Pozzo G. (2016) Compendio di Tomografia Computerizzata e TC multistrato, UTET

[Daniel 2016] Daniel G. (2016) Microscope techniques for understanding wood cell structure and biodegradation. Secondary xylem biology: origins, functions, and applications. Cambridge: Academic Press p. 309–43.

[Donato et al, 2012] Donato ID, Lazzara G. (2012) Porosity determination with helium pycnometry as a method to characterize waterlogged woods and the efficacy of the conservation treatments. Archaeometry 54(5):906–15.

[Donato et al, 2010] Donato DI, Lazzara G, Milioto S. (2010) Thermogravimetric analysis: a tool to evaluate the ability of mixtures in consolidating waterlogged archaeo- logical woods. J Therm Anal Calorim.101(3):1085–91.

[Federico 2010] E. Del Federico, S. Centeno, C. Kehlet, P. Currier, D. Stockman & A. Jerschow (2010) Unilateral NMR applied to the conservation of works of art. Analytical and Bioanalytical Chemistry, vol. 396, pages 213–220.

[Florance 2006] Florance ER (2006) Magnetic Resonance Imaging (MRI) of Oak Trees Infected with Phytophthora ramorum to Determine Potential

Avenues of Infection in Bark. In: Frankel, Susan J.; Shea, Patrick J.; and Haverty, Michael I., tech. coords. Proceedings of the sudden oak death second science symposium: the state of our knowledge. Gen. Tech. Rep. PSW-GTR-196. Albany, CA: Pacific Southwest Research Station, Forest Service, U.S. Department of Agriculture: 91-99 General Technical Report PSW-GTR-196. Doi: 10.2737/PSW-GTR-196

[Fosbinder 2012] Fosbinder RA, Orth D. (2012) Essentials of Radiologic Science. 1st ed. Philadelphia, PA: Wolters Kluwer Health

[Fukada 1965] Fukada E (1965) Piezoelectric effect in wood and other crystalline polymers. 2nd Symp NDT of wood, Washington State University, Pullmann, pp 143-170

[Fukada 1956] Fukada E, Yasuda S, Kohara J, Okamoto H (1956) Dynamic Young's modulus and piezoelectric constants of old timber. Bull Kabayasi Inst Phys Res 6:104-107

[Garcia 2011] Garcia M A (2011) Surface plasmons in metallic nanoparticles: fundamentals and applications J. Phys. D: Appl. Phys. 44 283001

[Giachi et al, 2003] Giachi G, Bettazzi F, Chimichi S, Staccioli G. (2003) Chemical characterisation of degraded wood in ships discovered in a recent excavation of the Etruscan and Roman harbour of Pisa. J Cult Herit 4(2):75–83.

[Gierlinger 2007] Gierlinger N (2007) The potential of Raman microscopy and Raman imaging in plant research, Journal of Spectroscopy Vol. 21

[Giordano 1981] Giordano G (1981) Tecnologia del legno, Volume I: La materia prima, UTET, Torino

[Goldman 2008] Goldman L.W. (2008) Principles of CT: Multislice CT. Journal of Nuclear Medicine Technology 36:57-68. doi: 10.2967/jnmt.107.044826

[Hall et al 1986] Hall LD and Rajanayag (1986) Evaluation of the distribution of water in wood by use of three-dimensional proton NMR. Wood Sci. Technol. 20:329-333

[Haneka 2012] Haneka K, K. Deforce, M. N. Boone, D. Van Loo, M. Dierick, J. Van Acker and J. Van Den Bulcke (2012) X-ray sub-micron tomography as a tool for the study of archeological wood preserved through the corrosion of metal objects, Archeometry, pag. 893-905.

[Hardwood-Nash 1979] Hardwood-Nash D. C. (1979) Computed tomography of ancient Egyptian mummies. Journal of Computer Assisted Tomography 3(6):768-773.
[Harmsen 2015] Harmsen et al., Sci. Transl. Med., 2015, Vol. 7, p. 271
[Hart 1971] Hart G (1971) Macroscopic structure of hardwoods, Teaching aid n. 5 and 6, TRADA
[Hartley 1994] Hartley D, F. A. Kamke and H. Peemoeller, 1994 "Holzforschung" 48, 474–479
[Hearmon 1948] Hearmon RFS (1948) The elasticity of wood and plywood. Dept Sci Ind Res For Prod Res Spec Report no 7. HMSO, London, 87 p
[Hedges 1990] Hedges JI. (1990) The Chemistry of Archaeological Wood. In: Archaeological Wood. 1990; p. 111–40.
[High et al, 2016] High K, Milner N, Panter I, Demarchi B, Penkman KEH (2016) Lessons from Star Carr on the vulnerability of organic archaeological remains to environ- mental change. Proc Natl Acad Sci USA113(46):12957–62.
[High 2020] Kirsty E. High and Kirsty E. H. Penkman (2020) A review of analytical methods for assessing preservation in waterlogged archaeological wood and their application in practice, Herit Sci 8:83 https://doi.org/10.1186/s40494-020-00422-y
[Hoadley 1990] Hoadley R B (1990) Identifying Wood. Accurate results with simple tools. Newtown, CT.Taunton Press
[Hoffmann et al, 1990] Hoffmann P, Jones MA. (1990) Structure and degradation process for water- loggedarchaeological wood. In: Archaeological Wood. 1990. p. 35–65
[Hoyle 1961] Hoyle RJ (1961) A nondestructive test for stiffness of structural lumber. For Prod J 11 6:251-254
[Horiba website] https://www.horiba.com/fr/scientific/products/raman-spectroscopy/raman-imaging/
[Horig 1935] Horig H (1935) Theory of elasticity of anisotropic solids applied to wood (Anwendung der Elastizitatstheorie anisotroper Korper auf Messungen an Holz). Ing Arch VI:8-14
[Hounsfield 1973] Hounsfield, G.N. (1973) Computerized transverse axial scanning tomography. Br. J. Radio. 46: 1016

[Hounsfield 1980] Hounsfield, G. (1980) Computed medical imaging. Science 210 (4465): 22-28.
[IAWA 1989] IAWA (1989) List of Microscopic Features for Hardwood Identification, IAWA Bull N. S., 10, 219-232
[InsideWood 2004] InsideWood Open Access database http://insidewood.lib.ncsu.edu/search
[Jacquiot 1955] Jacquiot C (1955) Atlas d'anatomie des bois des conifers, CTB Paris
[Jacquiot 1973] Jacquiot C, Trenard Y, Dirol D (1973) Atlas d'anatomie des bois des Angiospermes, CTB Paris
[Jagels 1981] Jagels R. (1981) A deterioration evaluation procedure for waterlogged wood. In: Grattan D., editor. Proceedings of the ICOM Waterlogged wood working group conference, Ottawa. Ottawa; 1981. p. 69–72.
[James 1959] James WL (1959) A method for rapid measurement of the rate of decay of free vibrations. USDA, FPL Bull no 2154, USDA, Madison, WI
[Jayne 1955] Jayne BA (1955) A nondestructive test of glue bond quality. For Prod J 5 5:294-301
[Jayne 1972] Jayne BA (1972) Theory and design of wood and fiber composite materials. Syracuse University Press, Syracuse, NY, 418 pp
[Jensen et al, 2006] Jensen P, Gregory DJ. (2006) Selected physical parameters to characterize the state of preservation of waterlogged archaeological wood: a practical guide for their determination. J Archaeol Sci. 33(4):551–9.
[Kalender 2000] Kalender W. A. (2000) Computed Tomography: Fundamentals, System Technology, Image Quality, Applications, Publicis MCD Verlag
[Kaick and Delorme 2005] Kaick G. and S. Delorme (2005) Computed tomography in various fields outside medicine. European Radiology Supplements. 15(Suppl 4): d74. doi:https://doi.org/10.1007/s10406-005-0138-1.
[Kanazawa et al, 2017] Kanazawa Y, Yamada T, Kido A, Fujimoto K, Takakura K, Hayashi H, Fushimi Y, Kozawa S, Koizumi K, Okuni M, Ueda N, Togashi K (2017) Internal evaluation of impregnation treatment of

waterlogged wood; relation between concentration of internal materials and relaxation time using magnetic resonance imaging. J MAGN RESON IMAGING, 38:196–201. Doi: https://doi.org/10.1016/j.mri.2017.01.010

[Karsten et al, 2010] Karsten A, Earl G. (2010) The stirling castle wood recording project. A pilot study to compare traditional and innovative recording techniques for waterlogged wood. Res Rep English Herit. 65:1–40.

[Kaufman 2003] Kaufman B.M. (2003) CT's nonmedical uses. Radiologic Technology 74:81- 83.

[Kekkonen et al 2010] Kekkonen, V.-V. Telkki, J. Jokisaari (2010) Effect of Thermal Modification on Wood Cell Structures Observed by Pulsed-Field-Gradient Stimulated-Echo NMR J. Phys. Chem. C, 114, 18693

[Knight et al, 2019] Knight KY, Cousins TA, Parham D. (2019) A comparison of biodegrada- tion caused by Teredinidae (Mollusca:Bivalvia), Limnoriidae (Crustacea:Isopoda), and C. terebans (Crustacea:Amphipoda) across 4 shipwreck sites in the English Channel. J Archaeol Sci Rep. 23:854–67.

[Kobayashi et al 2019] Kobayashi K., Okochi T., Lee W. H., Sugiyama J., Hwang S. W., (2019) Non-destructive method for wood identification using conventional X-ray computed tomography data, Journal of Cultural Heritage 38 pp 88-93.

[Kollmann 1951] Kollmann F (1951) Technology of wood and wood based composites (Technologie des Holzesund der Holzwerkstoffe). Springer, Berlin Heidelberg New York, 1048 pp

[Kollman et al., 1960] Kollmann FFP, Krech M (1960) Dynamic measurements of wood elastic properties and damping. (Dynamische Messung der elastischen Holzeigenschaften und der Dampfung). Holz Roh Werkst 18 2:41-45

[Kubovský et al 2020] Kubovský, D. Kačíková, F. Kačík, (2020) Structural Changes of Oak Wood Main Components Caused by Thermal Modification, Polymers 12 485

[Larmour 2010] Larmour IA, K. Fauldsa, D. Graham, Chem. Sci., 2010, Vol. 1, p. 151

[Li et al, 2014] Li MY, Fang BS, Zhao Y, Tong T, Hou XH, Tong H. (2014) Investigation into the deterioration process of archaeological bamboo strips

of China from four different periods by chemical and anatomical analysis. Polym Degrad Stab. 109:71–8. https://doi.org/10.1016/j.polymdegradstab.2014.06.022.

[Lindgren 1991] Lindgren, LO. (1991) Medical CAT-scanning: X-ray absorption coefficients, CT-numbers and their relation to wood density. Wood Science and Technology 25(5): 341-349. doi: 10.1007/BF00226173

[Longo et al, 2018] Longo S, Mormina E, Granata F, Mallamace D, Longo M, Capuani S (2018) Investigation of an Egyptian Mummy board by using Clinical Multi-slice Computed Tomography, Studies in Conservation. Doi: https://doi.org/10.1080/00393630.2018.1439805

[Longo 2020] Longo S., Capuani S., Granata F., Neri F., Fazio E. (2020), "Clinical Computed Tomography and Surfaced-Enhanced Raman Scattering characterization of ancient pigments", ACTA IMEKO Special Issue (Under review).

[Longo 2020] Longo S., Corsaro C., Granata F., Fazio E. (2020), "Clinical Computed Tomography, FTIR and Raman spectroscopies for analyzing wood structural properties", Microchemical Journal (Under review)

[Longo 2020] Longo S., Egizi F., Di Trani M.G., Stagno V., Gili T., Fazio E., Daly A., Capuani S. (2020), "Waterlogged wood investigations by Magnetic Resonance Imaging clinical scanner", in progress for Wood Science and Technology

[Longo 2020] Longo S., Granata F., Fazio E., Capuani S. (2020), "Non-destructive characterisation of wood and pigments using clinical x-ray computed tomography densitometry", Studies in Conservation (Under review)

[Longo et al, 2019] Longo S, Granata F, Capuani S, Neri F, Fazio E (2019) Chemical-structural analysis of wooden painted specimens by clinical multi-slice computed tomography (MSCT) and surface-enhanced Raman scattering (SERS), 2019 IMEKO TC4 International Conference on Metrology for Archaeology and Cultural Heritage, MetroArchaeo 2019, 324-329 ISBN 978-929900845-4

[Longo et al 2020] Longo S., Capuani S., Corsaro C., Fazio E. (2020), Silver Fir characterized by Micro-imaging NMR and FTIR Spectroscopy, IOP Conference Series: Material Science and Engineering, Vol. 777 012004, Proceedings of Functional Material for Cultural Heritage (Fun4Heritage) 5-

6 Settembre 2019 Matera https://doi.org/10.1088/1757-899X/777/1/012004.

[Longo et al 2018] Longo S., Mormina E., Granata F., Mallamace D., Corsaro C., Longo M., Capuani S. and Fazio E. (2018) Multislice Computed Tomography applied to Cultural Heritage: preliminary experience on an Egyptian polychrome wooden coffin, Università di Messina Activity Report del Dottorato di Ricerca in Fisica 2018, pag. 50-53, ISSN 2038-5889

[Lucejko et al, 2015] Lucejko JJ, Modugno F, Ribechini E, Tamburini D, Colombini MP. (2015) Analytical instrumental techniques to study archaeological wood degradation. Appl Spectrosc Rev. 50(7):584–625.

[Łucejko et al, 2018] Łucejko JJ, Mattonai M, Zborowska M, Tamburini D, Cofta G, Cantisani E, et al. (2018) Deterioration effects of wet environments and brown rot fungus Coniophora puteana on pine wood in the archaeological site of Biskupin (Poland). Microchem J.138:132–46.

[Łucejko et al, 2020] Lucejko JJ, Tamburini D, Zborowska M, Babiński L, Modugno F, Colombini MP. (2020) Oak wood degradation processes induced by the burial environment in the archaeological site of Biskupin (Poland). Herit Sci. 8(1):1–12. https://doi.org/10.1186/s40494-020-00390-3.

[Macchioni et al, 2018] Macchioni N, Pecoraro E, Pizzo B. (2018) The measurement of maximum water content (MWC) on waterlogged archaeological wood: a comparison between three different methodologies. J Cult Herit. 30:51–6. https://doi.org/10.1016/j.culher.2017.10.005.

[Macchioni et al, 2012] Macchioni N, Pizzo B, Capretti C, Giachi G. (2012) How an integrated diagnostic approach can help in a correct evaluation of the state of preservation of waterlogged archaeological wooden artefacts. J Archaeol Sci.

[Marrucci 2006] Marrucci, C. Manzo, D. Paparo, Phys. Rev. Lett., 2006, Vol. 96, p. 163905

[Martin 2006] Martin, E.J. (2006) Physics for Radiation Protection: A Handbook. Wiley, Weinheim.

[Martinez et al, 2005] Martínez ÁT, Speranza M, Ruiz-Dueñas FJ, Ferreira P, Camarero S, Guillén F, et al. (2005) Biodegradation oflignocellulosics: microbial, chemical, and enzymatic aspects of the fungal attack of lignin. Int Microbiol8(3):195–204.

[Messeri 1967] Messeri A (1967) La struttura della parete cellulare e la sua importanza nella tecnologia del legno, Annali dell'Accademia Italiana di Scienze Forestali, vol. XVI

[Mizuno et al, 2010] Mizuno S, Torizu R, Sugiyama J. (2010) Wood identification of a wooden mask using synchrotron X-ray microtomography. J Archaeol Sci. 37(11):2842–5.

[Montaina et al 2020] Montaina L., Longo S., Galotta G., Tranquilli G., Saccuman R., Capuani S. (2020), Assessment of the Wooden Support of a Seventeenth-century Dutch Painting by Clinical Multi-slice Computed Tomography (MSCT), Studies in Conservation, (In print) https://doi.org/10.1080/00393630.2020.1757881.

[Morigi 2007] Morigi M. P., Casali F., Bettuzzi M., Bianconi D., Brancaccio R., Cornaccchia S., Pasini A., Rossi A., Aldrovandi A. and D. Cauzzi (2007) CT investigation of two paintings by Gentile Da Fabriano. Nuclear Instruments and Methods in Physics Research A 580 (1):735-738 doi:10.1016/j.nima.2007.05.140

[Morigi 2010] Morigi M. P., Casali F., Bettuzzi M., Brancaccio R. and V. D'Errico (2010) Application of X-ray Computed Tomography to Cultural Heritage Diagnostics. Applied Physics, vol. 100, Issue 3: 653-661. doi: 10.1007/s00339-010-5648-6

[Müller 2001] Müller U, R. Bammer, E. Halmschlager, R. Stollberger, R. Wimmer (2001) "Detection of fungal wood decay using Magnetic Resonance Imaging" Springer Verlag 2001 59190-194

[Müller and Bammer 1998] Müller U, R. Bammer, (1998) "Assesment of pathologies in lumber using MRI and MR-parameter mapping." magnetic resonance material in physics biology and medicine (magma) 6, supplement 1: 157

[Nardi Berti 2006] Nardi Berti R (2006) Anatomical structure of the wood and identification of the most frequent uses Italian woods. Trento

[Nilsson 1990] Nilsson, T. and Daniel,G. (1990) Structure and the aging process of dry archaeological wood. In Rowell, R.M. and Barbour R.J.,Archaeological wood: Properties, chemistry and preservation. American chemical society. Washington D.C., 67-86.

[Nilsson et al, 2012] Nilsson T, Rowell R. (2012) Historical wood—structure andproperties. J Cult Herit.13(3):S5–9. https://doi.org/10.1016/j.culher.2012.03.016.

[Ona 2003] Ona, T.; Ohshima, J.; Adachi, K.; Yokota, S.; Yoshizawa, N., A Rapid Quantitative Method to Assess Eucalyptus Wood Properties for Kraft Pulp Production by FT-Raman Spectroscopy; J. Pulp Paper Sci. 2003, 29, 6–10

[Opilik 2013] Opilik, L.; Schmid, T.; Zenobi, R.; Annu. Rev. Anal. Chem.. 2013, 6, 379

[Panter et al, 1997] Panter I, Spriggs J. (1997) Condition assessment and conservation strategies for waterlogged wood assemblages. In: Hoffman P, Grant T, Spriggs J, Daley T, editors. Proceedings of the ICOM-CC Wet Organic Archaeologi- cal Materials conference, York. York; p. 185–201.

[Parisi 2016] Parisi C., Pelosi C., Santamaria U., Pogliani P., Agresti G. and S. Longo (2016) The Conservation project of a liturgical object: the houses of Infant Jesus of Prague in the Church of Saint Mary of Providence at Macchia Giarre (Italy). European Journal of Science and Theology 12:2 235-244.

[Parkers and Watkinsons 2007] Parkers P. and D. Watkinsons (2007) Computed tomography and X-Radiography of a Coffin from Dynasty 21/22 in Decorated surfaces of ancient Egyptian objects: technology, deterioration and conservation, edited by J. Dawson, C. Rozeik and M. M. Wrigth, 58-66. Cambridge: Archetype Publications.

[Pedersen et al, 2013] Pedersen NB, Bjordal CG, Jensen P, Felby C. (2013) Bacterial degradation of archaeological wood in anoxic waterlogged environments. In: Harding SE (ed) Stability of complexcarbohydrate strucres: biofuels, foods, vac- cines and shipwrecks; p 160–87.

[Pellerin 1965] Pellerin RF (1965) A vibrational approach to nondestructive testing of structurallumber. For Prod J 153:93-101

[Phillips 1941] Phillips EWJ (1941) The identification of coniferous by their microscopic structure, Journal of the Linnaean Society of London vol LII n. 343, London

[Piombino-Mascali 2014] Piombino-Mascali D., Jankauskas R., Snitkuviene A., McKnight L., Longo M. and S. Longo (2014) Radiological

assessment of two pseudo-mummies from the National Museum of Lithuania. Journal of the Society for the Study of Egyptian Antiquities, 40:71-79. ISSN: 0383-9753.

[Pizzo et al, 2010] Pizzo B, Giachi G, Fiorentino L. (2010) Evaluation of the applicability of con- ventional methods for the chemical characterization of waterlogged archaeological wood. Archaeometry 52(4):656–67.

[Polge 1978] Polge H (1978) Fifteen years of wood radiation densitometry. Wood Sci TechnoI12:187-196

[Primak 2009] Primak, A.N., Ramirez Giraldo, J.C., Liu, X., Yu, L. and McCollough, C.H. (2009), Improved dual-energy material discrimination for dual-source CT by means of additional spectral filtration. Med. Phys., 36: 1359-1369. doi:10.1118/1.3083567

[Proietti 2005] N. Proietti, D. Capitani, R. Lamanna, F. Presciutti, E. Rossi & A.L. Segre (2005) Fresco paintings studied by unilateral NMR. Journal of Magnetic Resonance, vol. 177,
no. 1, pages 111 – 117

[Proietti 2006] N. Proietti, D. Capitani, S. Cozzolino, M. Valentini, E. Pedemonte, E. Princi, S. Vicini & A.L. Segre (2006) In situ and frontal polymerization for the consolidation of porous stones: A unilateral NMR and magnetic resonance imaging study. The Journal of Physical Chemistry B, vol. 110, no. 47, pages 23719–23728

[Proietti 2007] N. Proietti, D. Capitani, E. Rossi, S. Cozzolino & A.L. Segre (2007) Unilateral NMR study of a XVI century wall painted. Journal of Magnetic Resonance, vol. 186, no. 2, pages 311 – 318

[Proietti 2014] Proietti N, Capitani D, Di Tullio V (2014) Applications of Nuclear Magnetic Resonance Sensors to Cultural Heritage. Sensors 14, 6977-6997; doi: 10.3390/s140406977

[Purcell 1946] Purcell EM, Torrey HC and Pound RV, (1946) Phys Rev. 69 37

[Radon 1917] Radon, J. (1917) Über die Bestimmung von Funktionen durch ihre Integralwerte längs gewisser Mannigfaltigkeiten. Ber. Ver. Sächs. Akad. Wiss. Leipzig, Math-Phys. Kl.,
69:262–277 (in German)

[Re 2012] Re A., Albertin F., Bortolin C., Brancaccio R., Buscaglia P., Corsi J., Cotto G. et al. (2012) Results of the Italian neu_ART project, IOP Conferences Series: Materials Science and Engineering 37:012007. doi: 10.1088/1757-899X/37/1/012007.

[Re 2016] Re A., Lo Giudice A., Nervo M., Buscaglia P., Luciani P., Borla M. and C. Grieco (2016) The importance of tomography studying wooden artefacts: a comparison with radiography in the case of a coffin lid from Ancient Egypt. International Journal of Conservation Science 7(2):935-944.

[Romagnoli et al, 2018] Romagnoli M, Galotta G, Antonelli F, Sidoti G, Humar M, Kržišnik D, et al. (2018) Micro-morphological, physical and thermogravimetric analyses of waterlogged archaeological wood from the prehistoric village of Gran Carro (Lake Bolsena-Italy). J Cult Herit. 33:30–8.

[Rossi 1999] Rossi M., Casali F., Chirco P., Morigi MP, Nava E., Querzola E., Zanarini M. (1999) X-ray 3D computed tomography of bronze archaelogical samples. IEEE Transactions on Nuclear Science 46(4):897-903. doi: 10.1109/23.790700

[Rühli 2007] Rühli FJ, T. Böni, J. Perlo, F. Casanova, M. Baias, E. Egarter & B. Blümich (2007) Non-invasive spatial tissue discrimination in ancient mummies and bones in situ by portable nuclear magnetic resonance. Journal of Cultural Heritage, vol. 8, no. 3, pages 257 – 263,

[Schienwind 1990] Schienwind AP (1990) Physical and mechanical properties of archeological wood. In: Rowell RM,

[Sehlstedt-Persson 2006] Sehlstedt-Persson, M., Johansson, D., and Morén, T., (2006) Effect of heat treatment on the microstructure of pine, spruce and birch and the influence on capillary absorption. In: Proceedings of the 5th IUFRO Symposium Wood Structure and Properties '06", Sliač – Sielnica, Slovakia, 251–255;

[Senft 1962] Senft JF, Suddarth SK, Angleton RD (1962) A new approach to stress grading of lumber. For Prod J 124:183-186

[Seracini 2005] Seracini F. (2005) Indagine TAC della struttura lignea e della superficie pittorica [CAT investigation of the wooden structure and pictorial layer] in La Coce di Bernardo Daddi del Museo Poldi Pezzoli:

ricerche e conservazione [The Cross of Bernardo Daddi of Poldi Pezzoli Museum: scientific research and conservation] edited by Marco Ciatti, 85-89. Florence: Edifir Edizioni.

[Serway 2015] Serway RA, Jewett JW (2015) Principi di fisica, Edises

[Sharma 2003] Sharma S, F. Casanova, W. Wache, A.L. Segre & B. Blümich (2003) Analysis of historical porous building materials by the NMR-MOUSE. Magnetic Resonance Imaging, vol. 21, no. 3-4, pages 249 – 255

[Shen 1998] Shen, Q.; Rahiala, H.; Rosenholm, J.B., Evaluation of the Structure and Acid–Base Properties of Bulk Wood by FT-Raman Spectroscopy; J. Colloid Interface Sci. 1998, 206, 558–568

[Signorini 2014] Signorini G, Di Giulio G, Fioravanti M (2014) Wood in cultural heritage, guide to the determination of wood species. Perugia.

[Sirr 1999] Sirr S. A. and J. R. Waddle. (1999) Use of CT in detection of internal damage and repair and determination of authenticity in high-quality bowed stringed instruments. Radiographics 19(3):639-646.

[Sobue 1993] Sobue N (1993) Nondestructive characterization of wood. Mokuzai Gakkaishi 39:973-979

[Sodini et al, 2012] Sodini N, Dreossi D, Chen R, Fioravanti M, Giordano A, Herrestal P, et al. (2012) Non-invasive microstructural analysis of bowed stringed instruments with synchrotron radiation X-ray microtomography. J Cult Herit. 13(3 SUPPL.):44–9.

[Southwell et al, 2008] Southwell ACR, Bultman JD. (2008) Marine Borer Resistance of Untreated Woods Over Long Periods of Immersion in Tropical Waters Published by : The Association for Tropical Biology and Conservation Stable URL : http://www.jstor.org/stable/2989709. 3(1):81–107.

[Stelzner et al 2015] Stelzner J., Million S., (2015) X-ray Computed Tomography for the anatomical and dendrochronological analysis of archaeological wood, Journal of Archaeological Science 55 pp 188-196.

[Steppe 2004] Steppe K., Cnudde V., Girard C., Lemeur R., Cnudde J.P. and P. Jacobs (2004) Use of X-ray computed microtomography for non-

invasive determinations of wood anatomical characteristics. Journal of Structural Biology 148:11-21. doi: 10.1016/j.jsb.2004.05.001

[Stewart 2012] Stewart, S.; Priore, R. J.; Nelson, M. P.; Treado, P. J.; Annu. Rev. Anal. Chem.. 2012, 5, 337.;

[Stoel 2008] Stoel B. C.and T. M. Borman. (2008) A comparison of wood density between classical Cremonese and modern violins. PloS One 3(7):e2554. doi:10.1371/journal.pone.0002554

[Taconis 2005] Taconis W. K. (2005) Mummification in Ancient Egypt, with a history of the investigation of Egyptian mummies. Chap. 2 in Egyptian Mummies. Radiological Atlas of the collections in the National Museum of Antiquities at Leiden, edited by Maarten J. Raven and W. K: Taconis, 48-51. Turnhout: Brepols Publisher.

[Torgovnikov 1993] Torgovnikov GI (1993) Dielectric properties of wood and wood based materials. Springer, Berlin Heidelberg New York, 196 pp

[Tri-Bahtiar 2016] Tri-Bahtiar E, Nugroho N, Rahman MM, Kartika AR, Wirawan W, Hermawan D (2016) Estimation the remaining service-lifetime of wooden structure of geothermal cooling tower, Case Studies in Construction Materials, 6:91-102

[Tuniz 2012] Tuniz C., Bernardini F., Turk I., Dimkaroski L., Mancini L.,Dreossi D. (2012) Did Neanderthals play music? X-ray computed microtomography of the Divje Babe 'Flute'. Archeometry, 54(3): 581 590. doi: 10.1111/j.1475-4754.2011.00630.x

[Umesh 2019] Umesh P. Agarwal, Molecules 2019, 24, 1659

[Urso et al, 2014] Urso T, Piva T, Crivellaro A (2014) Clear African woods marketed in Italy: naming and identification of wood species. Second international congress of silviculture Florence

[Wang 1986] Wang PC, Chang SJ (1986) Nuclear Magnetic Resonance Imaging of Wood. WOOD FIBER SCI. 18: 308-314.

[Wariishi 2002] Wariishi, H.; Kihara, M.; Takayama, M.; Tanaka, H., Nondestructive Monitoring of Wood Decay Process Using FT-Raman Technique; Kami Parupu Kenkyu Happyokai Koen Yoshishu 2002, 69, 8–11

[WebMineral] Web mineral database http://webmineral.com/

[Wheeler and Bass 1998] Wheeler E. A., Baas P.,)1998) Wood identification a review, IAWA Journal, Vol. 19 (3) pp 241-264.

[WITec] WITec GmbH. "Characterization of Polymer Films and Coatings". *AZoM*. 08 September 2020. https://www.azom.com/article.aspx?ArticleID=14888

[Wood anatomy] www.woodanatomy.ch

[Youngquist and Hamilton 1999] Youngquist JA, Hamilton TE (1999) The next century of wood products utilization: a call for reflection and innovation. Proc Int Conf on effective utilization of plantation timber, Chi -Tou, Taiwan. For Prod Assoc ROC Bull 16:1-9

[Zanolli 2014] Zanolli C., Bondioli L., Coppa A., Dean C.M., Bayle P., Candilio F., Capuani S. et al. (2014) The late early pleistocene human dental remains from Uadi Aalad and Mulhuli-Amo (Buia), Eritrean Danakil: macromorphology and microstructure. Journal of human evolution 74:96-113. doi: 10.1016/j.jhevol.2014.04.005.

[Zisi 2017] Zisi A, Dix JK (2017) Simulating mass loss of decaying waterlogged wood: A technique for studying ultrasound propagation velocity in waterlogged archaeological wood, Journal of Cultural Heritage, Doi: https://doi.org/10.1016/j.culher.2018.02.016

[Zoia et al, 2017] Zoia L, Tamburini D, Orlandi M, Łucejko JJ, Salanti A, Tolppa EL, et al. (2017) Chemical characterisation of the whole plant cell wall of archaeological wood: an integrated approach. Anal Bioanal Chem. 409(17):4233–45.

Appendix

Chemical constituents of wood

Today, it is essential to know some aspects of wood ultrastructure.
This is due not only to an accomplished knowledge of the anatomical structure but above all to a full understanding of certain physical behaviours such as anisotropy, adsorbent and desorbed, as well as mechanical properties such as viscosity and the mechanistic behaviour of the material.
This appendix shows the structure of the most important constituent polymers of wood (cellulose, hemicellulose, and lignin) and how, among them, they give life to complex structures that constitute the structure of the cell wall.

1. Cellulose

Cellulose $(C_6H_{10}O_5)_n$ is one of the most abundant compounds in nature. Inside wood, it is the most important element with percentages ranging from 40 to 60% (Nardi Berti 2006). It is a homogeneous and linear polymer composed of many units of glucopyranose (β-D). This form of glucose takes on a characteristic spatial configuration reminiscent of the shape of a chair. If we look at Figure 1, we can see the presence of oxydrilic groups in

the equatorial position that favour the formation of glycosidic bonds between the carbon, at position 1, of a glucose molecule and that of the next molecule, in position 4.

The union between two glucose molecules is called cellobioses, or the elementary unit of cellulose. The degree of polymerization is included between 3000 and 5000 units.

Cellulose in nature is present in both the crystalline and non-crystalline state and has two allelomorphic forms called cellulose I and cellulose II. The main difference between them lies is that in the case of cellulose I, the individual chains aggregate together in parallel and keeping the same towards, while in the second, the chains have an anti-parallel pattern.

Cellulose I is more abundant, and two sub-allelomorphic structures called cellulose Iα and Iβ are known.

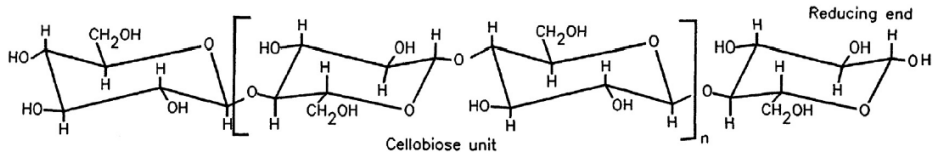

Figure 1 - The molecular structure of cellulose (Bajpai 2018, Elsevier with permissions).

Looking at the structure of an elementary cellulose chain (Fig. 1), it is possible to observe that for each unit of glucose there are 3 oxydrilic groups (OH) of carbon atoms in position 2, 3 and 6. Carbon oxygen, on the other hand, is in position 5 and allows to give rise to additional intra and intermolecular bonds. In this case, the bonds are predominantly of Van Der Waals and hydrogen bonds. Intra-molecular bonds have the function of increasing the gliding stability of the chain by favouring the formation of intermolecular bonds. Of course, the addition does not happen randomly, but they follow precise patterns depending on whether it is cellulose Iα or cellulose Iβ. In fig. 2, representative patterns of the triclinic structure of cellulose Iα and monocline of cellulose Iβ.

These two structures have a density of 1,582 g cm^{-3} for triclinic and 1.599 g cm^{-3} for monocline. It gives more excellent thermodynamic stability to the monocline shape. Hardwoods are richer in monocline shape than softwood. Studies have shown how high-temperature treatments can induce the transformation of cellulose Iα into Iβ.

Inside wood, cellulose is in the form of fibrils with varying sizes and lengths. Each can hold up to 200 elementary chains. The structure of the fibrils is composed of purely crystalline areas alternated with amorphous areas. Studies have shown that in the case of cellulose Iβ, amorphous areas have reactivity attributed to the breakdown of intramolecular bonds of groups in position 2 and 6. In contrast, the groups of native cellulose, in position 3 and 5 remain stable.

2. Hemicellulose

Inside wood, along with cellulose, there are other polysaccharides called hemicellulose. They compose 20 to 30% of the wood and are the prominent influencers in determining the physical-mechanical behaviours of wood. Hemicelluloses are also polymers that derive from the aggregation of sugars and acids. D-xylose, D-mannose, L-arabinose, D-glucose and D-rhamnose represent sugars. 4D-O-glucuronic, D-glucuronic, and D-galacturonic reprisal the acids.

The composition is different between softwoods and hardwoods. Sometimes it also depends on the species. Galactic glucomannans, glucuronoarabinoxylan and arabinogalactans generally prevail in conifers Glucuronoxylan and glucomannan in hardwoods.

Compared to cellulose, hemicelluloses consist of the aggregation of different acids and sugars (heteropolymer chains). It has a much lower degree of polymerization (200-300 units) (Fig. 2). They can be sideways oriented and perpendicular to the main chain. Sometimes oxydrilic groups (OH) can be partially replaced in positions 2 and 3 by an acetylic group (CH_3CO).

From a structural point of view, the low degree of polymerization and the presence of side chains, do not allow the formation of organized structures such as those of crystalline cellulose. This causes a strong hemicellulose hygroscopicity due to the presence of a high number of oxydrilic groups engaged in any molecular bonding. Therefore, the hemicellulose is more soluble and determines the vicious behaviours of wood.

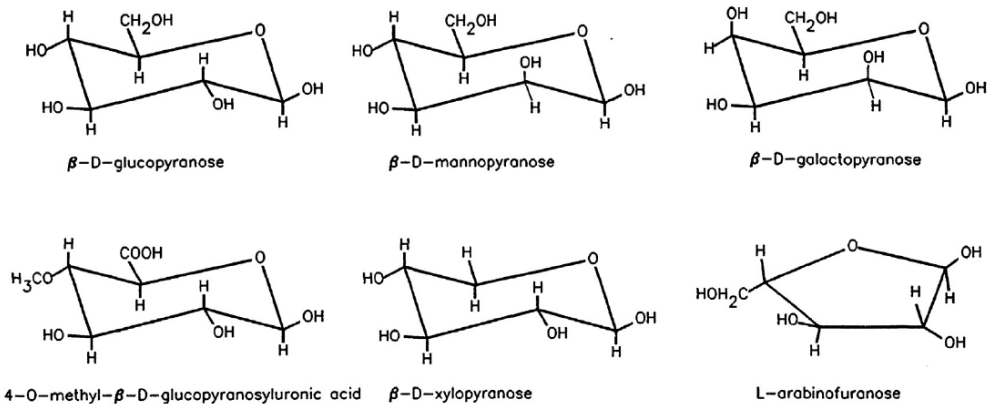

Figure 2 - The principal monomer of hemicellulose (Bajpai 2018, Elsevier with permissions).

3. Lignin

The third main component of wood is lignin. Its qualitative and quantitative composition varies between softwood and hardwoods, respectively, 25-35% and 18-20%. It is a complex amorphous high molecular weight polymer built from phenyl propane units. The polymerization occurs after a hydrogenation process by enzymes. The best-known polymerization model is the 16-unit phenylpropane, but the degree of polymerization is likely to be much higher and reach 100 units (Fig. 3).

The bonds that can be established are predominantly ether bindings and C-C bonds.

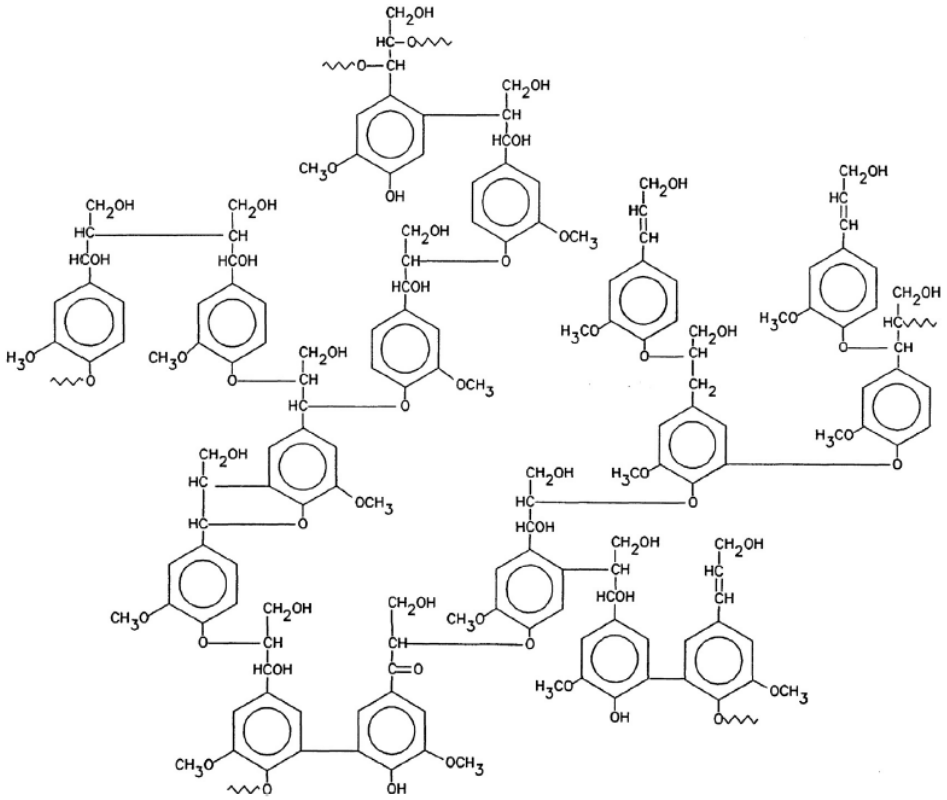

Figure 3 - Representative molecular structure of softwood lignin (Bajpai 2018, Elsevier with permissions).

4. Extractives

Extractives are chemicals in the wood that can be removed using solvents. Mainly consisting of fats, fatty acids, fatty alcohols, phenols, terpenes, steroids, resin acids, rosin, waxes, and many other minor organic compounds. These exist as monomers, dimers, and oligomers.

Generally, most of the extractives inside wood are in the heartwood respect than sapwood. Some of them are responsible for the colour, smell, and durability of the wood.

Acknowledgments

It is necessary to dedicate this thesis space to all the people who have contributed to the completion of this research work.

First of all, I thank my tutor, Professor Enza Fazio, who followed me with dedication and expertise, accompanying me in the world of Raman and IR spectroscopy, giving me the courage to move forward even when I thought I could not do it.

I would also like to thank my co-tutor, Dr Silvia Capuani, Professor Francesca Granata and Dr Carmelo Corsaro, for being my point of reference for any doubt and constant help during all phases of the experimentation.

I would also like to thank Dr Alina Adams, for her extreme courtesy and for hosting me in her NMR laboratory at RWTH Aachen University.

Thanks also to Dr Aoife Daly for hosting me in her TIMBER ERC Project at the University of Copenhagen and for teaching me wood anatomy and dendrochronology.

I would also like to thank the MIFT Department of the University of Messina for welcoming me despite my humanistic behavior and thanks to the Coordinator Professor Vincenza Crupi, for her availability and kindness. It was a pleasure to be a PhD student at University of Messina.

Last but not least, thanks to my family and my father who transmitted me the passion for research and imaging.